Numerical Analysis of Double-O-Tube Shield Tunnelling

A thesis submitted to Imperial College London in partial fulfilment of the requirements for the degree of Doctor of Philosophy

by

Ding Zhou

Department of Civil and Environmental Engineering

Imperial College London

London SW7 2AZ

March 2022

Persistence is fruitful.

坚持就是胜利

DECLARATION

The work presented in this thesis was undertaken in the Department of Civil and Environmental Engineering at Imperial College London. This thesis is the result of my own work and any quotation from, or description of, the work of others has been appropriately referenced, whether published or unpublished. This thesis is not the same as any that I have submitted for any degree, diploma, or other qualification at any other university. No part of this thesis has been or is being concurrently submitted for any such degree, diploma, or other qualification.

The copyright of this thesis rests with the author and is made available under a Creative Commons Attribution Non-Commercial No Derivatives licence. Researchers are free to copy, distribute or transmit the thesis on the condition that they attribute it, that they do not use it for commercial purposes and that they do not alter, transform, or build upon it. For any reuse or redistribution, researchers must make clear to others the licence terms of this work.

Ding Zhou

London, March 2022

Abstract

Underground tunnels play an important role in the mass transportation systems in modern cities. The ground movements induced by tunnel excavation in short term and long term are of great concern due to their potentially irrecoverable impact on the surrounding buildings and services. The numerical modelling, in conjunction with well documented case studies to validate the modelling approach, is an efficient methodology for adequate and robust predictions of the ground response caused by tunnelling. The Double-O-Tube (DOT) shield tunnelling is a new technology developed since 1989, and has been applied in over 20 engineering cases in China and Japan. Due to its unique double tube cross-sectional shape, the DOT tunnel is expected to perform differently in mechanical terms compared to traditional twin tunnels. Therefore, a systematic study of its engineering behaviour, of the ground response and of tunnel lining is necessary. This research involves numerical simulations and investigation of DOT construction in soft clay and stiff clay conditions, represented by Shanghai clay and London clay respectively, using Imperial College Finite Element Program (ICFEP).

In the first part of the thesis, the Shanghai clay and the whole ground profile are characterised referring to the laboratory data and field experimental evidence. A numerical model is developed in ICFEP for the case of DOT tunnel in the Shanghai Metro system, applying an extended Modified Cam Clay (MCC) model to represent the ground conditions and discretising the tunnel lining with elastic beam elements. The predicted short-term settlement troughs achieve good agreement with the field monitoring data, validating the reliability of the numerical model. Additional sensitivity studies investigate the conditions of the tunnel lining joints and the effects of the pressure exerted by grouting in the constructions process.

The second part of the thesis focuses on the modelling of the reinforced concrete segments of tunnel lining using an advanced elasto-plastic concrete model. The model validation is performed with the simulation of loading tests on a single lining segment performed in the laboratory, demonstrating very close agreement between the predicted and measured segment deflections under applied load and an accurate onset of cracking in concrete. Such a concrete model is applied in the analysss of DOT tunnelling in Shanghai to investigate its merits against a simpler lining representation.

Finally, the application of DOT tunnelling is explored in stiff clay ground conditions, utilising the Jubilee Line Extension and the Crossrail case studies in London clay, and applying an advanced kinematic surface hardening model for soil behaviour. The comparison of numerical predictions against field monitoring data demonstrates comparable magnitudes of ground movements mobilised by DOT tunnelling with respect to conventional twin tunnelling.

Acknowledgements

I would like to express my deepest gratitude to my supervisor Prof. Lidija Zdravkovic for providing continuous guidance and help throughout the project. Her supervision greatly enhanced my geotechnical knowledge and research ability over the past four years. Despite the difficulties and inconveniences caused by the Covid-19 pandemic, my research still carried out normally and the thesis has been completed in time with her dedicated support. I am also grateful to Prof. David Potts for his generous time in supporting any issues encountered with running ICFEP, as well as for his constructive comments on my early and late stage progress reviews. As the core research tool in my project, the platform of ICFEP developed by both of them is highly acknowledged.

My research is fully funded by Chinese Scholarship Council (CSC), covering my tuition fees and living expenses for four academic years. Their financial support is greatly appreciated. I would also like to acknowledge the Imperial College London and their Graduate School, who gave me a lot of opportunity to attend training courses free of charge to develop various transferable skills and for helping with academic English writing, presentation and time management. Especially in the year of my writing-up, Lidija, Dr Lorraine Craig and a few other staff within college gave me timely and efficient help to overcome some difficulties in my life, their kindness will never be forgotten in my life.

I feel very lucky to have worked and studied in the Geotechnics section, Department of Civil and Environmental Engineering. I will always remember the help and useful suggestions offered by Prof. Jamie Standing, Dr. David Taborda, Dr. Stavroula Kontoe and other research staff on my first and third years' colloquia, and sometimes during the lunch-time in the lab or in ICFEP rooms. I would also like to thank my colleagues Ryan, David, Benjamin, Giulia, and other numerical based researchers, for answering my academic questions and teaching me some tips of numerical analysis. Tara, Zixiao and Sihua, who worked in DEM, geology and lab testing respectively, have also shared their useful experience with me that broadens my horizons. They also helped a lot in my daily life in London. Special thanks are given to Wenjie and Tingfa, who continuously retained an interest in my research and career like elder brothers. I have learnt a lot from them. Furthermore, I would particularly thank Mattia, a UROP student who worked with me on the DOT simulations in London clay and provided some help with the data output. We spent very happy time working on this in the ICFEP rooms.

Finally, I would give sincere thanks to my mom Shuzhen and my dad Zhangchao from the bottom of my heart. They gave me infinite energy and faith to remain enthusiastic and happy with my work and life. Their love is absolutely irreplaceable for me in my life.

Table of Contents

DECLARATION 3

Abstract 4

Acknowledgements 5

LIST OF FIGURES 11

LIST OF TABLES 20

Chapter 1 Introduction 22

1.1 Background and motivation for research 22

1.2 Research methodology 23

1.3 Thesis outline 24

Chapter 2 Literature Review 26

2.1 Contemporary conventional tunnelling methods 26

2.1.1 New Austrian Tunnelling Method (NATM) 26

2.1.2 Earth Pressure Balance Method (EPBM) 29

2.1.3 Cut-and-cover method 31

2.2 DOT tunnelling technology 32

2.3 Tunnel lining 37

2.3.1 Tunnel lining behaviour 37

2.3.2 Research on concrete tunnel lining 40

2.4 Empirical methods to estimate ground movements 41

2.4.1 Peck-Fujita method for single tunnel 41

2.4.2 Superposition method for twin tunnels 42

2.4.3 Empirical methods to predict the settlement of DOT 43

2.5 Summary points 45

Chapter 3 Development of the Shanghai ground model 47

3.1 Introduction 47
3.2 Ground conditions in Shanghai 48
3.2.1 Layering of Shanghai sediments 48
3.2.2 Characteristics of aquifers and the land subsidence 51
3.3 Main properties of Shanghai clay 54
3.3.1 Basic characterisation of Shanghai clay 54
3.3.2 Permeability of the Shanghai clay 59
3.4 Selection and calibration of a constitutive model 60
3.4.1 Introduction of the extended Modified Cam Clay (MCC) model 60
3.4.2 Calibration of the extended Modified Cam Clay (MCC) model 63
3.4.3 Undrain shear strength of the Shanghai clay 70
3.4.4 Introduction of the Imperial College Generalised Small Strain Stiffness model (ICG3S) 71
3.4.5 Calibration of the ICG3S model 73
3.5 Shear Stiffness Degradation 75
3.6 Summary of parameters in extended MCC model and ICG3S model 77
3.7 Summary points 78
Chapter 4.Numerical model of the Shanghai DOT tunnelling case study 79
4.1 Introduction 79
4.2 Base case analysis 79
4.2.1 Background of the base case analysis 79
4.2.2 Initialisation of ground conditions 81
4.2.3 Beam element lining model 82
4.2.4 Simulation process and boundary conditions of the base case analysis 84
4.2.5 Results of base case analysis and discussion 87
4.3 Parametric study 98
4.3.1 Construction simulation methods 98
4.3.2 Lining properties 101

4.4 Influence of grouting in DOT constructions 105
4.4.1 Synchronous grouting pressure diffusion 105
4.4.2 Strength evolution of the grouted soil 107
4.4.3 Small strain stiffness of the cemented soil 109
4.4.4 Numerical modelling of DOT with grouting simulation 111
4.5 Summary points 119
Chapter 5.Development of the modelling framework for DOT concrete segment 121
5.1 Introduction of a concrete constitutive model 121
5.1.1 Some existing concrete models 121
5.1.2 Modified Chen concrete model 122
5.1.3 A nonlocal strain-softening method for the analysis of concrete loading 127
5.2 Reinforced concrete characterisation and modelling 128
5.2.1 Introduction of the reinforcement design for the lining segment 128
5.2.2 Bar element and softening plastic model for reinforcement 131
5.3 Calibration of the modified Chen concrete constitutive model 132
5.3.1 Shear strength of C50 concrete 133
5.3.2 Compressive strength of C50 concrete 133
5.3.3 Tensile strength of C50 concrete 136
5.3.4 Summary of modified Chen model parameters for C50 concrete 137
5.4 Laboratory experiments on single concrete segments 139
5.4.1 Design of the single segment test 139
5.4.2 Details of the single concrete segment in the tests 140
5.4.3 Arrangement of measurements 141
5.5 Validation of the concrete model 142
5.5.1 2D modelling of the single segment test 142
5.5.2 Deflection of the segment mid-arch point 144
5.5.3 Strain evolution in the reinforcement 146

5.5.4 Cracking of the concrete in PZW1 test 148
5.5.5 Cracking of the concrete in PZW2 test 150
5.5.6 Sensitivity of DL and the interface stiffness in PZW2 simulation 153
5.5.7 Evolution of concrete strain on the side of segment at mid-arc position 154
5.5.8 Failure mechanism of the single segment under jack loading for the tests 158
5.5.9 Investigation of the concrete grade (PZW1) 158
5.6 3D analysis of the single segment PZW1 test 161
5.6.1 Mesh and boundary conditions of the 3D single segment test 161
5.6.2 Comparison of the results between 3D and 2D analysis 162
5.7 Summary points 165
Chapter 6.Base case DOT tunnel analysis with advanced concrete model 166
6.1 Discretisation of the Shanghai case study with solid-element lining 166
6.2 Comparison of the results against beam-element lining 169
6.2.1 Ground response induced from tunnelling 169
6.2.2 Internal forces of the lining 171
6.3 Summary points 181
Chapter 7.Study of Twin tunnels and DOT in stiff clay 182
7.1 Introduction 182
7.2 Ground conditions in London 182
7.3 Main characteristics of London clay 186
7.4 Selection and calibration of a constitutive models 188
7.4.1 The modified two surface kinematic hardening soil model (M2-SKH) 188
7.4.2 Modelling of tunnel lining 193
7.5 Numerical modelling of tunnels at St James Park and at Hyde Park 193
7.5.1 Numerical modelling of tunnelling at Saint James' Park 193
7.5.2 Numerical modelling of tunnels at Hyde Park 203
7.6 Ground surface movements due to tunnelling 208

7.6.1 Ground surface movements due to tunnelling in short term 209
7.6.2 Long term settlement of ground surface 222
7.7 Subsurface ground surface movements due to tunnelling 227
7.7.1 St James' Park 227
7.7.2 Hyde Park 236
7.8 Summary points 240
Chapter 8.Conclusions and recommendations for future research 242
8.1 Introduction 242
8.2 Shanghai geology and Development of the Shanghai ground model 243
8.3 Numerical model of the Shanghai DOT tunnelling case study 244
8.4 Development of the modelling framework for DOT concrete segment 245
8.5 Base case DOT tunnel analysis with advanced concrete model 246
8.6 Study of Twin tunnels and DOT in stiff clay 247
8.7 Recommendations for future research 249
Reference 251

LIST OF FIGURES

Figure 2.1: Structure of lining constructed with umbrella arch method (Ocak & Selcuk, 2017) 28
Figure 2.2: Graph of soil particle distribution curves suitable for EPBM (British Tunnelling Society in association with the Institution of Civil Engineers, 2005) 30
Figure 2.3: DOT machine (photo from geor.co.jp) 33
Figure 2.4: Segment types of DOT lining (Sun 2007). a) upper seagull segment; b) lower seagull segment; c) column segment 34
Figure 2.5: Connection of the tunnel lining. A) Staggered installation among adjacent rings; b) M27 bolts for segments connection. 34
Figure 2.6: The photo of DOT lining in the site of Shanghai Metro Line 6 35
Figure 2.7: Influence of DOT rolling in the ground settlement (Yonei, 2000) 36
Figure 2.8: Structure of the composite segment (Zhang & Koizumi, 2010) 39
Figure 2.9: Predicted settlement of twin tunnels by superposition method (Laefer & Kim, 2004) 43
Figure 2.10: Calculation of DOT settlement with superposition method (Zhu et al., 2006) 44
Figure 2.11: Calculation of DOT settlement with equalised circular method (by Lv et al., 2006) 45
Figure 3.1: Plan view of the Shanghai area and the cross-section lines AA' and BB' (Xu et al., 2009) . 49
Figure 3.2: Cross-section A-A' (in **.**Figure 3.1) of the Quaternary Strata of Shanghai ground (Xu et al., 2009; based on SGEAEB, 2002) 50
Figure 3.3 Geotechnical properties of Shanghai clay (Wu, et al., 2014) 56
Figure 3.4: Shanghai soil profile near Hongqiao Airport (Liu et al., 2019) 57
Figure 3.5: a) pore water pressure distribution; b) profile of vertical effective stress. 59
Figure 3.6: Profiles of Shanghai clay permeability. a) Located at the skew position between Line 11 and Line 4 of the Shanghai Metro (Zhang & Huang, 2013); b) located at the east side of Huangpu River, Metro Line 9 (Tan & Wei, 2012); c) Profile of permeability adopted for the numerical modelling of Shanghai clay in this research 60
Figure 3.7: a) Yield surface; b) the isotropic virgin consolidation line in p' - J space 61
Figure 3.8: Stress path of undrained triaxial compression test ..... **Error! Bookmark not defined.**
Figure 3.9: Coefficient of compressibility a) Cc; b) λ 63
Figure 3.10: Interpretation κ from unloading curves in e-lnp' plane: a) K_0 consolidation test (Jiu & Huang, 2017); b) isotropic triaxial compression test on five sets of specimens (Sun et al., 2010) 64
Figure 3.11: Profile of compressibility built for modelling: a) The slope of NCL λ; b) The slope of swelling line κ 65
Figure 3.12: OCR value of the Shanghai clay. a) Determined from oedometer test, FVT and the average value of FVT (Gao & Chen, 2017); b) The characterised profile of OCR in the model compared against

the average value derived from FVT 66
Figure 3.13: Change of K_0 during the K_0 consolidation test for saturated Shanghai clay (vertical stress controlled). a) Consolidated to 180kPa effective vertical stress; b) consolidated to 350kPa effective vertical stress and then unloading; c) consolidated to 750kPa effective vertical stress and then unloading. 68
Figure 3.14: Change of K_0 during the K_0 consolidation test for saturated Shanghai clay (radial stress controlled). a) Consolidated to 100kPa effective radial stress; b) consolidated to 200kPa effective radial stress and then unloading; c) consolidated to 400kPa effective radial stress and then unloading 68
Figure 3.15: Relationship between K_0 and OCR values for Shanghai clay. a) radial pressure unloaded from 200kPa to 100kPa; b) radial pressure unloaded from 400kPa to 200kPa. (modified from Jiu & Huang, 2017) 69
Figure 3.16: K_0 profile of Shanghai clay modelling. 70
Figure 3.17: Undrained shear strength profile in comparison with the measured data from Shanghai Metro Line 2 (Lee et al., 1999) 71
Figure 3.18: Degradation curve of shear stiffness 72
Figure 3.19: Maximum shear stiffness evolving with mean effective stress in different layers 74
Figure 3.20: Maximum stiffness distribution for modelling Shanghai clay 75
Figure 3.21: Normalized shear stiffness with shear strain for Shanghai clay (Zhang et al., 2017) 76
Figure 4.1: Location of DOT tunnel section of Shanghai Metro Line 6 80
Figure 4.2: Two dimensional mesh for the base case analysis 82
Figure 4.3: Geometry information of the tunnel lining for the modelling 83
Figure 4.4: modelling of DOT lining and joint (short beam element highlighted with spots) 83
Figure 4.5: The applied normal support stress around the tunnel boundary during excavating. a) incremental stress; b) total support stress after 50 increments; c) removal of the normal supporting stress. 85
Figure 4.6: Development of maximum settlement and the speed of Shanghai Metro Line 2. a) Maximum settlement; b) Settlement rate (data from Ao & Zhang, 2011). 87
Figure 4.7: Predicted surface settlement compared against field data. a) The settlement troughs; b) the depth of DOT tunnel in the simulation (measured data from Wei et al. (2011)). 88
Figure 4.8: Interpreted volume loss for a number of DOT rings on Metro Line 6 (Lv & Zhang, 2006) . 89
Figure 4.9: Settlement of ground surface of DOT simulation for short term. 90
Figure 4.10: Subsurface settlement troughs: a) after excavation; b) 28 days after excavation; c) 100 days after excavation; d) 1000 days after excavation. 91
Figure 4.11: Measurement of long term settlement of Shanghai Metro Line 2 on different sections (Ao

& Zhang, 2011). 92
Figure 4.12: Long term settlement predicted for DOT. a) transverse settlement; b) maximum settlement 93
Figure 4.13: The evolution of pore water pressure in short and long term (kPa): a) end of excavation at increment 50; b) 1000 days consolidation; c) end of long term consolidation 95
Figure 4.14: Distribution of internal force along the lining. a) axial force; b) bending moment 96
Figure 4.15: Predicted deformation shape of the DOT ring in long term (80 years) 97
Figure 4.16: Settlement of ground surface in DOT simulation using volume loss control method 99
Figure 4.17: Comparison of settlement between two simulation methods on different stages. a) after excavation; b) 100 days after excavation; 99
Figure 4.18: Stabilised bending moment among different concrete grades 101
Figure 4.19: Stabilised axial force among different concrete grades 102
Figure 4.20: Distribution of lining internal force for different joint stiffness. a) 7 days after excavation; b) 28 days; c) 100 days; d) 1000 days; e) 80 years; 104
Figure 4.21: Evolution of grouting pressure during the tunnelling from Sophia tunnel project in Betuwe (Qiao et al., 2018) 106
Figure 4.22: grouts diffusion into the soil (Ye et al., 2018) 106
Figure 4.23: strength of cement stabilised soil with different cement content and curing environment (modified from Bahar et al., (2004)) 108
Figure 4.24: Influence of cement content on strength of clays (modified from Wang et al., 2010) 109
Figure 4.25: Maximum small strain shear modulus of cemented kaolinite with curing time: a) 10% cement; b) 15% cement; c) 20% cement (modified from Fatahi et al., (2013)) 110
Figure 4.26: Maximum shear modulus with deviatoric strength q for a variety of cemented soils (Rinaldi & Santamarina, 2008; Tatsuoka & Shinbuya, 1991) 111
Figure 4.27: The DOT mesh of Shanghai Metro Line 6 (Ring 130; the shadow area is the construction gap for grouting) 112
Figure 4.28: Demonstration of bidirectional grouting pressure 113
Figure 4.29: Evolution of linear properties of the grouts during the curing period (Oh & Ziegler, 2014) 114
Figure 4.30: Settlement development after grouting under different pressures and reduction ratios: a)200kPa grouting pressure; b) 300kPa grouting pressure; c) 400kPa grouting pressure; d) settlement trough of the ground surface at 100 days after tunnelling under the grouting pressure of 200kPa without pressure reduction on the lining. 116
Figure 4.31: The deviation of settlement evolution curves among different grouting pressures: a) 95% pressure reduction on the lining; b) 90% pressure reduction on the lining. 116

Figure 4.32: Axial force (hooping force) of DOT lining at the end of consolidation terms: a) short term (100 days); b) end of long term (80 years)..... 117
Figure 4.33:Bending moment of DOT lining at the end of consolidation terms: a) short term (100 days); b) end of long term (80 years) 118
Figure 4.34: Axial force (hooping force) of DOT lining at the end of consolidation terms: a) short term (100 days); b) end of long term (80 years)..... 118
Figure 4.35: Bending moment of DOT lining at the end of consolidation terms: a) short term (100 days); b) end of long term (80 years) 119
Figure 5.1: the yield surfaces of compression and tension for Chen concrete model in a) biaxial space; b) J-P stress space (from Schutz, 2010)..... 123
Figure 5.2: Stress-strain relation of concrete under uniaxial loading condition (from Chen, 1982) .. 123
Figure 5.3: Modified yield surface and original yield surface in a) Biaxial tension space; b) J-P tension stress space 125
Figure 5.4: Normalised stress-strain relation for concrete in compression 126
Figure 5.5: Normalised stress-strain relation for concrete in tension (exponential option of softening) 127
Figure 5.6: View of individual segments 129
Figure 5.7: Reinforcement of a single segment (Plan view) 129
Figure 5.8: Cross-section type 1 of the segment with stiffener and the main reinforcements..... 129
Figure 5.9: Cross-section type 2 of the segment with stirrup and the main reinforcement 129
Figure 5.10: Typical stress-strain curve of reinforcement in tension (Eurocode 3)..... 130
Figure 5.11: Softening plastic strain characterisation of the reinforcement modelled with bar element 132
Figure 5.12: Schematic of stress-strain relation for concrete under uniaxial compressive loading (Model Code for Concrete Structures (2010)) 134
Figure 5.13: Schematic of initial tangent modulus E_{ci} and reduced modulus E_c (Model Code for Concrete Structures, 2010) 135
Figure 5.14: Compression curve of C50 concrete calibrated for the model..... 135
Figure 5.15: a) schematic of stress-strain relation for concrete under tensile loading; b) stress-strain relation calibrated for C50 concrete. 137
Figure 5.16: Testing arrangement of the single segment loading PZW1: a) photograph of the set up; b) schematic of the loading and boundary conditions (unit:mm). 140
Figure 5.17: Testing arrangement of the single segment loading PZW2: a) photograph of the equipment; b) schematic of the loading and boundary conditions..... 140
Figure 5.18: Alignment of strain gauges for main reinforcement (Zhou, 2011) 142

Figure 5.19: Schematic of the strain gauges glued on the concrete of the segment 142
Figure 5.20: 2D mesh for single concrete segment testing a) PZW1; b) PZW2. 143
Figure 5.21: Evolution of middle deflection during the test a) PZW1; b) PZW2 145
Figure 5.22: Illustration of mesh deformation of the segment under jack loading a) PZW1; b) PZW2 146
Figure 5.23: Axial strain of reinforcement at middle positions for PZW1 test: a) Lower reinforcement; b) upper reinforcement. 147
Figure 5.24: Axial strain of reinforcement at middle positions for PZW2 test: a) Lower reinforcement; b) upper reinforcement. 147
Figure 5.25: Axial force-strain relation of a) upper reinforcement; b) lower reinforcement in the loading test of the segment 148
Figure 5.26: Cracks of the concrete in PZW1 test when the segment came to failure a) view from under the intrados side; b) crack across the segment body – view on one longitudinal segment side 149
Figure 5.27: The evolution of horizontal stress across the mid-arc cross-section with loads from numerical analysis (PZW1) 150
Figure 5.28: Cracks of the concrete in PZW2 test when the segment came to failure a) intrados side; b) crack across the segment body on one side 151
Figure 5.29: The evolution of horizontal stress across the mid-arc cross-section with loads from numerical analysis (PZW2) 151
Figure 5.30: Orientation of accumulated principle stress under failure load (1248.15kN) in PZW2 test. a) major (tensile) principle stress; b) minor (compressive) principle stress. 152
Figure 5.31: The evolution of deflection for different DL value 153
Figure 5.32: The evolution of deflection for different joint stiffness 154
Figure 5.33: Evolution of concrete horizontal strain on the mid-arc extrados under loading in PZW1 test 155
Figure 5.34: Evolution of concrete horizontal strain on the mid-arc intrados and two trisection points under loading in PZW1 test 156
Figure 5.35: Evolution of concrete horizontal strain on the mid-arc extrados under loading in PZW2 test 156
Figure 5.36: Evolution of concrete horizontal strain on the mid-arc intrados and two trisection points under lower level load in PZW2 test 157
Figure 5.37: Evolution of concrete horizontal strain on the mid-arc intrados and two trisection points in PZW2 test 157
Figure 5.38: Comparison of mechanical behaviours between C30 and C50 a) compressive strain; b) tensile strain 159

Figure 5.39: Deflection of C30 concrete segment under jack loading 160
Figure 5.40: Axial strain of reinforcement at middle positions for C30 segment: a) Lower reinforcement; b) upper reinforcement. 160
Figure 5.41: 3D mesh for single segment loading test 162
Figure 5.42: Distribution of main reinforcement in the 3D model 162
Figure 5.43: Comparison of segment deflection between 2D and 3D analysis 163
Figure 5.44: Axial strain of reinforcement at mid-arc position in 3D analysis: a) Lower reinforcement; b) upper reinforcement. 163
Figure 5.45: Horizontal strain of concrete at mid-arc position in 3D analysis: a) mid-arc extrados; b) 10cm to mid-arc extrados; c) 10 cm to mid-arc intrados; d) mid-arc intrados 164
Figure 6.1: Two dimensional mesh for the base case analysis with solid element lining 166
Figure 6.2: Mesh details for the concrete lining. a) half DOT ring; b) detailed components at a joint. 167
Figure 6.3: Alignment of the bolts on the joint 168
Figure 6.4: Tied degrees of freedom for the nodes 1 and 2. 169
Figure 6.5: Comparison of ground settlement using two element types for modelling the DOT lining. a) surface settlement at 100 days and 100 days after excavation; b) 2m depth settlement at 100 days after excavation; c) 6m depth settlement at 100 days; d) 10m depth settlement at 100 days. 170
Figure 6.6: Comparison of long term settlement between two element types lining. 171
Figure 6.7: Bending moments along the distance curve. a) 100 days; b) 80 years. 172
Figure 6.8: Axial forces (hoop force) along the distance curve. a) 100 days; b) 80 years. 173
Figure 6.9: Lining deformation at 80 years after tunnelling. a) Solid-element lining; b) Beam element lining 173
Figure 6.10: Contours of principal stresses at 80 years. a) major (compressive) principle stress $\sigma 3$; b) minor (tensile) principle stress $\sigma 1$ 174
Figure 6.11: Orientations of principal stresses at 80 years. a) major (compressive) principle stress $\sigma 3$; b) minor (tensile) principle stress $\sigma 1$ 174
Figure 6.12: Mean effective stress p' (positive in tension). a) 100 days ; b) 80 years 175
Figure 6.13: Deviatoric stress J. a) 100 days ; b) 80 years 175
Figure 6.14: Change of stress level. a) 100 days; b) 80 years. 176
Figure 6.15: Axial force of reinforcement. a) Extrados reinforcement; b) Intrados reinforcement 177
Figure 6.16: Internal force of the bolts. a) Axial force; b) Bending moment. 178
Figure 6.17: Comparison on bending moment between original and softer bolts (80 years). a) bending moment; b) axial force 179
Figure 6.18: Comparison on stress level between original and softer bolts. a) 100 days; b) 80 years.

.....180
Figure 7.1: Ground profile and twin tunnel boring position at St. James' Park adopted for numerical modelling (Avgerinos, 2014) 184
Figure 7.2: Ground profile and twin tunnel boring position at Hyde Park adopted for modelling 185
Figure 7.3： Ground profile and pore water distribution of (a) St. James' Park; (b) Hyde Park 185
Figure 7.4: Normalised stiffness degradation curves for a) undrained triaxial compression; b) undrained triaxial extension (modified after Hight et al., 2007). 187
Figure 7.5: Compression and swelling curves from natural and reconstituted specimens of London clay unit A and B2 (Gasparre & Coop, 2008).....187
Figure 7.6: The M2-SKH model: a) outer bounding surface and the kinematic yield surface ('bubble'); b) different shapes for yield and potential surface in the deviatoric plane 189
Figure 7.7: Calibration of B2 layer, comparing with tests (Avgerinos, 2014): a) oedometer compression curve; b) stress path from triaxial compression test; c) stiffness degradation from triaxial compression tests;.....192
Figure 7.8: Finite element mesh for twin tunnels simulation at St. James' Park.....194
Figure 7.9: Schemes of stress history reproduction a) deactivating top two layers; b) incrementally unloading overburden pressure 196
Figure 7.10: Ground profile and pore water distribution (hydrostatic) at the end of geological history 196
Figure 7.11: Sketch of the stress path in geoligical history reproduction for London clay 197
Figure 7.12: K_0 profile predicted for two calibrations a) at the end of erosion (inc 200);b) at the end of geological history (inc. 230). 198
Figure 7.13: a) $p0'$ and b) p' profile along the depth at the end of geological history (inc. 230). 199
Figure 7.14: $p0'/p'$ profile along the depth at the end of geological history.....199
Figure 7.15: DOT mesh for 'deeper' case at St. James' Park 201
Figure 7.16: DOT mesh for 'shallower' case at St. James' Park 201
Figure 7.17: geometry of DOT ring applied in DOT simulations at St. James' Park 201
Figure 7.18: Profile of anisotropic permeability of London clay A3 and B2 units 203
Figure 7.19: Mesh of twin tunnels analysis for Crossrail tunnel at Hyde Park site.....204
Figure 7.20: Profile of a) K_0 and b) Yield stress ratio (YSR) before and after the underdrainage 205
Figure 7.21: Mesh for DOT modelling at Hyde Park 206
Figure 7.22: Profile of anisotropic permeability of London clay A3 and B2 units 207
Figure 7.23: Cross-section map of rod extensometers and eletrolevel inclinometers installation positions (Nyren, 1998).....208
Figure 7.24: Cross-section map of rod extensometer boreholes in the main instrumentation alignment

(after Wan, 2014b). 209
Figure 7.25: Ground surface settlement due to westbound tunnel construction. 210
Figure 7.26: Normalised ground surface settlement troughs due to westbound tunnel. 210
Figure 7.27: Settlement of twin tunnels compared to field data 211
Figure 7.28: Development of westbound tunnel settlement during the intermediate period 211
Figure 7.29: Predicted settlement for 'deeper' DOT in short term (low triaxial). 213
Figure 7.30: Predicted settlement for 'shallower' DOT in short term (low triaxial). 213
Figure 7.31: Normalised settlement of 'deeper' DOT and westbound tunnels immediately after excavation 213
Figure 7.32: Normalised settlement of 'deeper' DOT and 'shallower' DOT. 214
Figure 7.33: Comparison of settlement troughs after single tunnel (wb)/ DOT excavation. 215
Figure 7.34: Comparison of settlement troughs after twin tunnels (wb&eb) / DOT excavation 215
Figure 7.35: Settlement of ground surface after westbound excavation in Hyde Park site a) predicted settlement against field data; b) normalised settlement 217
Figure 7.36: Settlement of ground surface prior to excavation of the eastbound tunnel: a) impermeable lining; b) permeable lining 218
Figure 7.37: Normalised settlement of ground surface prior to eastbound excavation 218
Figure 7.38: Settlement of ground surface: a) due to eastbound tunnelling; b) overall settlement immediately after eb with field data deducted from Gaussian approximation 219
Figure 7.39: Predicted settlement of twin tunnelling for short term in Hyde Park site: a) impermeable lining; b) permeable lining 220
Figure 7.40: Settlement of ground surface after DOT excavation in Hyde Park site. a) settlement troughs; b) normalised settlement 221
Figure 7.41: Evolution of surface settlement after DOT excavation for short term: a) impermeable lining; b) permeable lining 222
Figure 7.42: Comparison of settlement troughs between DOT and twin tunnels for short term. a) impermeable lining; b) permeable lining 222
Figure 7.43: Predicted settlement for twin tunnels after eastbound tunnelling for long term (low triaxial). 223
Figure 7.44: Predicted settlement for twin tunnels after eastbound tunnelling for long term (high both) 224
Figure 7.45: Predicted settlement for twin tunnels for tunnel life term (high both). 224
Figure 7.46: Long term settlement of 'deeper' DOT tunnel 225
Figure 7.47: Long term settlement of 'shallower' DOT tunnel 225
Figure 7.48: Evolution of the maximum ground surface settlement of tunnelling in St James' park 226

Figure 7.49: Predicted settlement of ground surface in Hyde Park site for long term: a) twin tunnels; b) DOT tunnel 227
Figure 7.50: Subsurface settlement measured at A, B and C axes (-ve is settlement), after WB tunnel construction. 228
Figure 7.51: Horizontal displacement measured at C axis, after WB tunnel construction. 229
Figure 7.52: Comparison of subsurface vertical displacement on A, B &C lines after eastbound construction and 1 year post EB construction 230
Figure 7.53: Alignment of monitoring axes in DOT simulation: (a) deeper DOT; (b) shallower DOT . 231
Figure 7.54: Subsurface vertical displacement along a) Ax and b) Bx axes; horizontal displacement along c) Ax axis; 'deeper DOT' simulation in short term; 'low triaxial' calibration 233
Figure 7.55: Subsurface vertical displacement along a) Ax and b) Bx axes; horizontal displacement along c) Ax axis; 'shallower DOT' simulation in short term; 'low triaxial' calibration 234
Figure 7.56: Subsurface settlement along Ax and Bx of 'deeper DOT' simulation in long term 235
Figure 7.57: Long term (100 years) subsurface vertical displacement at a) A (Ax); b) B (Bx) axes..... 236
Figure 7.58: Subsurface settlement after WB/DOT excavation for twin/DOT tunnels at different depths 237
Figure 7.59: Subsurface settlement prior to EB excavation/74 days after DOT excavation for twin/DOT tunnels at different depths 239
Figure 7.60: Predicted subsurface settlement troughs of twin/DOT tunnels at different depths for long term (permeable lining) 240

LIST OF TABLES

Table 2.1: Main technical index of the DOT machine for tunneling in Shanghai Metro Line 6 (Sun, 2007) 33
Table 3.1: Quaternary stratigraphic chart (Modified from SGEAEB 2002) 51
Table 3.2: Aquifer conditions of Holocene series and Pleistocene series (modified after Xu et al., 2009) 52
Table 3.3: The data of factors influencing the subsidence of the urban area of Shanghai 54
Table 3.4: Shear strength of the soil at the site of excavation near Hongqiao Airport (Liu et al, 2019) 56
Table 3.5: Soil conditions of lot 9 in Shanghai Metro Line 6 (modified after Sun, 2007) 58
Table 3.6: Summary of parameters required for calibration of the S_u profile 62
Table 3.7: Summary of parameters calibrated for the small strain stiffness degradation 73
Table 3.8: Parameters for maximum shear stiffness expression determined via linear regression 74
Table 3.9: Parameters for extended MCC model and ICG3S model 77
Table 4.1: Ground layering and the mechanical properties for the base analysis 82
Table 4.2: Mechanical properties DOT lining in the base case analysis 83
Table 4.3: Sequence of DOT tunnelling and post-construction analysis 86
Table 4.4: The volume loss and the maximum settlement measured from the field at 100 days (Wei et al., 2011) 88
Table 4.5: Maximum settlement and volume loss on the ground surface of DOT simulation 90
Table 4.6: The volume loss output at different depths for short term analysis 91
Table 4.7: The sequence of tunnel simulation using volume loss control method 100
Table 4.8: The series of simulation on different concrete grades 101
Table 4.9: The series of simulation on different joint stiffness 102
Table 4.10: Reduced grouting pressure acting on the lining segment considering infiltration 107
Table 4.11: Simulation of grouting pressure around the lining 113
Table 4.12: Linear properties development of grouting material with time 114
Table 5.1: Information of reinforcement of the single segment 130
Table 5.2: The mechanical parameters of HRB reinforcement bar (Eurocode 3) 131
Table 5.3: Parameters determined for the softening plastic model in reinforcement characterisation 132
Table 5.4: Peak strain of a concrete prism under axial compression test (assuming characteristic strength $fcu = 50MPa$) 134
Table 5.5: Parameters adopted for C50 concrete compression characterisation 136

Table 5.6: Parameters adopted for C50 concrete tension characterisation..... 137
Table 5.7: Calibrated parameters of concrete in the modified Chen concrete model..... 138
Table 5.8: Information of reinforcement cage for the single segment 141
Table 5.9: Mechanical properties of the main reinforcement and the concrete 141
Table 5.10: Incremental loading on the segment..... 143
Table 5.11: The maximum tensile plastic strain at the mid-arc of intrados in PZW2 test..... 152
Table 5.12: Parameters calibrated for C30 concrete in the modified Chen concrete model..... 159
Table 6.1: Linear properties of the bolt 167
Table 6.2: Proportion of bolts contributing to the bending resistance 177
Table 6.3: Contributions of bolts and concrete on joints to the axial force resistance..... 178
Table 7.1: Parameters of 'bubble' model calibrated for London clay 192
Table 7.2: Analysis stages of twin tunnels simulation for the case at St. James' Park 195
Table 7.3: Volume loss and unloading percentage for DOT tunnel and westbound twin tunnel 200
Table 7.4: Analysis stages of DOT tunnels simulation for the case at St. James' Park 202
Table 7.5: Permeability profile of the London clay (St James' Park) 202
Table 7.6: Construction sequence of Crossrail tunnel modelling 205
Table 7.7: Construction sequence of DOT modelling at Hyde Park..... 206
Table 7.8: Anisotropic permeability adopted for the simulation of tunnelling in Hyde Park..... 208
Table 7.9: Volume loss achieved in the analysis for each case..... 216
Table 7.10: Unloading percentage of tunnelling analysis for Hyde Park site 216
Table 7.11: Maximum settlement of the ground surface post construction of WB and DOT..... 221
Table 7.12: Maximum settlement of ground surface in long term..... 226

Chapter 1. Introduction

1.1 Background and motivation for research

Tunnelling construction is important in the traffic system around the world. Much attention is being paid to developing tunnel engineering to meet the increasing quality demand posed by improving safety factors, prolonging service life and reducing impact on surrounding structures. The ground surface settlement, structure serviceability, and long-term displacement behaviour are of vital importance to tunnelling and other underground structures design. Therefore, soil properties, groundwater level, construction schemes and materials for building structures should be carefully taken into consideration in the design work. Several methods have been developed and applied to predict the tunnelling-induced ground movements and the likely damage of buildings and other existing services, among which numerical analysis plays a significant part in modern tunnel design and is recognised as providing far better predictive reliability than conventional methods. In most cases, tunnels are subjected to pressers mobilised by soil and ground water, and the evolution of the stress state is highly dependent on the consolidation of the soil post construction. Therefore, a complete characterisation of the hydraulic boundary conditions in the tunnelling problem is essential, and the numerical simulation of the tunnelling is usually hydro-mechanically coupled.

The conventional tunnelling methods, such as New Austrian Tunnelling Method (NATM), Earth Pressure Balance Method (EPBM) and Cut-and-cover method, have been well developed in the last century, gaining solid theoretical base and the experience in engineering practice. The suitability and the principles of these tunnelling forms have been systematically studied and established.

The Double-O-Tube (DOT) shield tunnelling is a new technology developed in Japan and has been applied in some countries and areas such as China and Taiwan in recent years, mainly in soft ground conditions comprising soft silty clays. While DOT tunnelling potentially significantly improves the utilisation of an underground space, the induced ground movements compared to those from conventional twin tunnelling could be problematic. The numerical analysis method is the principal approach towards quantifying the effects of DOT tunnelling.

The research aims to provide and in-depth understanding of the DOT tunnelling methodology currently applied in soft clays, and to extend its application to tunnelling in stiff clays, evaluating merits of DOT tunnelling in relation to standard tunnel construction and producing guidance for practical design.

1.2 Research methodology

The research project develops an advanced hydro-mechanically coupled numerical model of tunnelling processes, focusing especially on DOT tunnels, in an urban environment, aiming to study the tunnelling-induced ground movements in both short term and long term. The objective is to examine the potential for unfavourable ground displacement to occur and to devise guidelines for DOT design in the urban area. The research process includes the following aspects:

Advanced numerical modelling

Develop numerical models of the twin tunnels and DOT shield tunnelling in 2D coupled finite element analyses using the finite element software ICFEP (Potts & Zdravkovic, 1999, 2001) to simulate the construction and the post-construction tunnel-soil interaction. Particular attention is given to the lining properties, ground conditions and boundary condition. The parameters of soil and tunnelling supporting structures (lining and the joints) are based on the actual data of the existing tunnelling construction in Shanghai and London. These case studies enable the validation of the developed numerical models, from which further parametric studies are performed to investigate the tunnel-soil interaction in different ground conditions, as well as the applicability of existing lining design. Both short- and long-term conditions are examined.

The lining segment, which is made of reinforced concrete, and the circumferential joints with a bolt connection, are modelled with appropriate advanced constitutive models for concrete and steel, calibrated with realistic mechanical information from the case study. The role of lining segments in the tunnel serviceability is investigated.

Numerical analysis and settlement prediction

Combined with the case of DOT shield tunnelling constructed in Shanghai and the simulated DOT construction in London, some problems in the process of tunnel construction are analysed and explained by numerical analysis method. The predicted ground response helps to assess the engineering performance of the DOT in the soft clay and stiff clay in long term. The mechanical difference between DOT and the single tube tunnelling is also investigated.

The unique construction process is an important part of the technology, which influences the engineering quality and serviceability of the tunnels. Using numerical analysis method, the contribution of each step including the tunnel drainage conditions and grouting around the tunnel opening are analysed and discussed.

The hydraulic boundary conditions of the tunnel lining are also investigated and discussed, in conjunction with reproducing a realistic profile of pore water distribution. The permeable and

impermeable conditions are simulated for both DOT and twin tunnels, representing extreme conditions for the tunnel serviceability in terms of its water proofing function. Their influence on the ground surface and subsurface settlement is investigated and discussed.

1.3 Thesis outline

The thesis is divided into the following remaining chapters:

Chapter 2: A review of the literature, introducing the characteristics of conventional tunnels and DOT technology is presented. Some essential pros and cons of these tunnelling methods are revealed. Attention is further focused on the existing research into lining materials and their application, as well as on the empirical and practical solutions, which have been widely accepted, to predict ground movements induced by both the conventional twin tunnels and DOT tunnelling.

Chapter3: The geological ground conditions of the Shanghai area are reviewed from the available literature and a consistent ground profile is derived from the various data source. The main focus is on the Holocene division in the shallower depth, where the tunnels are excavated, and on the hydraulic conditions in these layers. The engineering division for the DOT simulation is determined, and the profiles of hydro-mechanical soil properties are established based on field and laboratory data. Both extended modified Cam clay (MCC) model and a nonlinear small strain ICG3S model, which characterised the shear strength and the small strain stiffness behaviour of soft clay in Shanghai respectively, are calibrated.

Chapter 4: The DOT tunnel case constructed on the Shanghai Metro Line 6 is introduced, and the appropriate numerical model is developed based on the project information from the relevant data sources. The simulation of the DOT tunnelling is carried out over a realistic time scale and the construction sequence, with the segmental tunnel lining being represented by elastic beam element connected by joints in the shape of small beam elements. The ground model is characterised by the soil constitutive models calibrated in Chapter 3. The short term and long term ground responses are analysed and interpreted from the numerical simulations, including the sensitivity studies on the lining joint stiffness, as well as on the magnitude of the grouting pressure.

Chapter 5: To assess the modelling assumptions introduced with the beam-element DOT tunnel lining, the study with a solid concrete lining model is carried out, using an advanced modified Chen concrete model. The model is calibrated against the laboratory test results and the codes of practice, and as such is then validated through ICFEP finite element simulations of laboratory experiments perfomed on a single segment test. The comparable results between the analysis and the lab data indicate the adequate modelling of concrete lining in the simulation.

Chapter 6: Following the satisfactory validation results for the concrete segments, the lining in the base case analysis from Chapter 4 is remodelled using the continuum solid elements, incorporating the concrete reinforcement modelled with bar elements. The same ground conditions and the lining construction sequence are analysed. The results of the solid-element lining indicate the validity of the beam-element lining assumption for serviceability conditions.

Chapter 7: Two twin tunnel cases in London clay, the Jubilee Line Extension (JLE) at St. James' Park and Crossrail tunnel at Hyde Park, are introduced and simulated. The ground characterisation is conducted based on the study of Avgerinos (2014). The simulations of DOT construction at corresponding depths and at each of the sites site are conducted in addition to conventional twin tunnel simulations. This numerical investigations demonstrate that the DOT construction in stiff clay conditions induces ground movements comparable to conventional tunnelling.

Chapter 8: The main conclusions from this research are summarised and discussed, including possible directions for future research.

Chapter 2. Literature Review

2.1 Contemporary conventional tunnelling methods

2.1.1 New Austrian Tunnelling Method (NATM)

The New Austrian Tunnelling Method (NATM) was firstly introduced in 1934 and was initially applied for tunnelling in rock masses. The method follows the basic idea of releasing the ground pressure due to tunnel excavation and relying on the high strength of the rock to enable natural equilibrium to be reached without requiring support (lining). The 'relaxing' of rock mass around the tunnel takes some time before a new equilibrium is reached. An obvious advantage of this method is that the support is not required. On the contrary, an over-stiff lining or supporting structure installed in the early stage will face the high pressure from the rock and consequently the support structure may fail. This was discovered after the construction of Trans-Iranian Railway one hundred years ago, where shear fractures were observed on the concrete vault in contact with the rock (Golser et al., 2020).

The shotcrete, or sprayed concrete, anchors, steel mesh and rock bolts are applied in rock tunnel lining construction to prevent loosening of the rock surface after tunnel excavation that usually uses explosives. The first practice of this method in Austria was in the Massenberg tunnel near Leoben and both elements were proven work well. The shotcrete is widely used due to easy operation, low cost and good comprehensive mechanical properties. Rose (1985) and Morgan (1993) reviewed the development of the shotcrete in NATM in the history of engineering. Oraee et al. (2011) presented the techniques of dry mixed shotcrete, wet mixed shotcrete, steel-fibre reinforced shotcrete and mesh-reinforced shotcrete, adapting different geological conditions and tunnel design. The mesh-reinforced shotcrete is widely adopted as the steel mesh greatly improves the ductility of the shotcrete layer, and this supporting form plays important role in stabilising the contact surface regardless the relatively weak ground condition. The temporary supporting shell, also known as outer lining is usually thin and flexible, fully contacting the ground to diminish stress concentration and the flexure.

In 1993, three NATM tunnels at Heathrow airport collapsed, and it became an important lesson for this tunnelling form with sprayed concrete lining (SCL) application in the clay area. The detailed reasons have been reported in Anon (2000), involving substandard construction in the initial length of the Central Terminal Area concourse tunnel, damage caused by jack grouting, parallel tunnel construction and badly executed repairs etc. It was the first time that the NATM technique applied in London clay, and the tunnel was excavated in stages, from crown excavation , bench excavation to invert excavation, following the conventional sequence that is applied in rock ground conditions. The geological condition over the airport area is considered uniform, and the stress measurement was not

carried out before the construction. The major collapse occurred after a chain of events: acceleration of the movements in the concourse tunnel; the invert was detected damaged; spallation and the crack of the lining occurred after repairing invert; concourse tunnel invert failed and the continuing cracks and movements stopped the recovery work. Three major collapses, involving down-line platform tunnel, up-line platform tunnel and the ground under Camborne house and over the concourse tunnel, occurred over three days from 21 Oct. 1994 to 23 Oct. 1994. Health and Safety Executive (1996) analysed the data of NATM incidents around the world from 1973 to 1994. It has been concluded that the tunnelling in the urban area has more ratio of collapse, and the consequential cost is much higher. Anon (1996) introduced two measurements that should be taken for the application of NATM in soft ground: short excavations in terms of dimensions and duration; quick synchronous sprayed concrete ring construction.

The NATM shows strong adaptability to the geological environment in some other cases. Irshad & Larry (1988) reported a case of NATM tunnel in the soft ground in Washington DC, and highlighted that this method is versatile as the outer lining can be flexibly designed depending on the local ground conditions. Therefore, this tunnelling form is suitable for the area with high variation of soil properties. Rohtang Tunnel in the Indian Himalayas (Reichenspurner & Riedel, 2020) is a successful case for NATM tunnel construction in high altitude area (>3000m) although some challenges such as friable soils and rapid change of rock formation were faced. Ome Tunnel constructed in Tokyo, Japan has proven that the NATM is also applicable for the construction of double-tier tunnel with large cross-section (Haruyama et al., 2005).

The permanent supporting structure, also called inner lining, of NATM after integration of the tunnel into the ground is usually made of reinforced concrete lining. The installation is carried out at the rear of the tunnel while the shotcrete is sprayed in front. The time gap between two phases can be several months to allow the formation of the new mechanical equilibrium after the deformation of the ground. The water proof sheet or membrane is designed to mitigate the ground water effect on the lining.

It is noted that the first layer of lining, composed of reinforcement mesh and sprayed shotcrete undertakes most of the ground pressure in the early stage. Therefore, there are limitations of this method in some cases. Niedbalski et al. (2008) reported the application of NATM in difficult geological conditions in the Laliki tunnel project, where the tunnel was constructed in flysch rock mass, and they revealed some problems exposed in this case: The high dip of the ground strata results in the asymmetrical settlement of the surface, and the clay stone content is found to exacerbate the shear deformation of the ground. They also reported that the incorrect evaluation of the rock conditions requires extra supporting measures taken for the tunnel.

Ocak & Selcuk (2017) suggested that for soft rock and weak ground area, the NATM may not be sufficient to control the ground deformation. In such case, the umbrella arch method (UAM) is suggested despite longer construction time and higher cost. Compared to NATM, the UAM introduces longitudinal bars installed aside the lining to improve the stability of the structure (see Figure 2.1). The double shell structure, consisting of the reinforced shotcrete layer and the inner reinforced concrete lining, is the most important characteristic of NATM. Barton (2017) reviewed and compared the NATM and Norwegian Method of Tunnelling (NMT), and the latter is single shell form. His study found that NATM has significantly higher cost of concrete material, labour and the construction time. The engineering risk may be greatly increased under poor rock quality conditions for NATM in the phase of temporary supporting structure.

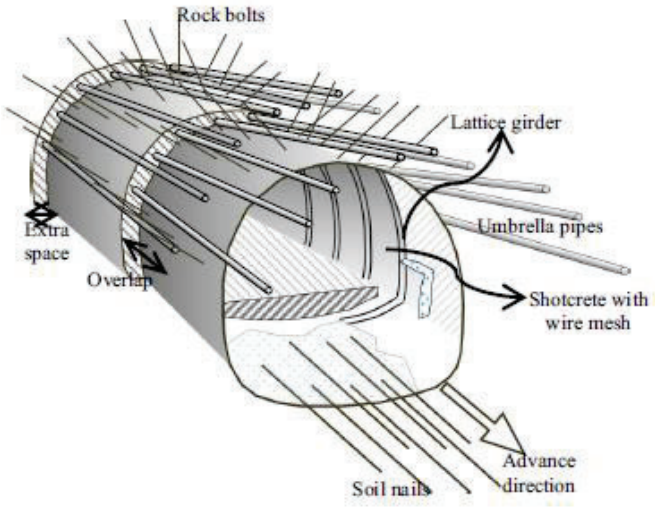


Figure 2.1: Structure of lining constructed with umbrella arch method (Ocak & Selcuk, 2017)

Fang et al. (2012) highlighted two conditions that must be satisfied for NATM applied in shallow tunnelling in the soft ground: the stable cutting face and the dry tunnelling condition. Some principles such as shorter advance length, fast installation of rigid support, fast ring closure for this type of tunnelling project were summarised in their study. Zhang et al. (2018) pointed out that NATM is not applicable when the tunnel face is not stable, and they gave an evaluation method on the front soil stability via establishing a model based on limit equilibrium calculation. It is found that the face bolts make significant improvement to the face stability in terms of increasing the shear strength of soil.

In general, the geological condition of the ground is the key factor for the application of NATM. The design of temporary support is flexible and adaptive for the variation of the soil properties, but higher risk may be raised under conditions of extreme weak or soft soils.

2.1.2 Earth Pressure Balance Method (EPBM)

The earth pressure balance method is popular in urban area underground tunnel construction. The excavation is carried out with tunnel boring machine (TBM), and the chamber, which forms a good seal shield, resists the earth pressure and infiltration of ground water and slurry during the excavation phase. The cutting wheel against the tunnel face is driven with hydraulic pressure of the machine, and usually the maximum speed of rotation is two revolutions per minute. The cutting face is in mechanical equilibrium to the earth pressure to ensure the stability of the soil in front. This balance is controlled with the hydraulic thrust. The speed of cutter's revolution, as well as conveying the soil slurry, should be monitored carefully to control the volume loss and rear lining construction, and thus minimizes the ground disturbance. The tunnel lining ring, which is usually made of prefabricated reinforced concrete segments, is commenced at the shield area of the TBM. The installation of segments is carried out with an erector inside the machine. The bolts, which can be applied to radial or circumferential joints, fix the segments and rings together. In general, the EPBM has obvious advantage of increasing the tunnelling speed due to simultaneous phases of tunnel excavation and lining construction. It does not have double shell structure as NATM or the requirement of temporary support. This tunnelling method has been widely used and well developed in a many major cities around the world, and a lot of engineering experience has been gained. The detailed characteristics of EPBM tunnelling are introduced in Chapman et al. (2010). Chapman et al. (2010) introduced that the EPBM is suitable for the cohesive soil with stiff to soft consistency. The advantage of this method is, when the properties of excavated material is not ideal to maintain sufficient stability, the soil can be conditioned using water, bentonite, clay or foam with polymer etc. Then it makes it possible to apply EPBM in the ground with coarse-grained ground conditions. They suggested that the injection of the conditioning agents through the rotating cutter-head is the most efficient as it is mixed into the material directly. Slurry TBM (STBM) is another important choice for cohesionless soils such as coarse gravels. The slurry, which is formed with bentonite to the water, or some other polymers, is introduced to help with the transportation of the coarse materials. In this method, the required pressure for the face stability is achieved by the fluid pressure in the plenum, which is behind the cutter-head, and the air pressure in terms of compressed bubble in the top of plenum. The latter ensures a constant pressure value in the plenum.

The EPBM and STBM have similar working philosophy but the application should be selected according to the ground conditions. As suggest by BTS/ICE (2005), the EPBM technique works better in silty ground, whereas STBM is suitable for granular materials. A general range of ground conditions for each method has been suggested in Figure 2.2. An alternative selection criteria is the permeability of the ground. It is suggested that the STBM is applicable for the ground with conductivity higher than

10^{-5} m/s, whereas the EPBM for lower permeable soil.

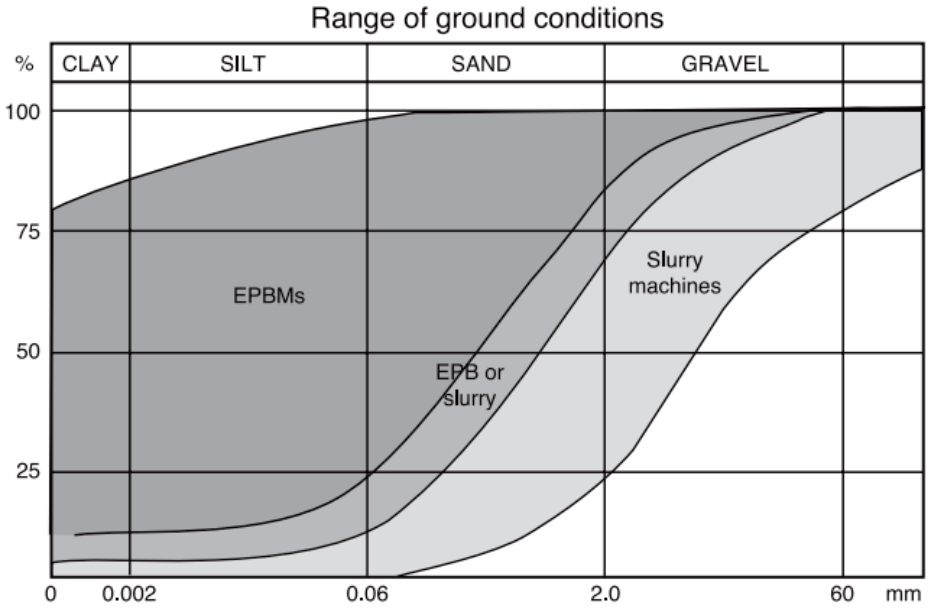


Figure 2.2: Graph of soil particle distribution curves suitable for EPBM (British Tunnelling Society in association with the Institution of Civil Engineers, 2005)

The Crossrail twin tunnels in London clay are a typical case of EPBM tunnelling. The tunnel boring machine has the cutter head of 7.1m diameter and 11m body length (Wan et al., 2012). In this project, two types of cutting configuration, ripper and clay spade, were used in the westbound and eastbound tunnel respectively. According to the study of Wan et al. (2012), it is believed that the type of cutters does not make significant difference in the caused volume loss. The shield is advanced with the hydraulic thrust pushing against the installed lining ring. The outer diameter of the tunnel is 6.2m, and the gap between the lining and the soil is fulfilled with grout. Eight pressure sensors are installed behind the cutter head to provide real time data, and that helps the system to control the tunnelling operations to reduce the ground disturbance. In this project, Wan et al. (2019) identified the arching effect, which performs in terms of transferring the ground load to the sides of opening, via analysing the change of horizontal ground stress and the pore water pressure in the vicinity of the tunnel. A clear evolution of the pore water pressure for explaining the mechanism of arching effect was presented. The analysis of these tunnels is presented in Chapter 7 of this thesis.

Standing & Selemetas (2013) reported the field monitoring data of the Channel Tail Rail Link (CTRL) EPBM tunnelling project also in the London clay. The data shows a smaller overall settlement due to tunnel excavation compared to the values of open-face shield tunnelling. The heaving of the ground, which is caused by face pressure and the tail-skin grouting, is highlighted in their study. They also suggested that the contribution of the face pressure and the grouting operation to the ground

response is difficult to assess, and therefore, the numerical analysis is necessary to quantify this issue.

Zheng et al. (2015) conducted a test of the EPBM tunnelling in the soft ground in Tianjin, China, and carried out the parametric study on the influence of skin friction, face pressure and cutter toque to the ground response under green field condition. It was found that in the deep tunnel advancing process, the skin friction causes the major impact on the ground response. The higher skin friction increases the surface and subsurface settlement whilst reduces the ground heave beneath the tunnel invert. The lower face pressure and larger tunnel torque also intensify the settlement, but the latter was found acting mainly on the crown of the tunnel.

As for the tunnelling in the rock based ground condition, in comparison with NATM, of which the boring is completed through sequential drilling and blasting, the tunnelling with TBM shows advantage of less support requirement due to low disturbance to the rock mass (Jodl & Resch, 2011). For stiff ground conditions such as strong rock mass, only a single layer lining is required but the tunnel leakage is more likely to occur. Therefore, from the aspect of water proof, the lining structure of tunnelling with TBM is not perfect.

2.1.3 Cut-and-cover method

The technique of cut-and-cover for tunnelling was developed earlier than NATM and EPBM. A summary of cut-and–cover cases were given by Peck (1969), and an empirical formula for predicting surface settlement was introduced. In this method, the tunnel lining is constructed after excavating a trench, and then a roof covering the tunnel is built, which is designed for resisting the loading on the ground surface.

The applications of cut-and-cover method in the tunnelling projects can be divided into bottom-up method and top-down method, distinguished with the sequence of support construction and the trench excavation. The trench excavation and temporary support construction is firstly carried out in the bottom-up method. The roof is covered after the construction of the tunnel. In the top-down method, however, the supporting structures of the tunnel, such as slurry wall and piles, are penetrated first downwards from the ground surface. Anon (2004) introduced the form of press-in piles using silent piler in Japan for constructing temporary and permanent supports in this top-down method. This pre-cast structure type significantly reduces the vibration and the disturbance of the ground. The tunnel cover, which is designed as permanent supporting structure, is built up after shallow excavation on the ground surface. The excavation of the tunnel is then carried out beneath the cover. The top-down method has advantage of early reinstatement of the ground surface, where the area could be pavement or highway under service. Either method does not require specific machine or shield for temporary support, and are suitable for shallow tunnel construction.

Powderham (1994) reviewed some cases of cut-and-cover tunnelling, such as Channel Tunnel at Holywell and Castle Hill and Limehouse Link tunnel in London, and pointed out that this method has drawback of higher cost, which includes the excessive consumption of supporting materials and labour due to over-conservative scheme of tunnel design. Therefore, an observational method was introduced, aiming at saving time and cost for the project. In this method, Powerham proposed the progressive modification of the design during the construction based on real time data observation, and then an economical scheme could be raised. For example, the design for three tunnels at Castle Hill East, where the cut-and-cover method was applied, requires a large amount of steel material for temporary support. The application of observational method, in which the ground condition is analysed synchronously while tunnelling, generated a less conservative scheme for design, and achieved reduction of 20% for steel used in the project.

2.2 DOT tunnelling technology

The Double-O-Tube (DOT) shield tunnelling technology was firstly invented in Japan in 1981, when the patent of DOT design was applied. The tunnel is excavated with DOT machine, which has twin cutters in front, and the shield is formed with two circles integrated as double-O shape (see Figure 2.3). In the past three decades since 1990, there are over 20 engineering cases of DOT constructed in China and Japan. The shield machine of DOT is produced by Japanese companies such as Ishikawajima-Harima Heavy Industries. It has two spoke cutters in front, which rotates simultaneously at the speed of 1 revolution per minute in opposite directions while tunnel advancing, and a synchronous grouting system. The grouts are injected from the top groove of the head. Chow (2006) analysed a DOT case in Shanghai and pointed out that the spoke shape design may result in larger ground deformation due to the formation of vacuum zone behind the cutters. During the tunnelling, the machine face cannot tightly contact the soil, and consequently the generated support is not as sufficient as the TBM applied in EPBM. Therefore, the grouting pressure is the key parameter that should be controlled well to avoid the ground heave or overlarge settlement. Chow (2006) also reported that the soil on the top groove may move forward with the machine and result in larger ground disturbance.

The lining is installed in the form of staggered ring. Each ring consists of eight normal segments and two seagull segments. The segments are installed with an erector and connected using bolts. The detailed geometry information about DOT lining is introduced in Chapter 4, and a case study of DOT in Shanghai Metro system is presented.



Figure 2.3: DOT machine (photo from geor.co.jp)

The DOT technology is subject to the shield tunnelling approach, and the tunnelling process and the philosophy of lining construction is similar to EPBM. Compared with the conventional tunnelling methods for single tunnels as introduced above, the DOT method has greatly saved the underground space and increased the tunnelling efficiency. The speed of DOT advancing, taking the project Metro Line 6 in Shanghai for example, can reach from 3 to 7m per day. The twin tubes are constructed at the same time, avoiding the disturbance between two tunnels in conventional methods. This tunnelling form is suitable for urban area with high density of population and underground structures.

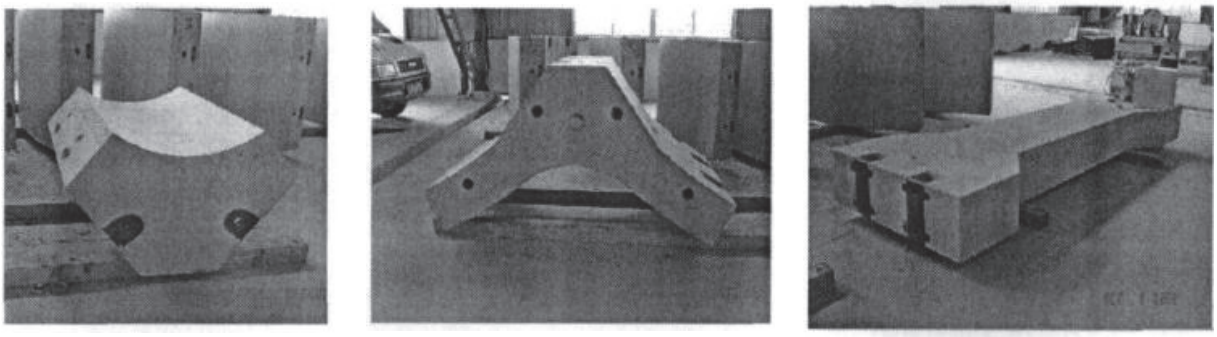
The main characteristics of the DOT machine used in the Shanghai Metro Line 6 are listed in Table 2.1. The outer dimension is slightly larger than the diameter of the tunnel (6.3m), and consequently the ground loss and so induced settlement is inevitable. It is noted that the DOT machines applied in other cases in Shanghai have slight difference in the technical index from those shown in Table 2.1, for example, the DOT machine in Metro Line 8 has the thrust force of 68,600kN and the length of 12,745mm. But these differences are considered to have little influence on the characteristics of mechanical response of the ground.

Table 2.1: Main technical index of the DOT machine for tunneling in Shanghai Metro Line 6 (Sun, 2007)

	Technical index	**Details**
The EPBM body	Outer dimension	6,520mm x 11,120mm
	Inner dimension	6,370mm x 10,970mm
	Length	12,760mm
	Thrust force	60,612kN
Cutter plates	Driving mode	Electrical driving
	Rotation speed	0.83 or 0.41r/min
	Maximum rated torque	5451kN.m

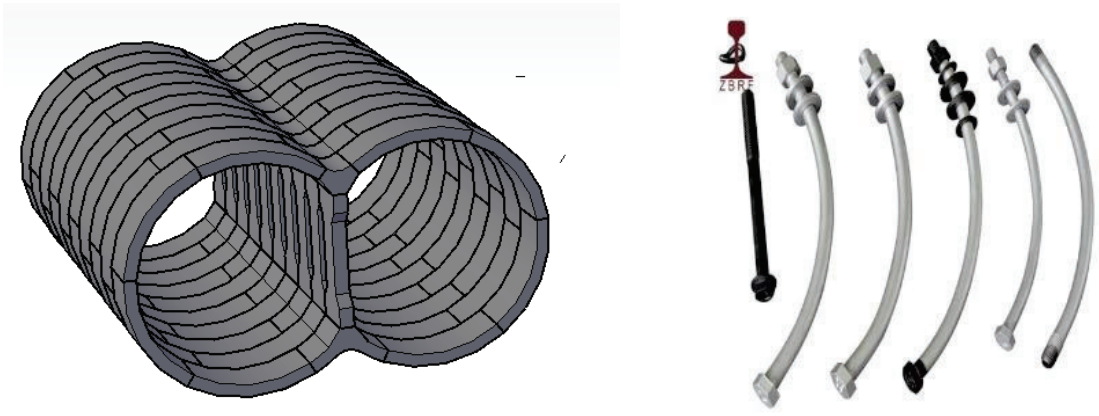
Maximum torque	8177kN.m
Cutter length	120mm
Number of cutters	2 x 2 (Hydraulic driven)
Dumping speed	162m^3/h
Range of rotation error correction	±1°

The DOT lining is made of pre-fabricated concrete, and two types of seagull segments are specially designed for the connection between twin tubes. Figure 2.4 shows the shapes of these segments applied in the DOT section of Shanghai Metro Line 6. The connection between adjacent rings was achieved with M27 (pitch, or called diameter = 27mm) bolts, and the staggered form was adopted to avoid continuous interface among lining rings in the longitudinal direction (see Figure 2.5 and the field photo in Figure 2.6). In this research, the lining was modelled with beam elements in the numerical analysis in Chapter 4, and solid elements implementing concrete model in Chapter 6.



(a) (b) (c)

Figure 2.4: Segment types of DOT lining (Sun 2007). a) upper seagull segment; b) lower seagull segment; c) column segment



(a) (b)

Figure 2.5: Connection of the tunnel lining. A) Staggered installation among adjacent rings; b) M27 bolts for segments connection.



Figure 2.6: The photo of DOT lining in the site of Shanghai Metro Line 6

Fang et al. (2012) reviewed the whole 20 cases of DOT shield tunnelling in Japan and China that were constructed before 2010, and noted that most of them are serving as underground tubes in the urban cities such as Shanghai. The tunnel length in these projects varies from 300m to 2000m, and all of these cases are constructed in shallow ground (depth < 35m). In their study of the case of DOT in Taipei, the cost of DOT shield tunnelling is about 1.5 times of the conventional single tunnel, and the major reason is the high price of DOT shield machine. However, the construction period was shorter by 32% compared to twin tunnels, and according to their study of tunnel simulation under the same ground conditions, less settlement is induced by DOT than the same size twin tunnels.

In 2007, the extension of Shanghai Metro Line 2 was commenced, and the DOT shield tunnelling technology was applied. Unfortunately during the construction, an abnormal settlement took place, the maximum value of which reached about 0.8m. Ye et al. (2015) reported this case and concluded that the main reason was the improper control of simultaneous backfill grouting in the early stage of excavation. The cement accumulated on the skin of the front plate and the efficiency of grouting was lowered under the constant grouting pressure, resulting in the insufficient volume of grout flowing into the gap. In their study, the operation and the management system of the DOT machine is considered more important compared to normal TBM, requiring regular machine maintenance to be performed.

The face stability of the shield is mainly concerned for DOT tunnelling due to the special spoke form cutters, which looks like bike spoke in the wheel, of the machine (see Figure 2.3), which is a significant difference from the TBM. The soil mass collapses towards the tunnel when the supporting pressure is

not sufficient. Yang et al. (2013) analysed the mechanism of face instability caused by insufficient support via limit analysis theorem. They found that under the ground condition of sand and silt, the collapse of soil around the tunnel results in the rapid settlement on the ground surface. The results from analytical solution and the numerical modelling reached good agreement in their study, showing reasonable mechanism of the face instability problem in the DOT.

The rolling problem has been raised as another major concern for the DOT machine while tunnelling. The machine loses its balance under some adverse conditions and leads to the asymmetric settlement of the ground (see Figure 2.7). It seems that this phenomenon is inevitable for DOT due to several inherent factors (Shen et al. 2006, 2009, 2010): a) unbalanced weight and asymmetric geometry of the DOT shield, which provides reaction force for jack thrusting forward; 2) the variance of earth pressure acting on the machine; 3) the difference of torques on two spoke cutters; 4) the difference in trolley tractions on both sides; 5) the grouting problem in which the material is filled unevenly. Huang & Zeng (2017) analysed the influence of the DOT rolling on the ground, and summarised the features of induced ground deformation. The most direct consequence of rolling is causing asymmetric ground settlement. The maximum settlement is significantly increased at the left side of tunnel while rolling anticlockwise.

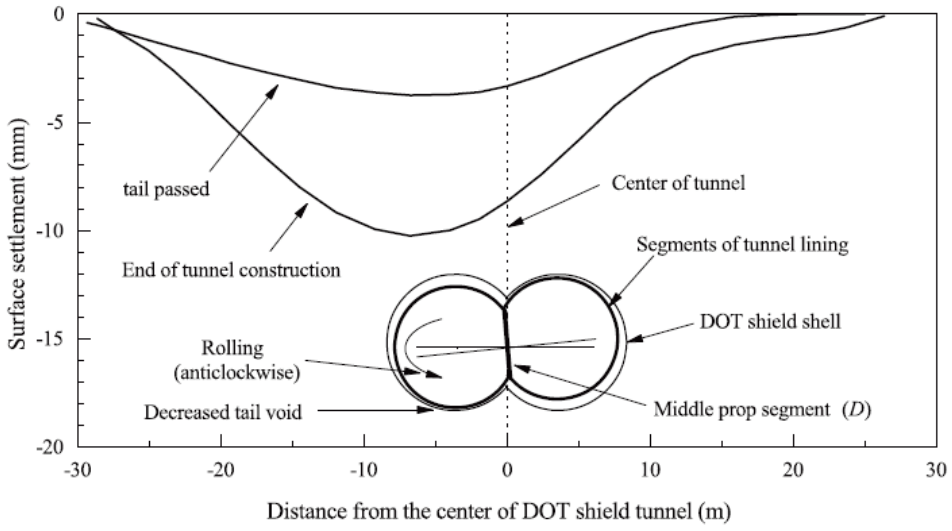


Figure 2.7: Influence of DOT rolling in the ground settlement (Yonei, 2000)

The correction of the rolling is usually carried out using grouting on the opposite side of rolling. The grouting pressure forces the shield to maintain horizontal balance. Shen et al. (2009) investigated the influence cause by this operation using finite element method. They analysed the internal force of lining and concluded that the operation of rolling correction would significantly change the distribution of lining internal force, and this is suggested to be taken into account for the design of

lining. For instance, the rolling corrections at the angle of 0.6 to 3 degrees were found to result in five times larger bending moments.

In general, the DOT tunnelling technology is proven suitable for the underground construction in the urban area. Particular care is required for controlling face stability and the rolling of the machine in order to have full benefits of this tunnelling method.

2.3 Tunnel lining

2.3.1 Tunnel lining behaviour

With respect to the process of tunnelling and grouting, the lining reaction of the tunnel is critical for the lining serviceability. The concerned lining behaviour for the tunnel study mainly includes the internal lining force and the deformation, both of which are influenced by factors of the depth, ground water pressure and soil properties.

The internal force of the concrete lining for the NATM tunnels is hard to estimate because the major load from the ground has been resisted by the primary structures such as shotcrete and bolts. It is believed in long term, as the shotcrete and bolts deteriorate over time, the loading from the earth is generally transmitted to the concrete lining. However, this evolution of the load transmission is difficult to evaluate quantitatively. Koyama et al. (1995) pointed out that the design of NATM concrete lining based on Terzaghi's formula, from which the earth pressure acting on the lining is deduced, may be too conservative because the primary supporting structure is still able to contribute to the stability of the soil. Mashimo and Ishimura (2003) also revealed this problem as the measured load acting on the concrete lining is far from the ultimate value of design, implying the long term contribution of the primary supports should not be ignored. They obtained two sets of field measurement based on the gravelly ground and evaluated the actual loads acting on the lining for a more rational design of the lining. Jeong et al. (2014) introduced a Ground-Lining-Interaction model (GLI) for evaluating the load acting on the lining. In their study, the Terzaghi's formula is found suitable for soft rocks and soil, whilst the GLI model is adaptive for all rock grades. The reduction of load was up to 30% on the tunnel crown using this model, providing less conservative and more rational guidance for lining design.

The pore water pressure is considered a major factor affecting the lining in terms of leakage and the lining deterioration. Shin et al (2005) quantitatively analysed this effect on the secondary lining of a NATM tunnel, which is located at Seoul, using finite element method and proposed a design curve. In their study, the fully permeable lining, finite permeable lining and impermeable lining are analysed and compared in terms of the distribution of pore water pressure and structural forces in the lining. It was found that the lower permeability, which is dependent on the relative magnitude between the

lining and the soil, increases the pore water pressure acting on the lining. The total ground loading on the lining does not change the magnitude but changes the distribution when the tunnel is becoming more permeable. They also pointed out that the mechanical properties of the soil, such as soil stiffness, around the tunnel, have significant influence on the contribution of pore water to the ground loading.

Do et al. (2013) investigated the influence of lining joints on the segment in a 2D numerical analysis. The double-nodes connection, which contains 6 degrees of freedom, was employed for the simulation of joints. This joint model considered the rotational stiffness, axial stiffness and radial stiffness of the connection, which were found causing significant influence on the joint behaviour. In their study, the higher rotational stiffness and radial stiffness result in an increase of bending moment, and this conclusion will also be supported in the numerical investigation of joint stiffness in the Chapter 4 of this thesis. The ground stiffness has influence on the lining flexibility, and consequently, the lining reaction such as bending moment and axial force is decreased under higher soil stiffness condition. This is also concluded from the research of transversal jack force on the lining stress carried out by Cho at al (2017). Both researches show that the softer ground conditions lead to the larger deformation and displacement of the lining. Therefore, it can be concluded that additional concern should be raised for the design of the lining for soft ground tunnelling projects. Teachavorasinskun & Chub-uppakarn (2010) also clarify that the stiffness of tunnel joint has significant influence on the bending moment distribution. They concluded that the existence of joint in the tunnel lining reduces the value of bending moment compared to the elastic ring assumption in numerical modelling, and a reduction factor, which lowers angular stiffness of the joint, has been introduced to quantitatively describe this relation. It was also found that the more joints designed for the lining decreases the maximum bending moment. It is reasonable that the joint is designed softer in bending resistance compared to the lining segment, and in the Japanese codes of design Koyama (2003) this stiffness reduction by 20% is allowable.

In addition to the conventional reinforced concrete, the research on the lining made of other materials has been carried out. Zhang & Koizumi (2010) introduced a composite segment (see Figure 2.8), which is made of steel plate and infill concrete, and its mechanical behaviour was investigated with finite element analysis. Compared to the prefabricated reinforced concrete, this type of segment saves labour during the production due to thinner thickness, and it overcomes the easy damage of the segment corner during the transportation and assembling process because of the design of the thin steel frame box. The shape of the segment such as cross-section is arbitrary for designing work as the steel plate outside has good weldability. Higher stiffness is another advantage of the composite segment and that increases the mechanical capacity of the segment. Both laboratory tests and the numerical simulations on the single segment have demonstrated the great contribution that the steel

skin plate made to the ultimate bearing capacity of the structure. The shear studs play an important role in exerting the strength of infilled concrete, and that leads to concrete crushing instead of local buckling of the top skin plate when the segment comes to failure. They suggested that the guidance of the design for shear studs is necessary for the composite segment.

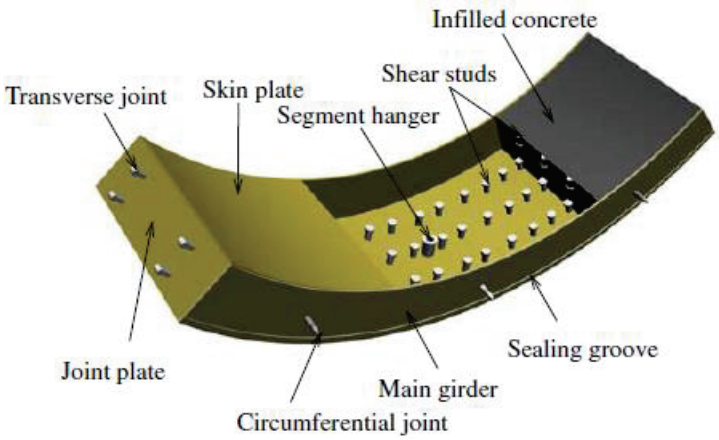


Figure 2.8: Structure of the composite segment (Zhang & Koizumi, 2010)

The cast-iron lining is another popular form in the modern tunnel structure, and it has been applied in the underground projects in London. Soga et al. (2014) studied the mechanical behaviours of the joints for this lining type, and a detailed numerical model was developed. The structure details including the bolts, panel and flanges were modelled, and their mechanical response under shear and bending loadings are investigated. A bolt-spring model was introduced for the joint, and the model has been validated against the measured data. It was found that the distortion of the flange, rather than the yielding of the bolts, lead to the angular deformation and hinging at the joints. The bolts connection plays the key role in the mechanical performance of the joints. The bolt-spring model is feasible to describe the bolts behaviour in circumferential direction, and a more precise mechanical response can be achieved. Yu et al. (2016) conducted a physical experiment on bolted grey cast iron (GCI) segments and implemented a complete instrumentation system to measure the detailed lining deformation and the joint opening. The test was simulated using numerical modelling by Tsiampousi et al. (2017) and the corresponding mechanical response was verified. The test is under the serviceability limit framework, and therefore, the response of the segment was elastic. It was found that the joint stiffness, of which the bolting system is formed, reduces when the opening increases, and the value can be much lower than of the mild steel. The influence of the joint is highlighted as it shows dominant effect on the segment arch.

2.3.2 Research on concrete tunnel lining

Concrete is one of the most widely used construction materials in the field of geotechnical engineering. This material takes advantages of the high strength, low permeability and good durability for underground structures. The lining of modern underground tunnels is usually made of sprayed concrete or prefabricated reinforced concrete segments, which form a ring when assembled.

Carlo et al. (2016) proposed a methodology for designing and checking the mechanical properties of the fibre-reinforced lining, with an appropriate characterisation of this material. Briffaut et al. (2016) performed laboratory test and numerical analysis on the early cracking of the fibre concreted lining segment and the latter involved mechanical analysis and thermo-chemical analysis. They emphasised that the fibre type and the lining thickness were key factors affecting an early stage appearance of transverse cracks. Abbas & Nedhi (2021) examined the mechanical properties of ultrahigh-performance concrete segments incorporating different steel fibres content in laboratory testing of scaled specimens and showed an important role played by hybrid fibres in improving compressive and tensile strength.

Despite the outstanding performance in durability and the strength of the high grade concrete, the deterioration and the erosion is still inevitable for tunnel lining segments underground. The aging and water leakage are coupled natural effects acting on the lining that cause the distortion and promote the reduction of tunnel serviceability. The corrosion of reinforcement steel inside the segment is also of concern for the long-term serviceability and safety design. Yasuda et al. (2021) introduced a laser sensing approach to detect the deterioration of the concrete caused by rebar corrosion. Lalague et al. (2016) introduced the ground penetration radar for detecting the rock fall on the tunnel concrete lining, which protects the self-standing inner linings in a double shell structure such as NATM tunnels. Nakamura et al. (2019) proposed an ‘Inspection Vehicle’, which overcomes the problem of time-consuming traditional aerial platform, for checking the aging of the concrete and for performing the maintenance of the tunnel. Paredes et al. (2011) established a constitutive model reflecting the compression-tension failure of the concrete under cyclic loading. The model is specifically designed for the reinforced concrete applied in wind turbine. The reinforcement orientation is considered and developed in their model, which precisely considered the contribution of steel bars incorporation with concrete. From the design view, a suitable constitutive model for correctly characterising the mechanical behaviours of the concrete will be useful in the prediction and the assessment of the structure under service and ultimate conditions.

The cracks are also the most common direct consequence of the lining erosion, and the development of cracks essentially causes impact on the tunnel safety and serviceability such as degradation of its water proof function. The comprehensive mechanism of concrete cracking is complicated and their

occurrence is considered inevitable. Therefore, it is important to assess and predict the risk of concrete cracks via analytical investigation or modelling as well as advanced detecting methods of the existing cracks.

The thermal response of concrete in tunnel lining is also of concern and the extreme conditions, such as the fire in a tunnel, are essentially affecting the structural strength. Du et al. (2018) carried out a scaled laboratory testing on concrete lining under fire and have developed a rule for the compressive strength degradation under higher surface temperature and longer time of exposure in the flame. Caggiano and Etse (2015) introduced a thermal-mechanical coupled model, describing the failure of concrete under high temperature. Torelli et al. (2018) proposed a similar model for characterising the concrete behaviour under high temperature. It has been pointed out that the maximum strength is dependent on the temperature and the material softening. The post-cracking behaviour is determined based on fracture energy.

2.4 Empirical methods to estimate ground movements

2.4.1 Peck-Fujita method for single tunnel

Peck (1969) introduced an empirical formula, expressed in the form of normal distribution, also known as Gaussian distribution, for estimating the ground surface settlement induced by a single tunnel:

$$S(y) = S_{max}\exp\left(-\frac{y^2}{2i^2}\right) \tag{2-1}$$

where $S(y)$ is the vertical settlement of the position offset from the central line of the tunnel by *y*; S_{max} is the maximum settlement, which theoretically occurs at the central line; *i* is the position of inflection point, which reflects the width of the settlement trough. The Peck's formula was introduced based on the collection of field data. The database of this formula was mainly conventional tunnelling form such as open cut method (cut-and-cover). This formula expediently provides an estimate of surface settlement. The shape of settlement trough generally follows the field observations for single tunnel in Peck's research. O'Reilly and New (1982) proposed a linear relationship between the settlement width and the depth of the tunnel centre:

$$i = KZ \tag{2-2}$$

where *Z* is the depth of the tunnel axis, and the width coefficient *K* is determined by the type of soil, such as *K=0.5* for clay and *K=0.25* for coarse grained soil.

Mair et al. (1993) deducted the maximum settlement of the surface from the volume loss of the tunnel v_l, which is theoretically equal to the enclosed area between the surface settlement trough and the horizontal line:

$$S_{max} = 0.00313 v_l (\frac{D^2}{i}) \tag{2-3}$$

where *D* is the diameter of the tunnel. The volume loss v_l is highly dependent on the ground conditions, tunnelling methods and supplementary measures (e.g. grouting) taken in the projects.

Fujita (1982) introduced the value of S_{max} selected for different shield types and different soils after statistically studying and summarising 94 cases in Japan since 1965. Fang et al. (1994) proposed this empirical method based on the theory of Peck and Fujita, and indicated good agreement of its prediction on the single tunnel induced settlement. A stability ratio *N* (Broms & Bennermark, 1967) was developed as

$$N = \frac{p_z - p_u}{S_u} \tag{2-4}$$

where p_z is the total vertical stress at depth of z below the tunnel centre; p_u is the atmospheric air pressure, and S_u is the undrained shear strength. This parameter becomes larger for weaker soils and the higher vertical pressure. Fang et al. (1994) pointed out that when the stability ratio is smaller than 4, the settlement is small and the prediction based on the Peck-Fujita method reaches good agreement with the field data. However, when the value is greater than 6, the empirical prediction method seems to underestimate the settlement. It is also noted from the research of Peck (1969) that for the stability ratio greater than 5, the soil fills into the tail void too fast, and consequently, larger ground deformation is caused.

2.4.2 Superposition method for twin tunnels

The prediction of surface settlement induced by twin tunnelling can be complicated due to additional soil disturbance caused by the interaction between tubes. Peck (1969) suggested that only when the twin tunnels are very close to each other, then the settlement curve can be approximately described using a single Gaussian distribution curve. Therefore, the direct implementation of Peck-Fujita method is limited in the case of twin tunnels. Instead, a superposition method has been introduced based on the Peck-Fujita configuration. As shown in Figure 2.9, the overall distribution of surface settlement is calculated via simply superimposing the settlement curve of the second tube, which can also be described as Gaussian distribution, to the trough of first tube.

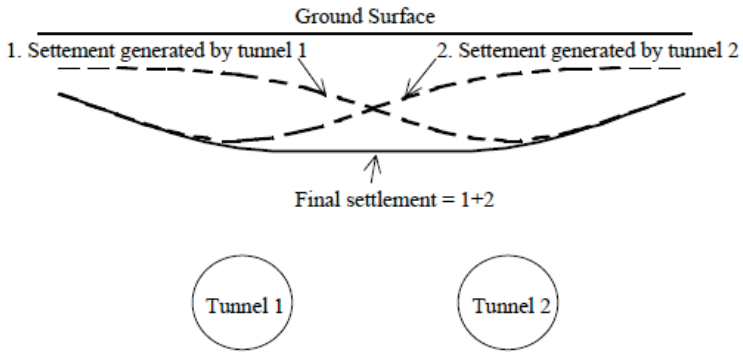


Figure 2.9: Predicted settlement of twin tunnels by superposition method (Laefer & Kim, 2004)

Suwansawat & Einstein (2007) studied a twin tunnel case constructed with EBPM in Bangkok and introduced the application of superposition method in estimating the surface settlement. They reported the monitoring settlement of twin tunnels and established the independent Gaussian curves for both tubes. It is noted that the overall settlement curve of twin tunnels may be asymmetrical due to the disturbance of the soil after the first bore, and consequently, the additional settlement induced by the second bore may lead to a different shape, although the maximum settlement of the second bore still occurs at the centre of the tunnel. In addition to the ground disturbance, the difference in the operational parameters such as the face pressure, grouting pressure also results in the different shape of the settlement trough induced by the second bore from the first one. In their study of EPBM tunnels in Bangkok, the superposition method achieved good agreement in the prediction of overall settlement. They emphasized that the application of this method has only been proven suitable for side-by-side twin tunnels constructed with EPBM, and further investigation is still needed for other types of twin tubes.

Laefer & Kim (2004) analysed the twin tunnel case constructed with NATM in Seoul, and predicted the settlement using superposition method. They found that the maximum settlement predicted for NATM tunnels matched the values for open shield tunnel proposed by Fujita (1982). The predicated settlement trough close to the central position between twin tunnels reached good agreement with the monitoring data. However, the outer parts, where the settlement position is far away from the tunnel axis, deviated and seemed to underestimate the value. The grouting effect is highlighted in their research as the volume loss has decreased to one third of the case without grouting.

2.4.3 Empirical methods to predict the settlement of DOT

Zhu et al. (2006) introduced a similar method as the superposition of the settlement curves calculated based on the Peck's formula to the DOT tunnel. It is assumed that the ground settlement induced by DOT tunnelling is the result of the joint action of two single circular shields, and thus, the overall

settlement is the superposition of the curves of two overlapping single circular shields. The settlement of each shield is calculated by Peck's formula, and the calculation diagram is shown in Figure 2.10. One significant advantage of this method is that the predicted trough has good agreement with the monitoring data (Wei et al., 2011; Zhu et al., 2006), in addition to obvious convenience of calculation. It was noted that the ratio between the tunnel outer dimension and the tunnel depth dominates the magnitudes of maximum settlement, rather than the single factor of tunnel size or buried depth. The larger tunnel diameter and shallower buried depth increases the maximum settlement, while the deeper and smaller tunnel leads to the reduction of maximum settlement. The wider trough is generated over larger buried depth, implying a wider impact on the ground surface.

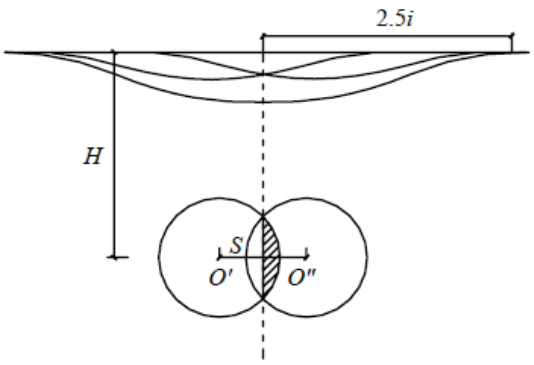


Figure 2.10: Calculation of DOT settlement with superposition method (Zhu et al., 2006)

Wei et al. (2011) pointed out that this method may overestimate the settlement value due to repeated calculation of the overlapped area of the double tubes at the DOT centre. Therefore, a correction factor, the value of which was about 0.80~0.85, multiplying the maximum settlement was introduced in their research to achieve consistency with the measured data. Further investigation based on statistical analysis of the engineering cases is needed for the selection of this correction factor.

An alternative method (see Figure 2.11), named equivalent circular method, has been introduced by Lv et al. (2006). The cross-section of the DOT is equalised to a single tunnel with the equivalent area, and the settlement trough is also calculated based on the Peck's formula, regarding the DOT as a conventional single tunnel. Therefore, this method also assumes Gaussian distribution of the surface settlement, and can predict the maximum value accurately with data of volume loss. However, the equivalent circular geometry may underestimate the width of the settlement (Wei et al., 2011) since the horizontal width of the tunnel is cut down after the transformation, and consequently, the influenced area of settlement may be underestimated.

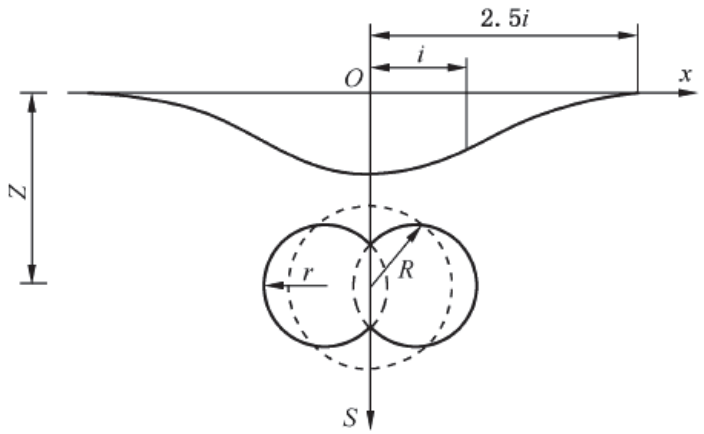


Figure 2.11: Calculation of DOT settlement with equalised circular method (by Lv et al., 2006)

Both methods provide a convenient approach to estimate the settlement of ground surface induced by the DOT construction. However, the prediction is considered of insufficient accuracy for the DOT design due to its particularity and the complexity of the ground condition such as soft clay in Shanghai. Therefore, an alternative prediction method, such as numerical simulation, for DOT settlement is needed.

2.5 Summary points

- Three typical conventional tunnelling methods, NATM, EPBM and Cut-and-cover method have been introduced in this chapter. All these methods have been applied widely and developed in the engineering field.. The general advantages and limitations of each method has been summarised and some important characteristics of the tunnel design is highlighted.
- The DOT shield tunnelling is a relatively new technology based on the design philosophy of the conventional shield tunnel. The number of DOT cases is not large (only about 20) around the world, and the variation of the corresponding geological conditions is small since all cases are located in Japan and east China. Some significant researches on the DOT construction and the induced ground response have been reported in this chapter, and the detailed concept of DOT tunnelling method has been described.
- The behaviour of tunnel lining is highly relevant for tunnel serviceability. The lining reaction is dependent on the ground conditions and pore water pressure distribution around the lining.
- Some empirical methods of predicting the ground settlement induced from tunnelling for single and twin / DOT tunnels have been introduced. These methods are based on the configuration proposed by Peck (1969) and are generally adaptive for different tunnelling forms. However, they

can only give the general shape of surface settlement trough, but cannot reveal the evolution of the surface settlement under different consolidation conditions. Therefore, the numerical simulation of the tunnelling is necessary for the precise reproduction of the ground response under different geological conditions and consolidation periods.

Chapter 3. Development of the Shanghai ground model

3.1 Introduction

Since 2004, a number of Double-O-Tube (DOT) tunnels have been constructed in Shanghai as sections of the underground metro system, the performance of this technology in soft clay ground conditions has been of high concern. The Shanghai area is known for thick soft clay layers with high groundwater level, considered to be far from ideal geological conditions for tunnelling work. Despite the significant amount of research that has investigated conventional single circular tunnels (tubes) in Shanghai, the DOT tunnelling differs substantially in the ground response due to its unique shape and construction technology, hence requiring a specific and systematic study to complement the existing knowledge gained from standard single or twin tunnelling in soft ground.

The definition of the ground conditions in Shanghai benefits from a considerable number of engineering works carried out in the area, from which a systematic and comprehensive data and ground characterisation could be found in the literature. This chapter first introduces the main characteristics of the geological conditions in Shanghai, focusing on the layering in the ground and on the groundwater, which are critical for underground construction. The definition of the layered ground profile was supported by data extracted from field investigations and laboratory experiments. Special attention was placed on the soft clay layer in which the DOT and conventional tunnels were excavated.

Subsequently, the development of the numerical ground model for the Shanghai area is presented, employing the finite element software ICFEP (Imperial College Finite Element Program), Potts & Zdravković (1999). A hydro-mechanically coupled finite element analysis was adopted for the simulation of the short- and long-term ground response due to tunnel construction. The soil layers in the ground profile were representative of normally consolidated to lightly overconsolidated conditions and therefore a Modified Cam Clay (MCC) model was selected as appropriate to simulate the soil response. The MCC model was extended to account for the small strain behaviour of the soil, in particular the nonlinear stiffness, which is essential for assessing the tunnelling-induced ground movements. This was done by introducing the ICG3S (Imperial College Generalised Small Strain Stiffness) model (Taborda et al., 2016) into the MCC model, as a small strain overlay. The calibration of such an extended MCC model, carried out based on the data extracted from core literature, is presented in detail. The developed numerical ground model and the calibrated constitutive model were used in the simulations of DOT tunnelling in Chapter 4.

3.2 Ground conditions in Shanghai

Shanghai is located in the estuary of the Yangtze River, in the east part of its delta entering the East China Sea (Figure 3.1). The marine deposit with a depth of about 300m from the ground surface (Liu & Liu., 2000; Wei, 2003) is the main content of the ground material that is of interest for the underground engineering works of Shanghai. This is underlain by bedrock, consisting mainly of acid granite (granite & granite porphyry) and intermediate rocks such as quartz diorite, quartz diorite porphyrite, diorite, diorite porphyrite & pyroxene diorite.

3.2.1 Layering of Shanghai sediments

The Shanghai soft sediments consist of soft silts and clays, generally classified into Tertiary and Quaternary sediments. The Quaternary System forming on the top is divided into Holocene and Pleistocene strata, in which the underground structures are mainly constructed (Xu et al., 2009). The elevation of most tunnelling works in the urban area was selected to be in the soft clay layers at a shallow depth (e.g. the DOT section of Shanghai Metro Line 6 is at a depth of around 13.7m; Zeng & Huang, 2016). Therefore, the investigation and characterisation of the geological and geotechnical conditions in the Quaternary strata were the core objectives in this research. The urban area, located in the administrative region of Shanghai (Figure 3.1), was of specific concern due to its long history of underground engineering works.

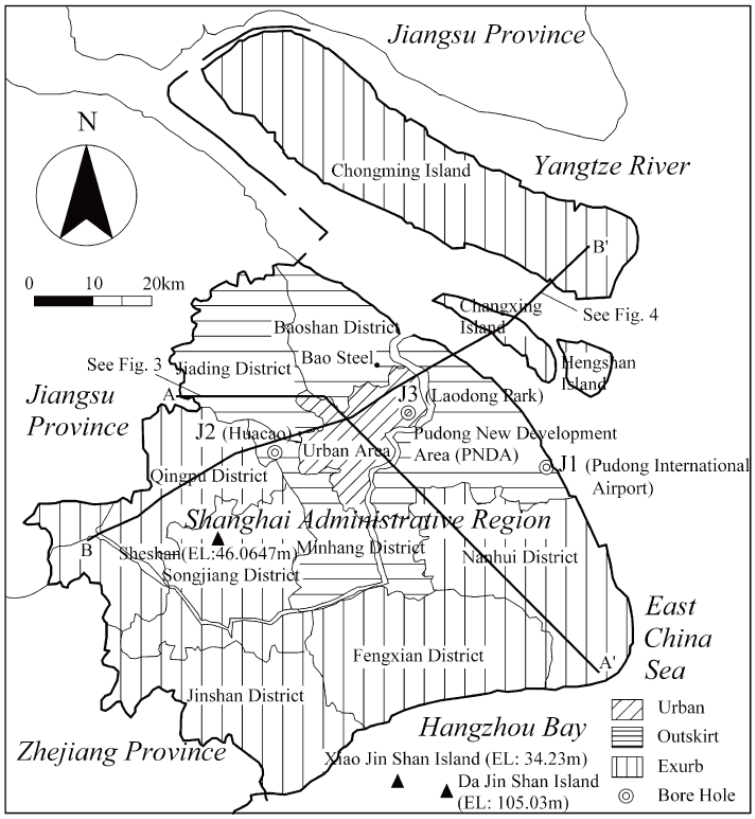


Figure 3.1: Plan view of the Shanghai area and the cross-section lines AA' and BB' (Xu et al., 2009)

A typical vertical cross-section of the Shanghai ground profile, along the line A-A' in Figure 3.1, is shown in Figure 3.2. The youngest Holocene strata were formed in around the top 30 m from the ground surface, followed by deeper and substantial Pleistocene strata which could be divided into upper, middle and lower series. The Pliocene Series, just above the bedrock, is reasonably thin and discontinuous. The divisions of the Quaternary deposits present a practically uniform stratification and the layers formed by consecutive geological periods demonstrate a continuous sedimentation history. The Holocene series on the top were formed about 10ka BP (thousands of years before present), and the Phreatic aquifer on the upper part, which is above the depth of around 22m (not shown in this figure), was formed 7.5 to 5ka BP when the climate became warm. The soil on the ground surface, also named filling or backfilled soil, was formed about 300 years ago with about 2-3m thickness, and this filling, classified from the aspect of engineering, usually includes the top hard shell of the Holocene strata due to their similar mechanical properties.

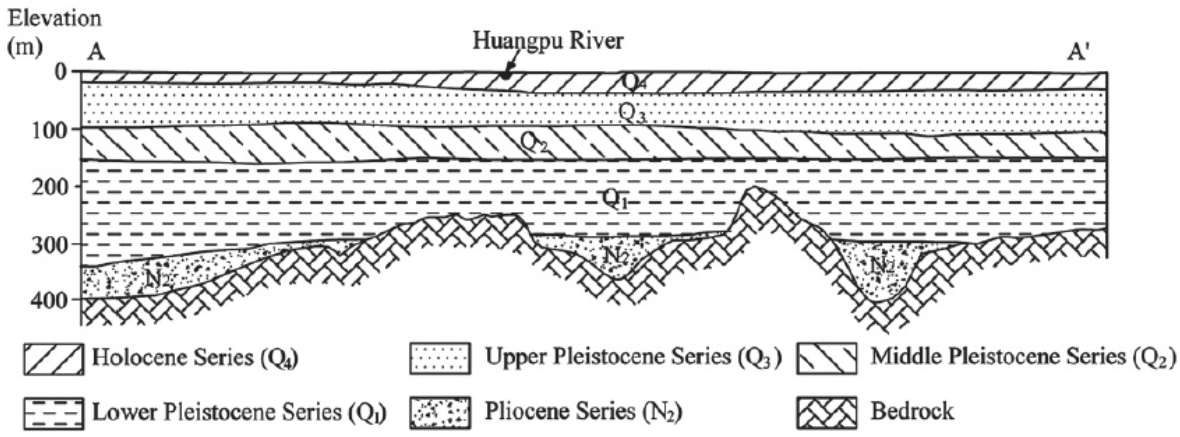


Figure 3.2: Cross-section A-A' (in Figure 3.1) of the Quaternary Strata of Shanghai ground (Xu et al., 2009; based on SGEAEB, 2002)

The divisions and the sub-divisions of the Quaternary strata has been studied by many researchers and have been summarised by the Shanghai Geological Environmental Atlas Editorial Board (SGEAEB, see Table 3.1). The Holocene series were subdivided referring to the age of the layers. It was noted that at the bottom of the late phase a thin sand layer, which is noted as 1st sand layer, or described as sandy silt layer in some literatures, in the late phase of Holocene strata in the table, was formed at the depth of around 2.8m to 5m and that this layer should not be ignored when building up the ground profile. The geological divisions defined for deposits formed in Quaternary Era could be primarily deduced from the soil composition and the characterisation, but some arguments on sub-divisions, involving the thickness and depth, have been raised in literature depending on the position of sampling. However, the general soil layering and the corresponding elevations were consistent among the geological investigation results.

Xu et al. (2009) introduced the reference of hydrogeology into layering, based on which the Quaternary deposit was divided into six layers from Holocene (1 layer) to Pleistocene series (5 layers), respectively. Each layer was subject to an aquifer group, identified as the phreatic aquifer on the top layer and artesian aquifers for other five layers. Six different aquitards separate the layers accordingly, which are formed from six cold-warm climate cycles in the geological history (Yu et al., 2004). The multi-aquifer-aquitard system (MAAS) was formed under the influence of geology, transgression and the climate change. The aquitards were formed during the cold period while the aquifers were formed during the warm period. It has been introduced in the research of ground layering of Shanghai geology by Yu et al. (2004) that the 'cold' and 'warm' layers in this area could be easily identified referring to the fossils found in the ground. This information is significant for understanding the relationship between divisions and the geological history. For example, it was concluded that during the 2.7 to 0.3ka the climate became warmer, and consequently the raising sea level formed the 1st sand layer

and the phreatic aquifer on the surface (see Table 3.1). Some essential mechanical features, such as stiffness and strength, have been summarised for these layers, and these with similar properties are merged into the same division in the classification of engineering layers. For example, the fill and the top Holocene layer (numbered with 1 and 2.1 in the table) are subject to the 'hard shell' layer, and both have been modelled as backfill in this research. The division based on engineering layers is considered more practical and convenient for the analysis of the construction in the ground.

Table 3.1: Quaternary stratigraphic chart (Modified from SGEAEB 2002)

Strata calendar		**Geological layer**		**Ave. elevation of strata surface (m)**	**Depth (m)**	**Engineering layers**
		No.	Name			
		1	Fill	3.7	0.0-0.7	
Holocene	Late phase	2.1	Brown yellow clay, silty clay	3.0	0.7-1.7	Hard shell
		2.2	Grey-black turfy clay	2.0	1.7-2.8	
		2.3	Grey silt, fine sand	0.9	2.8-4.0	1st sand layer
	Middle phase	3.1	Grey muddy silty clay (coastal plain region)	-0.3	4.0-4.5	1st soft clay layer
			Grey clay, silty clay (lacustrine plain region)	-0.8	4.5-5.0	
		3.2	Grey sandy silt	-1.3	5.0-10.6	
		4.1	Grey muddy silty clay	-6.9	10.6-12.0	
		4.2	Grey sandy silt	-8.3	12.0-17.7	
	Early phase	5.1.1	Grey clay	-14.0	17.7-21.7	2nd soft clay layer
		5.1.2	Grey silty clay	-18.0	21.7-29.7	
		5.2	Grey sandy clay	-26.0	29.7-32.2	
		5.3	Grey silty clay	-28.5	32.2-38.1	
Pleistocene		5.4	Grey-green silty clay	-34.4	38.1-40.2	
		6	Dark green-brown yellow clay, silty clay	-36.5	40.2-	1st hard clay layer

3.2.2 Characteristics of aquifers and the land subsidence

The study of aquifer groups is essential for ground layering and for understanding the land subsidence issues. The Holocene phreatic aquifer group was formed in the period of warming climate and the upper layers were composed of fine sand and silts as marine deposits. The lower part of the Holocene

division was identified as a low-pressure artesian aquifer at the depth from 15 to 22m (Xu et al., 2009). The groundwater in this series was fresh and was recharged by nature resources such as irrigation, rainfall and other surface water precipitation (e.g. river precipitation).

The main characteristics of the aquifers are summarised in Table 3.2. According to the table, the groundwater pumping mainly takes place in the confined aquifer layers of the Pleistocene series and, therefore, the hydraulic conditions of the Holocene and upper Pleistocene groups, where the tunnels are excavated, are less disturbed. The groundwater table varies from 0.5m to 1.5m (SGEAEB 2002) below the surface and it is seasonally dependent. Therefore, in this research, a hydrostatic pore water pressure distribution for the modelling of tunnel has been assumed, and the phreatic surface was determined at the depth of 0.5m. This table indicates a reasonable profile of hydrostatic pore water pressure distribution in the modelling of tunnelling in shallower layers (Depth<30m).

Table 3.2: Aquifer conditions of Holocene series and Pleistocene series (modified after Xu et al., 2009)

Multi-aquifer-aquitard system (MAAS)		**Characteristics**			**Pumping state**
Aquifer group	Aquifer layer	Depth (m)	Thickness (m)	Maximum value of SDC (m^3/(day*m))	
Holocene phreatic aquifer group (Aq0)	Phreatic aquifer	3-4	0-20	43.2	No artificial withdrawal.
	Low-pressure artesian aquifer	15-22	0-15		
Middle-upper Pleistocene confined aquifer group	Aquifer I	25-35	6-15	48	No artificial withdrawal
	Aquifer II	60-70	20-40	720	Main withdrawal layer
	Aquifer III	110-120	20-30	480	Main withdrawal layer
Lower Pleistocene confined aquifer group	Aquifer IV	160-190	30-50	720	Largest withdrawal layer
	Aquifer V	250-290	10-50	120	Main withdrawal layer

It is believed that the long history of groundwater pumping and underground construction in the Shanghai area has caused the problem of land subsidence. The corresponding mechanisms have been investigated by some researchers. The earliest recorded and monitored land subsidence of Shanghai started in 1921, and the speed of subsidence has increased since 1990 (Chai et al. 2004). Some measures have been undertaken to decrease the rate of the subsidence, achieving the value smaller than 5mm per year since 1966. However, from 1996 to 2009, the average rate of subsidence

dramatically increased to 12mm per year, and the accumulated urban area subsidence, measured between 1921 and 2009, had reached 1.97m (Xu et al., 2012; SMBPLR 2001–2009). Liu et al. (2008) derived a subsidence velocity field by building up a network of permanent scattered targets for tracking, incorporating InSAR (Interferometric Synthetic Aperture Radar) technology, and an average subsidence rate from 6mm to 26mm per year from the year 1992 to 2003 has been reported. The rates detected reflect a severe potential influence on the damage of buildings and structures.

The extensive underground construction since 1990, when the first underground metro line was constructed, has clearly contributed to ground subsidence. Xu et al. (2016) have given a discussion based on the principle of a strategic environmental assessment (SEA), which is a systematic evaluation methodology on environmental implication, and have pointed out that the main factor for subsidence of core urban area of Shanghai has been the high density of underground construction, rather than the withdrawal of groundwater. Xu et al. (2012) have conducted numerical simulations of two scenarios of underground structures in Shanghai, reporting that the excavation in the aquifer layer of the ground profile would lead to significant local land subsidence. Gong et al. (2005) identified two aspects caused by underground constructions that contribute to the land subsidence: excavation-induced ground loss and post-construction subsidence.

Some researchers, on the other hand, believe that the groundwater pumping accounts for the land subsidence predominantly. Gong et al. (2005) estimated that the underground construction contributed around 30% only to the land subsidence and that the groundwater pumping is the main reason. Chai et al. (2004) argued that the excessive pumping of ground water lowered the water table in the aquifer. Ye et al. (2016) presented the deformation characteristics of sedimentary layers of Shanghai, carrying out a 3D hydro-mechanically coupled modelling of subsidence to investigate the influence of pumping. They concluded that the withdrawal of groundwater caused the decline of water table and, additionally, led to the compression of multiple sedimentary layers due to the increase of effective stress. The analyses results highlighted a strong effect induced by ground water pumping on the soft soil compression in all layers, not only on the ground surface due to loading from buildings. The relationship between the ground water table, pumping rate and the land subsidence for Shanghai clay has been clarified by Shen & Xu (2011) via numerical modelling. Referring to their research, it was suggested that considering the large quantity of groundwater demand for industrial use, the recharging of ground water would have a significant effect in lowering the rate of subsidence. Their simulations have also revealed that the migration of pumping area (pumping at sub-urban area, for example) would still lead to the subsidence of the urban area due to the replenishing of the groundwater, which performs horizontal water flowing out in the layers from the urban area.

Shi et al. (2018) listed the factors which were believed attributing to the acceleration of land

subsidence: groundwater withdrawal, increasing population, economic activities, vehicles and expansion of high buildings (see Table 3.3). The rising of sea level, which decelerates the subsidence, was also considered. A statistics analysis in terms of multiple regression based on the collected data has been carried out and the weight of each factor has been studied. This statistical-based methodology for predicting long term ground subsidence could also be critical for engineering and municipal guidance. The factors listed are generally highly related to the mechanical effects acting on the soil such as the number of vehicles and buildings. The rise of sea level has been found to be beneficial for reducing land settlement due to the decreasing pressure difference.

Table 3.3: The data of factors influencing the subsidence of the urban area of Shanghai

Average annual values	**Years**			
	1978-1989	**1990-2000**	**2001-2010**	**2011-2016**
Subsidence (mm)	3.5	14.3	8.52	5.36
Groundwater usage ($\times 10^4$ m^3)	11,149.27	13,154.16	6,130.09	756.47
Sea level rise (mm)	9.26	4.38	2.42	12.92
Permanent resident growth ($\times 10^4$)	18.68	27.09	69.40	19.51
GDP growth ($\times 10^8$ yuan)	38.85	370.42	1266.20	1790.91
Number of vehicles ($\times 10^4$)	1.19	7.70	20.54	8.30
Number of high-rise buildings	62.70	316.18	1877.20	4279.40
Area growth of high-rise buildings($\times 10^4$ m^2)	78.70	590.55	1959.20	3329.20

Wu et al. (2017) indicated important contribution caused by the overall land subsidence to the tunnel settlement in long term, and this correlation should not be neglected. Therefore, the analysis of tunnelling-induced ground response for long term conditions would be complicated as the procedure of consolidation and deformation directly caused by excavation are not the only factor involved. The part of ground deformation induced by excavation is mainly in terms of subsurface compression, which includes all soft clay layers, not only surface settlement. Further details in relation to long-term settlements of the tunnel are discussed in Chapter 4.

3.3 Main properties of Shanghai clay

3.3.1 Basic characterisation of Shanghai clay

A considerable number of systematic geotechnical investigations of general properties of Shanghai clay in Holocene series, in which the underground construction has mainly taken place, have been carried out. The soil characterisation comprised the basic classification tests (such as particle size

distribution), as well as hydro-mechanical testing which is essential for numerical modelling and analysis. Some typical investigations on the Shanghai clay, locating at one construction site of Metro Line 1 and Shanghai Hongqiao airport, are introduced below, and the data were helpful to verify the reliability and authenticity of the profiles of basic mechanical properties, which are mainly based on the field data given in Sun (2007), built up for the modelling of DOT tunnelling in Shanghai Metro Line 6. The ground layering given from both investigations, which are presented in Figure 3.3 and Figure 3.4, basically follows the manner given in Table 3.1 despite some variance of the layer thickness and the difference of names.

Wu et al. (2014) investigated specimens taken with the Shelby thin-walled sampler from depths of 0 to 30m in a borehole located at Lianhua Road near the Metro Line 1. The experimental results from laboratory testing are summarised in Figure 3.3. Generally, a high proportion (>50%) of silt content was found in the soil in terms of particle size distribution, which contributed to the high permeability of the deposits. The proportion of clay was found to be higher from 5m to 15m depth, as part of the 1st compressible layer, which refers to the 1st soft clay layer in Table 3.1 (from 4m to 17.7m), defined in Figure 3.3. This was also identified as the muddy clay layer in ground divisions. The 2nd compressible layer (2nd soft clay layer in Table 3.1) was characterised by the predominant silt content.

The soft clay formed in the Holocene series in Shanghai is highly compressible and consequently a large deformation is expected for tunnelling. The undrained shearing strength of soil is mainly paid attention to for analysis of engineering work due to high groundwater table as mentioned in 3.2.2, and hence the soil is assumed saturated. The profile of undrained shear strength (S_u) could be primarily determined using variable testing approaches such as the unconfined compression test (Figure 3.3 shows a typical profile of S_u of Shanghai ground), during which the saturation and pore water pressure stabilisation are confirmed on the consolidated specimen before loading. The results is intuitive that the undrained shear strength increases with depth due to higher overburden pressure and so is mean effective stress of the soil. However, the strength could be extremely large in the backfill due to loading and weathering on the surface. The results in Figure 3.3 show the feature of higher strength at the depth near the surface and below 24m.

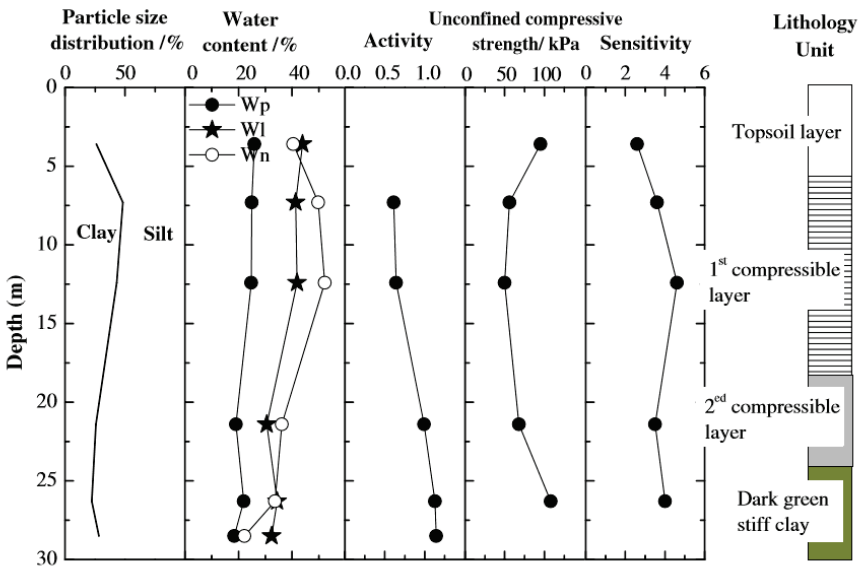


Figure 3.3 Geotechnical properties of Shanghai clay (Wu, et al., 2014)

Liu et al. (2019) studied an excavation project near Hongqiao Airport in the west of Shanghai and a profile of field vane shear strength, which reflected the strength of intact soil as given in Table 3.4. The soil at shallower depth above 30m had the vane shear strength between 25 to 45kPa and SPT blow counts, N, of just 1 to 3. In deeper layers this increased to 100kPa on average and an SPT blow count of 15 to 50, reflecting the increase in silt and sand content at depth. Similar results of SPT and vane shear strength have been given from the study of another deep excavation in Shanghai (Liu et al., 2011; Tan et al., 2013)).

Table 3.4: Shear strength of the soil at the site of excavation near Hongqiao Airport (Liu et al, 2019)

Layer	Thickness (m)	Field vane shear strength (kPa)	SPT N
Clay	2.21	25 – 42	1 - 2
Muddy silty clay	4	25 – 40	2 – 3
Muddy clay	3.72	25 – 40	1 – 2
Clay	15.56	25 – 45	1 – 2
Silty clay	3.01	< 80	12
Silt clay and silty sand	19.44	> 120	15 - 50

For the study of soil behaviour in an excavation at Hongqiao Airport, the consolidated-undrained triaxial testing was also employed to determine the critical mechanical properties (see Figure 3.4). The maximum and minimum envelopes plotted as dash curves, and the mean value plotted in between are shown.

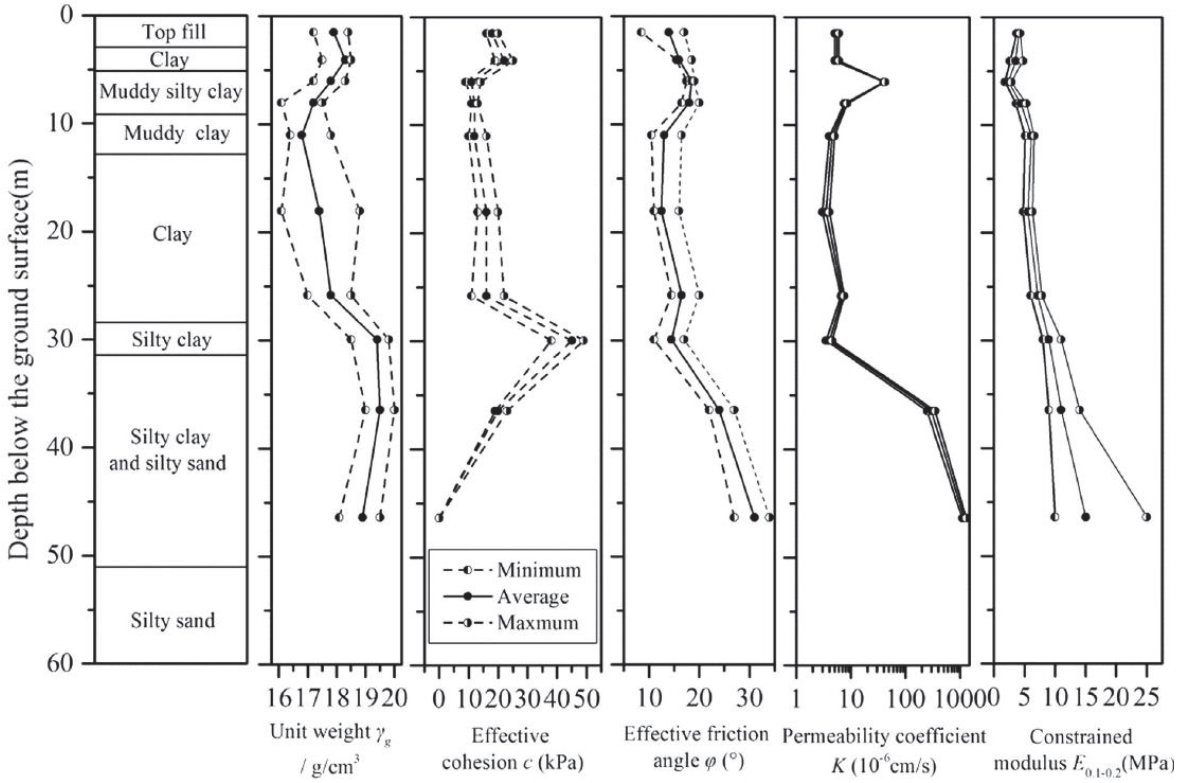


Figure 3.4: Shanghai soil profile near Hongqiao Airport (Liu et al., 2019)

The minimum and maximum values in Figure 3.4 revealed a reasonably narrow range of variation in the effective cohesion, c', and angle of shearing resistance, ϕ', at any depth. The presence of a thin sandy silt layer at around 5m depth is clearly visible in the permeability profile, as a sudden spike in the predominantly clay / silty clay formation. The angle of shearing resistance is also slightly higher. The ground division presented in this figure is considered typical and similar classification of the soil strata was given by Tan & Wei (2012), Ye et al. (2015) and Ding et al. (2007) respectively. The permeability profile shown in Figure 3.4 does not indicate directional dependence of permeability (i.e. vertical or horizontal). The profile of the saturated soil density shown in Figure 3.4, however, shows some variance even at the same depth. For example, the Clay layer from about 13m to 27m has the weight between 16kN/m^3 to 18kN/m^3. Therefore, a proper value in between the envelopes was determined in this research for each layer in the modelling of the ground as listed in Table 3.5.

The thin sandy silt layer is not always specified in some studies, as it can be missed in sampling and field testing. The depth of this layer varies from 4m to 7m as the thickness varies depending on the field location. Also, its expected impact on the mechanical analysis of the ground response is considered limited. However, this division exists and could be detected from CPT test (Ling et al., 2019). Therefore, the sandy silt layer should be considered in studies of shallow underground structures. As for the mechanical parameters, Tan et al. (2014) suggested the value of cohesion $c' = 4$kPa, and angle of shearing resistance $\phi' = 32.5^{\circ}$ to 35.5°, which is close to the value given from Sun (2007).

Sun (2007) listed the ground layering details for the DOT construction on Shanghai Metro Line 6 (Table 3.5), in which a thin sandy silt layer (layer 3-2) lies at the depth of around 6m to 7m. It is a little deeper compared to the general profile presented in Table 3.1. This depth, as well as the layering of the ground shown in Table 3.5, has been adopted for the analyses in this research since they were determined from the DOT construction field and are considered not causing much deviation from the general geological classification of the Shanghai clay (Table 3.1). The ground divisions for DOT tunnelling simulation discussed in Chapter 4 followed the layering in Table 3.5 and the case of the Shanghai Metro Line 6 construction.

Table 3.5: Soil conditions of lot 9 in Shanghai Metro Line 6 (modified after Sun, 2007)

Soil type		**Thickness (m)**	**Depth (m)**	**Unit weight (kN/m^3)**	**Direct shear test (peak value)**	
					***c'* (kPa)**	**ϕ' (°)**
1	Miscellaneous fill	1.00-4.00	0-2	17.5	10	25.0
2-1	Silty clay	0.60-2.20	2-4	18.2	23	20.0
2-2	Gray muddy silty clay	0.50-4.10	4-6	17.3	13	18.5
2-3	Sandy silt	0.60-3.50	6-7	18.2	3	35.0
3	Gray muddy silty clay	1.00-4.30	7-10	17.2	13	16.0
4	Gray muddy clay	7.00-10.00	10-20	17.1	14	11.0
5-1	Gray silty clay 1	2.20-5.90	20-25	17.5	16	14.0
5-2	Gray silty clay 2	10.00-	25-35	18.1	10	29.0

Note: In this research, the soil bulk unit weight, c' *and* ϕ' are assumed constant within the same layer, and the values were determines by selecting a proper magnitude between the two envelopes as shown in Figure 3.4.

As mentioned in the section 3.2.2, due to the phreatic aquifer group in the Holocene series, the profile of pore water pressure could be built as hydrostatic pressure in the modelling (see Figure 3.5a) and the table is at the depth of 0.5m below the surface, regarding as highest level around the year considered from most conservative way. Therefore, a suction stress exists on the ground surface with a magnitude of 4.9kPa, and because of the zero total stress in vertical direction on the surface, the corresponding vertical effective stress is a non-zero value (+4.9kPa). The profile of vertical effective stress is shown in Figure 3.5b.

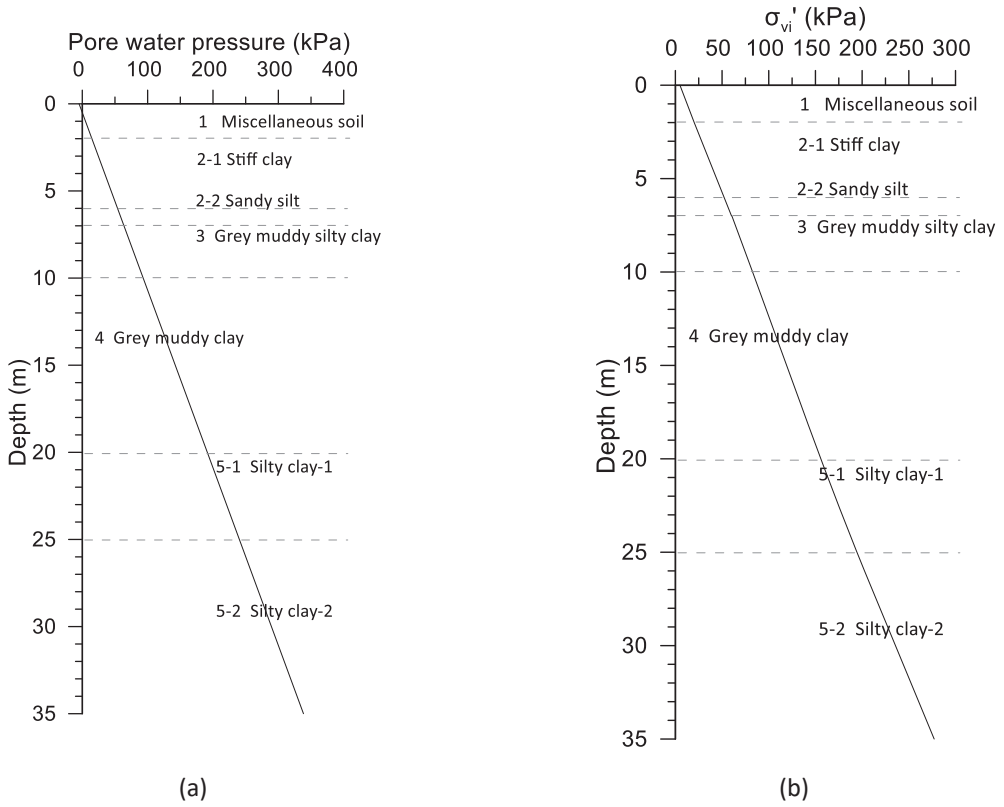


Figure 3.5: a) pore water pressure distribution; b) profile of vertical effective stress.

3.3.2 Permeability of the Shanghai clay

The Shanghai clay is considered highly permeable and consequently the water proofing is usually necessary in the engineering works (Wang & Xu, 2012). Song et al. (2018) carried out oedometer tests on permeability and the related anisotropy of Shanghai clay. The measurements of horizontal and vertical permeability were performed under different pressures. In their test, the specimen were prepared by ring cutting in horizontal and vertical directions, and thus two sets of tests were performed. It was concluded that the permeability coefficient was dependent on the void ratio, and the difference on pore structure between vertical and horizontal directions, meaning anisotropy, is confirmed. The soil structure was studied with electron scanning microscope, explaining the anisotropy is characterised but not obvious due to the flocculent structure formed in the geological history. This is compatible with the small difference on the permeability in two directions.

Two permeability profiles (Figure 3.6) for the Shanghai clay have been introduced by Zhang & Huang (2013), Figure 3.6a, and Tan & Wei (2012), Figure 3.6b. The two profiles are generally in good agreement and the magnitude of the coefficient of permeability is higher than that of some overconsolidated stiff clays, for example London clay that was studied in Chapter 7. The reason for this is the high silt content, as discussed by Zhang & Huang (2014), who also showed slight anisotropy in the permeability profile with the horizontal coefficient of permeability, k_h, being marginally higher

than the vertical, k_v. This provided some support for the flocculent structure theory introduced by Song et al. (2018).

In both profiles it could be argued that the linear interpolation for the value of the permeability coefficient between two measuring depths, especially at the depth of 7m, is not appropriate as the sandy silt layer is very thin. As the variance of the coefficient of permeability with depth is not large, the profile derived in Figure 3.6c was employed in the numerical modelling of DOT tunnelling discussed in Chapter 4.

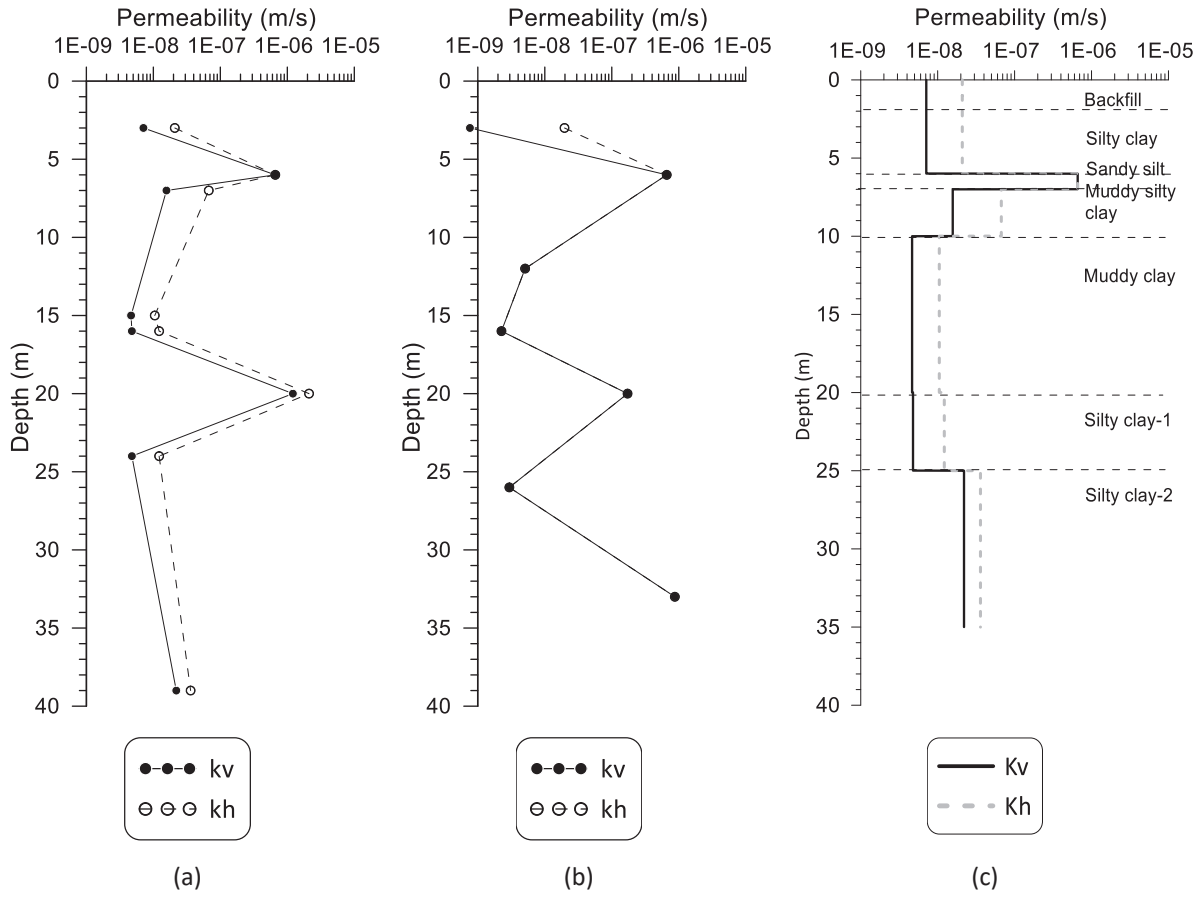


Figure 3.6: Profiles of Shanghai clay permeability. a) Located at the skew position between Line 11 and Line 4 of the Shanghai Metro (Zhang & Huang, 2013); b) located at the east side of Huangpu River, Metro Line 9 (Tan & Wei, 2012); c) Profile of permeability adopted for the numerical modelling of Shanghai clay in this research

3.4 Selection and calibration of a constitutive model

3.4.1 Introduction of the extended Modified Cam Clay (MCC) model

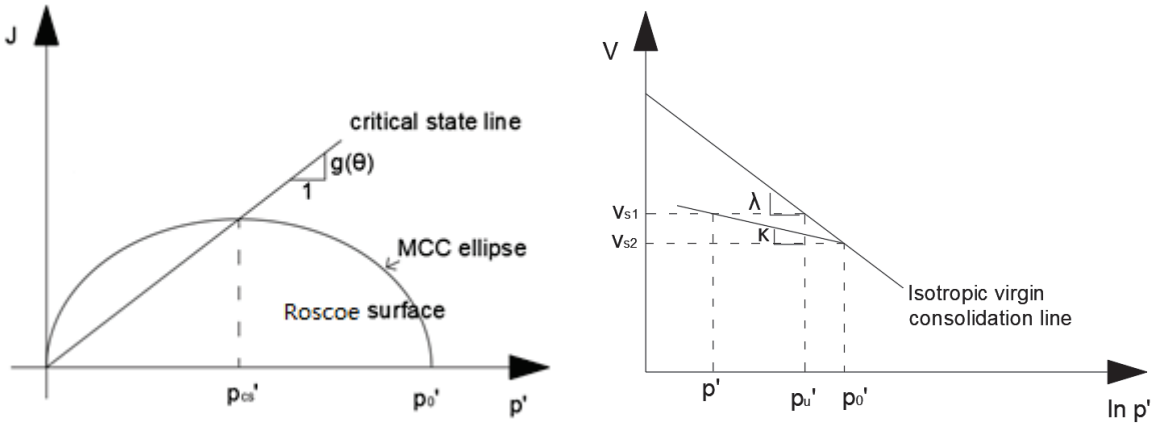
The Modified Cam Clay model (MCC) is based on the original formulation of Roscoe and Burland (1968), adopting an ellipse as a yield surface (see Figure 3.7a). This model is based on the critical state framework in reproducing the elasto-plastic soil behaviour. The soil hardening, also known as strain

hardening, behaves in terms of increasing shear resistance with strain in non-linear part for normally and lightly over consolidated clay. The yield surface expands with the stress and this hardening is dependent on the strain level of the soil. In this condition, the stress state is at the 'wet side', and the surface expands until the effective stress path reaches the CSL. As for heavily over-consolidated clay such as London clay, the strain softening is characterised on the 'dry side' of critical state, and the yield surface shrinks until the stress path touches the CSL.

The elliptical yield surface is expressed as

$$F = S^2 - \left(\frac{p_0'}{p'} - 1\right) = 0 \tag{3-1}$$

Where $S = \frac{J}{p' \cdot g(\theta)}$, $J = \left[{}^1/_2\, trace(\tilde{s}^2)\right]^{0.5}$, p_0' is the hardening parameter, and $p' = (\sigma_1' + \sigma_2' + \sigma_3')/3$. $\mathrm{g}(\theta) = \frac{\sin\varphi'}{cos\theta + \frac{1}{\sqrt{3}}\sin\theta\sin\varphi'}$, which is the slope of critical state line based on Mohr-Coulomb hexagon in the deviatoric plane; The hardening rule is: $\frac{dp_0'}{p_0'} = \frac{v \cdot d\varepsilon_v^p}{\lambda - \kappa}$, and the elastic bulk modulus is $K = \frac{v \cdot p'}{\kappa}$, assuming the compression and the swelling lines are straight (see Figure 3.7b).



(a) (b)

Figure 3.7: a) Yield surface in p'-J plane; b) the isotropic virgin consolidation line in p'-v plane

The soil behaviour is elastic until the stress state reaches the yield surface (the ellipse). Thus, the volumetric strain and the deviatoric strain become elasto-plastic after the yielding of the soil, and the incremental total strain could be expressed as $d\varepsilon_v = d\varepsilon_v^e + d\varepsilon_v^p$ and $d\varepsilon_d = d\varepsilon_d^e + d\varepsilon_d^p$ respectively. A ratio between incremental plastic volumetric strain and incremental plastic shear strain was introduced by Roscoe and Burland (1968) as:

$$\frac{d\varepsilon_v^p}{d\varepsilon_d^p} = (M^2 - \eta^2)/2\eta \tag{3-2}$$

where M is the slope of CSL for triaxial stress state in $p' - q$ plane; $\eta = q/p'$ and when $\eta = M$, the soil

comes to failure. The corresponding expression for *J – p'* plane is:

$$\frac{d\varepsilon_v^p}{d\varepsilon_d^p} = (\mathrm{g}(\theta)^2 - \left(\frac{J}{p'}\right)^2)/2(\frac{J}{p'}) \tag{3-3}$$

The undrained strength (S_u) of lightly over-consolidated soil such as Shanghai clay could be measured via consolidated undrained triaxial test, in-situ vane shear test or CPT test. This parameter is important in predicting the ground response induced by tunnelling or other underground activities in the Shanghai area. The formulation of the MCC model, as presented in Potts & Zdravković (1999), enables the S_u profile to be determined from the model input parameters and initial effective stresses in the ground, as given in Equation (3-4).

$$S_u = OCR\sigma'_{vi}g(\theta)\cos\theta\frac{(1+2K_o^{NC})}{6} \times (1+B^2)\left[\frac{2(1+2K_o^{OC})}{(1+2K_o^{NC})OCR(1+B^2)}\right]^{\frac{\kappa}{\lambda}} \tag{3-4}$$

Where $B = \sqrt{3}(1-K_0^{NC})/[g(-30^{\mathrm{o}})\left(1+2K_0^{NC}\right)$, σ'_{vi} is the initial vertical effective stress, λ is the gradient of the isotropic normal consolidation line,κ is the gradient of the swelling line, K_o^{NC} is the coefficient of earth pressure at rest for a normally consolidated state, K_o^{OC} is the coefficient of earth pressure at rest for an overconsolidated state and OCR is an overconsolidation ratio. The soft clay of the tunnelling layer in the Shanghai area is known as low over-consolidation ratio (lightly over-consolidated clay) and high compressibility, and the soil is considered isotropic with elasto-plastic property. The compressive layer for tunnelling experiences undrained mechanical process caused by tunnelling. Therefore, a profile of undrained shear strength of Shanghai clay has been developed, and the profiles of parameters involved in the model (see Table 3.6) are required. It is noted that the coefficient of lateral earth pressure K_o^{NC} is determined from $K_o^{NC} = 1 - \sin\varphi'$. The calibration of these parameters are introduced in the next section.

Table 3.6: Summary of parameters required for calibration of the S_u profile

Parameter	Description	Calibration/calculation
$\boldsymbol{OCR}$	Over consolidation ratio	Determined from various testing data
$\boldsymbol{\sigma'_{vi}}$	Effective vertical stress	Determined from the weight of soils and the pore water pressure
$\boldsymbol{g(\theta)}$	Slope of CSL in J – p' plane	Determined from the angle of shearing resistance
$\boldsymbol{K_o^{NC}}$	Coefficient of lateral earth pressure for normally consolidated soil	$K_o^{NC} = 1 - \sin\varphi'$
$\boldsymbol{K_o^{OC}}$	Coefficient of lateral earth pressure for over-consolidated soil	Calculated with K_o^{NC} and OCR value
$\boldsymbol{\kappa}$	Slope of swelling line in V - ln p' graph	Measured from K_0 consolidation test or isotropic compression test

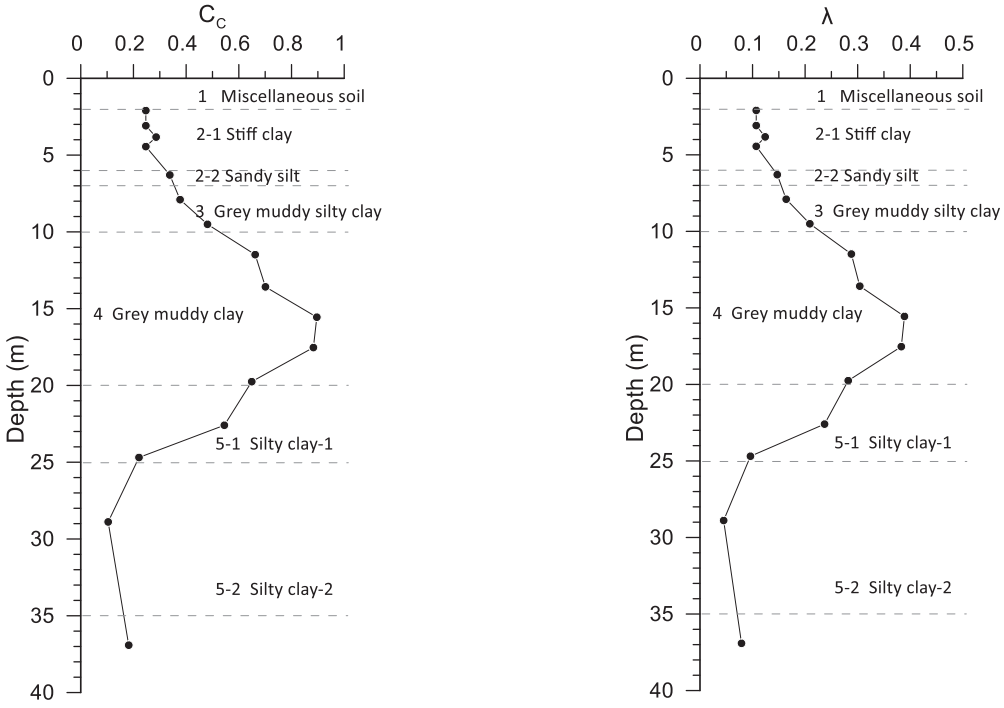
λ	Slope of NCL in V - ln p' graph	Derived from the coefficient of compression Cc from oedometer test

3.4.2 Calibration of the extended Modified Cam Clay (MCC) model

Profile of compressibility of Shanghai clay

The soil division of the soft clay layer from about 10m to 20m, as shown in Table 3.5, where the tunnelling is mainly carried out, is of highest compressibility and the lowest undrained shear strength. The soil profiles provided in the literature plotted based on the investigation of the deep excavation or tunnelling project in Shanghai have shown higher compressibility for lower undrained shear strength (see Figure 3.3).

The coefficient of compressibility *Cc* was determined from the oedometer test by measuring the gradient of the compression curve of the soil after yielding. In numerical analysis, a more general critical state parameter λ characterising the compressibility of the soil under mean effective stress is introduced. The λ distribution (Figure 3.8) in the field is calculated from $\lambda = Cc/2.303$, based on the soil profile of *Cc* values plotted by Shen et al. (2008) for the DOT site on the Shanghai Metro Line 6 in the Pudong New Development Area. The compressibility *Cc* was determined from oedometer tests performed on soils sampled from different depths. The result matches the soil layering features given by Wu et al. (2014), in which higher compressibility is found in soft clay layers from 5m to 24m.



(a) Profile of Cc (modified from Shen et al., 2008) (b) Profile of λ deduced from Cc

Figure 3.8: Coefficient of compressibility a) Cc; b) λ

The linear interpolation approach is adopted in this study to complete the profile of compressibility for all the layers. In the modelling of this study, the average value of the coefficient of compressibility λ is calculated for each layer, and thus a single magnitude is determined for simplicity (Figure 3.10a).

The slope of swelling line in v - ln p' graph, κ, is generally characterising the stiffness of the soil under over consolidated state. A K_0 consolidation test and an isotropic triaxial compression test on the Shanghai clay has been carried out by Jiu & Huang (2017) and Sun et al. (2010) respectively, from which *e-lnp'* graphs were plotted. The isotropic compression test performed regards the effective isotropic pressure as the mean effective stress. For K_0 consolidation test, the lateral strain is controlled and the evolution of cell pressure, known as lateral pressure is recorded. By combining vertical stress, pore pressure and lateral pressure recorded, the mean effective stress is calculated. In these tests, κ has been interpreted as $\kappa = 0.045$ and 0.050 respectively as the gradient of the unloading line in Figure 3.9. The results from these literatures are close and hence $\kappa = 0.045$ is adopted for the tunnelling layer.

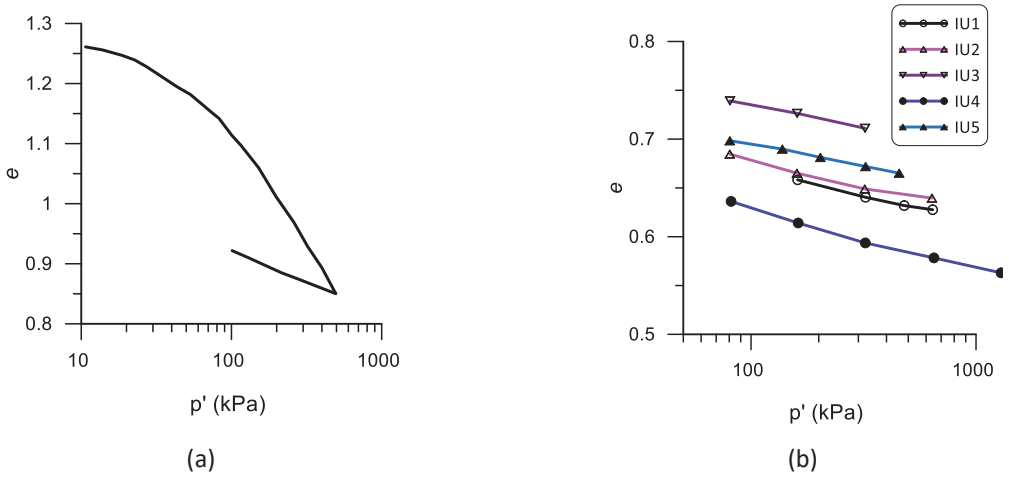


Figure 3.9: Interpretation κ from unloading curves in e-lnp' plane: a) K_0 consolidation test (Jiu & Huang, 2017); b) isotropic triaxial compression test on five sets of specimens (Sun et al., 2010)

The soil for both tests, however, was only sampled from the grey muddy clay layer (layer 4) where the ratio between two coefficients of compression $\lambda/\kappa = 6.47$. For lack of experimental data of other layers, the value of λ/κ is assumed to be constant for the whole ground strata. In numerical modelling for this study, the magnitudes of compressibility coefficients are constant, selected as the average value in each layer (see Figure 3.10).

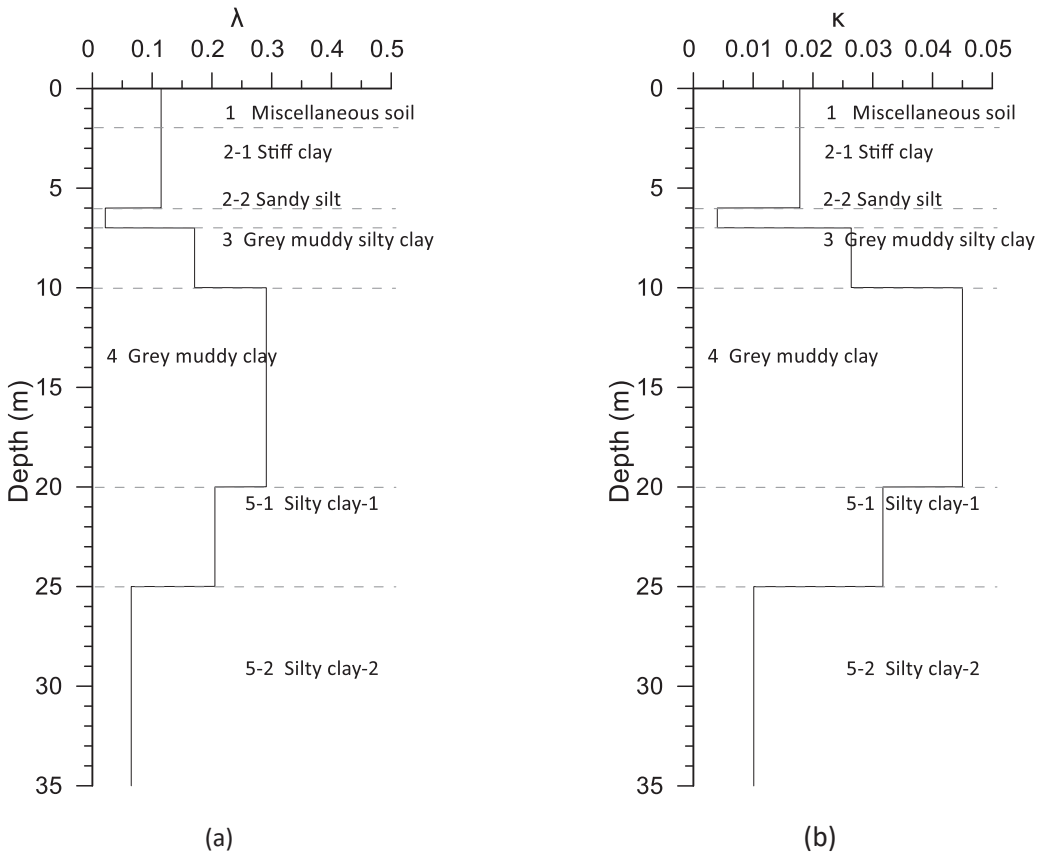


Figure 3.10: Profile of compressibility built for modelling: a) The slope of NCL λ; b) The slope of swelling line κ

OCR Value of Shanghai Clay

The over-consolidation ratio of the Shanghai clay could be found via laboratory test or field test. Ye & Ye (2016) conducted a laboratory test on the soil sampled from a construction site in Minhang district of Shanghai using a Shelby thin-walled tube sampler. The samples were taken from the Holocene and Pleistocene divisions, and they were considered undisturbed due to good protection during the sampling process. Conventional oedometer tests and uniaxial compression tests have been carried out on the undisturbed and remoulded samples to measure the OCR and sensitivity, respectively. It is found that the layer 2-1, which is on the top of Shanghai clay, is relatively highly consolidated. The layer 3 and layer 4 are of lower OCR value whilst high sensitivity. It has been explained in their study that the structure of layer 3 and layer 4 were formed from marine deposit while the layer 2 was formed under continental depositional environment, resulting in difference of structure and mechanical properties. For in-situ test, based on the observed relevance between shear strength of the soil and its OCR value, the following equation has been introduced by Jamiolkowski (1985):

$$\frac{s_u}{\sigma'_{v0}} = \left(\frac{s_u}{\sigma'_{v0}}\right)_{NC} OCR^m \tag{3-5}$$

The subscript *NC* refers to normal consolidation. *m* is the coefficient as the power of OCR value and is determined by the shear strength measurement method. Jamiolkowski (1985) mentioned that the value for *m* should be taken between 0.8 and 1.35. It is suggested that *m* = 1.0 for Shanghai clay

referring to the results of vane shear test (Gao & Chen, 2017). Some laboratory tests and field vane shear (FVT) tests (Gao & Chen, 2017) on characterising the over consolidation ratio of Shanghai clay have been conducted, and the results are summarised in Figure 3.11a. The oedometer results given by Wei & Hu (1980) show the OCR value varying from 1 to 1.2, and this range seems to be realistic. However, although the Shanghai clay is a coastal plain sedimentary material and is widely regarded as lightly over-consolidated, conventional oedometer test seems to underestimate the OCR value compared to the results given via field vane shear tests. On the contrary, the results of in-situ strength test indicate that the Shanghai clay is over-consolidated even in deeper layers (e.g. OCR=1.7 of 15-25 m). Secondary consolidation of the deep soils and the disturbance of sampling are two main reasons for the results difference between oedometer test and field test (Gao & Chen, 2017).

Generally. The OCR value decreases with the depth and is highest on the ground surface. The average OCR curve plotted in this figure could be a reference of OCR value distribution in modelling (see Figure 3.11b). Regarding some factors such as weathering near the ground surface, the OCR value of surface layer is always assumed much higher (Gao & Chen, 2017). Figure 3.11 shows the profile of OCR value adopted in this study, which is assigned extremely high magnitude on the top (assumed as 25 in the model) and decreases with the depth, for modelling the Shanghai clay. Generally, the profile has good agreement with the field measurement and the OCR value is linearly interpolated within each layer for simplicity in the model for this research.

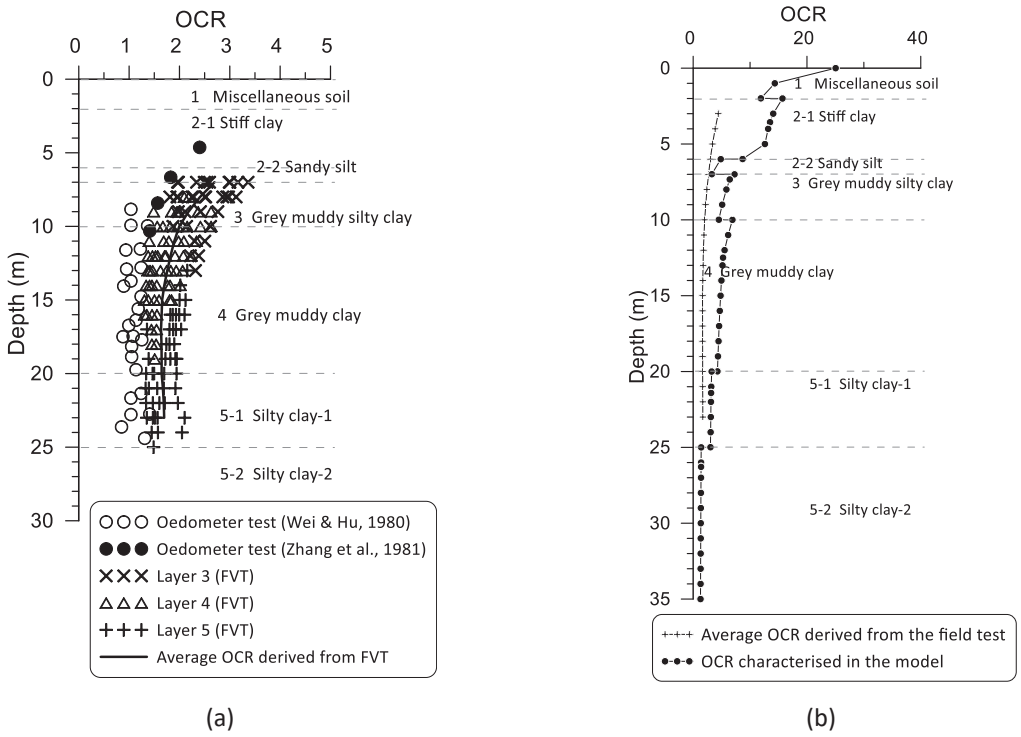


Figure 3.11: OCR value of the Shanghai clay. a) Determined from oedometer test, FVT and the average value of FVT (Gao & Chen, 2017); b) The characterised profile of OCR in the model compared against the average value derived from FVT

Lateral Pressure Coefficient K_0

The coefficient of lateral earth pressure K_0 is the ratio of effective stress between lateral and vertical components for the soil under intact condition. The determination of this value helps to deduct the mean effective stress and deviatoric stress of the soil for initial condition, and then the profile of undrained shear strength could be determined accordingly.

For over-consolidated this soil can be calculated by the following equation introduced by Mayne & Kulhawy (1982):

$$K_0 = K_{0nc} \times (OCR)^{\sin\varphi'} \quad (3\text{-}6)$$

where K_{0nc} refers to the lateral pressure coefficient of the soil under normal consolidation, and φ' is the angle of shearing resistance. Apparently the lateral pressure coefficient is of positive correlation with the OCR value, and the measurement of K_{0nc} could be the key in using this approach.

Jiu & Huang (2017) measured the value of K_{0nc} for the Shanghai clay sampled using thin tube sampling method from the muddy clay layer (labeled as layer 4 in this study). A triaxial K_0 consolidation test has been conducted on a specimen with 39.1mm in diameter and 80mm in height. Zero lateral strain was expected during the test and this was achieved by controlling the vertical pressure and the cell pressure respectively in the consolidation process, during which the stress condition is simultaneously input from the feedback of the lateral strain censor. Therefore, it would be tricky to ensure a precise zero lateral strain during the consolidation due to the lag of data feedback from the strain censor, and consequently some variance of is K_0 is prospected at the stable stage in the resulting curve.

The test was carried out from loading for consolidation to unloading for swelling procedure, from which the influence of OCR value on the lateral pressure coefficient could be interpreted. The stress conditions are achieved via: a) controlling effective vertical stress dominantly or b) controlling radial stress (cell pressure) dominantly. The results of both approaches for realising K_0 consolidation are shown in Figure 3.12 and Figure 3.13 below.

Figure 3.12 presents the results of vertical stress control method. The soil samples were consolidated to (a) 180kPa, (b) 350kPa and (c) 750kPa respectively, and then swelled via unloading of vertical stress for the latter two conditions. All these curves have shown the stage of stability at similar level, when the soil is yield and normally consolidated (OCR = 1) at the end of loading stage. Therefore K_{0nc}= 0.55 could be adopted for the normally consolidated Shanghai clay after yielding and this value is stable under higher pressure.

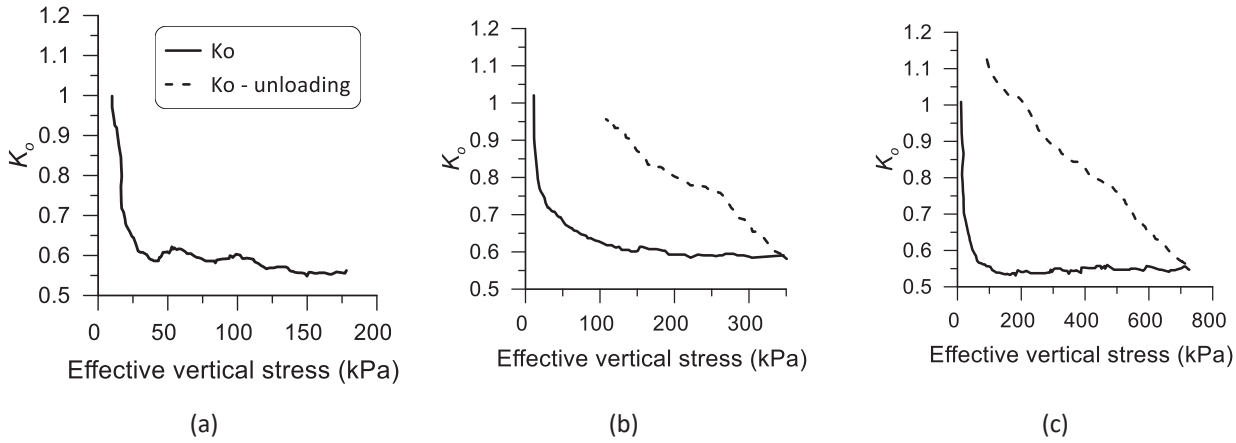


Figure 3.12: Change of K_0 during the K_0 consolidation test for saturated Shanghai clay (vertical stress controlled). a) Consolidated to 180kPa effective vertical stress; b) consolidated to 350kPa effective vertical stress and then unloading; c) consolidated to 750kPa effective vertical stress and then unloading.

The K_0 consolidation achieved via dominantly controlling radial stress leads to the same results of the lateral pressure coefficient for normally consolidated soil. The adopted value of K_{0nc}= 0.55 is also stable at the end of loading stage for a) 100kPa, b) 200kPa and c) 400kPa. It is noted that in both figures, the unloading stage, when the soil is over-consolidated, shows higher lateral pressure coefficient K_0 and the value increases with OCR. The correlation between these two variables as described in Equation 3-6 is proven strong according to the swelling results presented in Figure 3.12 and Figure 3.13.

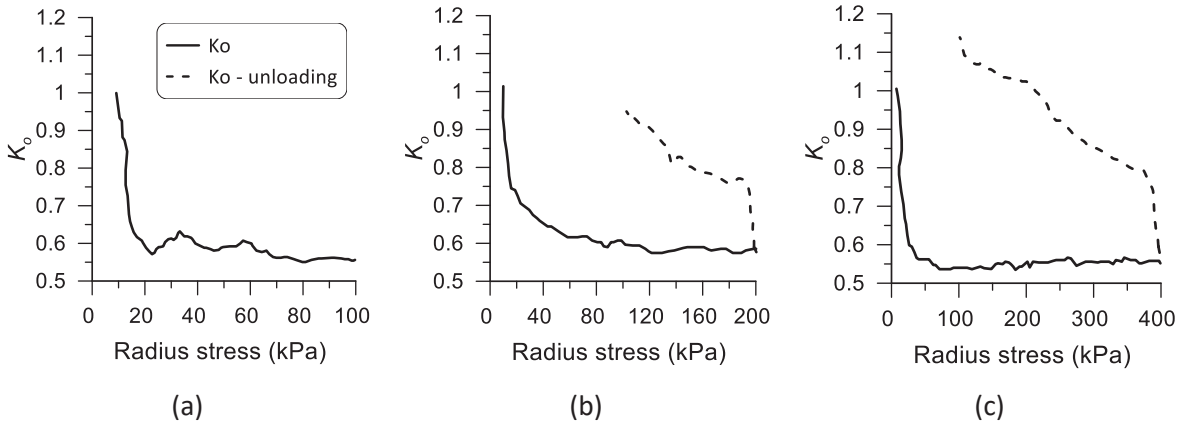


Figure 3.13: Change of K_0 during the K_0 consolidation test for saturated Shanghai clay (radial stress controlled). a) Consolidated to 100kPa effective radial stress; b) consolidated to 200kPa effective radial stress and then unloading; c) consolidated to 400kPa effective radial stress and then unloading

Therefore, the lateral pressure coefficient for the Shanghai clay, which is considered a slightly over consolidated material, was derived. The two unloading curves shown above in Figure 3.13 b) and c)

are discussed. The first one is unloading the radial pressure from 200kPa to 100kPa, and the other one is from 400kPa to 100kPa. The latter results in high OCR value for the clay. The evolution from both curves are plotted in Figure 3.14.

The comparisons between the testing results from unloading radial stress against the fitting curve predicted using Mayne & Kulhawy's equation in Figure 3.14 illustrate that less deviation occurs for $K_{0(oc)}$ from K_{0nc} when the OCR value is lower. Therefore, for deeper layers where the OCR value is less than 2, this equation is reliable of characterising the lateral pressure coefficient for Shanghai clay. The unloading testing results also indicates an upper boundary of the K_0, limited as 1.20. Therefore, for the soil near the ground surface, K_0 will be limited as 1.20.

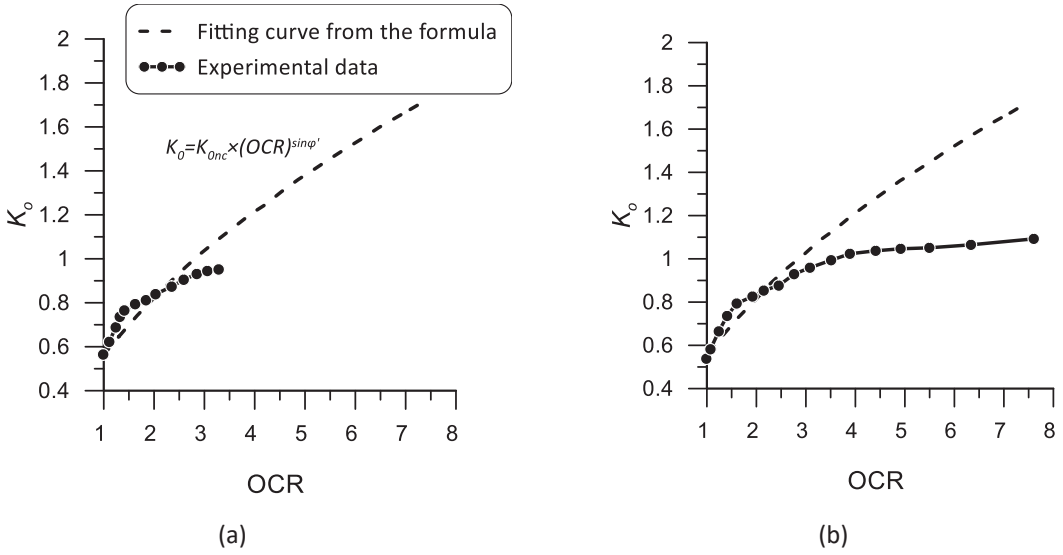


Figure 3.14: Relationship between K_0 and OCR values for Shanghai clay. a) radial pressure unloaded from 200kPa to 100kPa; b) radial pressure unloaded from 400kPa to 200kPa. (modified from Jiu & Huang, 2017)

Gu et al. (2019) performed another K_0 consolidation test, using GDS hollow cylinder apparatus on the Shanghai soil sampled from different depths. It was found that the value is 0.56 for the 30m specimen whilst 0.49 for the 70m specimen, showing a decrease trend along the depth, and this lower K_0 value for deeper soil may be caused by higher density of the soil resulting in higher stiffness.

In the numerical modelling for this research, the maximum value of K_0, which is applied on the ground surface, is assumed as 1.0 to ensure the vertical effective stress becoming the main principal stress. The profiles of lateral pressure coefficient adopted in the modelling of Shanghai soil are shown in Figure 3.15. Combined with the parameters introduced above, the lateral pressure coefficient helps to build up the profile of undrained shear strength of the soil.

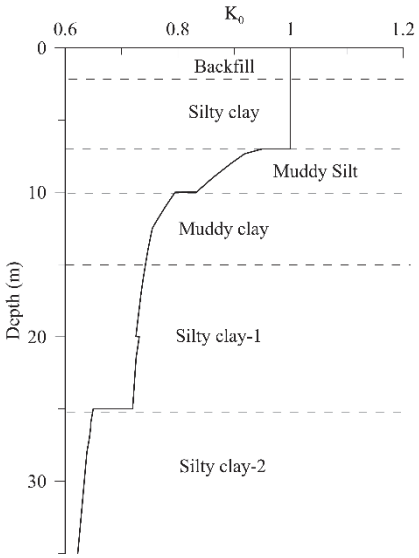


Figure 3.15: K_0 profile of Shanghai clay modelling.

3.4.3 Undrain shear strength of the Shanghai clay

The undrained strength of the soil S_u is calculated using the Equation 3-4 above, and the profile is plotted. Based on the data for soil properties in each layer, the undrained strength profile for Shanghai clay can be plotted. The value is compared with measured data from the construction site of Shanghai Metro Line 2 given by Lee et al. (1999) in Figure 3.16, which includes the undrain shear strength from triaxial test, field vane shear test and the CPT test. The measurement results given by Wu et al. (2014) is also added. The characterised S_u shown as a solid curve in the figure, calculated using extended MCC model, is proven of high accuracy and matches the file data well. Therefore, the Shanghai clay for tunnel simulation has been modelled, and the undrained shear strength is determined.

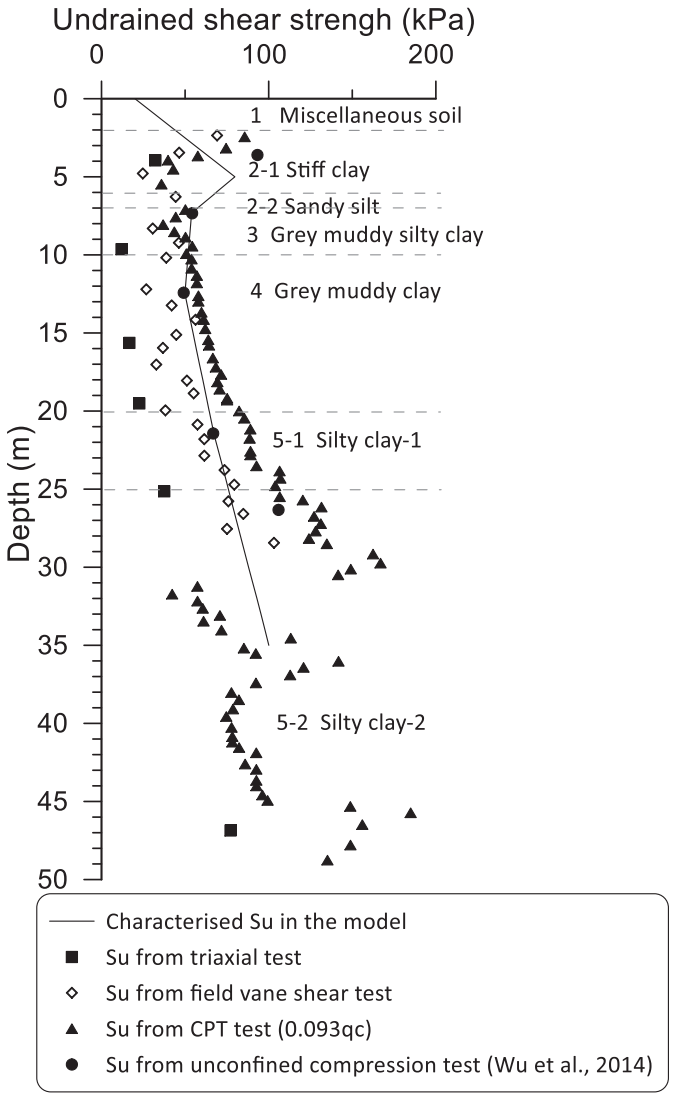


Figure 3.16: Undrained shear strength profile in comparison with the measured data from Shanghai Metro Line 2 (Lee et al., 1999)

3.4.4 Introduction of the Imperial College Generalised Small Strain Stiffness model (ICG3S)

The ground deformation predicted for tunnelling or excavation projects is considered highly dependent on the stiffness of the soil. Both the shear and bulk stiffness are highly nonlinear and dependent on the stress and strain levels. In particular, the stiffness degrades with an increasing strain in the small strain range and therefore the tangent shear stiffness evolution is important for predicting accurately ground movements.

The study on nonlinear elastic framework carried out by Taborda & Zdravkovic (2012) points out that the reproduction of tangent shear stiffness within small strain range is essential for numerical simulation. The Imperial College generalised small strain stiffness model has been introduced as an extension of the MCC model to replace the original nonlinear elastic formulation of the model.

A normalised tangent shear modulus is introduced instead of explicit expression (see Equation 3-7; Figure 3.17).

$$G_{tan}/G_{max} = R_{G,min} + \frac{(1 - R_{G,min})}{1 + (\frac{|E_d - E_{d,r}|}{n_G \times a})^b} \tag{3-7}$$

where G_{max} is the maximum tangent shear stiffness, a, b and $R_{G,min}$ are model parameters; n_G is a scaling factor. The parameter $n_G = 1$ is adopted in the equation according to the basic Masing rules (Masing, 1926) as the loading induced from excavation is regarded initial loading. In fact, the tunnel excavation does no experience cyclic loading procedure, and hence the loading is always initial. Similarly, E_d is the deviatoric strain and $E_{d,r}$ is the strain of the last reversal point under cyclic loading condition, and for tunnel excavation modelling this value is zero. It is noted that in the numerical modelling, a minimum value of stiffness should be defined since the degradation cannot reach zero, which causes error in calculation, in small strain range. Hence the stiffness shows $G_{tan} \geq G_{min}$, and the minimum stiffness G_{min} is registered as $G_{max} \cdot R_{G,min}$ (e.g $R_{G,min}$ = 0.1).

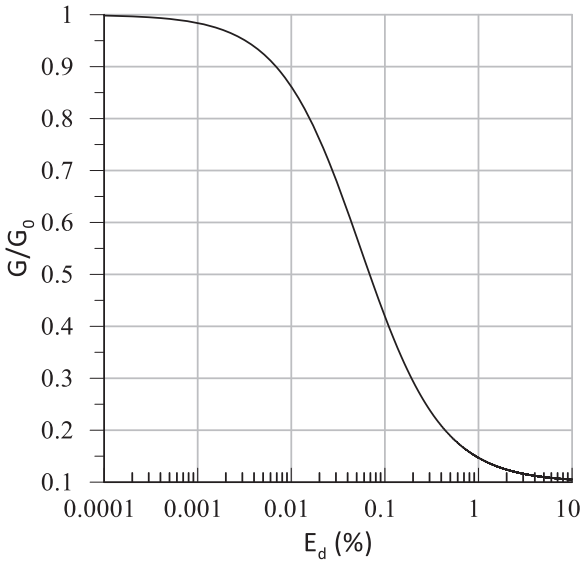


Figure 3.17: Degradation curve of shear stiffness

The maximum shear stiffness G_{max} could be expressed in the following equation:

$$G_{max} = G_0 \cdot f(e) \cdot (\frac{p'}{p'_{ref}})^{m_G} \tag{3-8}$$

where G_0 is the maximum shear stiffness of the material at the reference mean effective stress level; The function of void ratio $f(e)$ indicates the influence of void ratio on the stiffness value and a number of expressions are adopted; $\frac{p'}{p'_{ref}}$ is the ratio between mean effective stress and the reference value

(usually taken 100kPa); The index m_G needs calibration against the laboratory data. In fact, in the case of sufficient laboratory testing data, the value of $G_0$and m_G could be calibrated respectively and the function of void ratio could be set up as 1.0 for simplicity. Therefore, the maximum shear stiffness, which represents the stiffness at the beginning of the shearing, could be induced.

The expression of bulk stiffness under the same configuration follows the same manner with shear stiffness. The maximum stiffness is expressed as

$$K_{max} = K_0 \cdot f(e) \cdot (\frac{p'}{p'_{ref}})^{m_K} \tag{3-9}$$

where K_0 is the bulk stiffness at the reference stress level; $f(e)$ is the function of void ratio and it could be set up to 1.0 in the model; the index m_K is calibrated from the testing data. The bulk stiffness could also be induced with elastic modulus and Poisson's ratio, the latter could be assumed constant for a single material. A summary of parameters is given in Table 3.7.

Table 3.7: Summary of parameters calibrated for the small strain stiffness degradation

Parameter	Description	Calibration/calculation
$\boldsymbol{a, b, R_{G,min}}$	model parameters	Calibrated from degradation curve
$\boldsymbol{n_G}$	Scaling factor for shear stiffness degradation	Adopted as 1.0 due to the initial loading
$\boldsymbol{G_0}$	The maximum shear stiffness for reference stress condition	Measured from laboratory testing
$\boldsymbol{f(e)}$	Void ratio function	1.0 for simplicity
$\boldsymbol{m_G}$	Index of $\frac{p'}{p'_{ref}}$	Calibrated from laboratory testing
$\boldsymbol{p'_{ref}}$	reference mean effective stress	Determined from laboratory testing
$\boldsymbol{\mu}$	Poisson's ratio	Determined as a constant value for the soil

3.4.5 Calibration of the ICG3S model

The maximum shear stiffness, varying with the mean effective stress, has been measured for different depths. Tests upon different layers have been carried out by Zhang et al. (2017), in which the small strain stiffness was measured with a resonant column and bender elements. The soil samples were collected from the excavation of Shanghai Pudong International Financial Center at a depth of 30m via thin tube sampling. The tests consists of specimen groups preloaded under different confining pressures, and an equation introduced by Rampello et al. (1997) was used:

$$\frac{G_{max}}{p_r} = S_\eta (\frac{p'}{p_r})^n \tag{3-10}$$

where p_r is the reference pressure ($p_r = 100kPa$ in this test); S_η, n are parameters determined by the soil properties and p' is the mean effective stress. Substantially, this equation is using the same structure with Equation 3-8, describing the relationship between maximum shear stiffness and the mean effective stress. The parameters S_η, n registered are induced via linear regression of the obtained testing curves (see Figure 3.18).

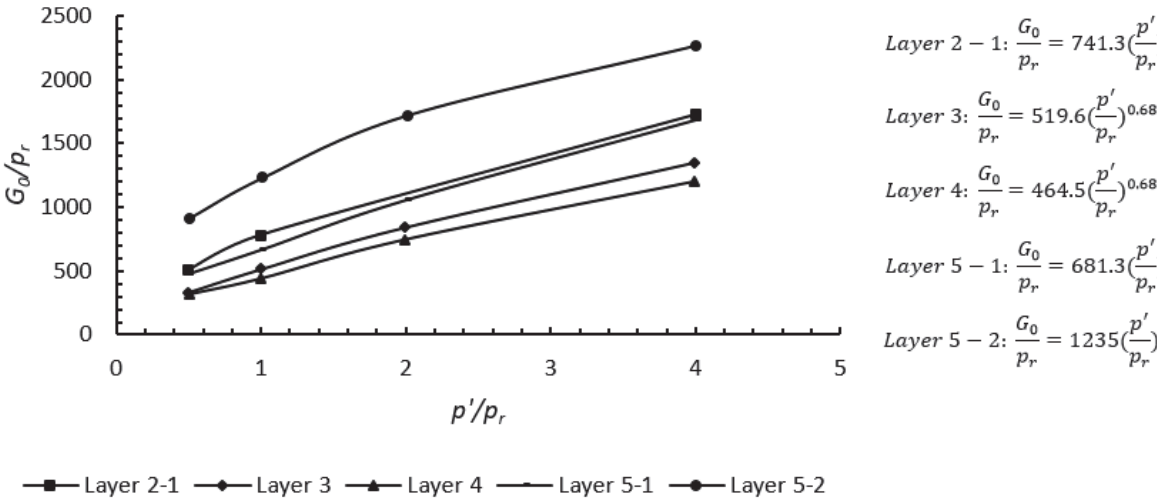


Figure 3.18: Maximum shear stiffness evolving with mean effective stress in different layers

The regression results of the maximum shear stiffness normalised by reference pressure is summarised in the Table 3.8. Therefore, a direct transformation from Equation 3-10 to 3-8 could be settled. For example, the first maximum stiffness of the layer 4 is expressed as $G_{max} = 46450 \cdot (\frac{p'}{p'_{ref}})^{0.68}$, the form which is consistent with the formula (Equation 3-8) introduced in ICG3S model, since $p_r = 100$, $S_\eta = 464.5$ and $n = 0.68$.

Table 3.8: Parameters for maximum shear stiffness expression determined via linear regression

Layers	Depth (m)	Description	S_η	n
2-1	2-6	Silty clay	741.3	0.60
3	7-10	Muddy silty clay	519.6	0.68
4	10-20	Grey muddy clay	464.5	0.68
5-1	20-25	Silty clay-1	681.3	0.65
5-2	25-35	Silty clay-2	1235	0.44

The parameter S_η defined, corresponding to $G_0 \cdot f(e)$ in the ICG3S model, reveals the maximum shear stiffness of the material at zero strain under reference pressure condition. The profile (see Figure 3.19) shows that the stiffness is the lowest in the 4th layer and the value increases in deeper layers. Regarding the normalised shear stiffness, which is expressed as the maximum value divided by mean effective stress, the variation among the layers becomes smaller. The results of maximum stiffness distribution along the depth have achieved good agreement with the experimental data of shear stiffness at zero strain condition given by Xie et al. (2016).

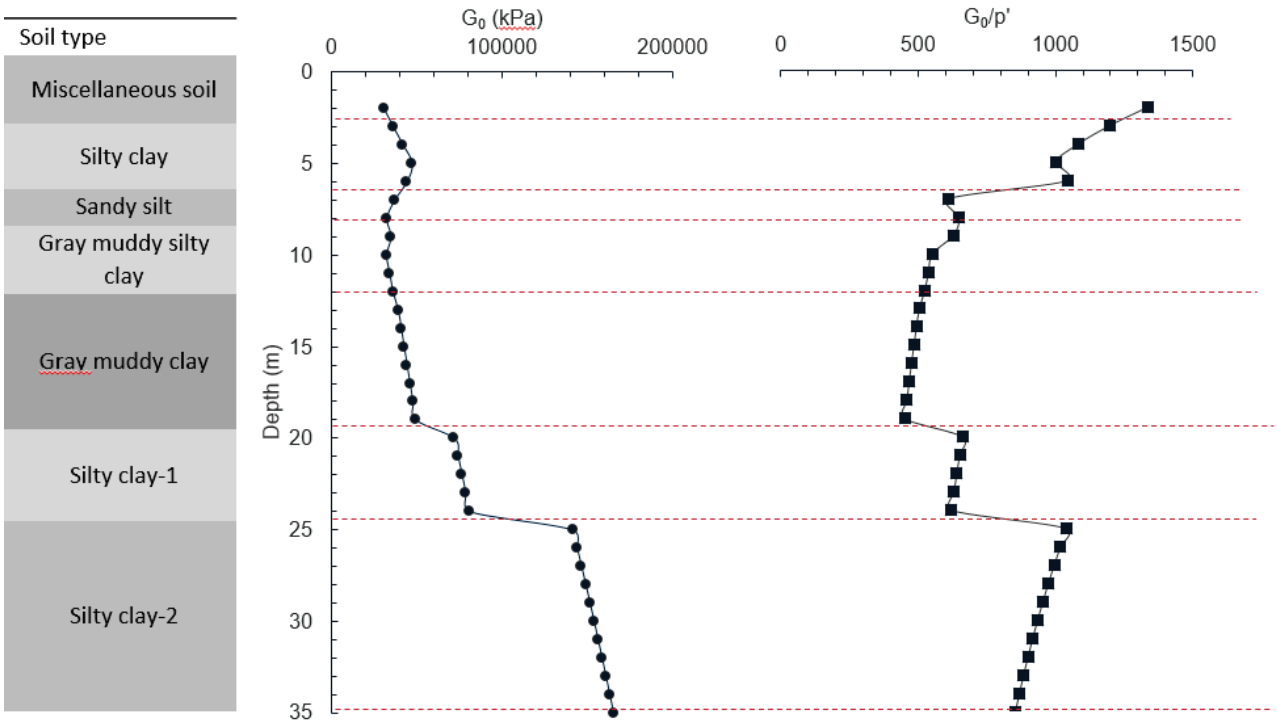


Figure 3.19: Maximum stiffness distribution for modelling Shanghai clay

During the K_0 consolidation test performed by Gu et al. (2019) introduced above, the initial shear stiffness of the soil sampled from 30m and 70m depths were measured by local bender elements. In their study, different stress paths for soil consolidation have been investigated, performed in terms of axial loading, lateral loading and constant p' loading consolidation. The results show little difference found among different stress paths. Therefore, Shanghai clay performs low stress path dependency in initial small strain stiffness.

3.5 Shear Stiffness Degradation

The static triaxial test conducted by Zhang et al. (2017) employed resonant column and bender elements to determine the small strain stiffness degradation of Shanghai clay. The local strain

transducer based on Hall Effect was employed and dynamic tests were carried out. The fitted degradation curve has been plotted (see Figure 3.20), showing a deduction of shear stiffness with strain. In their test series, the soil was loaded under a variety of cell pressure condition, simulating the in-situ stress condition in different depths.

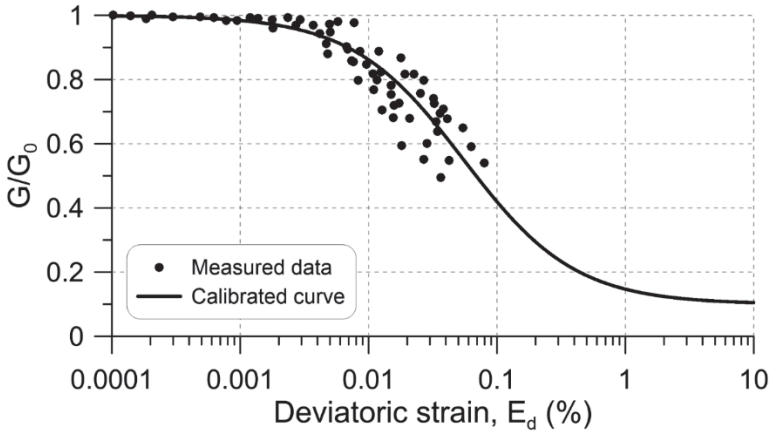


Figure 3.20: Normalized shear stiffness with shear strain for Shanghai clay (Zhang et al., 2017)

Hardin & Drnevich (1972) suggested that usually the degradation curve of shear modulus could be expressed in the form of a hyperbola:

$$\frac{G}{G_0} = \frac{1}{1+(\frac{\gamma}{\gamma_{ref}})^{\alpha}} \tag{3-11}$$

where $\frac{G}{G_0}$ is the normalised stiffness, and the parameter α & γ_{ref} could be determined from the fitting curve. It is suggested that $\alpha = 0.9$, $\gamma_{ref} = 0.07\%$ are adopted for the corresponding Equation 3-7 for the ICG3S model, where $b = 0.9$, $n_G = 1$, $E_{d,r} = 0$. Considering the general deviatoric strain $E_d = \sqrt{3}\gamma$, then $a = 0.07\% \times \sqrt{3} = 0.121\%$. Usually a minimum value of shear stiffness is assumed for larger strain so that the value of $R_{G,min}$ is taken larger than 0 (e.g. $R_{G,min} = 0.1$).

However, in the study of Gu et al. (2019), the stress-path dependency is emphasised on small strain stiffness degradation of Shanghai clay. They carried out undrained shear tests in the forms of axial unloading, lateral unloading and constant p' unloading, and different degradation curves have been plotted for each set. It is found that the shape differs especially at small strain range (<0.1%). The degradation curve of lateral unloading is significantly flatter and lower than the ones corresponding to other two unloading conditions. The reason explained in their study is the deviatoric stress increases in lateral unloading whilst decreases in other two unloading patterns, and the former results in a loading effect on the specimen, which generates internal structure reactions that lowers the stiffness. The results have good agreement with those reported by Hight et al. (2007) and Gasparre et al. (2007).

3.6 Summary of parameters in extended MCC model and ICG3S model

A summary of parameters adopted in both models for different layers of Shanghai clay is listed in Table 3.9.

Table 3.9: Parameters for extended MCC model and ICG3S model

	Description	**1**	**2-1**	**2-2**	**3**	**4**	**5-1**	**5-2**
v_1	Specific volume	2.151	2.337	2.244	2.805	3.692	3.046	2.163
λ	Slope of virgin consolidation line	0.115	0.115	0.0216	0.171	0.291	0.205	0.065
κ	Slope of swelling line	0.0178	0.0178	0.004	0.0264	0.0450	0.0317	0.0101
μ	Poisson ratio	0.33	0.32	0.32	0.32	0.33	0.26	0.29
$\sin\varphi'$	Angle of shear resistance	0.423	0.330	0.574	0.276	0.191	0.242	0.485
G_0	Basic maximum shear modulus (kPa)	/	74130.0	/	51940.0	46450.0	68130.0	123500.0
m_G	Index	/	0.60	/	0.68	0.68	0.65	0.44

3.7 Summary points

The engineering geological condition for tunnelling in Shanghai has been characterised, and the profile of ground layers is established in this chapter. Some important information of the ground condition and soil properties has been determined:

- The geological division of Shanghai ground has been clarified from macro scope. The layering of Holocene strata has been determined via literature survey. It provides basic information of the ground modelling for DOT analysis in Chapter 4.
- The hydrostatic pore water pressure distribution is determined for the DOT modelling in Shanghai clay according to the analysis of aquifer system in Shanghai ground. The profile of soil anisotropic permeability has been established from literature.
- The extended MCC model and ICG3S model, which are considered suitable for characterising undrained shear strength and small strain stiffness of soft clay respectively, have been calibrated against laboratory data and field measurements.
- The profile of undrained shear strength for Shanghai clay is built up, reaching good agreement with the field data. The extended MCC model and the calibration are therefore validated.

Chapter 4. Numerical model of the Shanghai DOT tunnelling case study

4.1 Introduction

The geological setting of the urban area of Shanghai was introduced in Chapter 3, together with the layering and hydro-mechanical characterisation of the ground profile. An extended modified Cam clay (MCC) model was selected to represent the soft soils in the ground profile and calibrated against the experimental data found in literature. The objective of this chapter was to develop a numerical model of a specific case study of DOT tunnelling in Shanghai, for the purpose of validating the numerical analysis approach of this type of tunnelling in soft clay ground conditions.

This chapter first introduces the selected case study, which was a DOT section of the Shanghai Metro Line 6. The details of the numerical model are presented next, including two methods to simulate tunnel construction, the volume loss control method and the boundary stress control method. The characteristics of both methods are discussed in the light of soft ground tunnelling. Both short- and long-term ground settlements are interpreted and compared against field data. In what forms the base analysis, the DOT tunnel lining was represented as an elastic ring using beam element, ignoring the segmental nature of the lining and the presence of an interface between segments.

The subsequent parametric study is introduced next, which represented the interface between lining segments with short beam elements of lower elastic stiffness. Additional parametric study was carried out on the segments' strength, calibrated against different concrete grade. Under different combinations of interface stiffness and segments' strength, the mechanical response of the lining, including axial force, shear force and bending moment, was interpreted and discussed, as well as the effect on the predicted ground movements.

Finally, the effect of grouting was considered, as this is a typical process used in soft ground tunnelling to strengthen the soil around the tunnel and improve the waterproofing. On the other hand, the grouting is expected to cause larger soil disturbance and the heaving around a tunnel. The process of simulating grouting is introduced and examined on the selected case study.

4.2 Base case analysis

4.2.1 Background of the base case analysis

Shanghai Metro Line 6 was constructed in the Pudong district in the east part of Shanghai (see Figure 4.1). The total length of the Metro Line 6 is 31.6km and the DOT section starts from Boxing Road

station to Yunshan Road station, with the length of 1712.6m (Sun 2007). The tunnel was excavated with earth pressure balance machine (EPBM) manufactured by the Mitsubishi Group Japan. Some key information of the DOT EPBM is listed in Table 2.1 in Chapter 2.

The thickness of the covering soil varied from 5.2m to 12m (Lv & Zhang, 2006). The elevation of tunnel crown varies from -2.288m to -6.492m (Depth from 6.0m to 10.2m), whilst the value for invert is from -8.288m to -12.492m (Depth from 12.0m to 16.2). Therefore the tunnel mainly passed through engineering layers 3 and layer 4 (see soil types in Table 3.5), identified as silty clay and muddy clay. The ground surface above the tunnel crown was a greenfield without buildings or any other major structures, according to the site information. The average width of the greenfield area was about 75m, centred above the tunnel crown. Based on this fact the width of a two dimensional (2D) finite element mesh in Figure 4.2, for plane strain analysis, was selected as 100m.

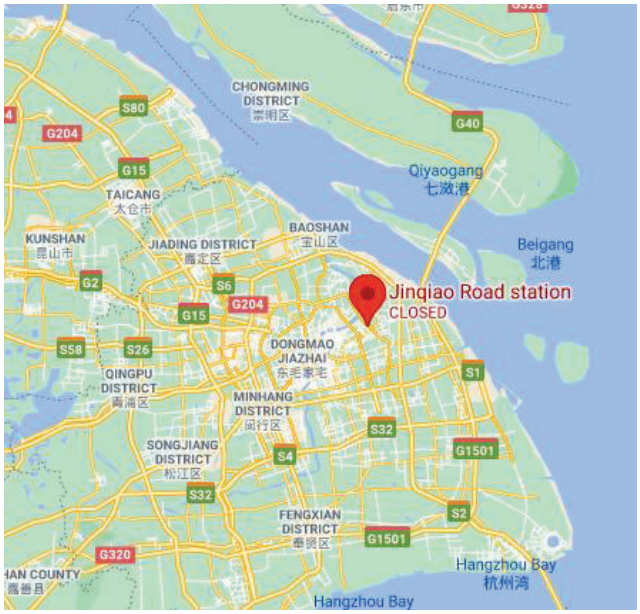


Figure 4.1: Location of DOT tunnel section of Shanghai Metro Line 6

The DOT lining was made of pre-fabricated concrete segments with the design strength of C50, which represents the uniaxial compressive strength of the concrete cube. Each ring consisted of 11 segments, including 8 standard segment, one upper seagull, one lower seagull and a column segment. The ring had the width of 1.2m and the thickness of 300mm (see Table 2.1) for the geometry of different segments). The information about reinforcement and its alignment in the lining was introduced in Chapter 5, as it is irrelevant in this chapter given that the lining was modelled with one dimensional beam elements.

The waterproof function is essentially emphasised for the lining design, and the impermeability level of the concrete for the DOT lining in Shanghai is P10, which satisfies no water leakage through the concrete under the static pore water pressure 1.0MPa, satisfying the serviceability of underground structures at depth between 10m to 30m (Chinese code GB 50164—2011). In the base case analysis, the lining was assumed impermeable after the construction and then an intermediate period, during which the lining is gradually becoming more permeable, is set up for short term analysis.

4.2.2 Initialisation of ground conditions

The numerical model of DOT tunnel construction on the Metro Line 6 was developed with the finite element code ICFEP (Potts & Zdravkovic, 1999). Two-dimensional (2D) geometry was discretised in a finite element (FE) mesh shown in Figure 4.2, which has the lateral dimension of 100m. The 2D plane strain analyses were hydro-mechanically coupled for the prediction of both short- and long-term ground response to DOT tunnelling. The FE mesh in Figure 4.2 also indicates the adopted ground profile. The ground water table was set up at 0.5m depth below the ground surface, which was deemed as high point within a year. The pore water pressure distribution with depth was assumed hydrostatic. The layering information and the corresponding bulk unit weight for each layer are summarised in Table 4.1, for the initialisation of the vertical effective stress in the ground profile. Therefore, the initial condition has been prescribed referring to the ground modelling introduced in Chapter 3, including the profile of the pore water pressure (Figure 3.5a), effective vertical stress (Figure 3.5b) and the earth pressure coefficient at rest (Figure 3.16).

The soil is modelled with 8-noded quadrilateral continuum elements. On both vertical boundaries, zero force is prescribed in the vertical direction, and the horizontal displacement is prevented (see Figure 4.2). The bottom boundary prevents displacements in both horizontal and vertical directions, while top boundary is prescribed zero force at surface nodes and thus is free to move. Constant pore water pressure and zero water flow are prescribed for vertical boundaries, phreatic surface and the bottom boundary, respectively.

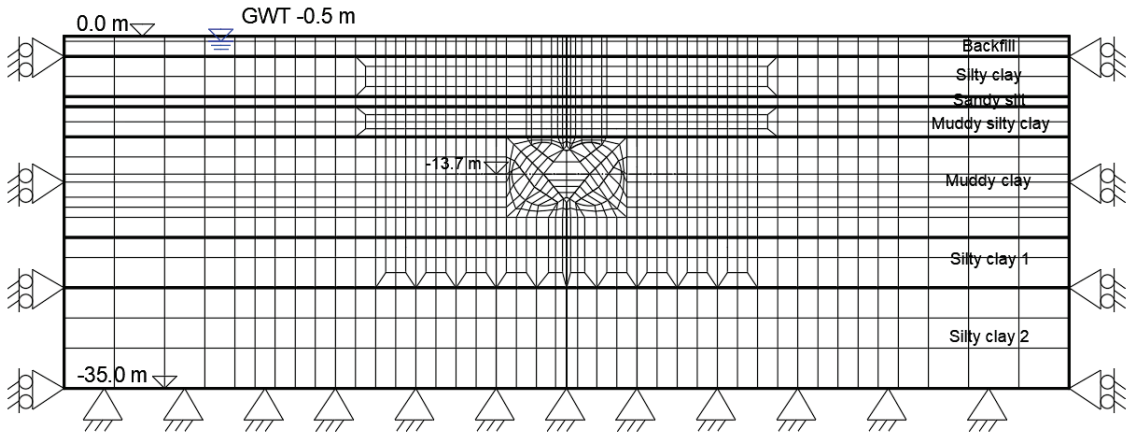


Figure 4.2: Two dimensional mesh for the base case analysis

Table 4.1: Ground layering and the mechanical properties for the base analysis

Layers	**Depth (m)**	γ_{sat} **(kN/m^3)**	ϕ' **(°)**
Backfill	0-2	17.5	25
Silty clay	2-6	17.8	19.3
Sandy silt	6-7	18.2	35
Muddy silty clay	7-10	17.2	16
Muddy clay	10-20	17.1	16
Silty clay-1	20-25	17.5	14
Silty clay-2	25-35	18.1	29

4.2.3 Beam element lining model

Figure 4.3 shows the geometry of the lining ring for this case study. As the lining was discretised with beam elements, there was no physical lining thickness in the mesh, but it was accounted for through the constitutive model for lining beam elements. The connection between segments was achieved with M27 bolts. The bolts were designed for high bending resistance. The overall deformation of the lining was expected to be small under serviceability condition, therefore an elastic lining ring was modelled in the base case analysis. The lining segments were modelled with 3-noded beam elements while the interface between segments was modelled with very short 3-noded beam elements (shown in Figure 4.4). The length of latter elements was 1/100 of the length of a single segment. The input parameters for an elastic beam model are given in Table 4.2.

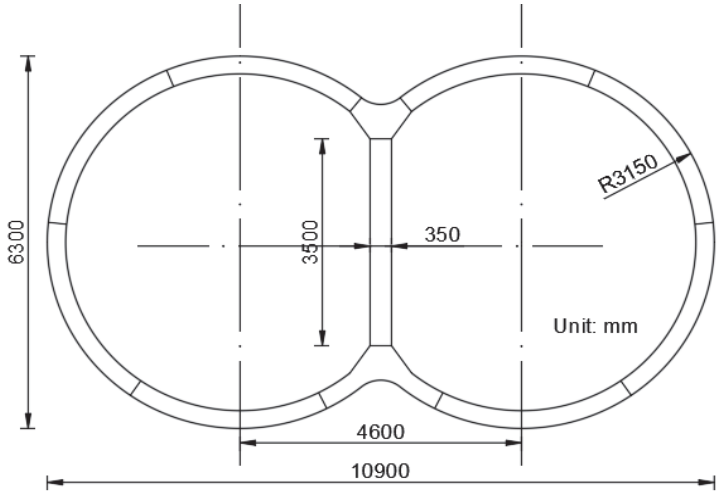


Figure 4.3: Geometry information of the tunnel lining for the modelling

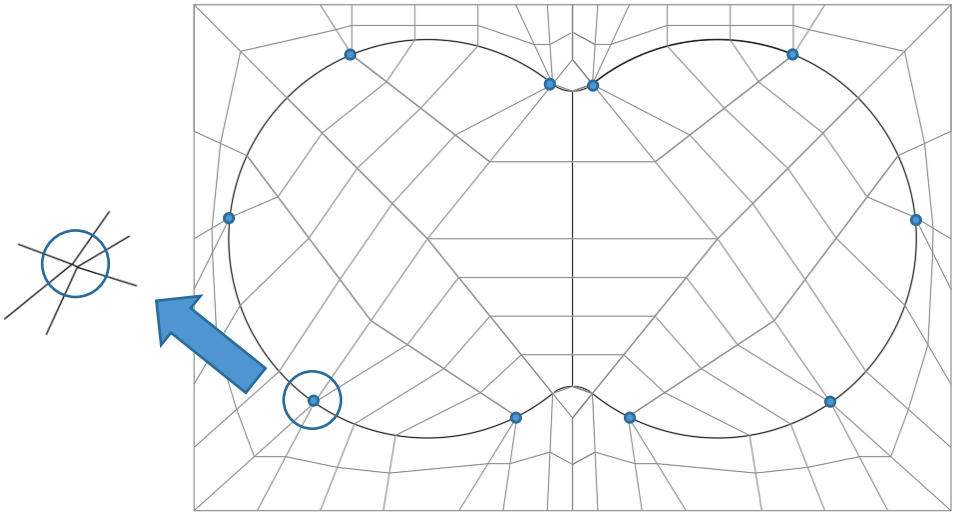


Figure 4.4: modelling of DOT lining and joint (short beam element highlighted with spots)

Table 4.2: Mechanical properties DOT lining in the base case analysis

Properties	**Magnitude**
Young's Modulus E (kPa)	3.45E7
Density (g/cm^3)	2.5
Poisson's ratio	0.2
Area of cross-section (m^2)	0.3
Second moment I (m^4)	2.25E-3

The hydraulic boundary condition around the DOT lining has been investigated. The lining is assumed impermeable, partially permeable and fully permeable respectively, exploring the difference of ground response under various hydraulic conditions. In base analysis, the lining is assumed

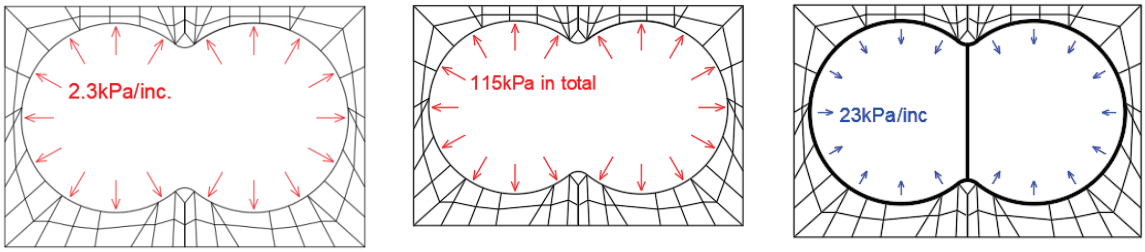
impermeable after construction, considering the water proof measure taken in the engineering. The lining turns into partially permeable for short term consolidation and fully permeable for long term consolidation, which is introduced later.

4.2.4 Simulation process and boundary conditions of the base case analysis

The simulation of DOT tunnelling process on the Shanghai Metro Line 6 case could be divided into three main stages: tunnel excavation and lining construction, short-term consolidation and long-term consolidation. The whole simulation was carried out over 85 increments and detailed construction sequence and boundary conditions at each stage are summarised in Table 4.3. The time scale for the tunnel excavation was determined from the realistic tunnelling speed. The period for short-term consolidation was defined as 3 years (as a period of available monitoring data against which to compare numerical predictions), whilst the long-term was up to 80 years.

In the first stage, the beam elements were removed from the FE mesh to establish the initial stresses in the ground in all soil elements. The DOT tunnel was then excavated over 50 increments, removing the soil elements in the tunnel area, while simultaneously increasing the support normal stress around the tunnel boundary, as shown in Figure 4.5a and Figure 4.5b. The simulation of tunnel excavation can also be carried out using an alternative traditional volume loss control method, which is introduced in Section 4.3.1 in this chapter. However, that method was found causing unrealistic uplift behaviour of the lining ring and consequently resulting in the over-large heaving in the soft clay. Therefore, the supporting stress method, which was found matching the realistic settlement behaviours of the DOT, was adopted in the base analysis.

The time step during excavation was very small in order to simulate an undrained excavation, while the support pressure was introduced to simulate the EPBM support. The appropriate magnitude of the support pressure was determined as 2.3kPa per increment, following a set of trial simulations and achieving a realistic ground volume loss as well as the surface settlement value induced by tunnel excavation. The total normal stress applied on the tunnel boundary was 115kPa after 50 increments. The lining construction was then carried out at increment 51, by re-introducing all beam elements simultaneously around the tunnel boundary. The temporary support pressure was assumed to remain in place for another 5 days, after which it was released incrementally at a rate of 23kPa/day (see Figure 4.5c and Table 4.4). This enabled the ground pressure to be transferred to the lining by the end of day 10 after tunnel excavation and lining construction. This early post-construction stage during which the tunnel boundary remained impermeable was completed by day 28.



(a) (b) (c)

Figure 4.5: The applied normal support stress around the tunnel boundary during excavating. a) incremental stress; b) total support stress after 50 increments; c) removal of the normal supporting stress.

A progressively changing relative permeability (RP) of the lining, which is the ratio between the lining permeability and the permeability of the surrounding soil, was introduced in the analysis from increment 66 to 80, when the simulation was in the intermediate stage from short term to long term. This stage simulates the procedure that the lining becomes gradually permeable in long term. Therefore, a lower permeability (0.1%) was set up after 28 days, and then followed by gradually increasing value at 100d, 200d, 500d and 1000d. In this analysis, the changing permeability of lining is realised by introducing the permeability value into a thin soil layer (only 1cm thick), modelled with solid elements, around the lining. The detailed process is shown in Table 4.3.

Table 4.3: Sequence of DOT tunnelling and post-construction analysis

Increment	Δt	Total time after excavation	Tunnelling simulation stage	Stress boundary condition	Hydraulic boundary condition
0	0	/	Deactivating tunnel lining	/	/
1~50 (50 inc.)	10hrs	/	Full excavation of DOT	Incrementally increasing supporting normal stress (2.3kPa/inc.) around the tunnel boundary (115kPa in total)	Impermeable
51	1hr	0 - 1hr	Lining construction (complete)	Supporting stress stays (115kPa)	Impermeable
52	1d	1hr -1d	Short term consolidation	Supporting stress stays (115kPa)	Impermeable
53	4d	1d - 5d	Short term consolidation	Supporting stress stays (115kPa)	Impermeable
54~63 (10 inc.)	5d (0.5d/inc.)	5d - 10d	Short term consolidation	Supporting stress released incrementally (23kPa/inc. from inc 55 to 59; 115kPa released in total)	Impermeable
64	10d	10d - 20d	Short term consolidation	/	Impermeable
65	8d	20d - 28d	Short term consolidation	/	Impermeable
66~70 (5 inc.)	72d (14.4d/inc.)	28d - 100d	Short term consolidation	/	Low permeability (relative permeability (RP) = 0.1%)
71~80 (10 inc.)	900d (90d/inc.)	100d - 1000d	Short term consolidation	/	Increasing relative permeability (see note)
81~85 (5 inc.)	77 years (15.4y/inc.)	1000d - about 80 years	Long term consolidation	/	Zero pore water pressure around the lining (assumed to be fully permeable)

Note: from inc.71 to inc 80, the RP changes at inc. 71 (RP = 1%; 100d); inc. 72 (RP = 2%; 200d); inc. 75 (RP = 10%; 500d); inc 80 (RP = 20%; 1000d).

4.2.5 Results of base case analysis and discussion

Short-term ground settlement

As explained in Section 4.2.4, the short term was defined as starting from the end of tunnel excavation to around 1000 days (or 3 years), during which a partially permeable lining was simulated, prescribing an increasing relative permeability of the lining to the soil. The pore water pressure regime, presented later in Figure 4.13, was shown to result in positive pore pressures around the tunnel at the end of excavation. This was opposite to excavations in stiff clays, which tend to result in suctions in the vicinity of the tunnel boundary after excavation (as shown in Chapter 7).

Field records on the short-term settlement were available from a single bore tunnelling on the Shanghai Metro Line 2 given by Ao & Zhang (2011). Figure 4.6 unveils an initially high rate of post-tunnelling settlement, which stabilised at around 100 days. Consequently, the short-term settlement was considered close to near 'completion' and it was believed that not much further ground motion would occur after 100 days on the premise that the lining constantly stays impermeable or very low permeable. It was also noticed that the settlement rate was decreasing substantially after around 40 days. This observation was important for the study of DOT simulation, in terms of selecting the time points for presenting the ground response in the current study.

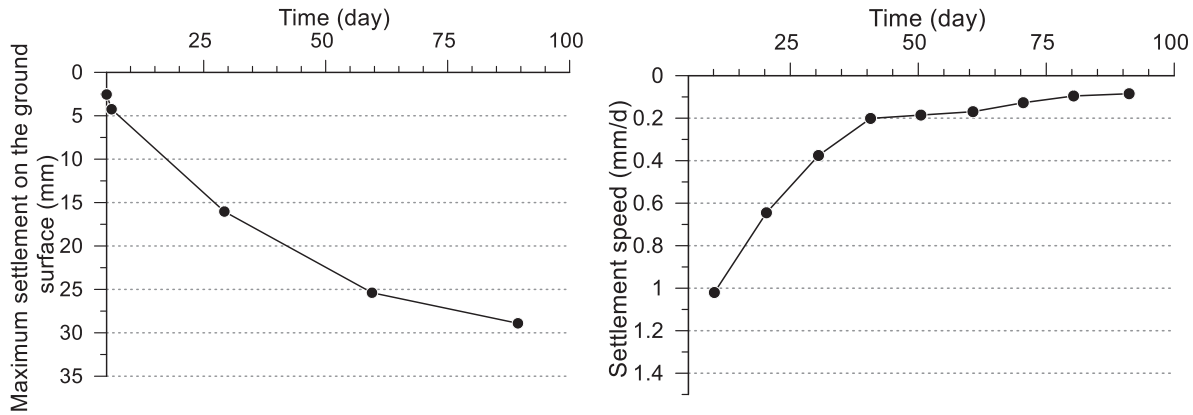
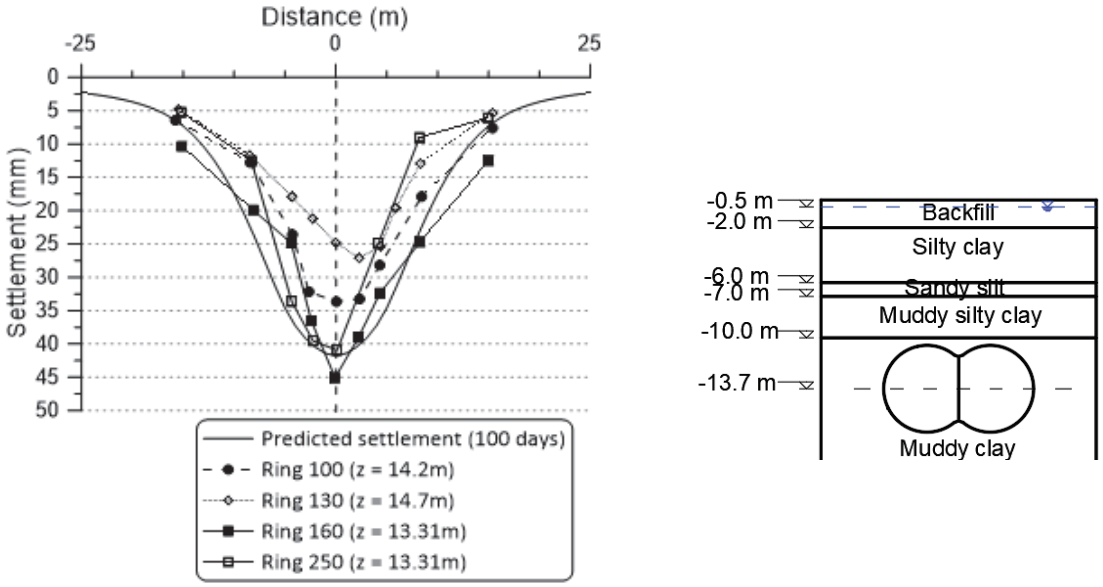


Figure 4.6: Development of maximum settlement and the speed of Shanghai Metro Line 2. a) Maximum settlement; b) Settlement rate (data from Ao & Zhang, 2011).

The settlement at 100 days post-construction was one of the main variables reported from monitoring, for the purpose of evaluating the quality of tunnelling. Wei et al. (2011) reported the 3-month (around 100 days) settlements in Figure 4.7 and Table 4.4, for specific lining rings of the DOT tunnel on the Shanghai Metro Line 6 (the subject of the base case analysis). The rings were numbered in sequence, indicating the relative position of the construction section along the whole line. The maximum transverse surface settlements summarised in Figure 4.7, together with the centre-line depth of each ring, clearly show that the shallower Ring 160 and Ring 250 (depth of 13.31m) mobilised larger surface

settlements (41 to 45mm), while deeper Ring 130 and Ring 100 (around 14.5m depth) caused less ground disturbance (30mm on average maximum surface settlement). This variation was also attributed to larger volume losses interpreted for the shallower rings. The volume loss for each ring, interpreted as dividing the enclosed area of the settlement trough by the tunnel cross-sectional area, varied from 0.81% to 1.40%, which was within the range of volume loss values summarised in Figure 4.8. The settlement troughs for selected rings presented in Figure 4.7 were consistently narrow by comparison to each other.



(a) *(b)*

Figure 4.7: Predicted surface settlement compared against field data. a) The settlement troughs; b) the depth of DOT tunnel in the simulation (measured data from Wei et al. (2011)).

Table 4.4: The volume loss and the maximum settlement measured from the field at 100 days (Wei et al., 2011)

	Ring 100	**Ring 130**	**Ring 160**	**Ring 250**
Vl (%)	1.05	0.81	1.32	1.40
S max (mm)	33.65	27.10	45.07	40.94
Depth (axial; m)	14.20	14.70	13.31	13.31

Figure 4.8 shows a variation of the interpreted volume loss at 100 days for several DOT rings on Metro Line 6 (Lv & Zhang, 2006), with values varying from 0.43% to 1.37%. These values did not deviate very much from the past experience of single tunnel constructions in the Shanghai area (0.35% - 1.35%). Based on this, the target volume loss of 1.15% immediately after excavation and 1.57% at 100d after excavation was adopted for the base case analysis. It is noted that the values of volume loss are interpreted from the field data by dividing the enclosed area of the surface settlement curve with the

cross-sectional area of DOT. Therefore, a slightly higher volume loss adopted in the numerical model is reasonable due to the wider settlement trough compared to the field data whilst the maximum settlements are close.

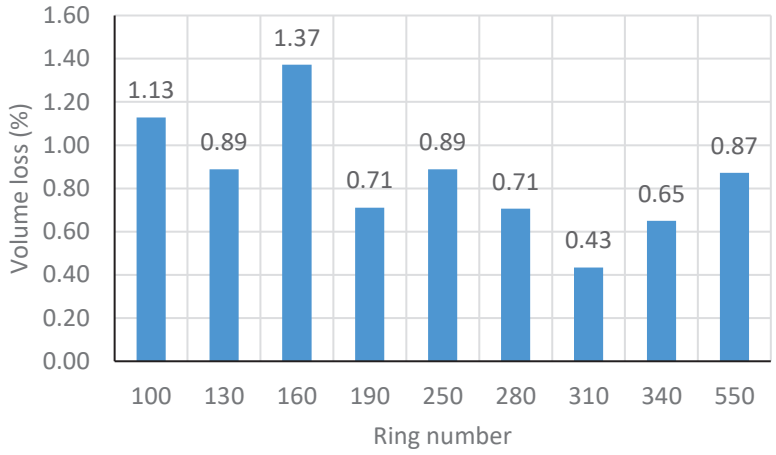


Figure 4.8: Interpreted volume loss for a number of DOT rings on Metro Line 6 (Lv & Zhang, 2006)

Figure 4.9 shows the predicted settlement trough at the ground surface, developing in the short-term, from DOT base case analysis. The corresponding volume losses are given in Table 4.5. As introduced in Section 4.2.4, the magnitude of the support pressure and its incremental release were determined by achieving a prescribed volume loss, as indicated above. Here, the volume loss is calculated by dividing the cross-section area of DOT with enclosed area of the settlement curve on the surface. The excavation resulted in 26mm immediate settlement and then increased by 14mm within 28 days, showing an initial high rate of settlement, then slowing down by 100 days, similar to the measured behaviour shown in Figure 4.6 for a single tunnel on Metro Line 2. The maximum settlement predicted at the 100 days was 43mm, having not changed significantly between 28 and 100 days. This magnitude compares favourably with maximum settlements reported in Table 4.4 and Figure 4.7. The shape of the surface settlement trough in Figure 4.7 is also comparable with measured at the same time instance. However, considering the lining deterioration and the joint leakage from a more conservative aspect, the increasing relative permeability of the lining is set up in the model from 100d to 1000d after construction. The settlement is still growing to 60mm at the time point of 1000d (3 years), which also matches the field observation in a long term scale (see Figure 4.11).

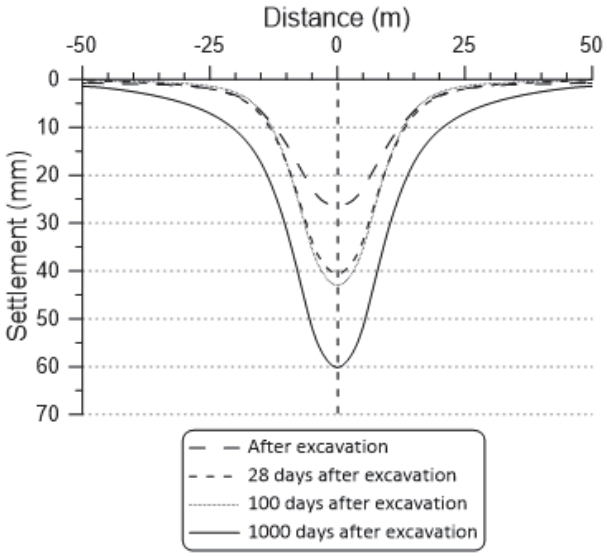


Figure 4.9: Settlement of ground surface of DOT simulation for short term.

Table 4.5: Maximum settlement and volume loss on the ground surface of DOT simulation

Time	Volume loss (%)	Maximum settlement (mm)
After excavation	1.15	26.4
28 days after excavation	1.51	40.6
100 days after excavation	1.57	41.7
1000 days after excavation	2.82	60.1

The subsurface settlements were interpreted and analysed for validating the assumption of undrained behaviour of the soil during excavation. The development of subsurface settlement troughs, at the same time scales, was investigated at depths 2m, 6m, 7m and 10m from the ground surface. All levels were above the tunnel crown and results were summarised in Figure 4.10.

The rate of subsurface settlements evolved similarly to that at the ground surface, with trough configurations at each sub-surface level being established at 100 days after excavation. In fact, a trial analysis of no change of lining permeability after 100 days was carried out, and the results show that little further settlement is developed under that condition. Therefore, the additional volume loss caused after 100 days to 1000 day is attributed to the change of relative permeability, and the time point 100 days is suitable for the settlement stabilisation for impermeable/very low permeable lining. The soil at the depth of 10m experiences the largest movement towards the tunnel, as would be expected. For each time points among the depths, the positions of inflection points on the trough, where the width of the curve is defined accordingly, are almost identical (see the illustration in Figure 4.10a). That reaches good agreement on the same volume loss for subsurface ground induced from the excavation among the depths as listed in Table 4.6. The top layer at the depth of 2m generates

higher volume loss due to drainage on the surface during the consolidation. In deeper layers, however, the soil is believed to experience undrained mechanical process after the excavation during the short term consolidation period. It is only exact after excavation that the soil among all depths performs pure undrained property with the volume loss 1.14% - 1.15%. It can be seen that, after 28 days, the volume loss on surface still increases while less further evolution in sublayers. Therefore, the assumption of undrained consolidation for short term is suitable for this ground case.

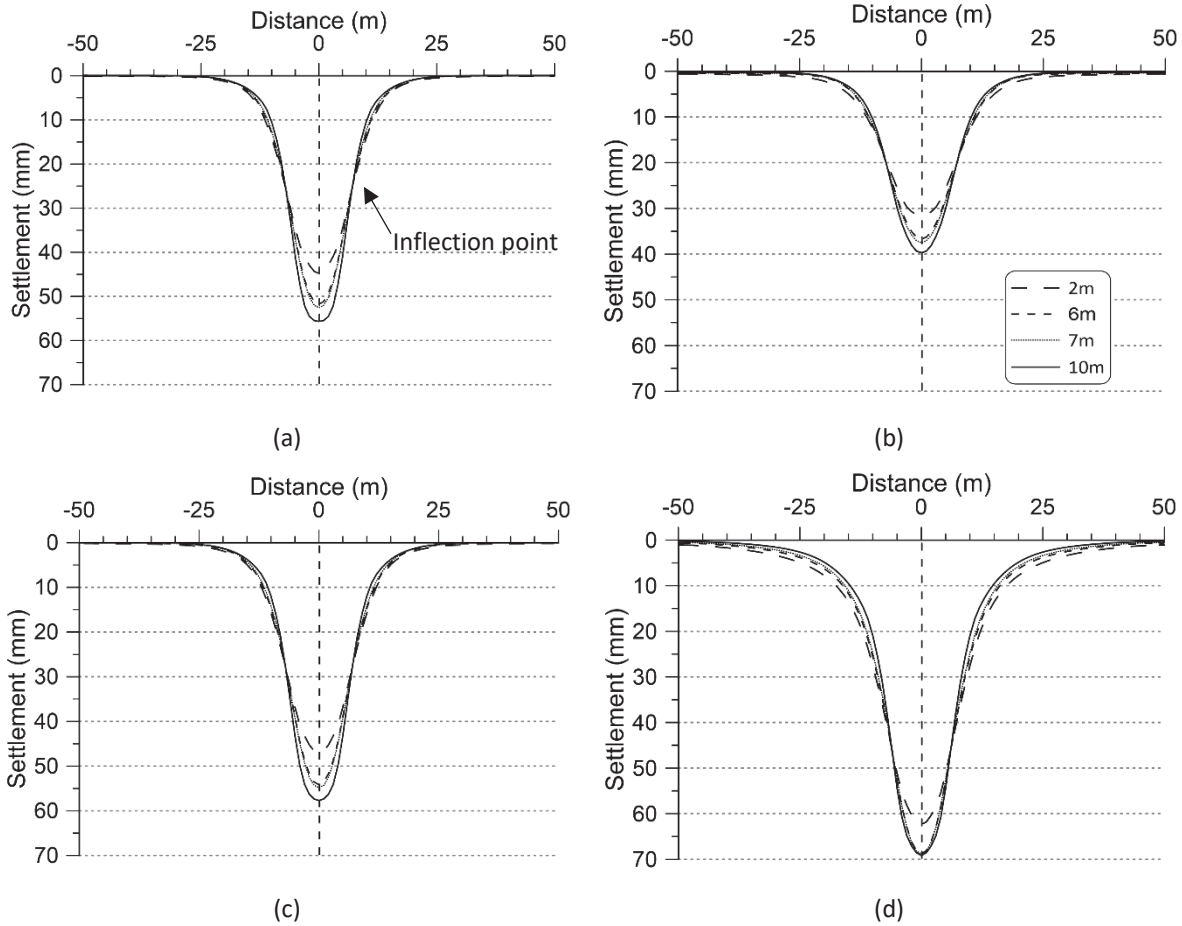


Figure 4.10: Subsurface settlement troughs: a) after excavation; b) 28 days after excavation; c) 100 days after excavation; d) 1000 days after excavation.

Table 4.6: The volume loss output at different depths for short term analysis

Depth	After excavation	28 days	100 days	1000 days
Surface	1.15%	1.51%	1.57%	2.82%
2m	1.14%	1.34%	1.29%	2.50%
6m	1.15%	1.40%	1.35%	2.43%
7m	1.14%	1.39%	1.34%	2.37%
10m	1.15%	1.45%	1.40%	2.24%

Long term settlement of the ground

The short-term ground response involved immediate settlement directly induced from excavation and the increasing part caused from soil consolidation with partly permeable lining. In the base case analysis, the long-term period was defined from 1000 days to 80 years, during which the tunnel lining was considered to have lost the waterproofing function. The lining was modelled as fully permeable, by prescribing a zero pore water pressure around the tunnel boundary.

For lack of data from DOT tunnels, the long-term settlement data of a single circular tunnel on Shanghai Metro Line 2 was considered (Figure 4.11). Each line in the figure represents the evolution of maximum settlement measured over 10 years after tunnelling, in the corresponding tunnel sections identified by stations along the line. Apparently, the long term settlement also has experienced decreasing rate, and mobilised to a stable value. The magnitude varies from 30mm to 160mm on different sections, and the variance among the sections is considered large, which could be accounted for by the difference of local site conditions. It is noted that the long term settlement starts show the tendency of stabilisation at around 5 years (from the year 2005) after construction for all sections, implying the similar consolidation rates for each tunnel. That reflects the consistence of ground and hydraulic conditions in Shanghai. Therefore, it can be expected that the long term settlement of DOT may follow the same pattern as the Shanghai Metro Line 2. Performing decreasing consolidation rate and reaching the stabilisation after 10 years.

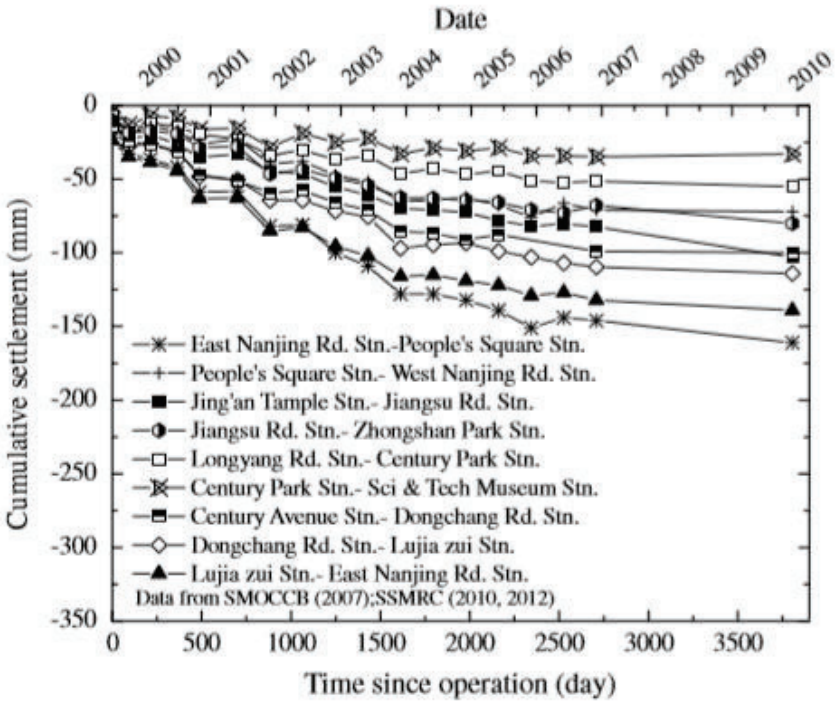


Figure 4.11: Measurement of long term settlement of Shanghai Metro Line 2 on different sections (Ao & Zhang, 2011).

The long term consolidation with more permeable lining leads to wider influenced area and the larger ground response. To objectively establish the long term settlement model, a wider mesh (500m width) has been built up for this long term analysis. The discretisation and the boundary conditions of the model follows the identical configuration as shown in Table 4.3. In fact, the only difference in boundary condition prescribed for long term analysis is only the zero pore water pressure around the lining, allowing free ground water flow.

The predicted settlement results of long term consolidation show the large expected settlement developed for the DOT (see Figure 4.12). As described in the part for Shanghai Metro Line 2 above, the maximum settlement starts to stabilise after 5 years, and consequently, the troughs for 10 years, 40 years and 80 years are almost overlapped, implying no further consolidation taking place after 10 years. Besides the higher permeability of the Shanghai clay, the groundwater condition and the extreme hydraulic boundary prescribed for the model attributes to the fast stabilisation of the ground settlement shown in the figure. In this analysis, rather than only the differential settlement is focused on, but the overall settlement is also concerned, which is performed as the parallel subsidence of the whole site. Therefore, the extension of the mesh, employing a wider width for modelling the DOT site, is necessary to assess the influenced region of this overall subsidence caused by long term consolidation. The characterisation of the maximum settlement evolution has good agreement with the recording data of the Shanghai Metro Line 2 in terms of time for stabilisation and the eventual value. Therefore, the assumption of full permeable lining for the DOT simulation in long term is considered suitable for reproducing the ground response. The first five years post construction can be the key period for consolidation induced settlement of tunnels in Shanghai clay.

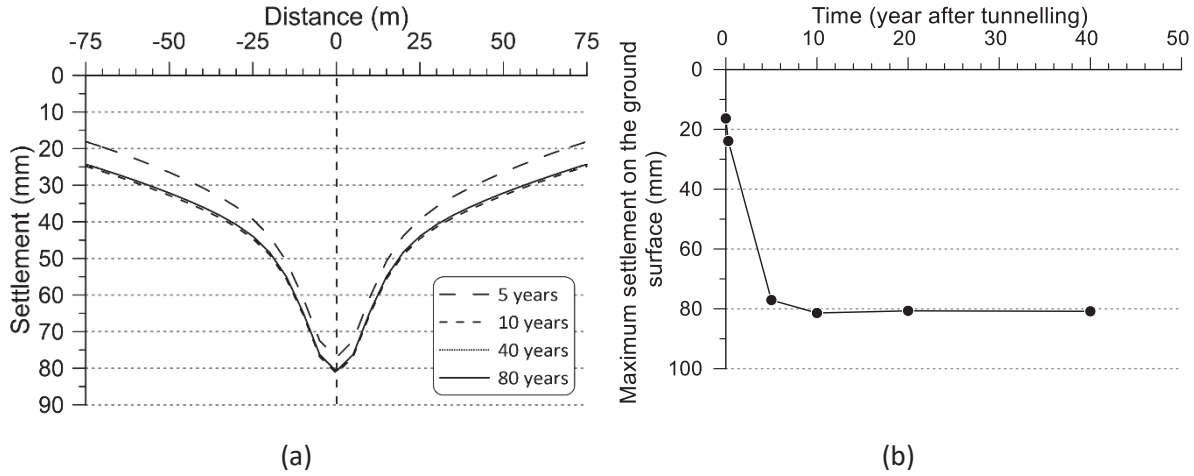
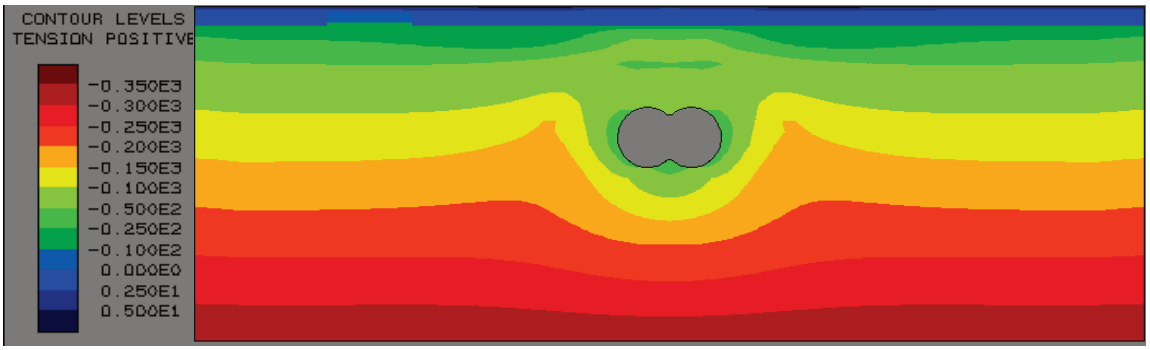


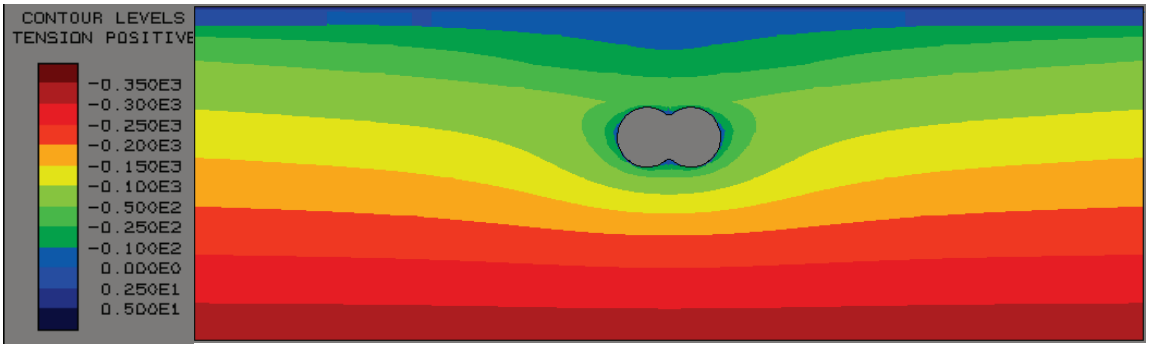
Figure 4.12: Long term settlement predicted for DOT. a) transverse settlement; b) maximum settlement

Evolution of pore water pressure

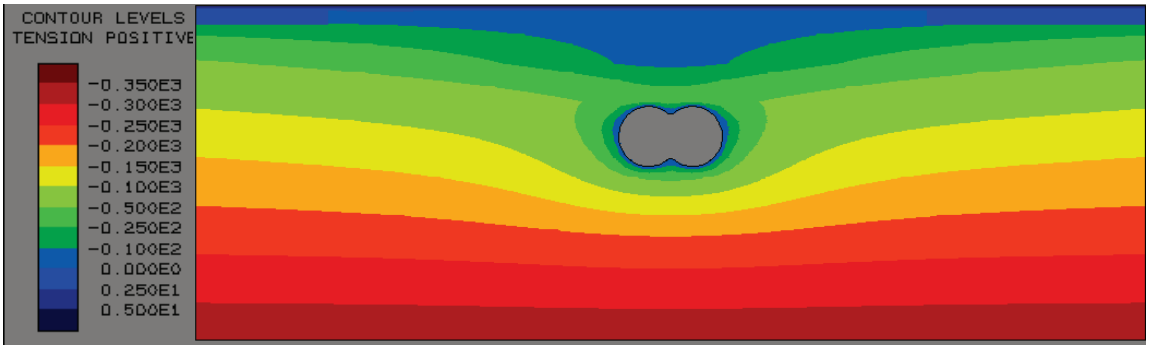
The response of pore water pressure induced from tunnel excavation and the consolidation post construction is considered causing important impact on the ground mechanical behaviour due to the change of effective stress. Three contour plots of pore water pressure distribution are shown in Figure 4.13. It can be seen that the excavation process results in changes of the pore water pressure around the tunnelling area, which evolve with time, and the gradient in vicinity to the lining is high (Figure 4.13a). This is because the lining is impermeable and the water pressure builds up, It then dissipates with time as the lining become more permeable gradually and fully permeable in the long ter. The gradient is flattened when it comes to 1000 days, which is the intermediate stage from the short term to long term, the ground water tends to be stabilised and the overall distribution approaches the long term shape (Figure 4.13b). The fully permeable condition in long term results in the massive evolution of ground water profile compared to the one after excavation. It is noted that the three contour figures are presented with the same scale of pore water pressure. Apparently, the tunnel has experienced increasing vertical effective stress after the conversion of hydraulic boundary condition from a partially permeable lining to the fully permeable condition (Figure 4.13c).



(a) end of excavation



(b) 1000 days after tunnelling



(c) 80 years after tunnelling

Figure 4.13: The evolution of pore water pressure in short and long term (kPa): a) end of excavation at increment 50; b) 1000 days consolidation; c) end of long term consolidation

Internal lining force of the DOT tunnel

The internal lining force distribution and lining deformation after tunnelling are important factors to assess the engineering risk and analyse the influence on lining serviceability. The internal forces, including bending moment and axial force (hoop force) have been investigated. In the base case analysis, the lining was modelled with beam elements as a continuous ring. Because of the geometric symmetry, the lining forces were interpreted in the half of the lining. The axial force inside the lining is caused by the overburden ground pressure and therefore this force can be reasonably uniform in the lining. The bending moment is related to the distorted shape of the lining ring, which accounts for serviceability of the tunnel.

The predicted distributions of axial force and bending moment in the lining, at various time instances, were shown in Figure 4.14. The values were plotted along the length of the lining, starting from the upper seagull position of the left half ring to the lower seagull position in the anti-clockwise direction. The distance is about 14m. In a trial analysis of no change of lining permeability in short term (3 years), the axial force and bending moment were established within the first 28 days and did not change significantly within the first 3 years of the lining being partially permeable. The axial force varied from 400kN to 500kN, showing a tendency of increasing value from the crown to the tunnel invert.

As for bending moment, the short term consolidation has not resulted in sharp evolution, and the peak value is only 22kN at 10 days. In long term, after the conversion of hydraulic boundary condition, not only the value of bending moment has increased, but the shape of distribution has changed (see Figure 4.14b). The maximum bending moment almost doubled compared to the short term result. The bending moment subjects to the differential normal stress loading on the lining from the ground increases during the consolidation process due to the developing vertical effective stress. The zero pore water pressure around the lining in long term causes great influence on the stress difference between the lining centre-line and the crown-invert line. After long term consolidation, which is from 1000 days to 80 years, the maximum bending moments occur at the distance of 7m and 13m, which

locate around the joint number 3 and number 5 respectively as shown in the figure. This result is consistent with the analysis of Zhou et al. (2005) and Hu & Zhang (2008), both of which gave analytical solution of the DOT lining force in Metro Line 8.

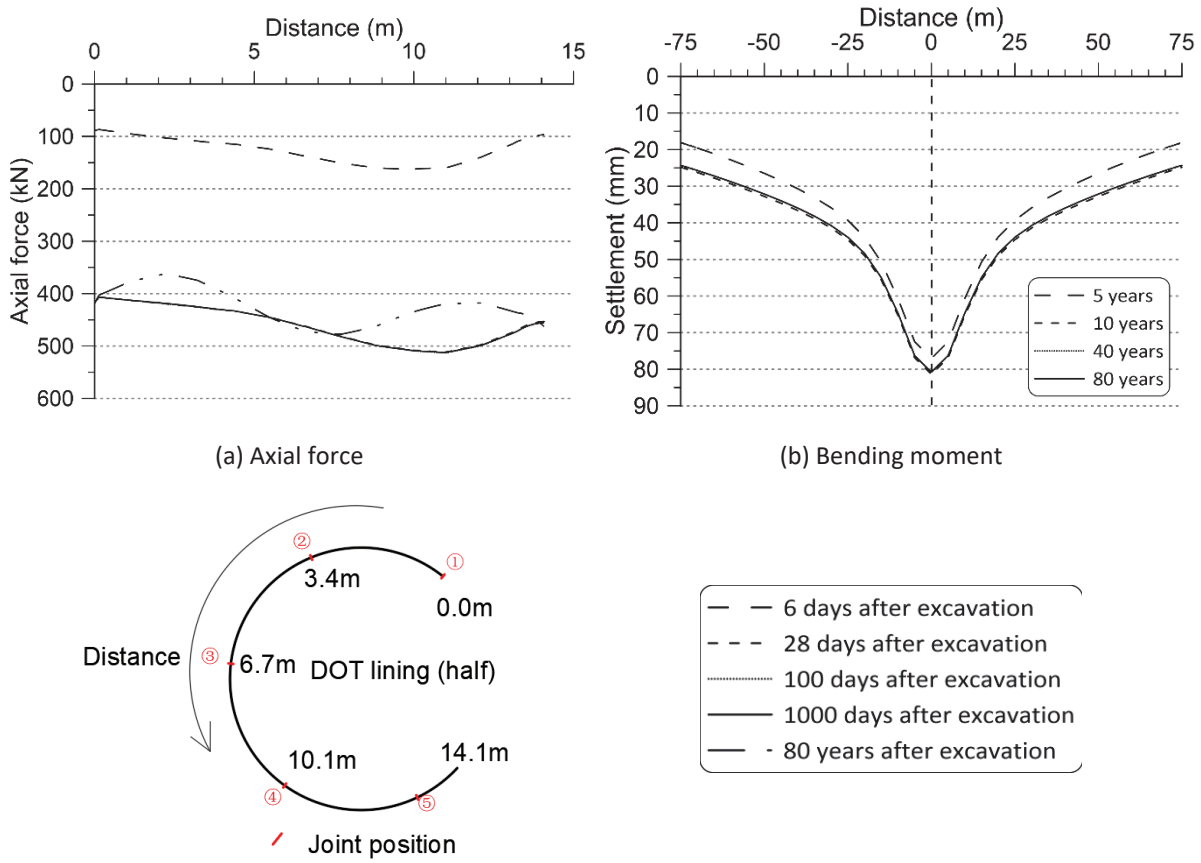


Figure 4.14: Distribution of internal force along the lining. a) axial force; b) bending moment

The displaced shape of DOT ring was considered important for serviceability. The long-term distortion (after 80 years) of the lining was shown in Figure 4.15, and the maximum displacement, which is in vertical direction, occurred at the tunnel crown in all stages. This indicates that the ring experienced 'squatting' under consolidation, which accounts for the occurrence of higher bending moments on joint number 3.

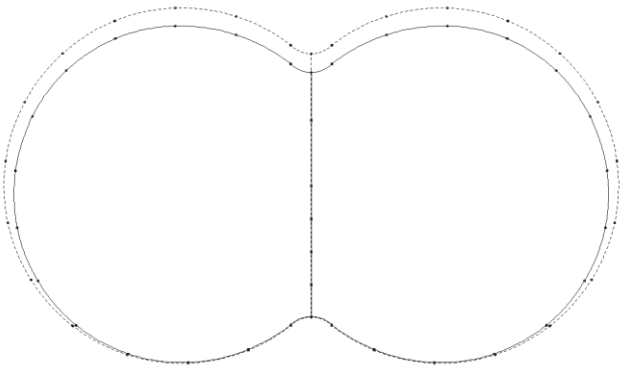


Figure 4.15: Predicted deformation shape of the DOT ring in long term (80 years)

4.3 Parametric study

4.3.1 Construction simulation methods

Two types of construction simulation methods were investigated prior to performing the base case analysis. One was the volume loss control method and the other the supporting stress control method. The latter method was adopted for the base case analysis, as discussed in Section 4.2.4, as it was considered more appropriate for the simulation of tunnelling in soft ground.

The volume loss control method has been widely employed in tunnel simulations and was attempted for the base case analysis (Shanghai Metro Line 6). As summarised in Table 4.7, excavation of DOT tunnel was carried out over 50 increments, and the lining is inserted at increment 19, when the ground loss on the surface reaches a target value of 1.2%. This increment of lining construction was determined after a series of trial simulations, and the lining construction was completed within one increment. All other steps of analysis and boundary conditions were the same as in the base case analysis, presented in Section 4.2.

Immediately after excavation, the maximum settlement reached 27mm, which was practically identical in magnitude and volume loss (about 1.27%) predicted in the analysis with the support stress control method of the volume loss (see Figure 4.16 & Figure 4.17a). However, after 28 days post construction, the settlement has decreased, which consequently implies the uplifting of the ground and the tunnel lining ring. In fact, this phenomenon has been observed in some engineering cases in Beijing, Shanghai and Guangzhou (Xiao et al., 2009), and the recorded upward displacement of the lining reached from 0 to 60mm for the tunnel with diameter of 6m in these engineering cases. The main reason for the upward moving of the tunnel is grouting under very high pressure at the tunnel invert and the buoyance from the ground water in short term. The redistribution of ground pressure around the lining due to tunnelling also contributes to the lining floating. However, it is noted that the upward displacement occurs immediately after the excavation and the behaviour is well controlled with the fast solidification of the grouts. Therefore, the uplifting of ground surface caused by ground movement and consolidation over the period of 28 days in the numerical simulation is over-predicted in the analysis and that impedes the evolution of settlement in short term. The stabilised short term settlement is apparently under-predicted by using volume loss control method compared against the result from base analysis (see Figure 4.16 & Figure 4.17b), and consequently the evolution of surface settlement performed is not realistic.

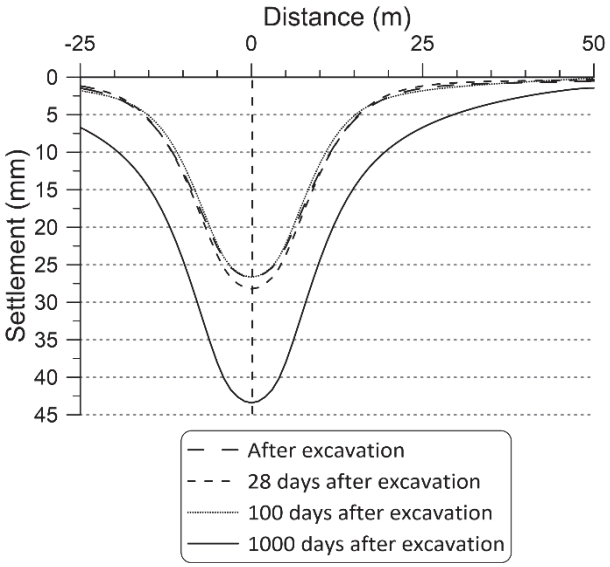


Figure 4.16: Settlement of ground surface in DOT simulation using volume loss control method

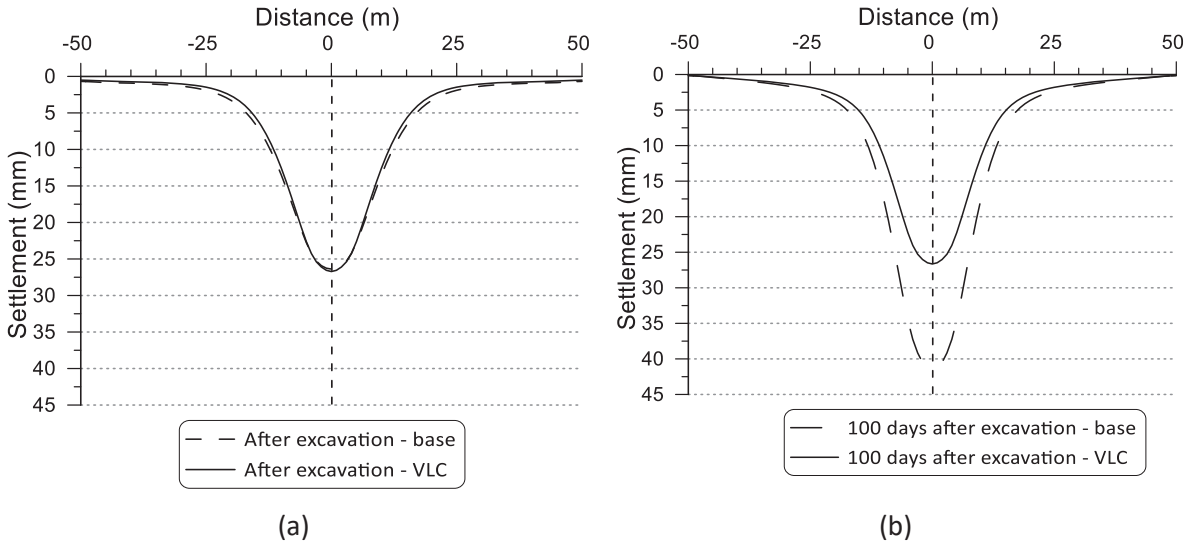


Figure 4.17: Comparison of settlement between two simulation methods on different stages. a) after excavation; b) 100 days after excavation;

Table 4.7: The sequence of tunnel simulation using volume loss control method

Increment	Δt	Total time after excavation	Tunnelling simulation stage	Hydraulic boundary condition
0	0	/	Deactivating tunnel lining	/
1~50 (50 inc.)	10h	/	Full excavation of DOT	/
19	1h	0	Lining construction (complete)	Impermeable
52	1d	1d	Short term consolidation	Impermeable
53	4d	5d	Short term consolidation	Impermeable
54~63 (10 inc.)	5d (0.5d/inc)	10d	Short term consolidation	Impermeable
64	10d	20d	Short term consolidation	Impermeable
65	8d	28d	Short term consolidation	Impermeable
66~70 (5 inc.)	72d (14.4d/inc.)	100d	Short term consolidation	Low permeability (relative permeability (RP) = 0.1%)
71~80 (10 inc.)	900d (90d/inc.)	1000d	Short term consolidation	Increasing permeability (the same with Table 4.3)
81~85 (5 inc.)	77 years (15.4y/inc,))	about 80 years	Long term consolidation	Zero pore water pressure around the lining (assumed to be fully permeable)

Note: the time scale and hydraulic boundary conditions are the same with base analysis. The only difference of volume-loss-control method is that the lining is installed at increment 19. Consequently, no additional stress boundary around the lining needs to be specified when using this method.

4.3.2 Lining properties

The DOT lining is made of C45 or C50 pre-fabricated concrete with high stiffness, the grade of which is determined for safety design. A series of tests of different concrete grades have been carried out to investigate the influence of concrete grade on the lining behaviour (Table 4.8). The lining modelled with elastic beam elements is characterised with corresponding maximum compressive strength and Young's modulus. In fact, the lining is under considered serviceability condition during and after tunnelling, and the failure of lining material happens where the material reaches ultimate conditions

Table 4.8: The series of simulation on different concrete grades

DATA FILE	Lining material (concrete)	maximum compressive strength	Young's modulus	Poisson's ratio
DOT_SML6_C20	C20	13500.0 kPa	2.55E7 kPa	0.2
DOT_SML6_C30	C30	20000.0 kPa	3.00E7 kPa	0.2
DOT_SML6_C40	C40	27000.0 kPa	3.25E7 kPa	0.2
DOT_SML6_Base	C50 (base)	32500.0 kPa	3.45E7 kPa	0.2

Note: the current analysis assumes the tunnel ring is elastic.

The distributions of bending moment and axial force after long term consolidation show similar shapes and magnitudes along the lining for different concrete grades (see Figure 4.18 & *Figure 4.19*). The curves of lining internal force for short term study are also highly overlapped in a similar manner, and therefore, those results are not presented here. It is concluded that the concrete grade of the lining does not play the essential role in the lining internal force under serviceability condition. As for the ultimate state, when the lining is loaded to failure, among various concrete grades, a detailed numerical investigation using concrete model is introduced in Chapter 5.

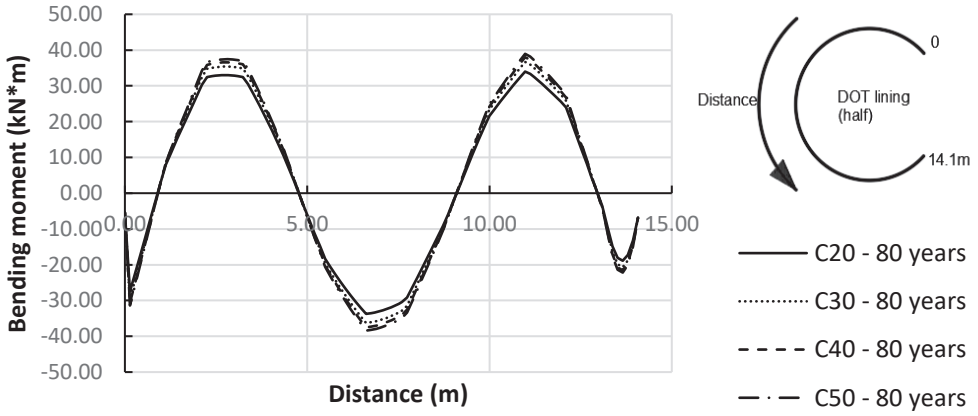


Figure 4.18: Stabilised bending moment among different concrete grades

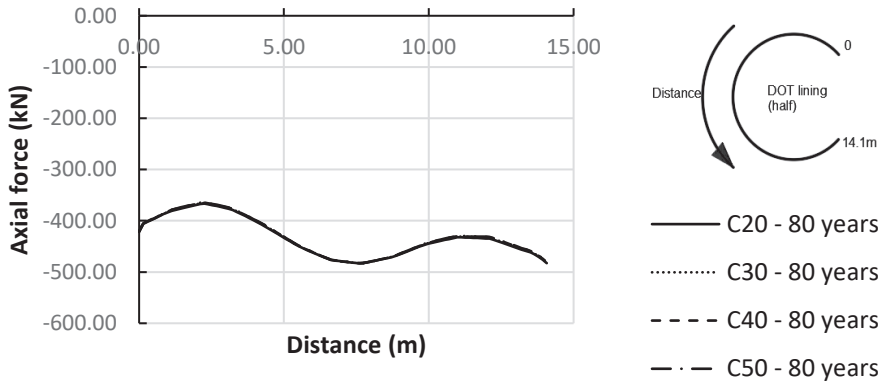


Figure 4.19: Stabilised axial force among different concrete grades

Joint stiffness study

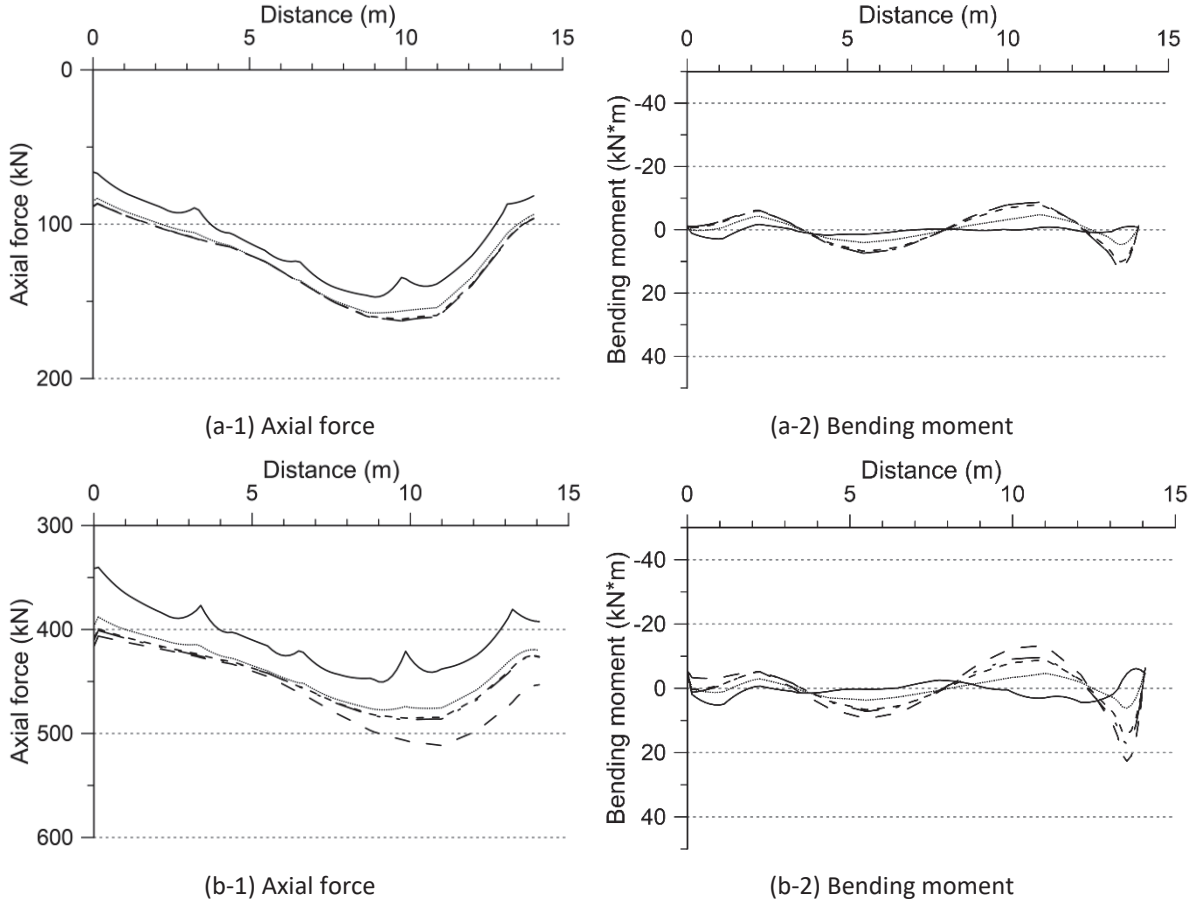
The staggered rule of lining ring assembling is adopted in the DOT construction, and therefore, the modelling of joints between segments, which are usually considered weak positions, are not specifically conducted in a lot of tunnelling simulations. However, it is believed that the stiffness of joints does influence the response of lining force, and consequently causes effect on the lining serviceability. The performance of a single ring is also essential in lining serviceability and the joint stiffness subject to the mechanical property of the whole ring, is discussed here. Therefore, the investigation on the 'softer' joints have been carried out based on scaling down the joint stiffness adopted in the base analysis, and a group of tests are listed below (see Table 4.9).

Table 4.9: The series of simulation on different joint stiffness

DATA FILE	Joint types	Young's modulus E (kPa)	Description
DOT_SML6_SOFTER2	Softer elastic joint - 2	3.45E5	100 times softer
DOT_SML6_SOFTER3	Softer elastic joint - 3	3.45E4	1000 times softer
DOT_SML6_SOFTER4	Softer elastic joint - 4	3.45E3	10000 times softer
DOT_SML6_STIFFER2	Stiffer elastic joint - 2	3.45E9	100 times stiffer
DOT_SML6_Base	Elastic ring (base; for comparison)	3.45E7 (C50 concrete)	/

The joints are still modelled with short beam elements, and the analyses are prescribed with identical boundary conditions. In this series test, the joint stiffness is classified in five magnitude levels. An objective reflection and modelling of the 'real' joint stiffness base on engineering reality will be difficult to conduct, which may needs a systematic laboratory testing on the assembled concrete ring in different joint cracking states. Considering the softening of joints are referred to the joints cracking or aging, the relevant stiffness grades based on the concrete lining are therefore assumed, to investigate the sensitivity of joint stiffness in the performance of lining internal force over different stages. The distribution of lining internal forces at 7 days, 28 days, 100 days, 1000 days and 80 years,

in terms of axial force and bending moment, are shown in Figure 4.20 below. It can be seen from the figures that under serviceability condition, the softer joints lead to smaller force reactions along the whole lining ring, which means the softer joints not only lower the stiffness of the joint position but also decrease the overall stiffness of the ring. Compared with the difference of axial forces, the distribution of bending moment, which is directly related to the lining cracking, shows more obvious influence caused by softer joints. It is noted that the long term consolidation condition, under which the tunnel is assumed fully permeable in the model, scales up the effect of soft joints. Therefore, it can be concluded that softer joints may attribute to protecting the lining segments in terms of lower the bending moment and that reduces the risk of concrete cracking, while high overall stiffness will be harmful for the whole structure in long term when the lining is fully permeable and higher difference of effective stress is generated around the lining.



(a-1) Axial force

(a-2) Bending moment

(b-1) Axial force

(b-2) Bending moment

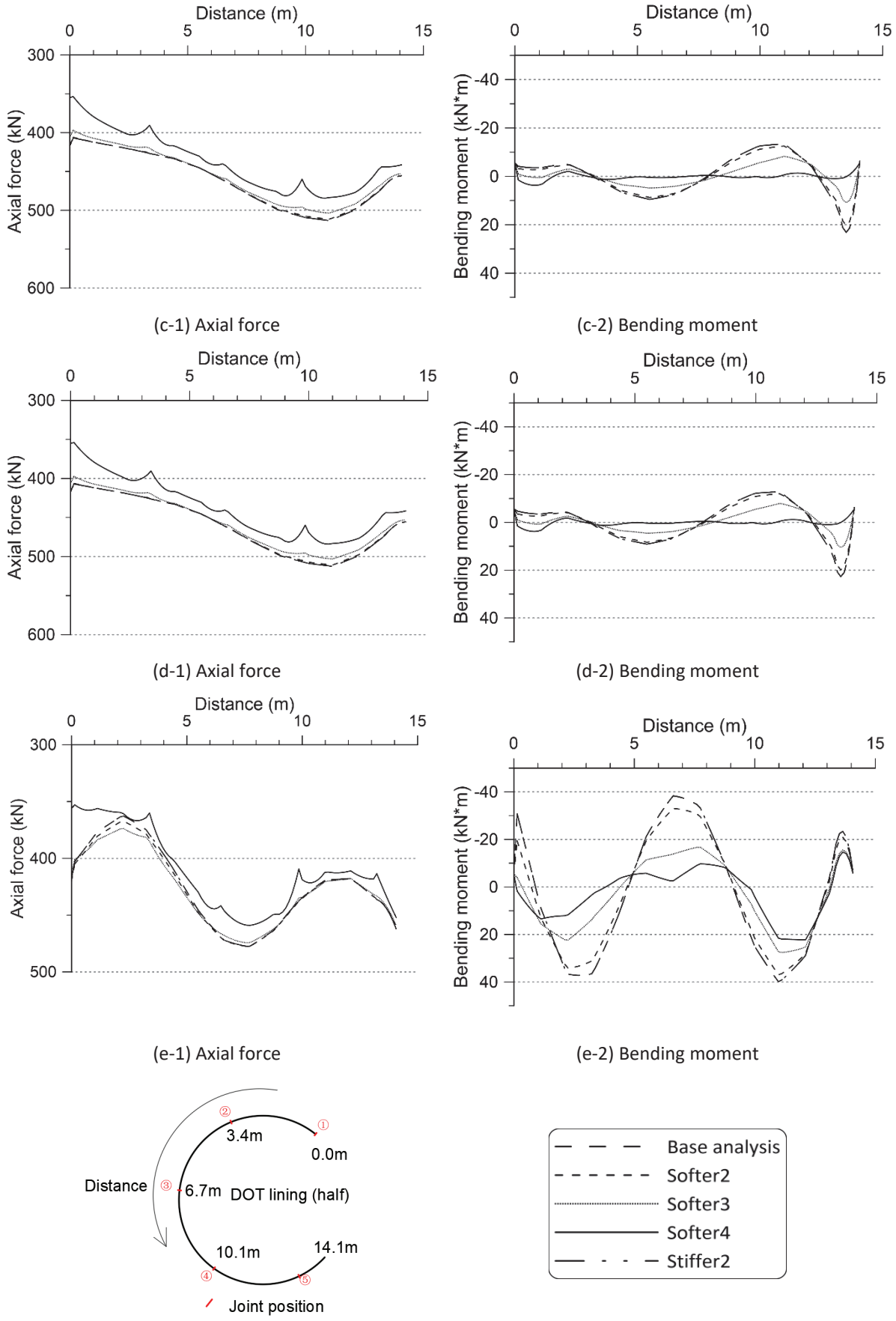


Figure 4.20: Distribution of lining internal force for different joint stiffness. a) 7 days after excavation; b) 28 days; c) 100 days; d) 1000 days; e) 80 years;

4.4 Influence of grouting in DOT constructions

The synchronous grouting process is applied during the construction of DOT tunnel. The grouts are injected from upper and lower seagull segments and fill the gap between the EPBM and the soil to reduce ground disturbance and stabilise the soil. The grouting operation has been simulated in this study, and the core characterisation involves grouting pressure generation and the evolution of stiffness of grouts around the lining, the latter attributes to the lining internal force reaction after tunnelling. The analyses are carried out under the configuration of base analysis introduced above.

4.4.1 Synchronous grouting pressure diffusion

The grouting material composes of water, bentonite, cement, retarding agent and accelerator (Shah et al., 2018), which realises functions of soil stabilisation, water proofing and reducing settlement induced by ground loss with compensation. The retarding agent guarantees the workability of the grout, leading to the material diffusion into the soil under high extra grouting pressure. After fully intrusion and then solidifying in a number of hours, the functions of soil stabilisation and water proofing are achieved and the corresponding properties of the grouted soil will develop in further 28 days.

The grouts are injected into the gap from the top and the bottom grooves of the lining. An appropriate control of grouting pressure is important. On the on hand, the compensation grouting reduces ground loss. On the other hand, the over large pressure causes further disturbance in the soil around. The value also depends on the ground condition, the grout material and the tunnelling speed of EPBM. In the DOT construction of Shanghai Metro Line 8, the grouting pressure is about 0.3MPa and the volume injection ratio is about 180%-200% (Chow, 2006). However, the distribution of grouting pressure is usually not uniform as due to complex diffusion conditions in the ground and the non-Newtonian fluid feature of the grouts. Wei et al (2012) has given an estimate of deviation of grouting pressure from 90% to 110% around the lining from the mean value (100%). Bai et al (2011) proposed a 15kPa/m pressure increasing gradient along the depth as measured from the field, suggesting the tunnel invert has about 90kPa higher pressure compared to that on the crown.

The grouting pressure generates at the tail of the EPBM, and the extra pressure dissolves fast while tunnelling. Qiao et al. (2018) presented the measured grouting pressure during the tunnelling from Sophia tunnel project in Betuwe (see Figure 4.21). From the start of synchronous grouting to the pressure stabilisation, where the value is balanced with earth pressure in natural state, the procedure takes less than 15 hours and for dissolving extra grouting pressure about 125kPa. Therefore, the resulting ground response during this period will be intense and sensitive to the pressure value.

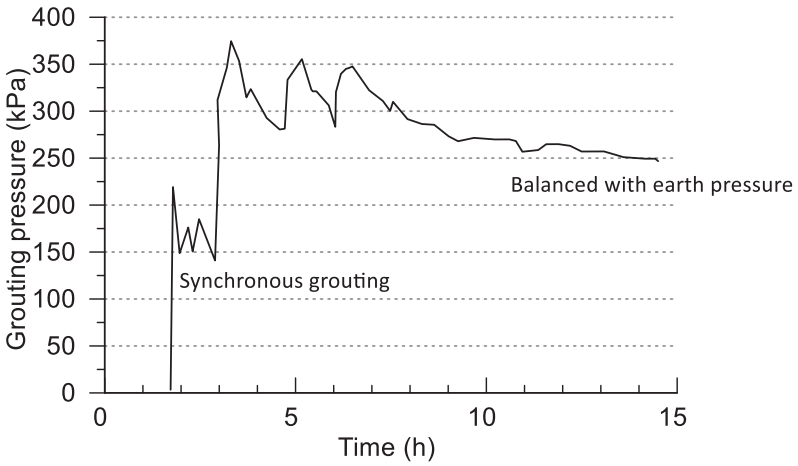


Figure 4.21: Evolution of grouting pressure during the tunnelling from Sophia tunnel project in Betuwe (Qiao et al., 2018)

The pressure drives grouts particles infiltrating into the surrounding soil. Ye et al. (2018) has demonstrated the mechanism of grouts diffusion into the soil while synchronous grouting (see Figure 4.22) and has highlighted the massive influence of grouting pressure control on the mechanical response of the lining. A half-spherical surface diffusion model was introduced, considering the soil porosity and the proportion of components in solid and liquid phase (the initial volume percentage of the particles in the grouts), for predicting the evolution of grouting pressure.

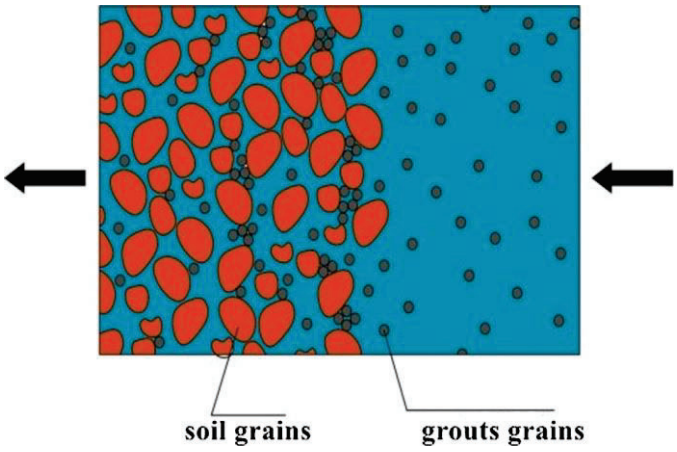


Figure 4.22: grouts diffusion into the soil (Ye et al., 2018)

Ye et al. (2018) pointed out that the grouts infiltration effect has influence on the distribution of grouting pressure on the segments. Theoretically, the grouting pressure acting on the lining is equal to the one acting on the surrounding soil. However, due to the variation of grain contents and the soil porosity, it has been found that even considering infiltration effect completely, the pressure acting on the lining is usually smaller than grouting pressure, and the reduction ratio is between 2.5% to 5%. In the contrary, regardless the infiltration ratio results in significant underestimate of the pressure acting on the lining (only 1/3 of the corresponding value considering full infiltration) due to grouting concentration, which means that the infiltration effect is actually beneficial for the uniform

distribution of the grouting pressure and better protection of the lining. This pressure reduction on the lining is also performed in this study (Table 4.10).

Table 4.10: Reduced grouting pressure acting on the lining segment considering infiltration

Grouting pressure (kPa)	Pressure on the lining segments (kPa)	Pressure ratio (%)
200	190	95.0
250	240	96.0
300	290	96.7
350	340	97.1
400	390	97.5

To determine the dissipation range and the depth of grout in the soil, several assumptions are adopted: the diffusion occurs uniformly in normal direction to the tunnel lining extrados, the cement content is of uniform distribution in the soil and thus the material is regarded homogeneous. According to the analytical interpretation on the DOT project of Shanghai Metro Line 6 (Wei et al., 2012) the distance of grouts dissipation could reach from 80cm to 100cm under the pressure of 400kPa to 600kPa. The injection ratio is from 140% to 180% in DOT synchronous grouting, and the hollow gap between the lining and soil is usually 10cm. it was suggested that the ideal time of grouting is about 100 minutes, allowing the full dissipation in the ground, while overtime grouting may lead to the shrinkage of the soil as the solidification takes place. Therefore, assuming the grouting distance is 90cm, injection ratio is 160%, the content of grout diffused into the soil could be calculated as about 5.8% of the volume in this study. The density of the cement mortar, which is similar to grouts, is approximately 25kN/m^3, and hence the change of gravity for the surrounding soil is also noticed.

4.4.2 Strength evolution of the grouted soil

In this study, the strength of grouted soil and the grouts does not cause much impact on the overall response of the ground since the gap for grouts and the grouted soil is very thin compared with the scale of the whole ground layers. Therefore, the nonlinear properties characterising the undrained shear strength of the grouts are not modelled in the simulation, whilst only the general linear properties are introduced. However, it is still necessary to understand the magnitude of maximum shear strength of this material.

Few investigations have been conducted on the strength of grouted soil in tunnelling constructions, and the mechanism of grouts solidification in the soil is still not fully understood. The configuration of the grouts diffusion shape and the strength formation is still not fully quantified to date due to the lack of observation method. Therefore, the study of cement-stabilised soil from literature is referred

to here. In that field, a great number of tests on cement-stabilised soil have been carried out, and the observed and noted strength revolution could be a reference for modelling grouted soil in the simulation practice.

Bahar et al., (2004) have reported an experimental study on a compacted cement-stabilised soil in Algeria. A clay sandy soil was compacted into blocks and then stabilised with cement, curing in dry or immersed conditions (see Figure 4.23). The results show that cementation contributes to the strength improvement of soil well. The compressive strength of the specimen is over 1.0 MPa for the immersed specimen, which was prepared in fully saturated condition regarding the soil underground, with 4% cement, and the magnitude increases significantly with cement content. The dry specimen evolves significantly higher strength. Therefore, the strength evolved in unsaturated clay sandy soil stabilised with cement is between those two extreme conditions.

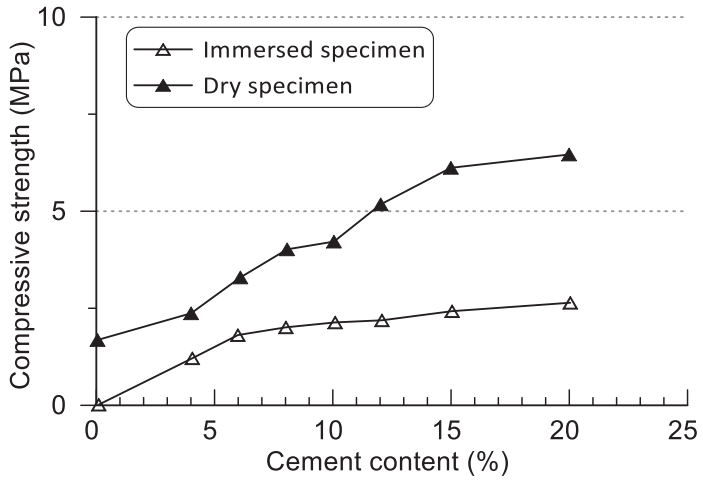


Figure 4.23: strength of cement stabilised soil with different cement content and curing environment (modified from Bahar et al., (2004))

Anagnostopoulos & Chatziangelou (2008) carried out a study on nine types of soil stabilised with cement: seven inorganic with high plasticity, one inorganic with medium plasticity and one organic with high plasticity. The material is mixed with deep cement mixing method, and a model has been introduced based on the regression analysis on different factors such as liquid limit, water content, cement percentage, sand content and curing time. A regression formula involving five variables: water content w (%), liquid limit wL(%), cement content C (%), sand content S (%) and curing time CT (days), has been introduced and validated as high correlation with measured data. Good agreement has been achieved with the formula and the laboratory data. This method, substantially, is employing statistical analysis to predict the strength response against time, and is considered lower cost and practical. However, the implementation field of their regression formula is not clear and has some limitations, as mentioned in their study that the regressed model is only suitable for sandy silt or silty clay, of

which the water content is lower. As for muddy clay in Shanghai, however, the regression underestimates the strength.

Wang et al. (2010) investigated the characteristics of strength development of the cement stabilised Shanghai clayey soil. The effect of cement content, initial PH value and the curing time have been discussed. The results over different types of soil in Shanghai are shown below (Figure 4.24). With increasing cement content and the curing time, the compressive strength of soil is apparently improved. The sets of Shanghai clay, though divided with different silt content, generally show the same manner and the sensitivity against cement content and the curing time. It is noted in their study that the soil from Chiba, Japan follows similar principle but performs different sensitivity of the strength evolution against cement compared to Shanghai clay, and that may be caused by the difference of mineral content. The 28-day strength is considered stabilised value for the cemented soil since the curve is observed flattened in their study, which shows similar behaviour with concrete.

Therefore, assuming an average content of cement 10% in the stabilised soil around tunnel lining in Shanghai soil layers, the maximum strength of the stabilised clay is determined as q_u(28days) = 300kPa in the model of this simulation. This value will be reached gradually within 28 days post grouting.

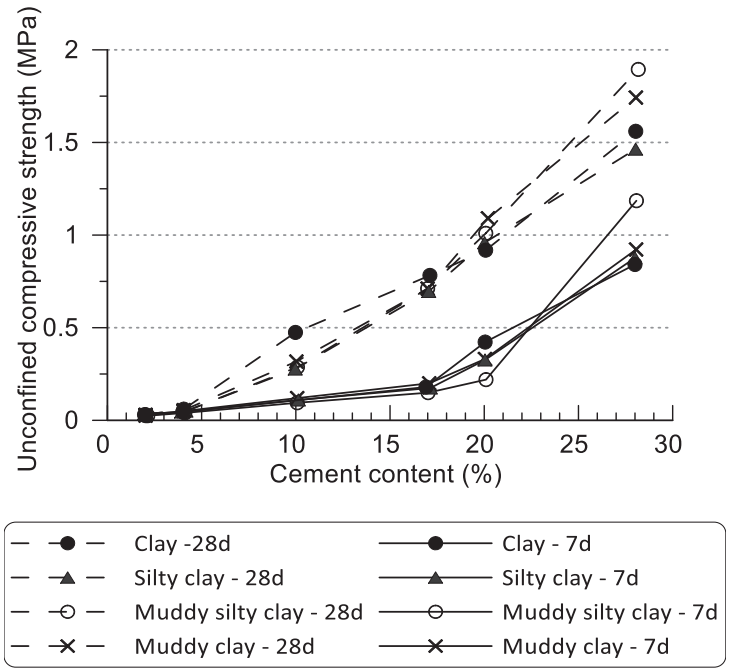


Figure 4.24: Influence of cement content on strength of clays (modified from Wang et al., 2010)

4.4.3 Small strain stiffness of the cemented soil

The cemented soil and the grouts are adjacent to the lining, and the corresponding impact on the ground deformation due to their specific stiffness evolution is inevitable. The characterisation of small strain stiffness properties, including maximum shear stiffness and the degradation principles, is

important for tunnelling simulation. Some laboratory tests on cemented soil are introduced as reference, based on which some assumptions are adopted and the parameters are determined for the numerical modelling in this study due to lack of field data.

Fatahi et al., (2013) has carried out a study on small-strain properties of kaolinite, which is stabilised with cement. 10%, 15% and 20% of cement content has been tested on Kaolinite, and after fully mixed and cured, bender element tests are performed to measure the maximum shear modulus (Figure 4.25). Obviously, the maximum shear stiffness of cemented clay is stabilised after 28 days, and higher magnitude is performed with increasing cement content. For the cemented soil (10%) and the grouts

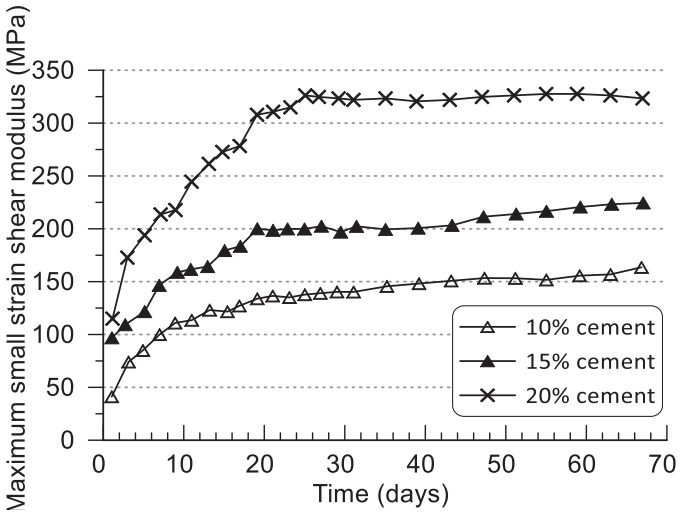


Figure 4.25: Maximum small strain shear modulus of cemented kaolinite with curing time: a) 10% cement; b) 15% cement; c) 20% cement (modified from Fatahi et al., (2013))

The maximum small strain stiffness is considered of high relevance with the shear strength of soils. Trhlikova et al. (2012) have agreed on the factor that the cementation results in higher stiffness compared with the natural clay under different pressures. Their experimental study shows that cemented kaolin clay contains 4% of cement in their experiment, and this achieved a significant improvement of small strain stiffness. Rinaldi & Santamarina (2008) have summarised this relation using various samples, and a positive correlation envelop is introduced (see Figure 4.26). It is shown that maximum tangent shear stiffness is usually between 200 q_{max} to 700 q_{max}.

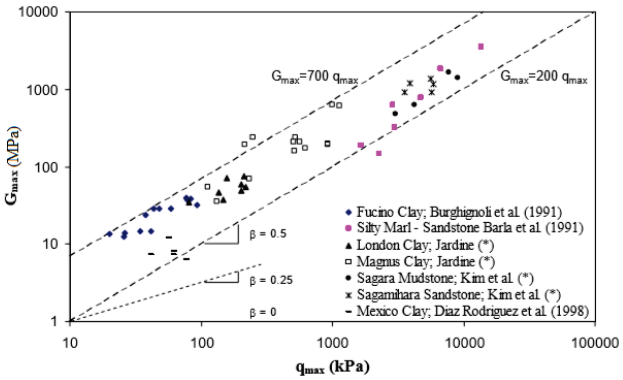


Figure 4.26: Maximum shear modulus with deviatoric strength q for a variety of cemented soils (Rinaldi & Santamarina, 2008; Tatsuoka & Shinbuya, 1991)

4.4.4 Numerical modelling of DOT with grouting simulation

Synchronous grouting is an important process in DOT construction, aiming at improving water proof ability, stabilising the soil and controlling the ground loss. The grouts filled in influences the internal force of lining in terms of grouting pressure generated around the tunnel and grouts hardening in the curing period. The modelling of DOT based on the configuration of base analysis has been carried out.

Both short term and long term ground response and the lining behaviour has been investigated with hydro-mechanical coupled analysis. The ground is modelled with solid elements, defined in different blocks for each layer. The soil behaviour is simulated with an extended MCC model (Roscoe & Burland, 1968; Potts & Zdravkovic, 1999) and the Imperial College Generalised Small Strain Stiffness model (ICG3S; Taborda & Zdravkovic, 2012), focusing on non-linear properties and small strain stiffness of the soil. Both models are calibrated in the previous chapter. The parametric study has been carried out on the basis of soil properties database built from literature survey.

Discretisation of the tunnelling ground

The finite element mesh is shown in Figure 4.27, modelling the soil and tunnel lining in terms of 8-noded quadrilateral elements and 3-noded beam elements respectively. The simulation is processed incrementally, involving a number of phases including excavation, lining construction, grouting and settlement phases in short term and long term. A stress control method has been employed to achieve the volume loss in numerical simulation compatible with the measured data well. The excavation is processed over the first 50 increments, which lasts 10 hours in total, followed by the DOT lining ring installation at increment 51. During this period, a uniformly increasing stress is generated along the lining, affecting towards the ground normally. This stress simulates the temporary support provided by the DOT machine while excavating, and is unloaded ten days later after the lining construction. The basic hydro-mechanical boundary conditions, including ground water table, precipitation and the

prescribed displacement of the mesh boundaries, follow the configuration of the base analysis introduced above. It is highlighted that the grouting area, also known as the construction gap between the DOT machine and the ground in reality, is modelled with solid elements around the lining shown as the shadow area in Figure 4.27. The geometry information of the mesh and the lining are the same with the base analysis.

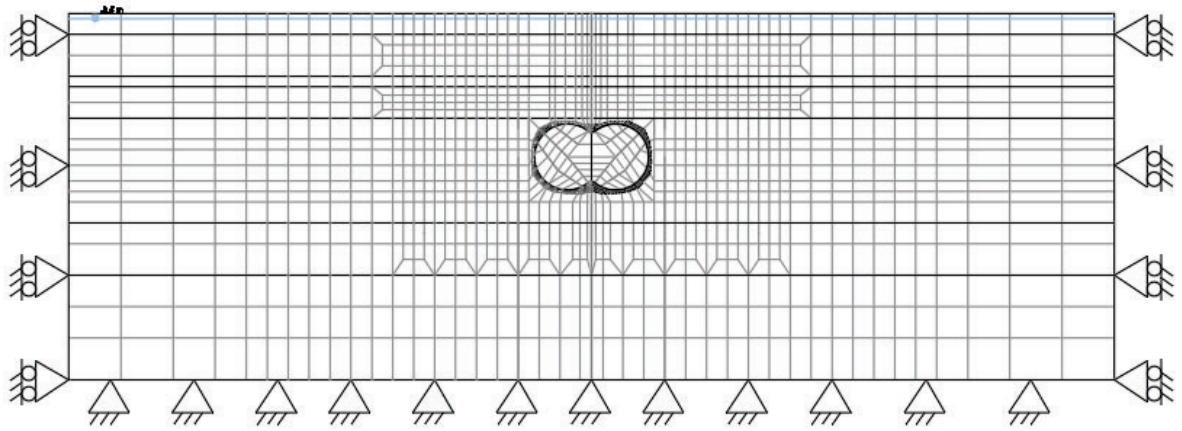


Figure 4.27: The DOT mesh of Shanghai Metro Line 6 (Ring 130; the shadow area is the construction gap for grouting)

Simulation of grouting pressure

The grouting pressure of DOT is from 0.3MPa to 0.5MPa (Wei et al., 2012). Considering the depth of 14m, where the DOT tunnelling takes place, the earth pressure is 200kPa around the tunnel, a 200kPa extra confining pressure condition is set up on the tunnel boundary when lining is constructed. This pressure is subsequently released in a short time referring to the field measurement (see Figure 4.21), which is performed in within one increment with time scale of 1 day after lining construction.

It should be noted that this pressure is bidirectional, acting on the lining and the ground in normal direction as shown in Figure 4.28. As introduced in 4.4.1 and the Table 4.10 that even under the condition that the grouts are fully infiltrated, the pressure acting on the lining is slightly reduced from the grouting pressure, and low magnitude may be reached when the infiltration does not completely occur. In fact, in 2D analysis, the pressure acting on the lining may be overestimated as the effecting area is not smeared in reality. The mechanical connections among the segment in longitudinal direction is apparently stronger than soil, and thus the slight reduction of pressure on the lining segment is reasonable. Therefore, a series of reduced pressure acting on the lining is performed in the simulation as listed in Table 4.11, where the 200kPa grouting pressure on the segment is added as a control set. Other two sets of analyses, following the same framework but with grouting pressure of

300kPa and 400kPa have also been conducted.

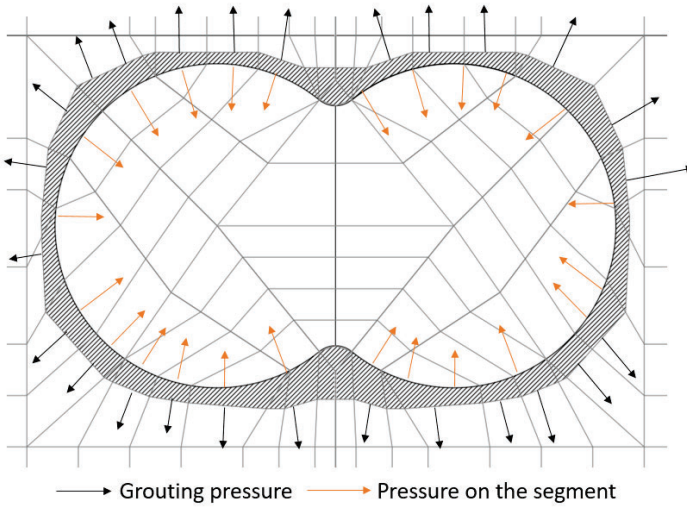


Figure 4.28: Demonstration of bidirectional grouting pressure

Table 4.11: Simulation of grouting pressure around the lining

Increment Number	Phase	Extra grouting pressure	Grouting pressure on the segment
51	Lining construction	200kPa	200kPa/198kPa/195kPa/190kPa/180kPa
52	A 1-day period after construction	-200kPa	-200kPa/-198kPa/-195kPa/-190kPa/-180kPa

Modelling of linear properties of grouts

A 28-day period is defined for the grouts curing in the model, during which the Young's modulus and Poisson ratio are changing. Oh & Ziegler (2014) have conducted a laboratory testing on the evolution of mechanical properties of the grouts within 28 days curing period, and the results of Young's modulus and Poisson ratio is presented (see *Figure 4.29*). It is found that the evolution of both parameters perform in the same manner with concrete in 28-days curing period, and the magnitudes stabilise after 28 days. Therefore, it is assumed in the simulation that no further evolution occurs after the curing period. The change of properties applied in the model over increments is shown in

Table *4.12* below referring to the experimental data recorded, and to achieve this, the card of change material properties has been introduced.

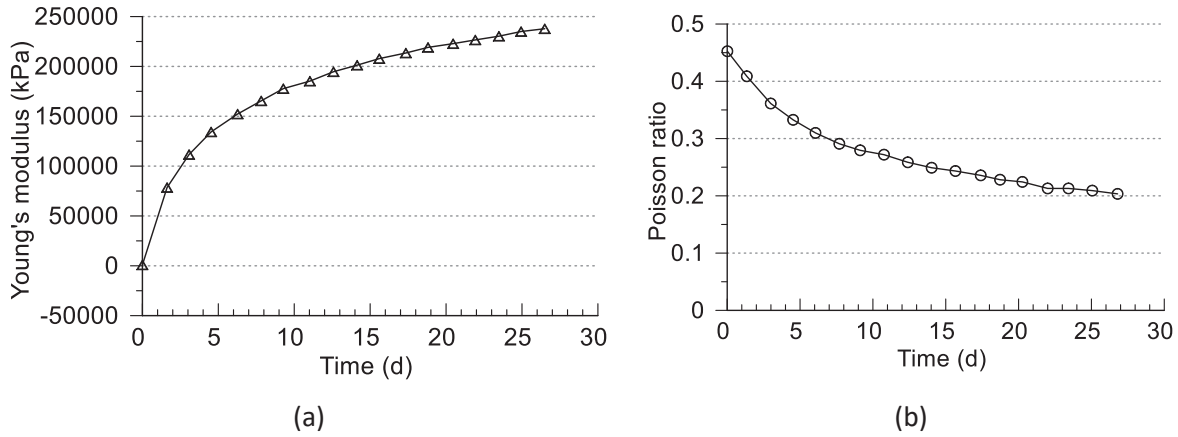


Figure 4.29: Evolution of linear properties of the grouts during the curing period (Oh & Ziegler, 2014)

Table 4.12: Linear properties development of grouting material with time

Grouts material No.	**Increment**	**Time (d)**	**Young's modulus (kPa)**	**Poisson ratio**	**Grouting pressure (kPa)**
1	51	Slurry state	1.0E1	0.49	200/300/400
2	52	1	8.0E4	0.42	0
3	53	5	1.3E5	0.34	-
4	54	10	1.75E5	0.27	-
5	64	20	2.1E5	0.24	-
6	65	28	2.4E5	0.25	-

The nonlinear properties of the grouts are not characterised in the model considering the negligible effect caused on the ground from the thin layer of grouts as mentioned above. The permeability of the grouts is assume the same with the soil in the tunnelling layer, and hence the magnitude is not specified here.

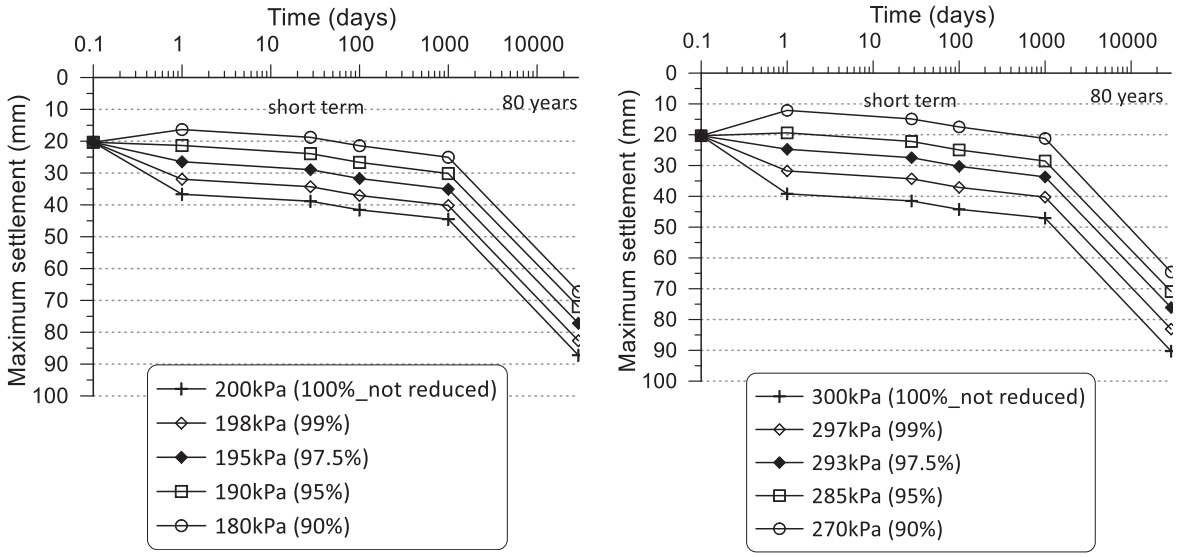
Results and discussion

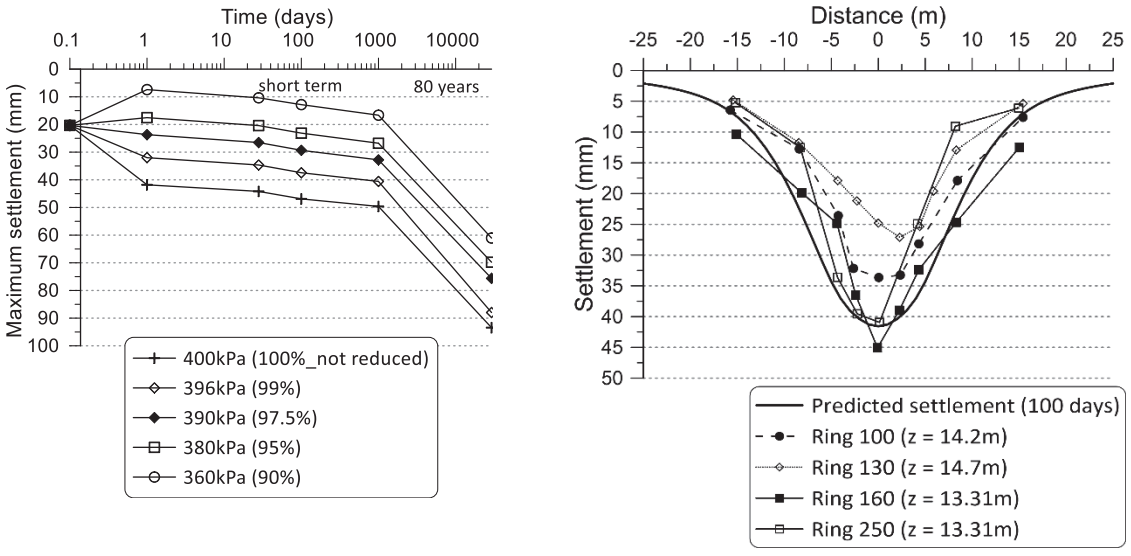
The evolution of the maximum settlement induced by tunnelling and the synchronous grouting for short term and long term is presented. The parallel analyses, as introduced above, include the grouting pressure of 200kPa, 300kPa and 400kPa and a series of reduced pressure is applied on the lining segments for the pressure study. The evolution of maximum settlement is shown in *Figure 4.30* below. It can be seen that the peak value occurs at the tunnel axis and the magnitude is highly dependent on the prescribed grouting pressure and the reduction ratio.

The reduced pressure applied on the lining segments shows significant effect in controlling settlement,

and the ground even behaves heaving after lining construction. For instance, the results of reduced pressure at 90% for all three analyses presented the reduction of the settlement one day after tunnel excavation. This behaviour is also commonly recorded in engineering practice and it has been summarised that the higher grouting pressure leads to uplifting movement of the lining ring. It is shown in the 400kPa group (Figure 4.30c and Figure 4.31b) that at the 90% of reduction ratio, the settlement has reduced to 7.4mm generating a massive impact on the ground. It is also noted that the evolution curves of maximum settlement are basically parallel, implying the non-correlation between the grouting pressure and the further settlement growing during short and long term consolidation period. The ground movement is not affected after the releasing of grouting pressure, though the influence caused by grouting is permanent.

In Figure 4.30d, the predicted settlement trough of the 200kPa group without pressure reduction on the lining shows good agreement with the field data and the base analysis results (see Figure 4.7), and therefore, this group could be regarded as a base analysis for grouting study. That means using the method of boundary stress control, the settlement of the ground surface in DOT simulation could still be precisely predicted and reproduced when the grouting pressure is taken into account.

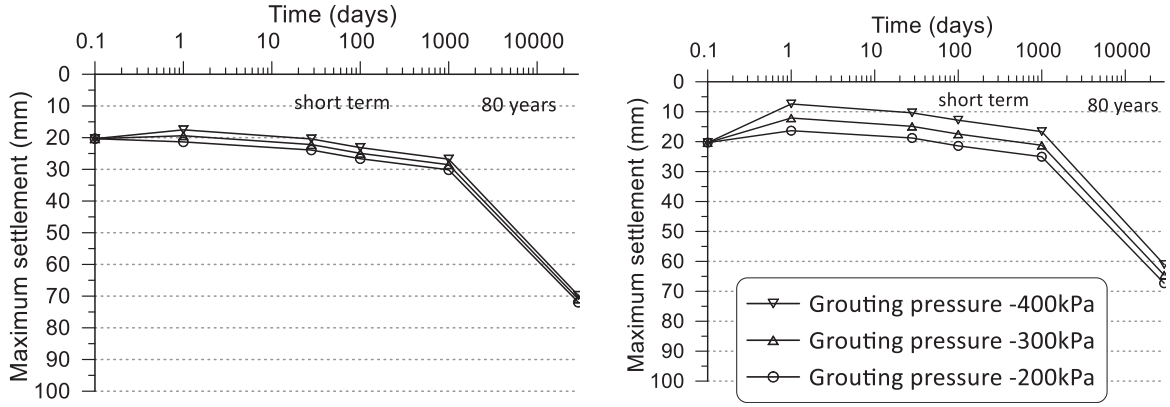




(c) (d)

Figure 4.30: Settlement development after grouting under different pressures and reduction ratios: a)200kPa grouting pressure; b) 300kPa grouting pressure; c) 400kPa grouting pressure; d) settlement trough of the ground surface at 100 days after tunnelling under the grouting pressure of 200kPa without pressure reduction on the lining.

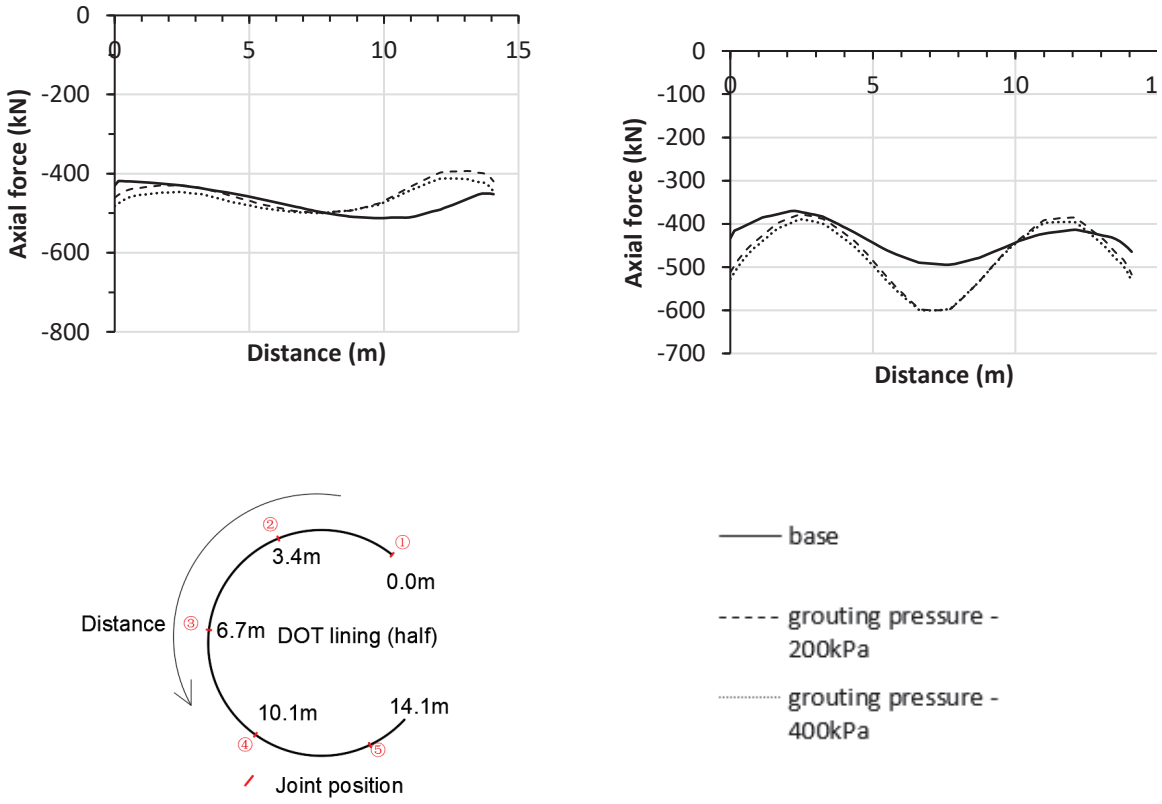
Profiles of surface settlement have indicated that the ground response is sensitive to the grouting pressure and the reduction ratio. The lower pressure acting on the segments, meaning lower reduction ratio, significantly results in larger deviation of the ground response under different grouting pressures (Figure 4.31). The mechanism of grouts infiltration and the pressure evolution is complex. Some researchers such as Ye et al (2018) and Lv (2012) have also pointed out that the grouting time also influences the resulting effects due to the characteristics of non-Newtonian fluid and the fast ground response while tunnelling.



(a) 95% pressure reduction (b) 90% pressure reduction

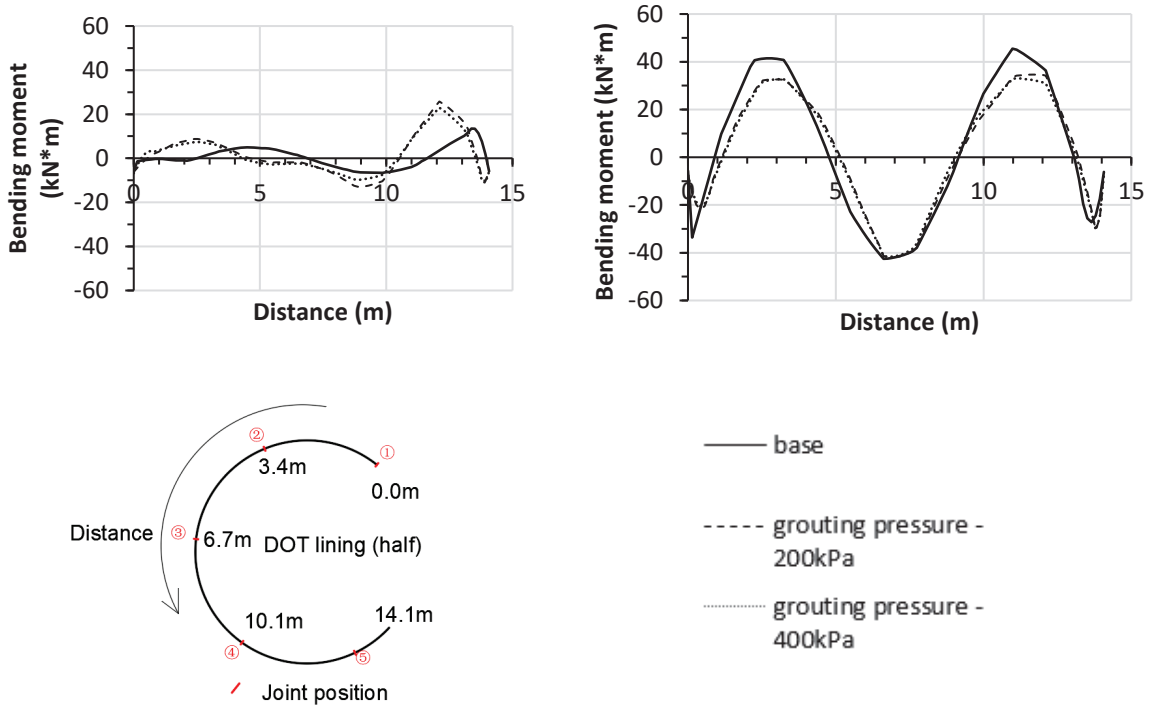
Figure 4.31: The deviation of settlement evolution curves among different grouting pressures: a) 95% pressure reduction on the lining; b) 90% pressure reduction on the lining.

The internal forces of the lining show significant difference for short term behaviour, including axial force and the bending moment (Figure 4.32 & Figure 4.33). It can be seen that the variation of grouting pressures does not lead to significant difference in the lining reaction either in short term or long term (after 80 years, see Figure 4.33b). After the completion of consolidation under fully permeable condition, the greater axial force is generated on the lining with grouting, though the magnitude is not influenced by the grouting pressure level (Figure 4.32b). The position of the peak point locates at the waist of the ring, where the distance is about 7m shown in both figures. The reduced pressure on the lining does not cause significant influence on the axial force and bending moment for long term consolidation (see Figure 4.34 & Figure 4.35), but the bending moment predicted for short term, when the lining is partially permeable, could be sensitive to the pressure level acting on the segments.



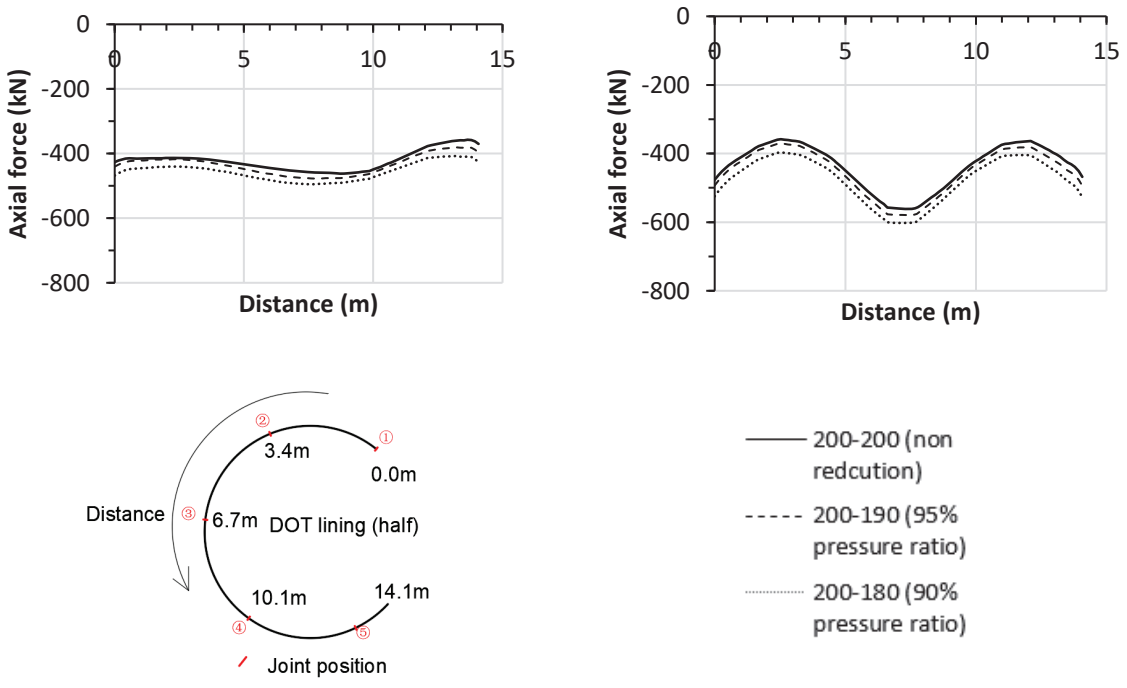
(a) 100 days (b) 80 years

Figure 4.32: Axial force (hooping force) of DOT lining at the end of consolidation terms: a) short term (100 days); b) end of long term (80 years)



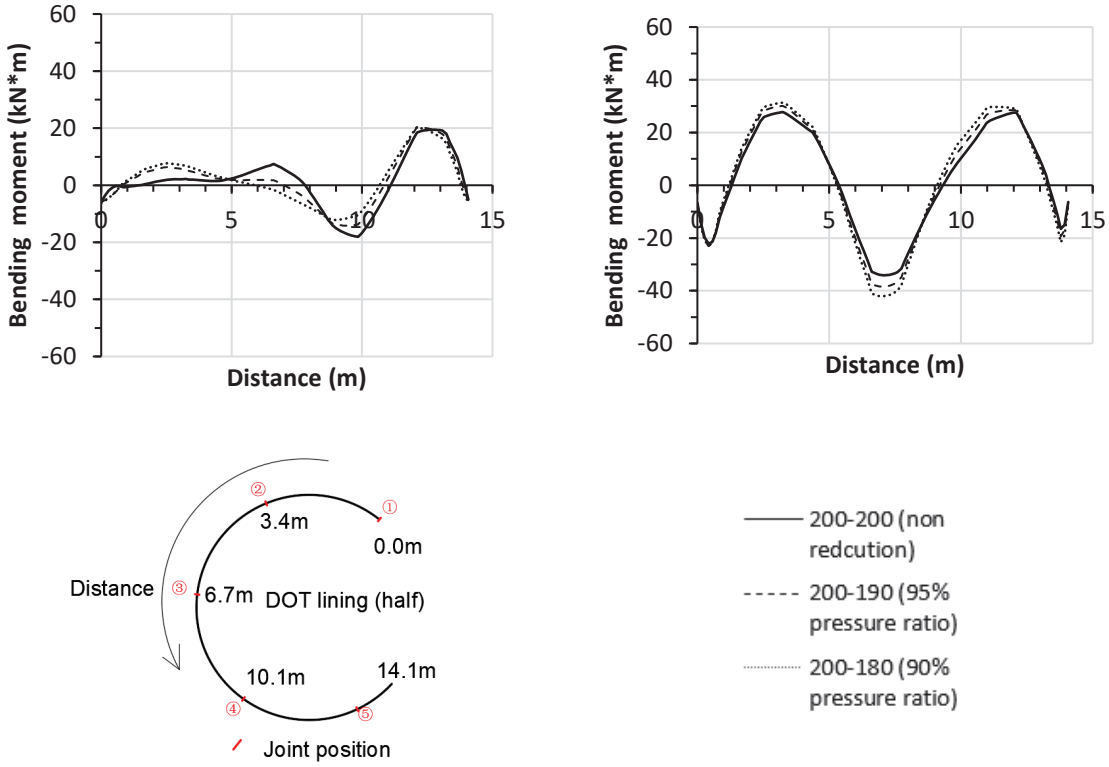
(a) 100 days (b) 80 years

Figure 4.33:Bending moment of DOT lining at the end of consolidation terms: a) short term (100 days); b) end of long term (80 years)



(a) 100 days (b) 80 years

Figure 4.34: Axial force (hooping force) of DOT lining at the end of consolidation terms: a) short term (100 days); b) end of long term (80 years)



(a) 100 days (b) 80 years

Figure 4.35: Bending moment of DOT lining at the end of consolidation terms: a) short term (100 days); b) end of long term (80 years)

4.5 Summary points

The analyses in this chapter investigated the simulation of DOT tunnelling in Shanghai soft clay, which is characterised using extended MCC model and ICG3S model for undrained shear strength and small strain stiffness respectively. A systematic numerical analysis and the corresponding predictions have been carried out. The parametric study on joint stiffness was carried out, and the simulation method for tunnel excavation was discussed.

- The extended MCC model is found suitable for characterising Shanghai clay and the calibration conducted in previous chapter performs well in DOT simulation. The short term ground surface settlement reached good agreement with file data on several numbers of rings, and the maximum settlement predicted for long term consolidation is expected according to historical measurement of tunnelling in Shanghai.
- The significant change of hydraulic boundary conditions around the lining from short term to long term leads to obvious difference of evolution of ground settlement, as well as the contours of pore water pressure. The sensitivity of the hydraulic boundary around the lining onward the ground response was highlighted.

- The beam elements are implemented in modelling tunnel lining and joints adopting elastic lining assumption.
- The boundary supporting stress method proposed for simulation of the tunnel excavation was proven applicable on soft clay condition. The synchronous grouting is an important operation in the tunnelling, and the corresponding influence on the ground response is inevitable. The grouts material properties were calibrated and the grouting pressure was considered the core factor in controlling ground settlement induced from consolidation post tunnelling.

Chapter 5. Development of the modelling framework for DOT concrete segment

5.1 Introduction of a concrete constitutive model

This chapter introduces a concrete constitutive model that was used in simulations of DOT tunnel lining with realistic representation of the segment geometry within the lining. The chapter first introduces the formulation of the adopted model, known as the modified Chen concrete model (Schutz, 2010; Schutz et al., 2011). The model is then calibrated against the codes of practice for concrete and validated on the simulation of two laboratory tests performed on a single segment. The model is then used in Chapter 6 for the analysis of the Shanghai case study, which was already presented in Chapter 4 with a simpler representation of the tunnel lining.

5.1.1 Some existing concrete models

The concrete material has been systematically studied in the civil engineering field. Due to complicated composition of the material, it is challenging to characterise the mechanical properties and various dependency factors in a single constitutive model, such as temperature, curing period, or fibre content. Most existing research is mainly focusing on specific core aspect of the material, depending on its application in a project, and hence modelling only the specific aspects of concrete behaviour.

Concrete cracking reflects the serviceability and the durability of the material and is therefore important for modelling. Matallah & Borderie (2009) developed a model describing the inelasticity damage of the concrete under monotonic or cyclic loading. The inelasticity of the concrete in the early loading stage was assumed to be caused by minor cracks in the material, and the elasticity recovered when the minor cracks were closed. A variable called Unitary Crack Opening was defined to describe the damage and inelasticity. Their analysis assumed the smeared cracking in the material and the implementation of the model was verified with laboratory data.

Wu et al. (2012) summarised a number of classic concrete models applied in the numerical study of concrete structures. Karagozian & Case Concrete model (KCC) (Crawford et al. 2011; Malvar et al. 1997) was identified as suitable for the simulation of reinforced concrete (RC) structures under blast or impact loading. The plastic flow function of this model can be associative, partially associative or non-associative to deal with different types of loading. This model has a yield surface, a peak strength surface and a residual strength surface, which are independent to each other. It is simple and can process the calculation by only inputting the value of unconfined strength and the density of the

material. KCC model enables the description of concrete behaviours such as strain softening after the peak strength, shear dilation and rate-dependency of the loading response. Winfrith Concrete model (Broadhouse, 1995) is another simple model to simulate the concrete response under impact loading, in which four parameters obtained from uniaxial compression, uniaxial tension, biaxial compression and biaxial tension are required as input model parameters. This model characterises strain softening in tension but is unable to simulate the one in compression. The Continuous Surface Cap model (CSC) (Murray 2007; Schwer and Murray 1994) includes a hardening compaction cap, combined with failure surface using a multiplicative formula. The hardening rule of the cap is expressed in an exponential reduction form based on maximum plastic volumetric strain. The model simulates the failure-softening behaviour but is found not suitable for low confinement condition such as reinforced concrete with stirrups.

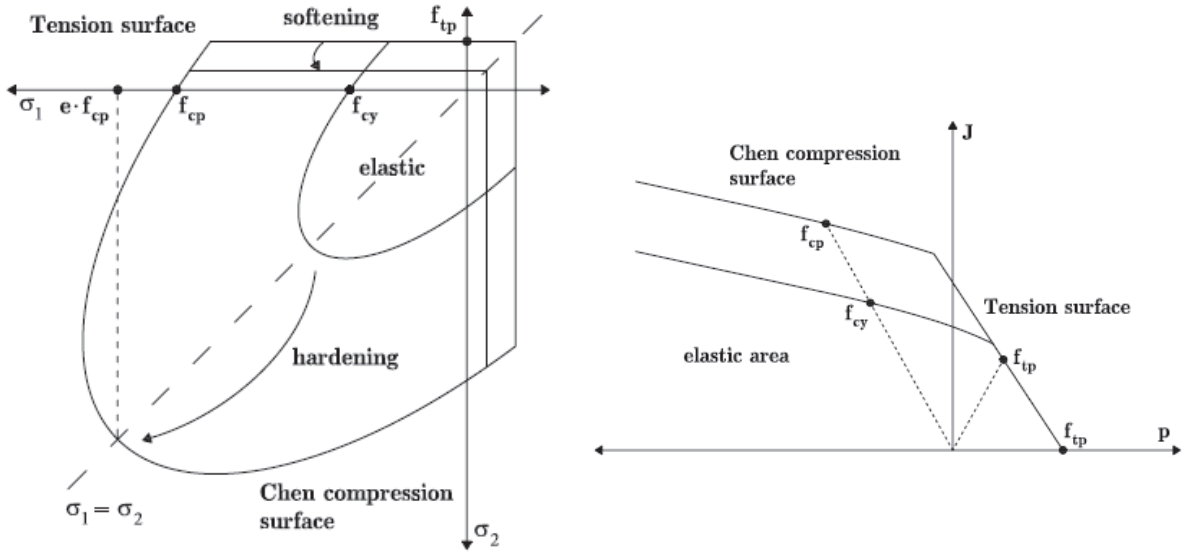
5.1.2 Modified Chen concrete model

5.1.2.1 Basic model framework

The modified Chen concrete model was implemented in ICFEP in the research of Schutz (2010) and Schutz et al. (2011), extending the original Chen concrete model (Chen & Chen 1975). The original Chen concrete model has the same stress-strain hardening rule for nonlinear behaviour of the concrete and the material is assumed isotropic. Schutz (2010) pointed out that the original Chen concrete model did not account for the difference of stress-strain relationship in compression and tension. Some important factors such as the time dependency and thermal effects were also not considered. Therefore, the modified Chen concrete model has introduced some significant modifications subject to the same framework, aiming at modelling the concrete in a more realistic manner. In the current research, only the core functions of the model that simulate the mechanical behaviour of concrete were considered, since the concrete lining segments were a simple prefabricated reinforced concrete. In the original Chen concrete model, the yield surface and the failure surface were defined with three material parameters for compression and tension stress conditions. The uniaxial stress space was divided into four stress zones: compression-compression zone, compression-tension zone, tension-compression zone and tension-tension zone. The functions for shapes of the compression zone were elliptical and the shape was considered suitable for describing the concrete yielding. The tension positive sign is adopted in this chapter.

The yield and plastic potential surfaces in compression and tension, from the original Chen concrete model, are shown in Figure 5.1. Associated plasticity is assumed and hence the plastic potential surfaces are identical to the yield surfaces. In this figure, f_{tp} & f_{cp} are tensile and compressive plastic strength respectively; f_{cy} is the compressive yield strength; a dimensionless scale factor *e* is introduced to describe the size of hardening compression surface. The uniaxial stress-strain relation

of the concrete is illustrated in Figure 5.2, where τ_0 is the yielding point and τ_u is the ultimate point of crushing and cracking.



(a) (b)

Figure 5.1: the yield surfaces of compression and tension for Chen concrete model in a) biaxial space; b) J-P stress space (from Schutz, 2010)

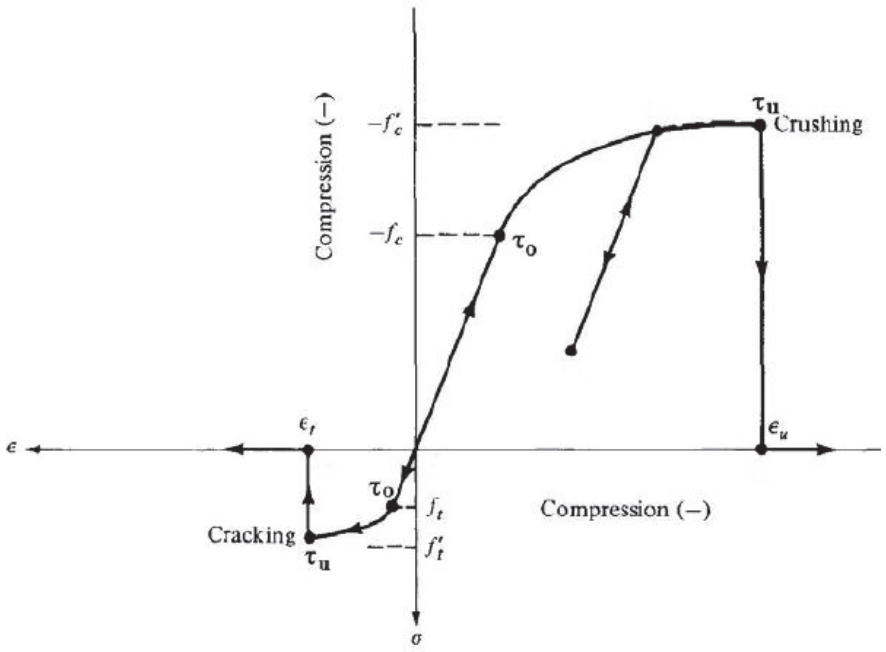


Figure 5.2: Stress-strain relation of concrete under uniaxial loading condition (from Chen, 1982)

In Figure 5.2, the curves in both compression and tension show the elasto-plastic behaviour of the material, and the strength drops to zero immediately as soon as the stress exceeds the peak value.

The material experiences crushing in compressive failure and cracking in tensile failure. The plastic hardening is assumed in this model as stress increase after the yielding value τ_0. However, the simplified post-peak behaviour seems unrealistic as it does not match the softening behaviour proposed in most concrete codes as shown later in Figure 5.12. Furthermore, the assumption of zero ultimate strength after failure may underestimate the overall strength of the structure.

In the modified Chen concrete model, the behaviour in compression followed the original framework and a strain hardening rule was defined. The following equation was introduced for the yield and plastic potential surfaces in compression:

$$F_e = P_e = J^2 + \frac{\alpha_e \cdot f_c \cdot p'}{F_s} - \frac{\beta_e f_c^2}{F_s^2} = 0 \tag{5-1}$$

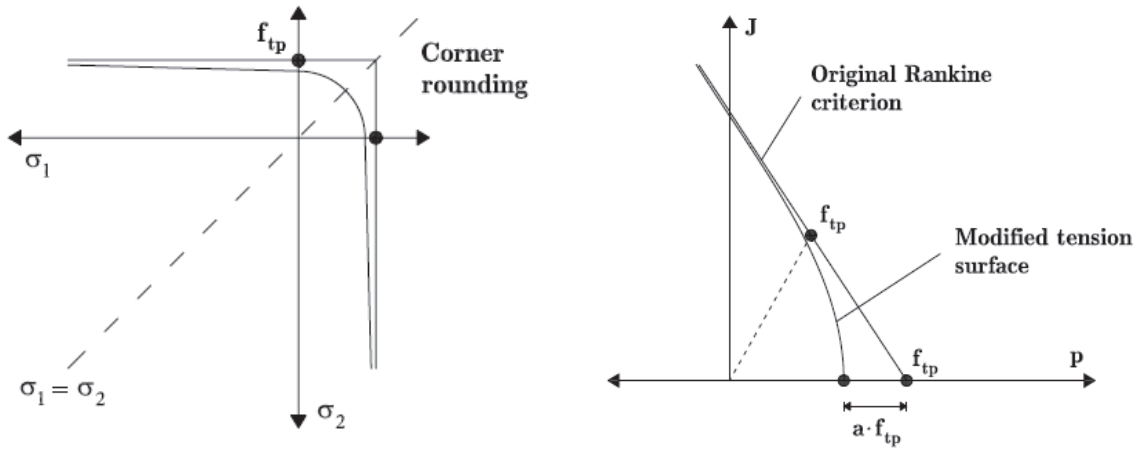
where $\alpha_e = {(e^2 - 1)}/{(2e - 1)}$ and $\beta_e = {2e - e^2}/{3(2e - 1)}$; F_s is the factor of safety; f_c if the compressive yield strength (f_{cy}) for the yield surface, and compressive plastic strength (f_{cp}) for the plastic potential surface; *p'* is the mean effective stress; e is a dimensionless parameter for biaxial strength, accounting for the 25% higher strength performed in biaxial compression test compared to uniaxial compression test (see Figure 5.1a). The value of e is usually adopted within the range of $1 < e < \frac{1+\sqrt{3}}{2}$.

A modified Rankine criterion after Thomee (2005) was adopted for the yield surface of tension. This modification adopted the rounding of the corner at the apex of the surface, and this improvement of the shape was considered suitable for the implementation in numerical analysis. The comparison of this surface between the modified and the original Rankine criterion is shown in Figure 5.3 and the corner rounding is highlighted. In both figures, f_{tp} is the tensile plastic strength.

Therefore, the tension yield surface and plastic potential surface were expressed as

$$F_t = P_t = p' + [\left(\frac{2J}{\sqrt{3}} \cdot \sin\left(\theta + \frac{2\pi}{3}\right)\right)^n + (\frac{a \cdot f_t}{F_s})^n]^{\frac{1}{n}} - \frac{f_t}{F_s} = 0 \tag{5-2}$$

where θ is lode angle; a is called apex tolerance representing the amplitude of modification from the original surface based on Rankine criterion (see Figure 5.3b); n is the parameter controlling the rounding of the surface; f_t should be noted as the tensile yield strength (f_{ty}) for the yield surface, and tensile plastic strength (f_{tp}) for the plastic potential surface.



(a) (b)

Figure 5.3: Modified yield surface and original yield surface in a) Biaxial tension space; b) J-P tension stress space

5.1.2.2 Hardening and softening rules for concrete in compression

To overcome the drawback of neglecting the post-peak strength behaviour of concrete, the modified Chen concrete model characterised the softening rule for uniaxial compression, with the complete normalised stress-strain curve shown in Figure 5.4, in which four zones for stress-strain relation are illustrated. It was noted that for compression conditions, the minor plastic principal strain ε_3^p dominated the deformation of the concrete, whilst the major principal strain ε_1^p was dominant for conditions in tension. The hardening parameter H_c is expressed in the normalised form, calculated as the ratio between the current minor principle strain ε_3^p and the peak plastic strain ε_{pc}^p:

$$H_c = {\varepsilon_3^p}\Big/{\varepsilon_{pc}^p} \tag{5-1}$$

and thus $H_c = 1$ when the minor plastic strain reaches the corresponding peak value of compression stress (when $f_{c,n} = 1$). The normalised compressive stress, $f_{c,n}$ is expressed as

$$f_{c,n} = {f_c}\Big/{f_{cp}} \tag{5-2}$$

where f_{cp} is the maximum compressive stress.

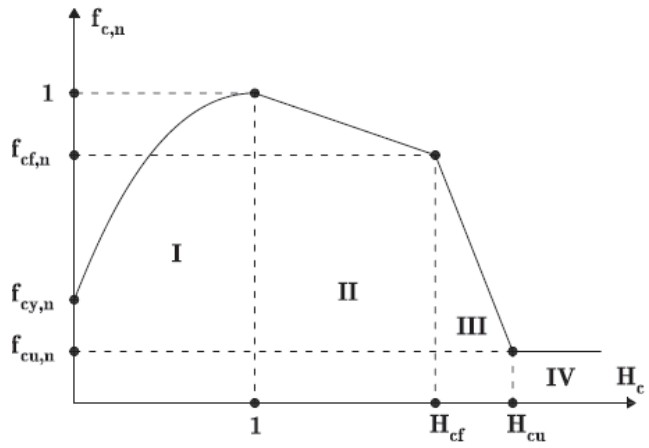


Figure 5.4: Normalised stress-strain relation for concrete in compression

The first region (labelled as zone I in Figure 5.4) presents the elasto-plastic behaviour of the concrete before the peak stress, and a parabolic curve is fitted. The material starts yielding at the normalised stress of $f_{cy,n}$ when the plastic strain is zero (or $H_c = 0$). The curve becomes asymptotic on the approach to the point of peak stress and is followed by linear pieced of different gradients post-peak. The concrete experiences the dissipation of fracture energy in-between the peak and the failure stresses (1<$H_c < H_{cf}$), during which the linear softening behaviour is assumed. It is noted that this softening part is not always observed in the laboratory experiments, especially for high strength concrete, because of crushing after the failure stress due to brittleness of the material. A linear stress reduction rule is introduced for the zone III after the failure of the concrete, and the normalised ultimate strength $f_{cu,n}$ is a non-zero constant, for which a small value is usually adopted. The non-zero ultimate compressive strength is important for the numerical stability of the solution process.

5.1.2.3 Hardening and softening rules for concrete in tension

A similar normalised expression for tensile stress and strain relation is established, and the uniaxial tensile stress is

$$f_{t,n} = {f_t}/{f_{tp}} \tag{5-3}$$

where f_{tp} is the peak tensile stress, representing the threshold for the cracking. The hardening parameter H_t is defined in a normalised form as

$$H_t = {\varepsilon_1^p}/{\varepsilon_{pt}^p} \tag{5-4}$$

where ε_1^p is the major principal plastic strain; ε_{pt}^p is the corresponding strain value at peak tensile stress. The stress-strain relation in uniaxial tension is shown in Figure 5.5, and three zones are noted

for different loading stages. It can be seen that the material is assumed to perform linear elasticity before the yielding tensile stress, the value of which is usually taken as $0.9f_{tp}$ referring to the design code for concrete structures (see Figure 5.15). The zone I represents the stage of concrete after yielding and before the peak tensile stress is reached ($0 < H_t < 1$) and a parabolic curve is introduced to represent the strain hardening in this zone. After the peak, this model introduced a strain softening zone for the concrete in tension (zone II) for describing post-peak strength, and a non-zero ultimate strength is defined after the softening stage (zone III). An exponential degradation is adopted in this study for softening, and the other functions such as linear softening is also considered appropriate. The material experiences the procedure of gradual dissipation of fracture energy in this stage. Therefore, from the aspect of the overall strength of the concrete structure, the material is considered performing strain softening for post-peak behavior, and the assumption of non-zero ultimate strength is realistic.

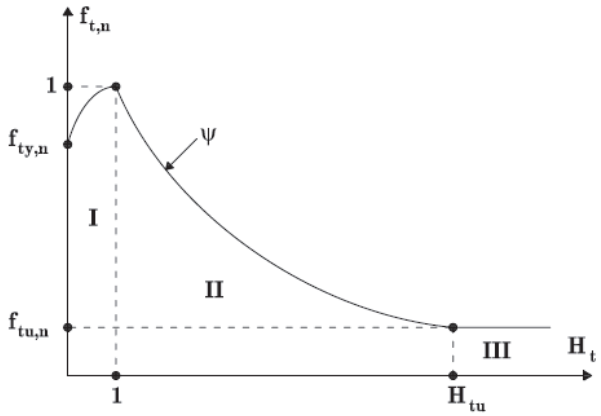


Figure 5.5: Normalised stress-strain relation for concrete in tension (exponential option of softening)

Other important functions of the modified Chen concrete model, including the concrete creep and time dependency, are not introduced here as they were not considered in the research presented in this thesis. In general, this model was considered suitable for numerical studies of concrete structures and is convenient for calibration.

5.1.3 A nonlocal strain-softening method for the analysis of concrete loading

The analysis of strain softening material using the finite element method enables realistic reproduction of its mechanical behaviour. However, with a standard (or local) approach of calculating strains, the developed shear surface in the material during the strain-softening path is mesh-dependent (i.e. it is not objective). This is because the local approach considers only strains from elements through which the shear surface propagates and therefore its position depends on the size of individual finite elements in the FE mesh. A non-local approach for evaluating strains in materials

with a strain softening behaviour has been considered by a number of authors as a possible solution to this problem. The method of Galavi & Schweiger (2010) was implemented in ICFEP (Summersgill et al,. 2017) due to its low mesh dependency and good stability. The method performs calculation of strains by an algorithm that takes into account a wider area around the shear surface defined by two parameters: an internal length and the radius of influence.

5.2 Reinforced concrete characterisation and modelling

5.2.1 Introduction of the reinforcement design for the lining segment

The prefabricated concrete segment used in tunnel lining on Shanghai Metro system contains around 140kg/t to 160 kg/t of steel. The alignments of reinforcement bars in tunnel lining follow a similar design to the example introduced in this section. In the current research, the lining segment in Shanghai Metro is assumed to have a width of 1.2m and thickness of 0.3m (Figure 5.6). Each ring contains 5 or 6 segments of identical fabrication. The radius of curvature depends on the tunnel diameter, usually varying from 6m to 8m.

In one single segment, the main reinforcement runs in the circumferential direction of the tunnel cross-section, near the extrados and the intrados of each segment, as shown in Figure 5.7 & Figure 5.8 and Table 5.1. Figure 5.8shows a special design, in which stiffeners (labelled 3) are added in the segments, for the lining rings under higher ground pressure condition. The pairs of the main reinforcement bars at each of the two localities are strapped by a stirrup at regular intervals, as shown in the cross-sectional view in Figure 5.8. The bars labelled as 4, 5 and 6 are hoop reinforcement whilst numbers 1 and 2 represent the main reinforcement in the circumferential direction of the tunnel ring.

It can be seen from the figures that the 16 main reinforcement bars in the circumferential direction contribute to the transmission of the axial force, bending moment and the shear force acting in the segment. Eight bars are assembled on the side of extrados and intrados, respectively, whereas the stirrup bars play the role of confinement. Therefore, in the numerical study of concrete lining segment only the main reinforcement bars are explicitly modelled.

In the tunnel segment design for the Shanghai underground, the main reinforcement, labelled number 1 and 2, usually has the diameter of 18mm. The 20mm bars are used in strengthened rings at locations under more problematic geological conditions. The reinforcement types are mainly HPB235 (Hot-rolled Plain Bars, yield strength ≥ 235 MPa, Peak strength ≥ 370 MPa) and HRB355 (Hot-rolled Ribbed Bars, Yield strength ≥ 355 MPa; Peak strength ≥ 470 MPa).

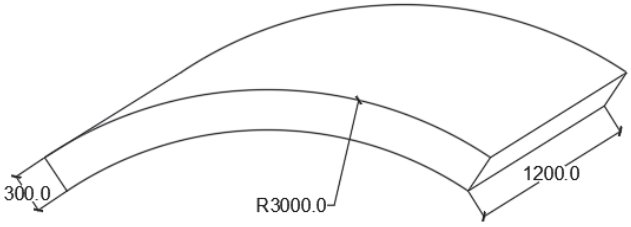


Figure 5.6: View of individual segments

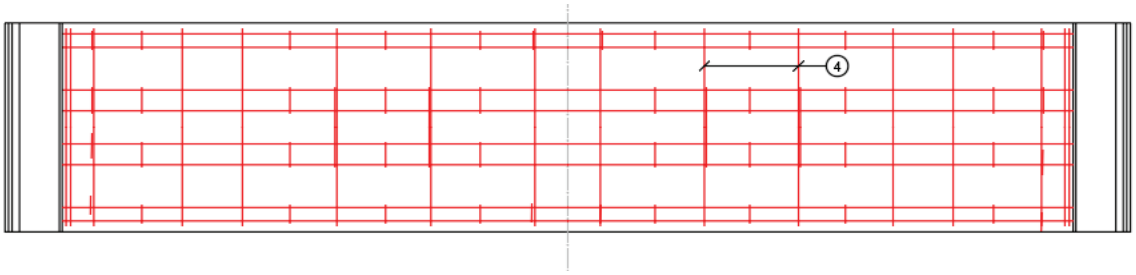


Figure 5.7: Reinforcement of a single segment (Plan view)

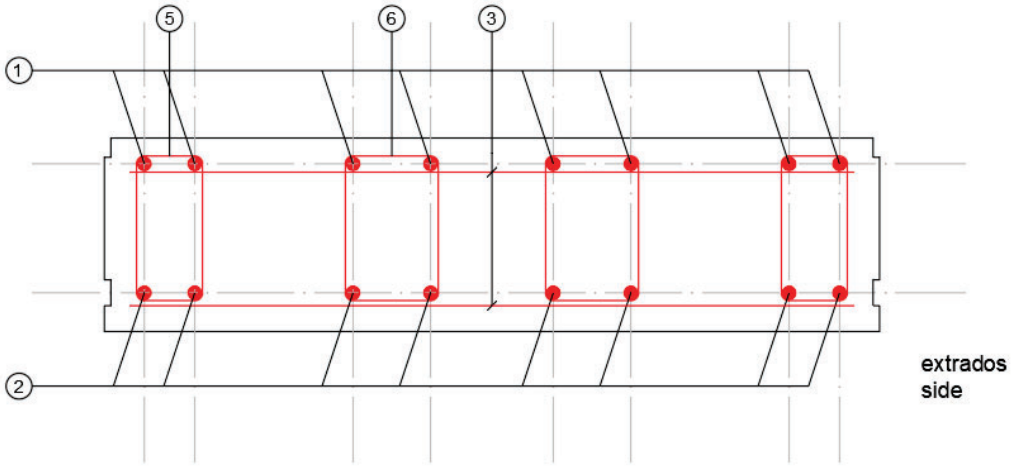


Figure 5.8: Cross-section type 1 of the segment with stiffener and the main reinforcements

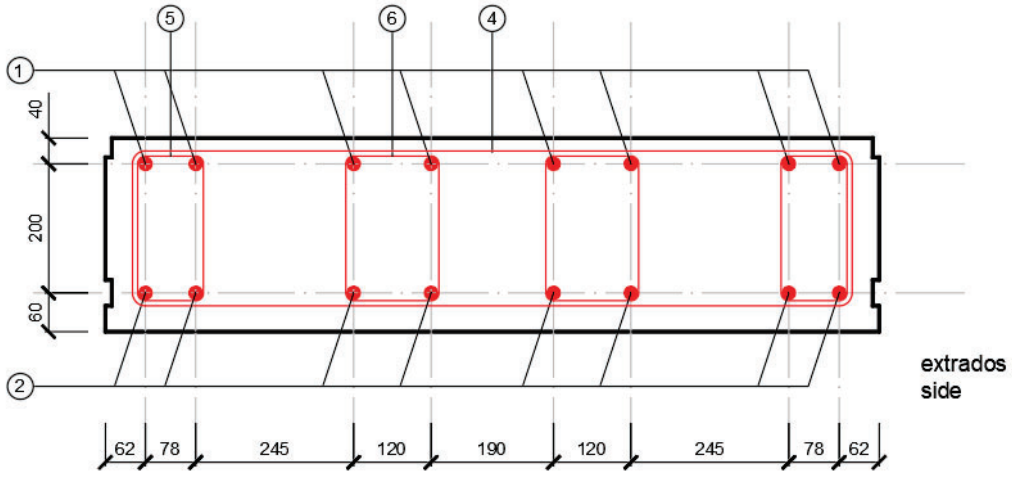


Figure 5.9: Cross-section type 2 of the segment with stirrup and the main reinforcement

Table 5.1: Information of reinforcement of the single segment

Reinforcement number	**1**	**2**	**3**	**4**	**5**	**6**
Type of steel bar	Main reinforcement	Main reinforcement	Stiffener	Stirrup	Stirrup	Stirrup
Position	Extrados	Intrados	Bolting position	See figures	See figures	See figures
Grade	HRB355	HRB355	HRB355	HPB235	HPB235	HPB235
Yield stress (MPa)	335	335	335	235	235	235
Diameter (mm)	18 or 20	18 or 20	18 or 20	8	8	8

Note: The relevant positions of different types of reinforcement in the single segment could be referred in Figure 5.7, Figure 5.8 & Figure 5.9.

The Eurocode 3 has given detailed mechanical information of the reinforcement with the grade of HRB355 and is taken as a reference for parameters adopted in this research. It is known that the tensile stress-strain curve of the reinforcement in the laboratory testing is usually characterised by the yield strength, the ductility period, and the peak strength in the late stage (see Figure 5.10). After the yielding at the end of elastic section, the curve dives a bit at the beginning of a ductile stage. This is described as strength softening in the model. The late stage of ductility, which is shown as the convex part on the right hand side, was not necessary to introduce in this study due to the very large strain at which it is mobilised, which was not achieved in the studied problem. Therefore, a constant strength is retained after the yielding point for reinforcement in the simulation.

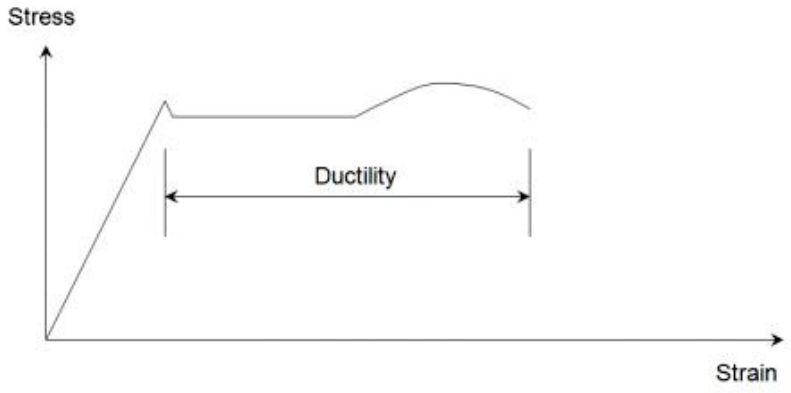


Figure 5.10: Typical stress-strain curve of reinforcement in tension (Eurocode 3)

The compressive properties are similar to the tensile ones and hence similar corresponding parameters could be adopted. The mechanical parameters referring to Eurocode 3 for HRB355 are

listed in Table 5.2.

Table 5.2: The mechanical parameters of HRB reinforcement bar (Eurocode 3)

Parameter	HRB355 steel bar
Elastic stiffness in compression and tension, E (GPa)	200
Compressive yield stress, f_{cy} (MPa)	355
Compressive peak strength, f_{cp} (MPa)	470
Compressive strain at yield stress, ε_{cy} (%)	0.178
Compressive strain at peak strength, ε_{cp} (%)	0.2
Tensile yield stress, f_{ty} (MPa)	355
Tensile peak strength, f_{tp} (MPa)	510
Tensile strain at yield stress, ε_{ty} (%)	0.178
Tensile strain at peak strength, ε_{tp} (%)	0.45

5.2.2 Bar element and softening plastic model for reinforcement

As introduced above, the reinforcement experiences purely elastic stage at the beginning and then becomes plastic when the yield stress is mobilised at a specified tensile strain. The strength softening subsequently takes place and the further response is elasto-plastic. This behaviour is the same in compression. The main segment reinforcement is represented with 3-noded bar elements in the numerical model of a lining segment. A bar element can only transmit an axial force and the selected constitutive model in ICFEP enables the simulation of the strain-softening of steel both for the compressive and tensile axial force, as shown in Figure 5.11. Table 5.3 summarises the parameters of this constitutive model.

The material modelled for reinforcement has a density $\rho = 7.85t/m^3$, Young's modulus $E = 2.0 \times 10^8\ kPa$ and Poisson ratio $\mu = 0.3$. The peak axial force shown in the table is determined by both the steel grade and the diameter of the reinforcement, and the cross-section area of bars are determined using equivalent area deducted for 2D analysis.

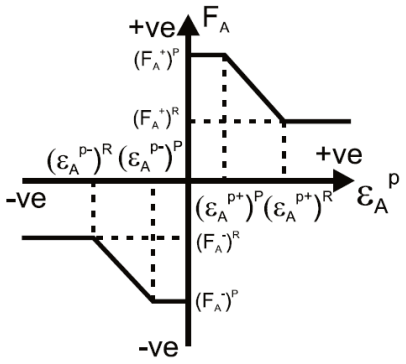


Figure 5.11: Softening plastic strain characterisation of the reinforcement modelled with bar element

Table 5.3: Parameters determined for the softening plastic model in reinforcement characterisation

Properties	**Description**	**Calibrated value**
ρ	Density (t/m^3)	7.85
E	Young's modulus (kPa)	2.0E08
μ	Poisson ratio	0.3
A	Cross-sectional area (m^2) - smeared	1.697E-3 (1.340E-3)
$F_A^+{}_{in}$	Peak +ve axial force (kN)	629.587 (497.14)
$\varepsilon_A^+{}_p$	Plastic axial strain at which hardening/softening starts (%)	0.022
$F_A^{R+}{}_{in}$	Residual +ve axial force (kN)	602.43 (475.7)
$\varepsilon_A^{R+}{}_p$	Plastic axial strain at which hardening/softening stops (%)	0.032
$F_A^-{}_{in}$	Peak -ve axial force (kN)	-629.587 (-497.14)
$\varepsilon_A^-{}_p$	Plastic axial strain at which hardening/softening starts	-0.022
$F_A^{R-}{}_{in}$	Residual -ve axial force (kN)	-602.43 (-475.7)
$\varepsilon_A^{R-}{}_p$	Plastic axial strain at which hardening/softening stops (%)	-0.032

Note: the values listed are for upper reinforcement, and the corresponding values for lower reinforcement, which has smaller diameter, is given in bracket.

5.3 Calibration of the modified Chen concrete constitutive model

The DOT lining segment is usually made of prefabricated reinforced concrete with the concrete grade of C45 or C50, defined as a high strength building material. According to properties described in Eurocode 2, the C50 concrete has a characteristic cylinder compressive strength of 50MPa, and the density is about 2500kg/m^3. The characteristic cube compressive strength is about 60MPa, which is adopted as the peak compressive strength for C50 concrete in this chapter. In this research, both the Chinese (GB 50164-2011: Standard for quality control of concrete) and European codes for concrete were referenced and the parameters were determined for both codes, showing little difference in the values between the two codes.

5.3.1 Shear strength of C50 concrete

The shear strength (v_c) of reinforced concrete is influenced by the area of reinforcement in the shear plane, represented by the cross-section shown in Figure 5.8 and Figure 5.9. The steel bars make significant contribution to the overall strength and, most importantly, improve the shearing resistance of concrete itself.

According to the code BS5400-4:1990, the shear strength v_c was determined as $v_c = 0.83\text{MPa}$, by using the formula below:

$$v_c = \frac{0.27}{\gamma_m}\left(\frac{100A_s}{b_w d}\right)^{\frac{1}{3}}(f_{cu})^{1/3} \tag{5-7}$$

where γ_m is taken as 1.25, b_w is the segment width (1.2m) and d is the lining thickness (0.3m); f_{cu} is the characteristic compressive strength of the concrete (50MPa for C50 concrete). In the single lining segment, applied in both single tunnels and DOT, introduced in this study, $16\Phi 18$ reinforcements are assembled in axial direction, and therefore the area of steel is $A_s = 16 \times \pi r^2 = 16 \times \frac{18^2\pi}{4} = 4072\text{mm}^2$. This results in the reinforcement ratio (%) of $\frac{100A_s}{b_w d} = 1.13\%$.

Eurocode 7 has defined the minimum allowable longitudinal tension reinforcement ratio and minimum shear reinforcement ratio, which represent the proportion of reinforcement in the cross-sectional area of the structure, as 0.197% and 0.107%, respectively, whilst the corresponding magnitude of tension reinforcement ratio in the Chinese code is 0.2%. The design of reinforcement cage of the segment, with parameters summarised in Table 5.1, has satisfied both codes, and therefore the shear strength of the concrete is determined.

5.3.2 Compressive strength of C50 concrete

The Model Code for Concrete Structures (Beverly, 2013) has given schematic presentation of the stress-strain relationship for concrete under uniaxial compressive loading (Figure 5.12). The strain at the peak compressive strength is dependent on the grade of concrete. The curve shows a non-linear response of the concrete under uniaxial loading and, therefore, an elasto-plastic constitutive relationship should be modelled.

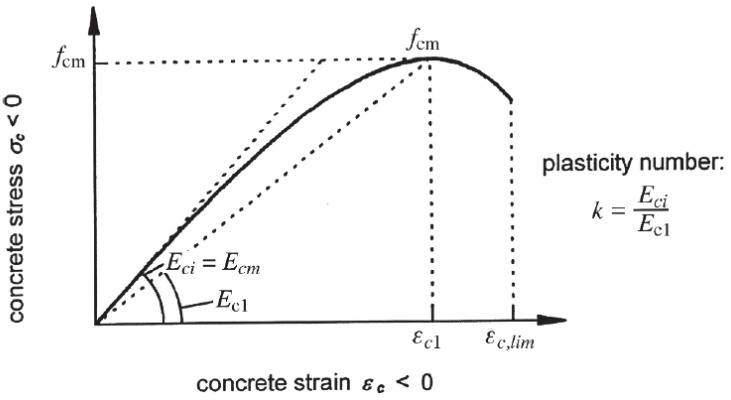


Figure 5.12: Schematic of stress-strain relation for concrete under uniaxial compressive loading (Model Code for Concrete Structures (2010))

From this code the equation for the stress-strain relation in Figure 5.13 is given below for $|\varepsilon_c| < |\varepsilon_{c,lim}|$:

$$\frac{\sigma_c}{f_{cm}} = -\left(\frac{k \cdot \eta - \eta^2}{1 + (k-2)\eta}\right) \tag{5-8}$$

where: $\eta = \varepsilon_c/\varepsilon_{cl}$; $k = E_{ci}/E_{cl}$ is defined as plasticity number; ε_{cl} is the strain corresponding to the peak compressive stress; E_{ci} refers to the initial modulus of tangent stiffness when the material could be approximated elastic; E_{cl} is the modulus of secant stiffness when the stress reaches peak value; f_{cm} is the peak strength of concrete (termed as f_{cp} in the modified Chan model in Figure 5.1 and Figure 5.4). $\varepsilon_{c,lim}$ is the maximum compressive strain at compressive failure strength, f_{cf}. It is noted that for C50 concrete, the maximum strain is usually difficult to reach and consequently the softening behaviour cannot be observed in the compression test from the laboratory. According to the experiments on compressive stress and strain on the concrete prism, there are several empirical equations to predict the peak strain of a concrete prism under axial compression test for high strength concrete, as listed in Table 5.4. The values listed have some variation and calibration was performed based on the code, as explained below.

Table 5.4: Peak strain of a concrete prism under axial compression test (assuming characteristic strength $f_{cu} = 50MPa$)

Empirical formulas concluded	**Peak strain calculated (‰)**
Ros.(1950) $\varepsilon_p = 0.546 + 0.0291 f_{cu}$	2.0
Saenz (1964) $\varepsilon_p = (1.028 - 0.108\sqrt[4]{f_{cu}})\sqrt[4]{f_{cu}}$	1.97
Brandzaeg (1929) $\varepsilon_p = \frac{f_{cu}}{5.97} + 0.26 f_{cu}$	2.64
Lin-Wang (2014) $\varepsilon_p = 0.833 + 0.121\sqrt{f_{cu}}$	1.69

The nonlinear compression curve shown in the schematic in Figure 5.12 indicates that the pure elastic section actually does not exist during the compression process. However, the early stage loading, when the compressive stress $\sigma_c < 0.4f_{cm}$, could still be approximated as a linear part. In the Model Code for Concrete Structures (2010), the secant modulus at the stress $\sigma_c = 0.4f_{cm}$ has been specified as a reduced modulus E_c, which is apparently smaller than the initial modulus E_{ci} and the loading state up to this stress level is regarded elastic (see Figure 5.13). For C50 concrete, this value is $E_c = 36.0GPa$. Therefore, a compression curve reflecting stress-strain relation of C50 concrete is derived (see Figure 5.14) and this shape is similar to the schematic shown in Figure 5.12. The mechanical parameters needed for calibration C50 concrete in compression, which is adopted in the modified Chen concrete model, are summarised in Table 5.5.

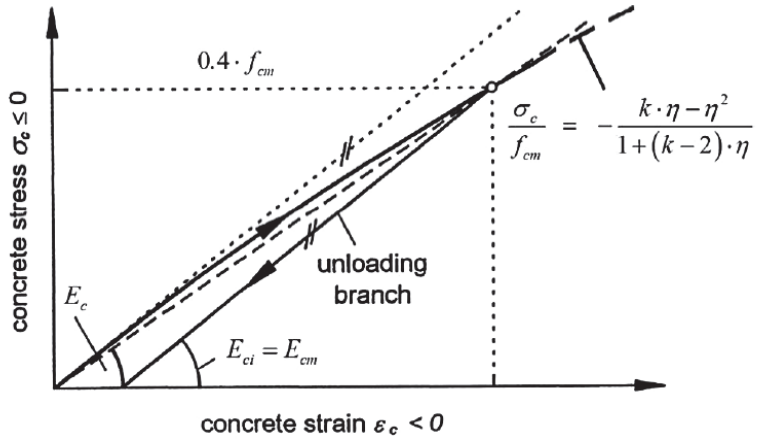


Figure 5.13: Schematic of initial tangent modulus E_{ci} and reduced modulus E_c (Model Code for Concrete Structures, 2010)

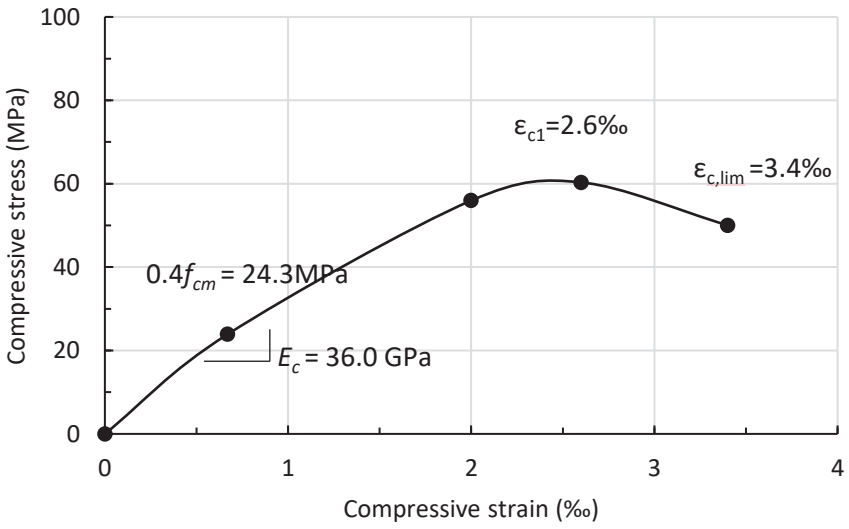


Figure 5.14: Compression curve of C50 concrete calibrated for the model

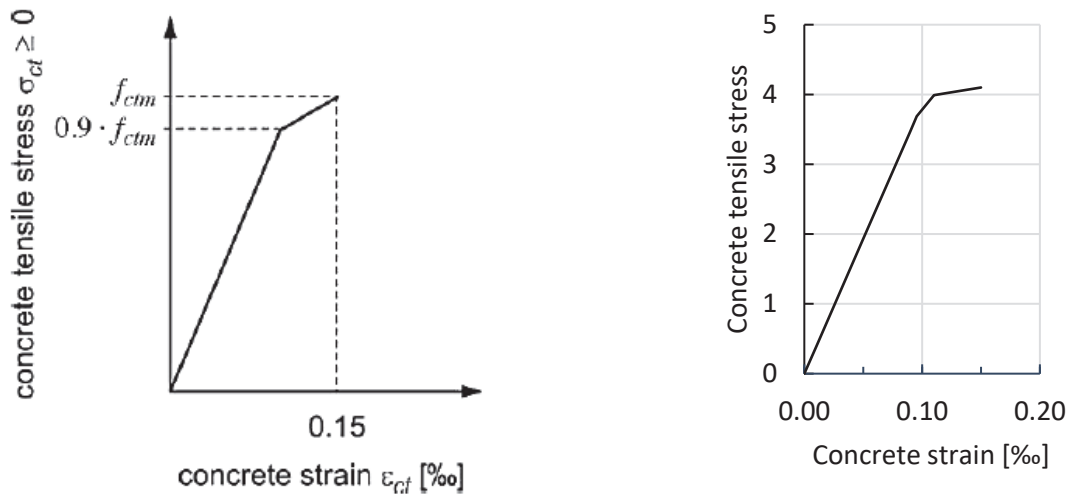
Therefore, the compressive characterisation for C50 concrete is summarised and listed in Table 5.5. The parameters of peak strength (f_{cp}), peak strain (ε_{c1}), failure strength (f_{cf}), failure strain $\varepsilon_{c,lim}$, could be reflected from the fitting stress-strain curve in Figure 5.14, from which the elastic strain ε_c is determined as 1.56 ‰. The initial modulus E_{ci},, secant modulus E_{c1} and E_c can be directly referred from the Model Code for Concrete Structures 2010.

Table 5.5: Parameters adopted for C50 concrete compression characterisation

Parameter	Description	Value
f_{cp} (Mpa)	Peak strength (noted f_{cm} in the code)	60.32
ε_{c1} (‰)	Peak strain	2.6
f_{cf} (Mpa)	Failure Strength	50.03
$\varepsilon_{c,lim}$ (‰)	Failure strain	3.4
E_{ci} (Gpa)	The initial modulus of elasticity at the concrete age of 28 days	38.6
E_{c1} (Gpa)	The secant modulus from the origin to the peak compressive stress	23.2
E_c (Gpa)	Reduced modulus of elasticity	36
K = Eci/Ec1	Plasticity number	1.66
f_{cy} (Mpa)	Yield Strength ($f_{cy} = 0.4f_{cm}$)	24.128
ε_c (‰)	Elastic strain	1.56

5.3.3 Tensile strength of C50 concrete

Model Code for Concrete Structures (2010) has defined the tensile strength of concrete as shown in Figure 5.15a. It is noted that regardless of the concrete grade, the maximum tensile strain is specified as 0.15**‰** at maximum tensile strength f_{ctm}, or named peak tensile strength, when the cracking occurs. The tensile strength evolution is divided into two linear stages, with the magnitude of the magnitude of the concrete tensile stress $\sigma_{tc} = 0.9 \cdot f_{ctm}$ regarded as the yield stress and hence as a boundary of the initial elastic behaviour in tension.



(a) (b)

Figure 5.15: a) schematic of stress-strain relation for concrete under tensile loading; b) stress-strain relation calibrated for C50 concrete.

The following equation is introduced to describe this relationship:

$$\sigma_{ct} = E_{ci} \cdot \varepsilon_{ct} \; for \; \sigma_{ct} \leq 0.9 \cdot f_{ctm}$$
$$\sigma_{ct} = f_{ctm} \cdot (1 - 0.1 \cdot \frac{0.00015 - \varepsilon_{ct}}{0.00015 - 0.9 \cdot f_{ctm}/E_{ci}}) \; for \; 0.9 \cdot f_{ctm} \leq \sigma_{ci} \leq f_{ctm} \quad (5\text{-}9)$$

where E_{ci} is the tangent modulus of the concrete in elastic range, shown in Figure 5.12; ε_{ct} is the tensile strain; σ_{ct} is the tensile stress and the f_{ctm} is the maximum tensile strength of the concrete, which is expressed as f_{tp}, named tensile peak strength. Therefore, the parameters for tension characterisation of the C50 concrete in the modified Chen constitutive model are summaries in Table 5.6.

Table 5.6: Parameters adopted for C50 concrete tension characterisation

Parameter	Description	Value
E_{ci} (Gpa)	Tangent modulus of elasticity	38.6
f_{ty} (=0.9f_{tp}; Mpa)	Tensile yield stress	3.69
f_{tp} (Mpa)	Tensile peak stress	4.1
ε_{tp} (‰)	Plastic strain at peak strength in tension	0.0545

5.3.4 Summary of modified Chen model parameters for C50 concrete

The linear stress-strain relation for early stage in compressive or tensile loading of concrete is approximated, and the elastic boundaries are defined with yield stresses f_{cy} = 0.4 f_{cp} for compression and f_{ty} = 0.9 f_{tp} for tension, respectively. Therefore, the complete stress-strain curve of concrete under

compression includes the early stage of linear elasticity, yielding stage reaching peak stress, failure stage and the post peak stage retaining ultimate strength (residual strength). However, it is known that the C50 concrete shows brittleness under compressive loading and it is difficult to determine the precise compressive strain at ultimate strength. Therefore, in this study, the ultimate compressive strength is assumed as 6.0MPa, which is 1/10 of the peak strength, whilst the plastic strain at ultimate strength is assumed as 0.25%. Similarly, the tensile ultimate strength is assumed as f_{tu} = 0.1MPa, and the coefficient of exponential softening after peak tensile stress, which lacks laboratory data support, is appropriately defined as 0.02.

Table 5.7: Calibrated parameters of concrete in the modified Chen concrete model

Parameter	**Segment – C50 concrete**
Density (t/m^3)	2.5
Young's modulus	3.45E7
Poisson ratio	0.2
Compressive yield stress, f_{cy} (MPa)	24.13
Compressive peak strength (also noted as f_{cm} in the code), f_{cp} (Mpa)	60.32
Compressive failure strength, f_{cf} (MPa)	50.03
Compressive ultimate strength, f_{cu} (MPa)	6.0
Plastic compressive strain at peak strength, ε_{cp} (%)	0.104
Plastic compressive strain at failure strength, ε_{cf} (%)	0.1712
Plastic compressive strain at ultimate strength, ε_{cu} (%)	0.25
Tensile yield stress, f_{ty} (MPa)	3.69
Tensile peak strength, f_{tp} (MPa)	4.1
Tensile ultimate strength, f_{tu} (MPa)	0.1
Plastic strain at peak strength in tension, ε_{tp} (%)	0.0055 (or 0.0545‰)
Coefficient of exponential softening after f_{tp}	0.02
Biaxial strength parameter, e	1.15

The additional parameters are required for the non-local strain softening method applied in the model, which solves the problem of mesh dependency in the analysis. The G&S method, as implemented in ICFEP (Summersgill et al., 2017) is adopted in this study, and the parameters for this method are introduced later in the chapter.

5.4 Laboratory experiments on single concrete segments

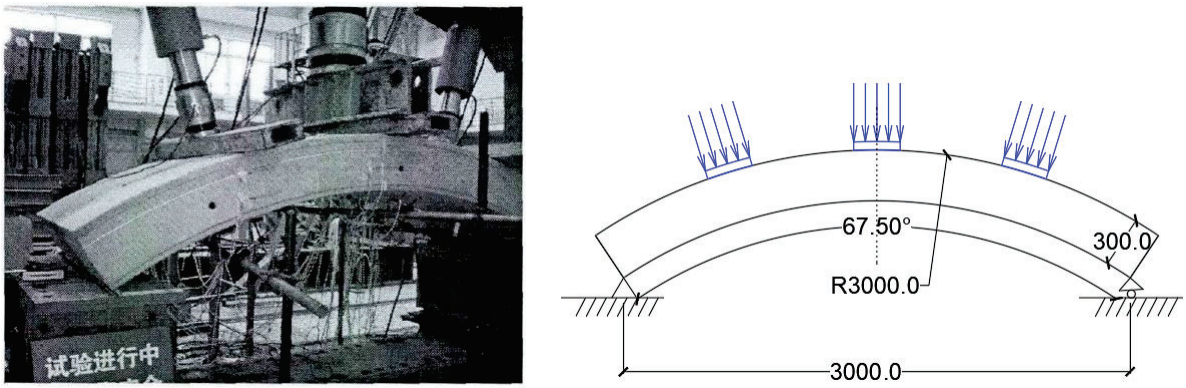
5.4.1 Design of the single segment test

The pressure exerted on the tunnel lining in underground condition is complex, comprising both the pressure of the ground and of the ground water. It is therefore difficult to precisely reproduce the realistic loading conditions on the lining ring, for testing in a laboratory. To verify the calibration of the concrete constitutive model presented in Section 5.3, numerical analyses were performed (discussed in Section 5.5) of appropriate laboratory experiments involving individual lining segments. For this purpose, a series of laboratory tests on full scale single concrete lining segments has been carried out by Zhou et al. (2012) at Dalian University of Technology. Two aspects of mechanical features, the resistance to cracking and the ultimate bearing capacity of the segment, were mainly investigated. Both capacities were quantified with loading tests under defined boundary conditions. In the current research, two specific tests were considered for modelling, as described below.

In the first test, named PZW1, a single reinforced concrete segment was loaded via three areas positioned on the extrados side of the segment, using jacks installed in the reaction frame (see Figure 5.16). The segment was supported at both ends as a simple beam, allowing horizontal displacement of the segment at one of the supports (Figure 5.16*Figure 5.17*b). The smooth steel plate was placed under the support to reduce the friction. It is noted that the load generated from each of the three jack was transferred to the segment extrados via a rubber pad. The implication of this for modelling was that a uniformly distributed stress across the width of each jack would be applied in the analysis. This design is very important for avoiding local failure of the concrete in the test.

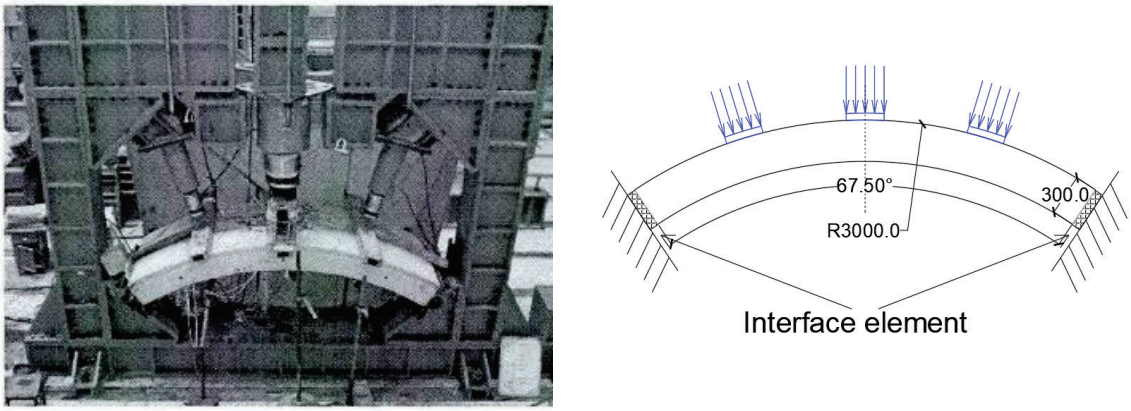
The second test, named PZW2, followed the same configuration of the PZW1, except for the boundary conditions at both ends of the segment (see Figure 5.17). In this test, the segment was supported normal to its cross-sectional surface at both ends, via inclined steel plates (see Figure 5.17a). Otherwise, the segment and its reinforcement alignment, as well as the pattern of jack loading, were the same as in test PZW1. Hence, the loads from three jacks were also modelled as evenly distributed stress (see Figure 5.17b). The supporting plates on both ends provide axial reaction force into the segment. The objective of PZW2 was to investigate the contribution of the axial reaction force from the plate support to the loading resistance of the segment. This boundary condition is akin to the segment assembly forming a lining ring in the real tunnel. It is noted that the boundary condition at both ends could not be simply regarded as ‘fixed displacements at all nodes’ in the numerical study, as the segment sides had freedom to move along the inclined plates, despite strong friction mobilised during the test. Furthermore, the tilting of the segment side in the contact with the plate was possible as neither end was bonded to the plate. Therefore, interface elements were introduced at both ends to model the contact between the segment and the plate.

The behaviour of both the main reinforcement bars and of concrete was recorded for both tests. The cracking load, yielding load and failure load of the segment were measured, giving an indication of the likely mechanical response of concrete lining segment under in underground condition. The tests lasted a few months due to the low rate of loading, which ensured a precise and complete record of segment reaction.



(a) (b)

Figure 5.16: Testing arrangement of the single segment loading PZW1: a) photograph of the set up; b) schematic of the loading and boundary conditions (unit:mm).



(a) (b)

Figure 5.17: Testing arrangement of the single segment loading PZW2: a) photograph of the equipment; b) schematic of the loading and boundary conditions.

5.4.2 Details of the single concrete segment in the tests

The single concrete segment was made of C50 concrete and the reinforcement cage, with the geometry resembling that of segments in a real lining of underground tunnels in Shanghai. The segment had outer radius of 3m, and inner radius of 2.7m. The thickness was 0.3m, and the width 1.2m. The central angle was 67.5 degree. Both tests were full scale to improve the data quality. The

reinforcement cage was very similar to the one used for DOT lining, and the details can be seen from Figure 5.7 and Figure 5.8. The information of all types of reinforcement used in the cage are listed in Table 5.8. It is noted that the upper reinforcement (labelled 1) with a larger diameter (18mm) refers to the bars on the extrados side of the lining, where larger axial stress along the lining circumference was expected. The lower reinforcement refers to the main bars (labelled 2) on the intrados side, as shown in Figure 5.8.

Table 5.8: Information of reinforcement cage for the single segment

Segment	Upper main reinforcement	Lower main reinforcement	Stirrup	Vertical reinforcement
PZW1/PZW2	8Φ18	8Φ16	72Φ8; 4Φ12	22Φ12

The 16 main reinforcement bars are dominant in providing bending and axial resistance of the segment. Therefore, the mechanical properties of these main reinforcement bars, as well as of C50 concrete for the segment, are measured via tension test before the segment test to ensure that the standard quality of the materials is met. The results summarised in Table 5.9 match the values given in the code, thus both materials are considered to be of appropriate quality.

Table 5.9: Mechanical properties of the main reinforcement and the concrete

Material	Yield Strength f_y (MPa)	Peak Strength f_p (MPa)	Yield Strain (10^{-6})	Young's Modulus E (GPa)
Concrete	-	66.9	-	34.5
Steel bar Φ16	371.1	527.5	2150	200
Steel bar Φ18	392.2	511.1	2219	200
Steel bar Φ18	371.2	534.3	2114	200

5.4.3 Arrangement of measurements

The strain gauges were pasted on the main reinforcement bars, labelled with number 1 and 2 in Figure 5.8, Figure 5.9 and Table 5.1, before pouring concrete. The gauges were measuring the strain of upper and lower reinforcement at the middle position of the segment, where the maximum strains were expected to develop under the applied load. The alignment of the strain gauges for upper and lower reinforcement, each labelled with a number and a number in bracket respectively, is shown in Figure 5.18.

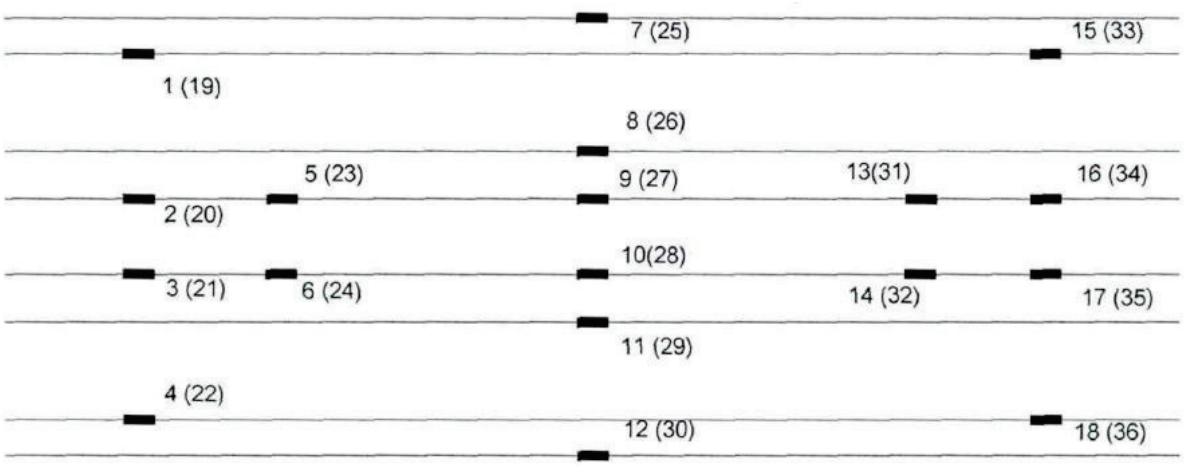


Figure 5.18: Alignment of strain gauges for main reinforcement (Zhou, 2011)

The resistance strain gauge technique was used for the measurement of concrete strain and the gauges were pasted on the surface of intrados, extrados and the sides of the segment, as shown in Figure 5.19. It was reasonable to focus the investigation of the concrete strain evolution in the middle range of the-segment where the cracks are likely to occur under the applied load. Additionally, a displacement transducer was installed at the middle of intrados, as shown by the red dot in Figure 5.19, to monitor vertical deflection. Furthermore, this data was used for monitoring of the loading rate during the test.

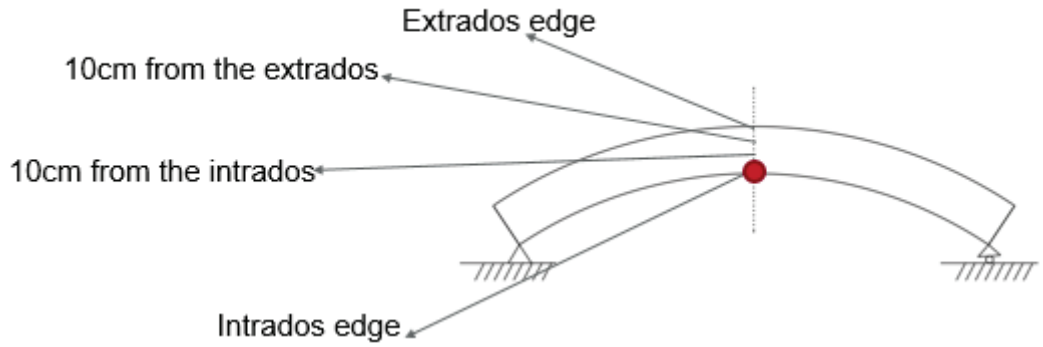


Figure 5.19: Schematic of the strain gauges glued on the concrete of the segment

5.5 Validation of the concrete model

5.5.1 2D modelling of the single segment test

Numerical simulations of the two laboratory experiments introduced in Section 5.4 were carried out with ICFEP (Potts & Zdravkovic, 1999, 2001). Analyses were conducted as two-dimensional (2D) plane strain, with FE meshes depicted in Figure 5.20, as there was no geometric variation in the out of plane

direction. Each mesh consisted of 450 8-noded quadrilateral solid elements. For test PZW1, one corner of the intrados is restricted from moving in both the vertical and the horizontal directions, while the opposite corner is restricted only in the vertical direction. The span between the two supports is 3.0m. For test PZW2, the displacements normal to the two inclined sides are prescribed as zero. The width of each distributed load is about 23.56mm (across three finite elements), simulating the load transfer with rubber pads in the tests.

The two sets of the main reinforcement bars are modelled with 3-noded elasto-plastic bar elements, characterised with the strain softening constitutive model. The bar elements, coloured in red in Figure 5.20, are located along the sides of solid elements. The upper reinforcement has a distance of 60mm from the extrados side, whilst the protection layer for lower reinforcement has 40mm thickness on the intrados side. The alignment of both main reinforcements follows the design of the segment in the laboratory test, and the parameters needed for the model are listed in Table 5.3. It is noted that for 2D simulation, the area of reinforcement is smeared by dividing the total area of 8 main reinforcement bars with the segment width in the z-direction, thus the unit becomes mm^2/m.

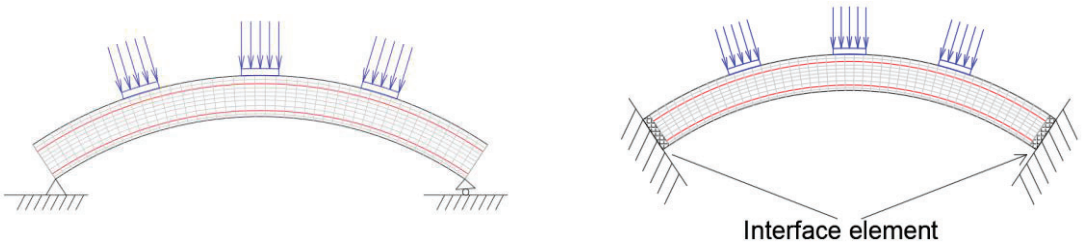


Figure 5.20: 2D mesh for single concrete segment testing a) PZW1; b) PZW2.

The loading of the segment is applied incrementally (see Table 5.10 for both tests) as a normal stress on the extrados, over three specific areas shown in Figure 5.20. The equivalent force of a single jack is calculated by multiplying the normal stress with the stress area.

Table 5.10: Incremental loading on the segment

Test	**Increments**	**Incremental normal stress (kPa / inc)**	**Equivalent force from a single jack (kN / inc)**
PZW1	1 - 40	20.0	4.71
	41 - 100	5.0	1.178
PZW2	1 - 100	100.0	23.55

The parameters for the modified Chen concrete model were summarised in Table 5.7. As discussed, the model also employs the non-local strain regularisation for strain softening behaviour, adopting the G&S approach. In the analysis of PZW1, the non-local parameter INETRNAL LENGTH was set at 0.06m and this value is considered suitable for the size of the mesh as the smallest element is about 0.02m*0.08m. In the base analysis, the RADIUS parameter was set as 0.18m. A series of trial simulations were carried out to investigate the sensitivity of the strain range to analysis results. It was found that the variation of LENGTH between 0.04m and 0.08m did not influence the mechanical response of the segment in test PZW1. However, in the analysis of PZW2, the selection of LENGTH caused some difference in segment response and it was found that the larger length of nonlocal softening evaluation range leads to higher loading resistance of the segment. The sensitivity of this parameter was investigated for test PZW2 and the LENGTH was set at 0.02m.

The properties of zero-thickness interface elements, employed in the simulation of test PZW2, were determined from trial analyses, as no other information from physical tests was available. They were considered to be elastic and value of the elastic shear stiffness, *Ks*, was determined as $8*10^4$ kN/m, the value of the elastic normal stiffness, *Kn*, was set at $8*10^5$ kN/m. The results of these trial tests are introduced in the section 5.5.6.

5.5.2 Deflection of the segment mid-arch point

The segment deflection at the mid-arc position of the intrados side was recorded (see Figure 5.21) and the corresponding numerical predictions are compared against the laboratory measurements. The agreement between the measured and predicted load-deflection curves is very satisfactory, despite slight over-predicton of ultimate load, thus verifying the overall stiffness of the structure in the numerical model.

In the PZW1 test, it is visible that the segment has experienced three deflection stages: I) the elastic stage; II) the elasto-plastic stage between 'yielding' and failure; III) the post failure stage. In the first stage, the segment shows good linear overall stiffness under the incremental loading, and the numerical prediction matches well with the measured data. The yielding is initiated at the load of about 90kN and is well captured by the model. The numerical prediction of the subsequent load-deflection shows a similar pattern to that measured, although slightly overpredicting the load at failure, which was measured at 191kN..

As for the test PZW2, the maximum load recorded in the laboratory is 1071kN, which is a much higher loading resistance compared to test PZW1. This demonstrated the effect of the boundary conditions and the normal reaction forces generated from the inclined steel plates. The deflection of the mid-arc intrados at the onset of failure is over 20mm, which is larger compared to the corresponding value in

PZW1 (12mm). The overall stiffness of the PZW2 segment is higher, as expected, but the measured load-deflection curve experiences a different pattern, with an uncertain determination of the yield load. However, the failure load is clearly defined in the test at 1071kN, but the numerical result overpredicts the failure load at about 1300kN, exhibiting two practically constant gradients of the load-deflection curve up to failure. The gradients change at the predicted yield load of around 600kN. While the agreement between the predicted and measured response in test PZW2 is generally satisfactory, the observed slight discrepancy could be attributed to the uncertainty of boundary conditions applied via the steel plates, as no movements are measured at those localities and therefore the real restrictions are not know.

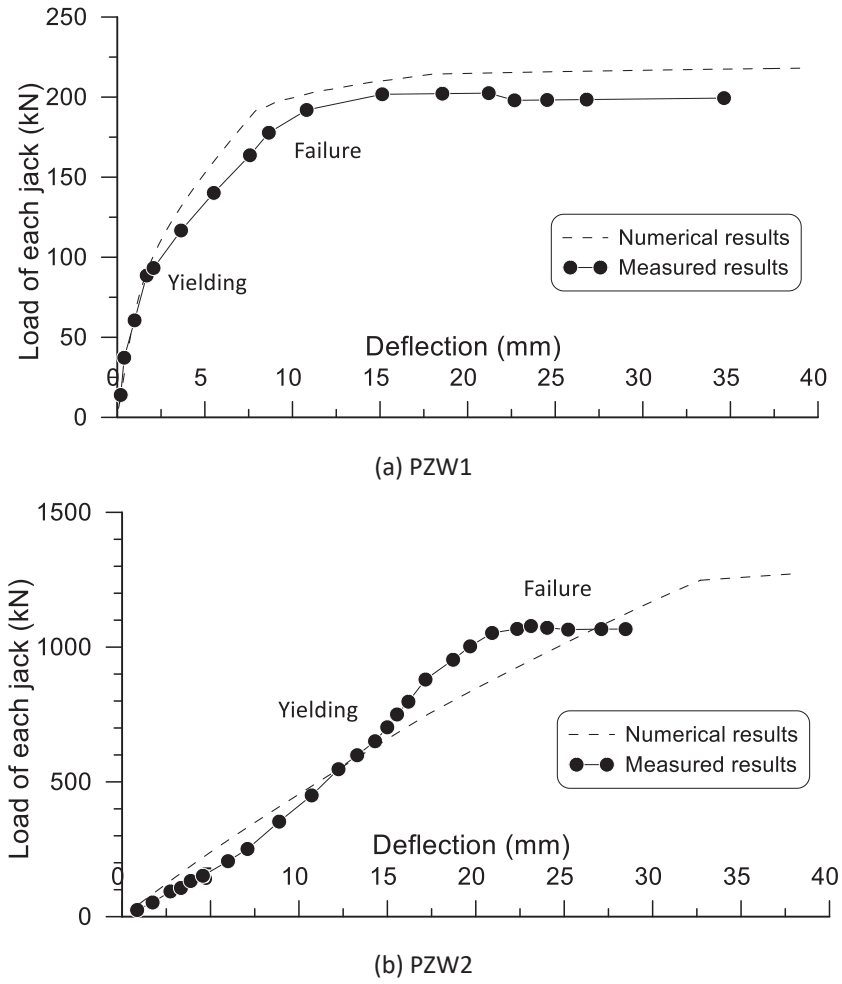
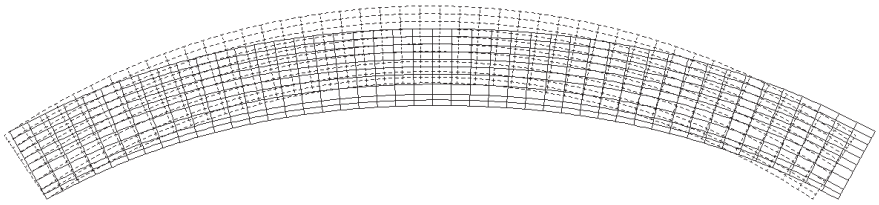
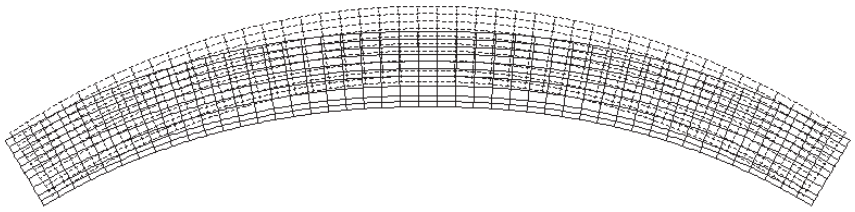


Figure 5.21: Evolution of middle deflection during the test a) PZW1; b) PZW2

The deformed mesh of the segment at the end of loading is illustrated in Figure 5.22 for both tests. In PZW1 test, the left hand side corner does not move as the displacements are fixed, while only the horizontal movement takes place at the right hand side corner. As for PZW2 test, the segment extends at both ends, gaining a normal reaction force from both joint elements.



(a) PZW1



(b) PZW2

Figure 5.22: Illustration of mesh deformation of the segment under jack loading a) PZW1; b) PZW2

5.5.3 Strain evolution in the reinforcement

Strain of reinforcement in PZW1

The evolution of the axial strain in both the upper and the lower main reinforcement, against the applied load on the segment, is shown in Figure 5.23 for the mid-arc position of the strain gauges (see Figure 5.20) and from both the measurements and numerical predictions. The lower reinforcement experiences only tensile axial strain (tension +ve convention) and it reaches the magnitude of about $2000\mu\varepsilon$ (0.2%) when the load on the segment reaches peak at 191kN. This is a small value of the mobilised strain and the test as a whole has recorded a maximum tensile strain of only around $5700\mu\varepsilon$ (0.57%). The model captures very well the measured strain evolution against the applied load.

The upper reinforcement at mid-arc position shows a mobilisation of compressive axial strain (compression –ve convention) for most of the segment loading, switching to tensile strain only after the peak load is reached at 191kN. The maximum compressive strain of around $300\mu\varepsilon$ (0.03%) is very well predicted by the model, which also captures well the whole strain evolution pattern.

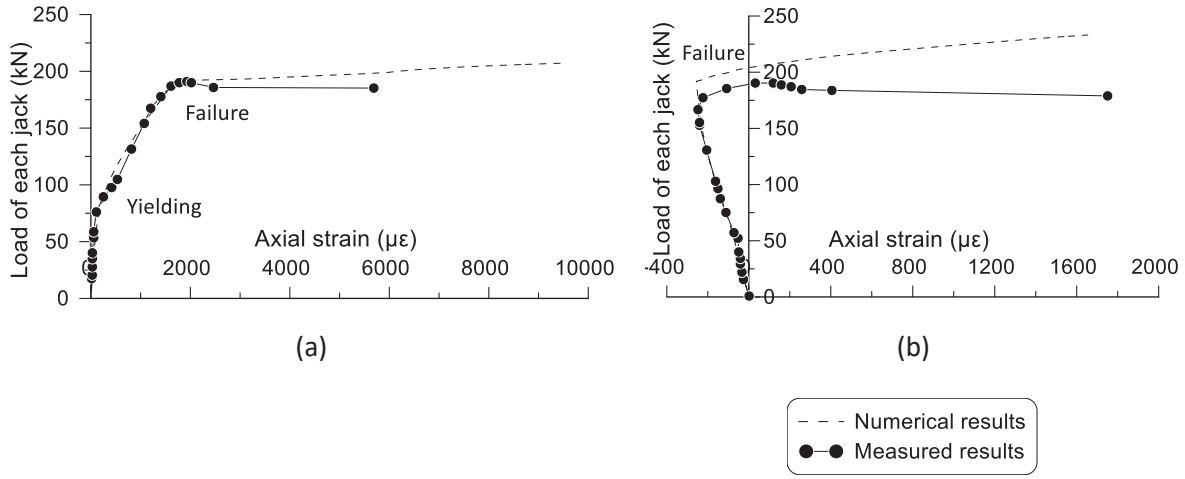


Figure 5.23: Axial strain of reinforcement at middle positions for PZW1 test: a) Lower reinforcement; b) upper reinforcement.

Strain of reinforcement in PZW2

Figure 5.24 shows the evolution of axial strains in the upper and lower reinforcement, against the applied load on the segment, at a similar mid-arc position shown in Figure 5.19. In this test the lower reinforcement is measured to be in tension throughout the test, similar to measurements in test PZW1. The maximum mobilised axial strain is around $10000\mu\varepsilon$ (1%), however the strain data are missing for the final loading stage to peak load of 1071kN. The model reproduces well this pattern, although it overpredict the maximum load as shown before in Figure 5.24.

The upper reinforcement is measured to be in compression throughout the test, with the maximum mobilised axial strain of around $2500\mu\varepsilon$ (0.25%). The model has reproduced this response, although mobilising a stiffer relationship between the reinforcement strain and the applied load. This again could be explained by the lack of knowledge on the exact restraints imposed by the boundary conditions for this test.

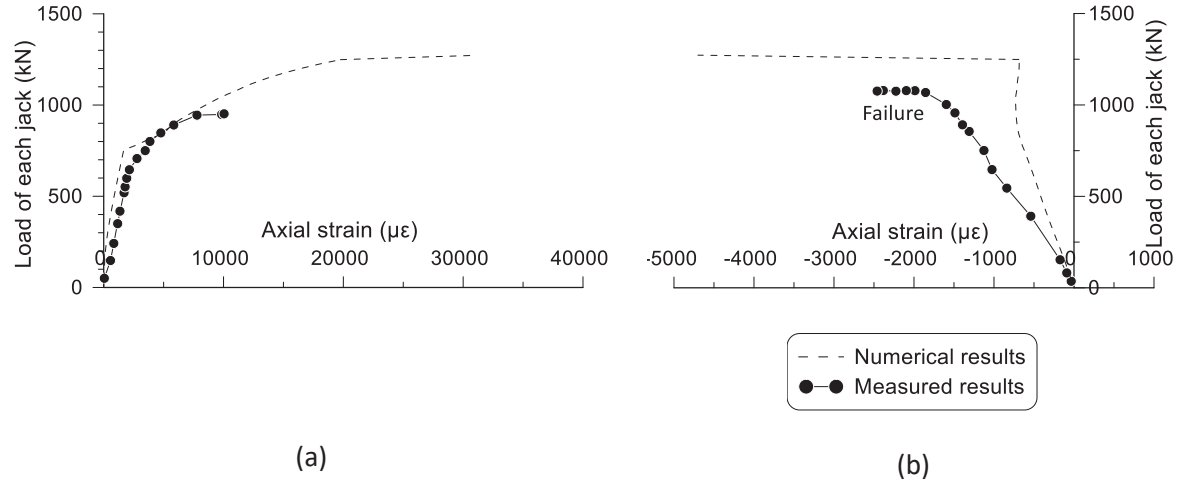
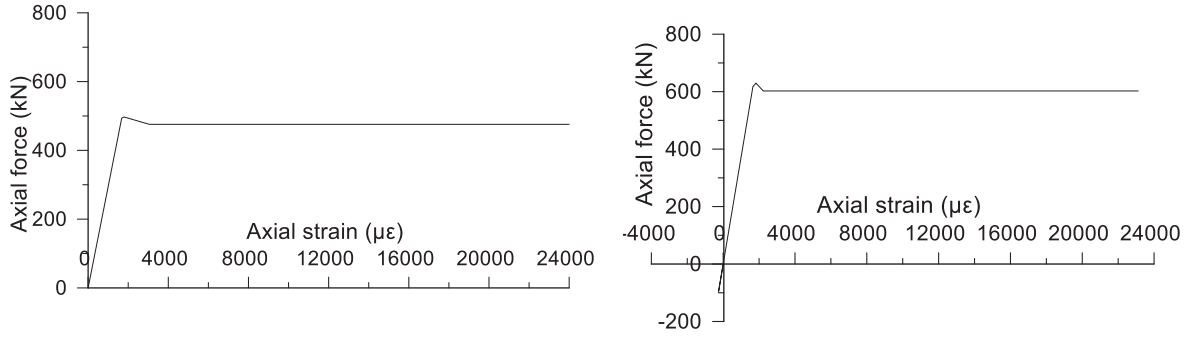


Figure 5.24: Axial strain of reinforcement at middle positions for PZW2 test: a) Lower reinforcement; b) upper reinforcement.

Verification of constitutive modelling for reinforcement

The predicted axial force- axial strain curves obtained from the analysis for both lower and upper reinforcements, at the mid-arc position in test PZW1, are shown in Figure 5.25. The evolution of strain against axial force shows features of strain softening of steel material, and the yielding strain is about 0.18% matching the chosen parameter for the constitutive model (see Table 5.3, the peak stress / Young's modulus = 355MPa / 200Gpa = 0.18%) . The lower reinforcement has lower peak axial force due to smaller diameter (16mm) compared to the upper one (18mm). The compressive strain for upper reinforcement is small compared to the tensile strain after failure. Linear elastic behaviour is predicted for both reinforcement bars before the yielding of the steel.



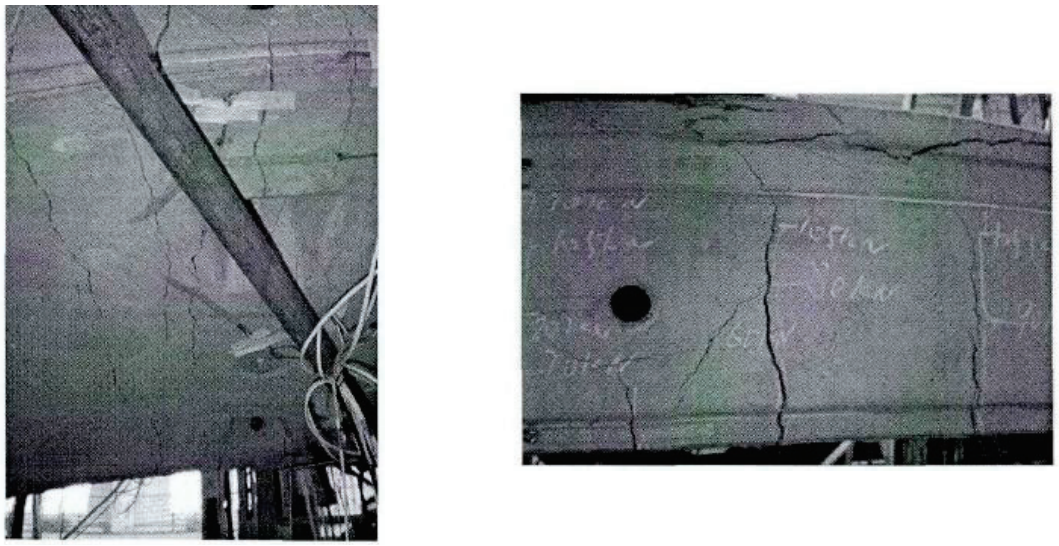
(a) lower reinforcement (b) upper reinforcement

Figure 5.25: Axial force-strain relation of a) upper reinforcement; b) lower reinforcement in the loading test of the segment

5.5.4 Cracking of the concrete in PZW1 test

According to the report on the laboratory testing (Zhou, 2011), some visible cracks were firstly observed at the load of 57kN in the test PZW1, located at the mid-arc position at the intrados. The crack width then expanded to 0.2mm under 124kN and usually this is the maximum allowable width of crack in engineering practice, at which the structure surface still retain water proof ability, according to the Chinese code (Code for design of concrete structures, 2010). More cracks appeared when the segment came to failure (Figure 5.26a) and the major crack in the mid-arc extended from the intrados to extrados side (Figure 5.26b). The length of cracks grew with load increase and reached almost across the whole thickness of the segment when it came to failure. The photo taken from the side view (Figure 5.26b), in which the segment thickness is shown, shows the progression of the crack, with the load magnitude etched next to it as it progressed. From this record, it can be inferred that the crack reached the mid-thickness of the segment when the load was 80kN and progressed to 2/3 of the thickness when the load reached 105kN. Some horizontal cracks are also observed near the extrados side when the segment came to failure, because of the shear failure induced by compressive stress on the extrados concrete. The minor cracks and one parallel crack near the major one could also be found

in this photo.



(a) (b)

Figure 5.26: Cracks of the concrete in PZW1 test when the segment came to failure a) view from under the intrados side; b) crack across the segment body – view on one longitudinal segment side

It is expected that the crack starts from the intrados side due to tensile stresses in the concrete developing on that side from the start of loading. The numerical simulation cannot reproduced the discontinuity of the crack in the FE mesh, however, the likely position and extent of the cracks can be inferred from other quantities. It is instructive to investigate the mobilised stress in the concrete in the mid-arc section under the applied load.

The profile of the horizontal stress along this section, from the numerical results, is plotted at several increments of loading in Figure 5.27. The distance on the graph reflects the 0.3m thickness of the segment and zero is located on the extrados. At 56kN (increment 12 of the analysis) the horizontal stress profile demonstrates the onset of cracking at the intrados, where the horizontal stress has approached the peak tensile strength $f_{tp} = 4.1$MPa (Table 5.7). This is in very good agreement with the reported 57kN of load as the onset of cracking. At the same time a compressive horizontal stress at extrados neared 5MPa.

As for the failure stage under the load of 191kN at increment 43 in the simulation, the concrete failure in tension progressed to around 0.1m distance from the extrados, implying the length of the tension crack of around 2/3 of the segment thickness, which is also in agreement with the observed tension crack propagation in Figure 5.26b. The maximum compressive stress at extrados at this stage is around 30MPa, indicating that the concrete has yielded ($f_{cy} = 24.1$MPa) but that the mobilised stress was

far from the peak compressive strength $f_{cp} = 60.3$MPa or the failure strength $f_{cf} = 50$ MPa (Table 5.7). For demonstration, Figure 5.27 shows the profiles of horizontal stress evolution in concrete for several intermediate stages. It is evident that the crack propagation slowed down between 150kN and 191kN of load, while at the same time the compressive stress in the extrados increased more rapidly than at the start of loading.

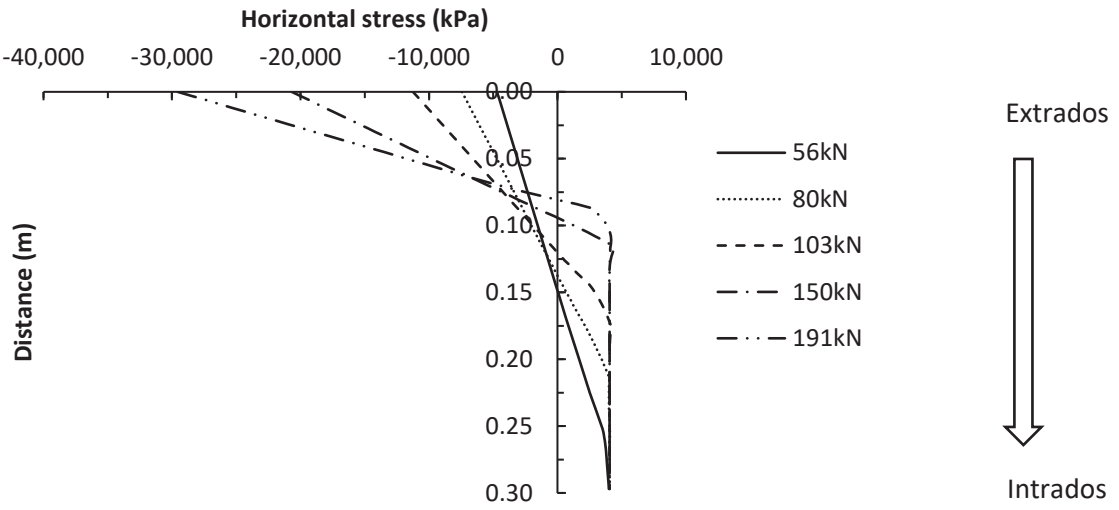


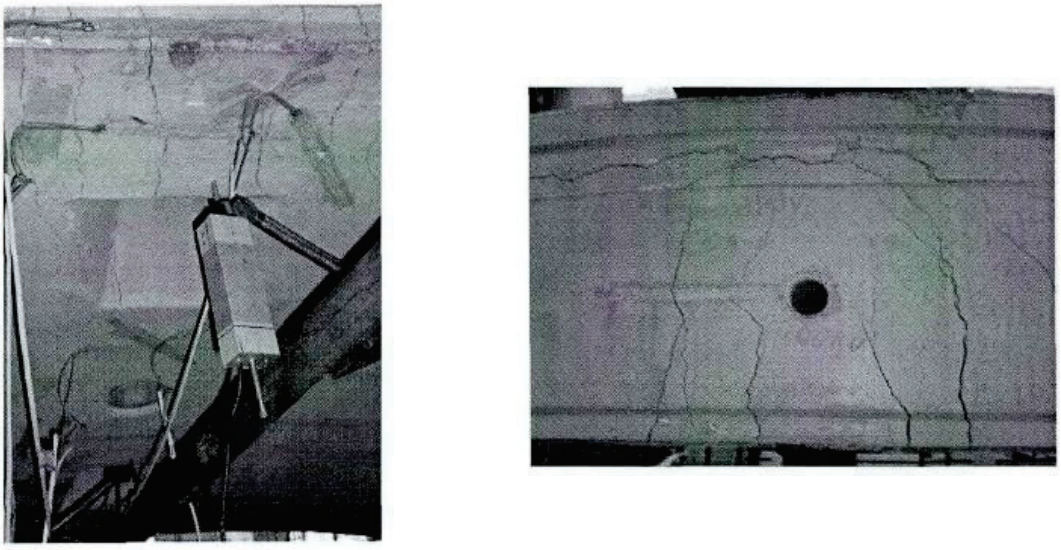
Figure 5.27: The evolution of horizontal stress across the mid-arc cross-section with loads from numerical analysis (PZW1)

5.5.5 Cracking of the concrete in PZW2 test

In PZW2 test, the visible crack of the segment appeared under the jack load of 80kN, and the width expands to 0.2mm under the load of 415kN in the laboratory test. The cracking also starts at the middle position of the segment intrados and a denser distribution is observed on the segment side as shown in Figure 5.28b. The distance between adjacent cracks is obviously smaller than that in PZW1 test as shown in Figure 5.26 above. It can be seen that the cracks evolve in a similar manner: vertical cracks extends from the intrados in upward direction, and on the extrados side, some horizontal cracks, which are caused by shear failure of the material, have occurred. The photo (Figure 5.28a) showing the view beneath the intrados side demonstrates the cracks extending in the perpendicular direction to the segment sides.

Similarly to the Figure 5.27, the profile of horizontal stress along the mid-arc section is plotted at different increments (Figure 5.29). At increment 4 (94kN), the crack at intrados side is likely to occur as the horizontal stress is approaching the peak tensile strength (4.1MPa). The horizontal stress on the extrados side, at the same time, is about 4MPa. This is a bit larger than the reported crack load (80kN). The crack also extended to about 2/3 of the thickness at the failure stage, when the load is

1248kN. The maximum compressive stress on the extrados side has already exceeded 60MPa, demonstrating the compressive failure of the concrete. It can be seen that after increment 38 (895kN), the compressive stress on the extrados is about to exceed the peak compressive strength, and the extension of the crack slowed down in the later stage. It is noted that the curve for the 1248kN, when the segment comes to failure, shows unrealistic value of the compressive stress on the upper part of the cross-section, and therefore, the data of this part may not be adoptable.



(a) (b)

Figure 5.28: Cracks of the concrete in PZW2 test when the segment came to failure a) intrados side; b) crack across the segment body on one side

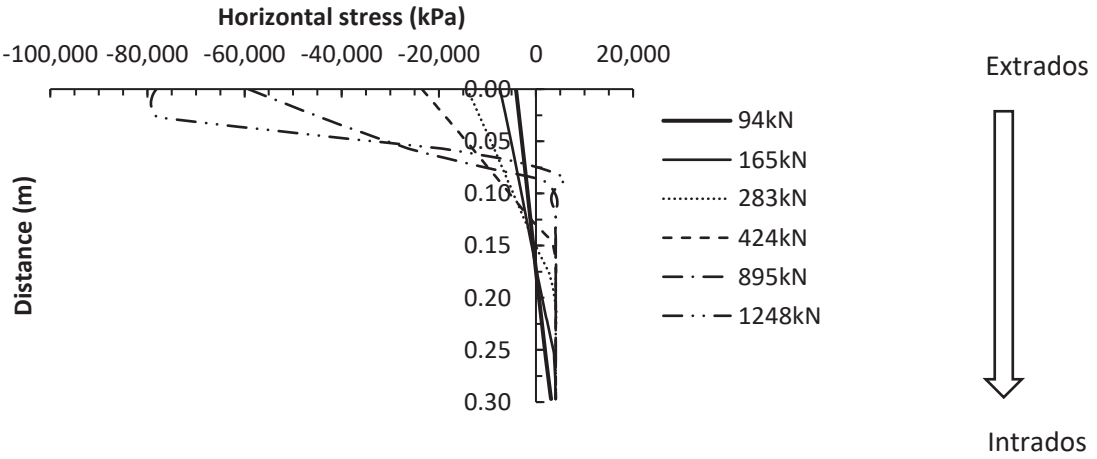


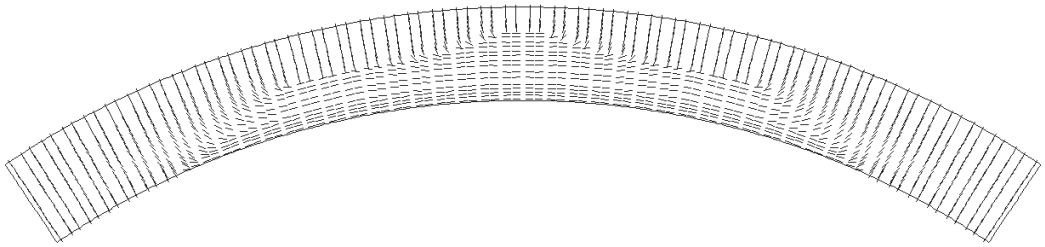
Figure 5.29: The evolution of horizontal stress across the mid-arc cross-section with loads from numerical analysis (PZW2)

The numerical simulation has given the assessment of the cracks in terms of the evolution of the hardening parameters. It is found that at increment 8, when the jack load is 188.4kN, the maximum plastic strain occurred at the mid-arc position of the intrados has reached 87.3 $\mu\varepsilon$. Therefore, the

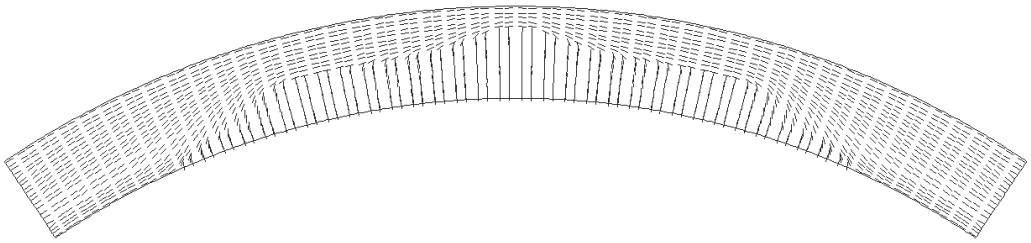
cracks may start from this increment in the analysis. The maximum plastic tensile strain occurring at the central intrados position, has been recorded (see Table 5.11). The maximum plastic strain exceeding the peak value of the material ($\boldsymbol{55\mu\varepsilon}$) indicates the tensile failure in terms of cracks. The Figure 5.30 shows the orientation of the principle stress under the failure load, and it demonstrates the area of the mid-intrados concrete undertaking tensile stress. Therefore, the considerable number of cracks can be expected in this region as shown in Figure 5.28b.

Table 5.11: The maximum tensile plastic strain at the mid-arc of intrados in PZW2 test

Increment	**7**	**8**	**12**	**18**	**23**	**53**
Load (kN)	164.9	188.4	282.6	423.9	541.7	1248.2
Max. $\boldsymbol{\varepsilon_1^{pl}}$ $\boldsymbol{(\mu\varepsilon)}$	53.8	87.3	288.0	719.6	1134.9	16586.0
> $\boldsymbol{55\mu\varepsilon}$	N	Y	Y	Y	Y	Y



(a) σ_1



(b) σ_3

Figure 5.30: Orientation of accumulated principle stress under failure load (1248.15kN) in PZW2 test. a) major (tensile) principle stress; b) minor (compressive) principle stress.

The plastic compressive strain for the concrete on the extrados side is also concerned for this analysis. It is found that the mid-arc position of the extrados came to plastic stage after the load of 541.65kN, and the value did not exceed the ultimate plastic compressive strain of C50 concrete at the failure stage. As shown in Figure 5.34 later, the maximum plastic compressive strain reached 0.0016945, also read as 1694.5 $\mu\varepsilon$, and it did not exceed the ultimate plastic strain 1840 $\mu\varepsilon$ for C50 concrete. Nevertheless, it is still possible to observe the compressive failure in the lab testing due to the variance of material properties. Therefore, compared to the PZW1 test, the strength of the material is fully

utilised in resisting the bending moment from the jack load. The whole cross-section of the mid-arc position has become plastic in the analysis, indicating a full contribution to the overall strength of the structure.

5.5.6 Sensitivity of DL and the interface stiffness in PZW2 simulation

The DEFINED LENGTH (DL) parameter in the concrete constitutive model defines the influence of weighting function and the RADIUS defines the range of elements that contribute to the calculation of the strain during material softening (Summersgill et al., 2017). In the base analysis, the RADIUS parameter was set as 0.06m (60mm), and the RADIUS is always three times magnitude of DL. In fact, the RADIUS parameter does not affect the mechanical response of the segment according to the analysis of both PZW1 and PZW2. The smallest element in the analysis has the size of 0.02m*0.08m (20mm*80mm), and therefore, the DL is determined as 20mm in the base analysis. A set of three parametric analyses is performed, studying the effect of DL value on the strength of the segment its deflection at mid-arc intrados point. It can be seen from Figure 5.31 that the larger DL value results in higher loading resistance of the segment, but it does not affect the stiffness of the segment. The maximum load reached about 1900kN when DL = 80mm. However, when the DL is smaller than 20mm, the overall strength of the segment is not influenced. In the base analysis, the DL = 20mm is selected, not only for avoiding over-predicting the results of failure load, but also having considered the distribution of the cracks in the laboratory testing as shown in Figure 5.28 above. The DL value should be smaller than the distance between two adjacent cracks, and therefore, the value 20mm for the base analysis of PZW2 is appropriate.

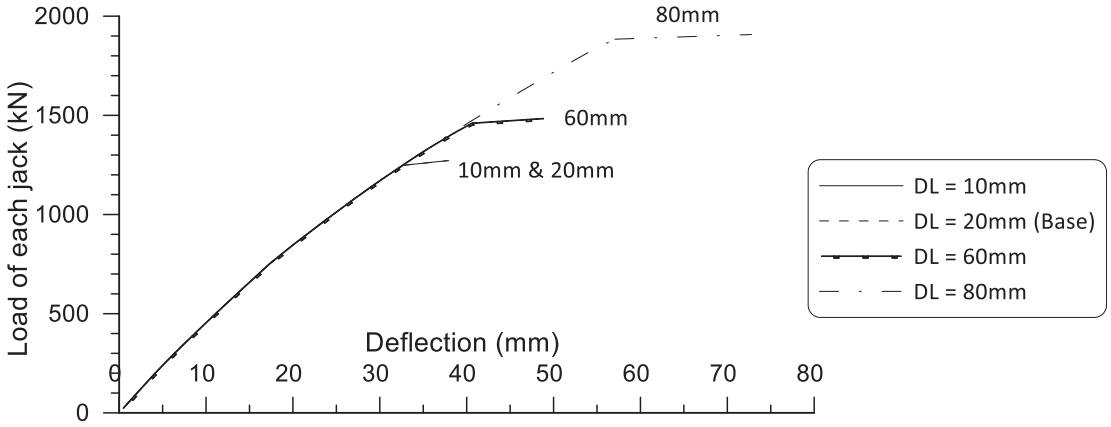


Figure 5.31: The evolution of deflection for different DL value

The stiffness for the interface elements on both ends of the segment reflects the stiffness of the steel

frame that supports and generates reaction force on the structure. Difference elastic normal and shear stiffness values of the interface elements have been applied in the trial analyses and the corresponding deflection response was compared. It is found that too large values results in higher segment stiffness and overestimation of its strength, while smaller stiffness values lead to soft response and small strength. Therefore, the combination of $K_S = 0.8 \times 10^5 kN/m$, $K_N = 0.8 \times 10^6 kN/m$ that reproduces reasonably well the average stiffness of the segment with some overprediciton of its strength was adopted for the main analysis.

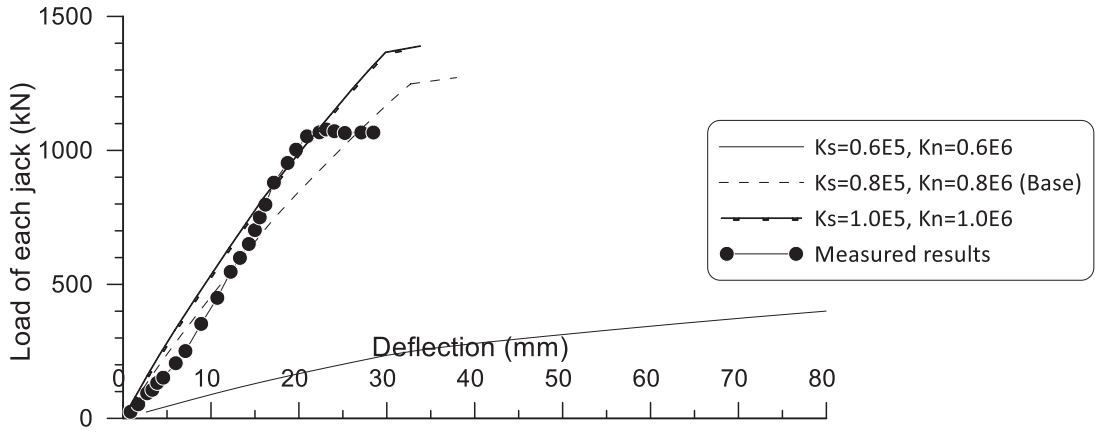


Figure 5.32: The evolution of deflection for different joint stiffness

5.5.7 Evolution of concrete strain on the side of segment at mid-arc position

Four concrete strain gauges have been glued on the side of the segment at mid-arc section, measuring the horizontal strain on the concrete surface during the test (Figure 5.19). The gauges are located on the extrados, intrados and two trisection points.

5.5.7.1 Concrete strain in PZW1 test

The extrados concrete was in compression during the test and thus the horizontal strain, which is the minor principal strain, is negative, as shown from the measurements in Figure 5.33. The numerical prediction, however, reproduces the same compression behaviour, but the response is much stiffer. It seems that the numerical prediction overestimated the stiffness of the segment, and the measured strain grew faster in the early stage of loading.

After the load of 90kN in the lab test, where the yielding of the segment was shown to occur in the deflection graph in Figure 5.21, the strain at the extrados gauge suddenly increased and accelerated (Figure 5.33). Such a behaviour is considered unrealistic as the strain value has exceeded the limit for compressive failure (3400 με) for concrete material, which was not seen in earlier interpretations of

the strain throughout the test. One explanation could be that the gauge was disturbed by concrete crushing in that region due to compression, or that it simply became unglued.

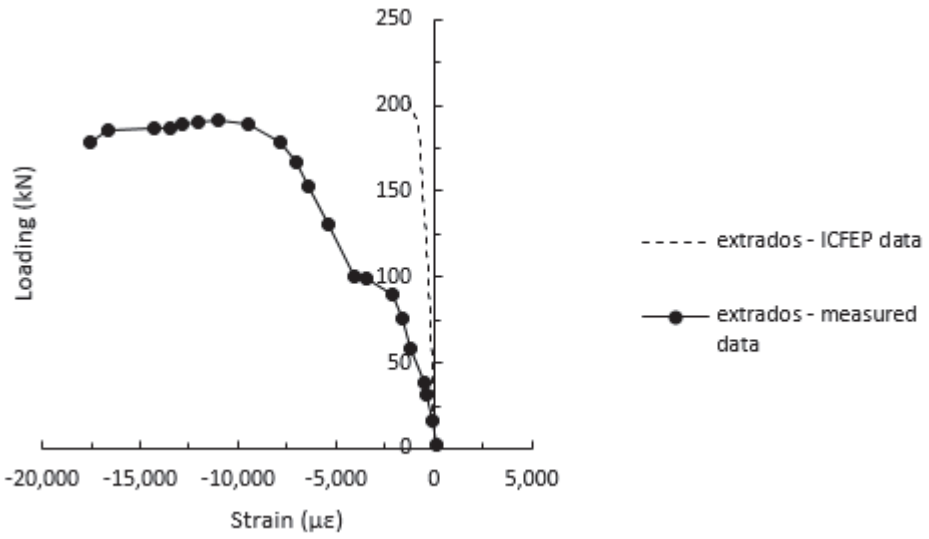


Figure 5.33: Evolution of concrete horizontal strain on the mid-arc extrados under loading in PZW1 test

The point at intrados performed pure tensile strain during the test. The value increased rapidly after yielding and there was data missing before the failure moment in the lab test. It can be interpreted that the expansion of the cracks on the mid-arc of the intrados made it difficult to measure the actual tensile strain on this position. The similar shape but with smaller magnitudes is found for the lower trisection point (Figure 5.34), which is labelled as 10cm to intrados in the figure, and the measurement was not available after the load of 127kN. As for upper trisection point, which is labelled as 10cm to extrados in the figure, either compression or tension was observed before the 'yielding' of the segment in both simulation and lab test results, indicating the neutral point under bending moment.

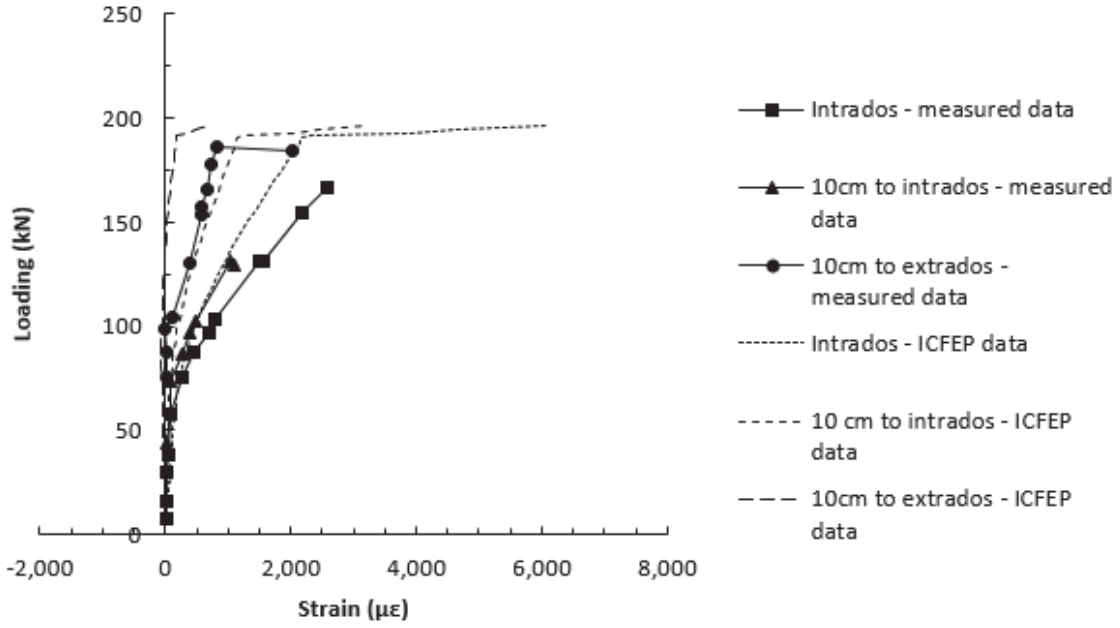


Figure 5.34: Evolution of concrete horizontal strain on the mid-arc intrados and two trisection points under loading in PZW1 test

5.5.7.2 Concrete strain in PZW2 test

The concrete strain on the side of the segment in PZW2 test has shown the similar rule with the PZW1 in terms of the compressive and tensile strain on the extrados and intrados, respectively. The strain measured on the extrados shows linear evolution against the load, and the peak value is less than 2000 με, indicating the failure is not reached. The good agreement has been reached for both curves in the early stage. However, the value increases rapidly after the 'yielding' of the segment at around 750kN in the numerical result, resulting in the overestimate of compressive strain from the simulation.

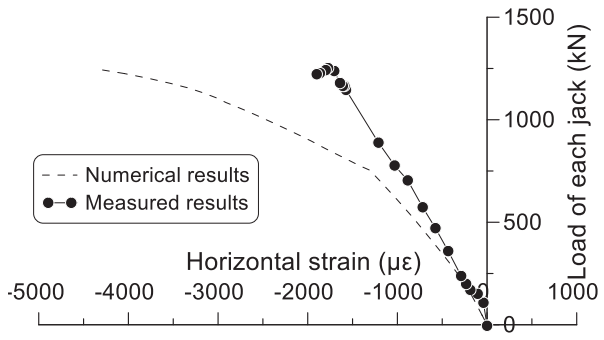


Figure 5.35: Evolution of concrete horizontal strain on the mid-arc extrados under loading in PZW2 test

It was unfortunate that the measured data for the horizontal strain are only available for the load under 500kN in the laboratory test due to the stoppage of the measuring system. Therefore, a comparison of the strain under lower level load is given first in the Figure 5.36 below. It can be seen

that it increases dramatically after the load about 150kN, and this trend is also followed by the numerical results. As introduced above that the ultimate strain for C50 concrete is about 155 με, and the exceeding value may result in the cracks of the material. Therefore, it is expected that in the lab testing, the visible crack firstly appeared under the load of 80kN on the intrados as the horizontal strain has reached 150 με (see Figure 5.36), while the corresponding load in the numerical simulation is 164kN.

The concrete at the position of 10m to the extrados side has been measured tensile stress in the test, whilst it performed compression in the numerical prediction. Therefore, the modelling of PZW2 test may have overestimated the compressive region and the cracking effect is not completely performed. It can be accounted for with the retaining strength contributed from both lower reinforcement and the concrete in the region of intrados where the material has already become pure plastic. The complete curves of strain evolution are shown in Figure 5.37 for the numerical results. It shows the strain keeps growing and accelerates after the 'yielding' of the segment. However, as mentioned, the data exceeding 155 με does not reflects the realistic concrete strain due to cracking failure.

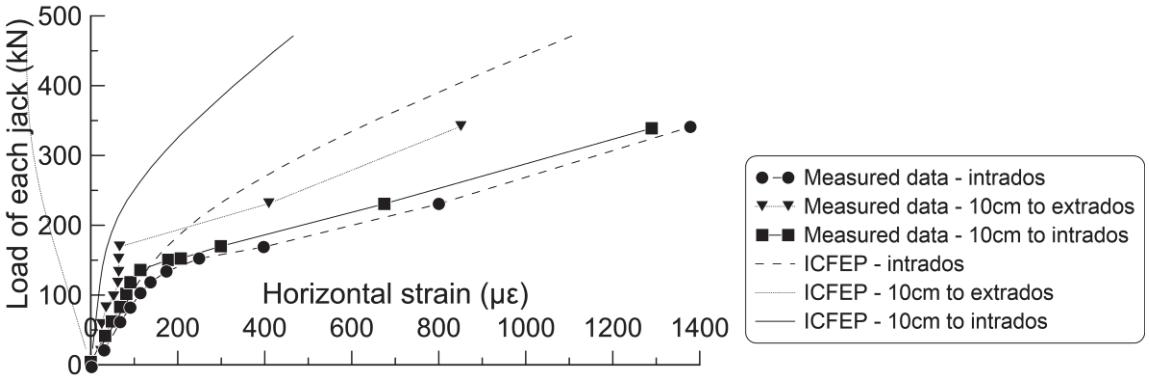


Figure 5.36: Evolution of concrete horizontal strain on the mid-arc intrados and two trisection points under lower level load in PZW2 test

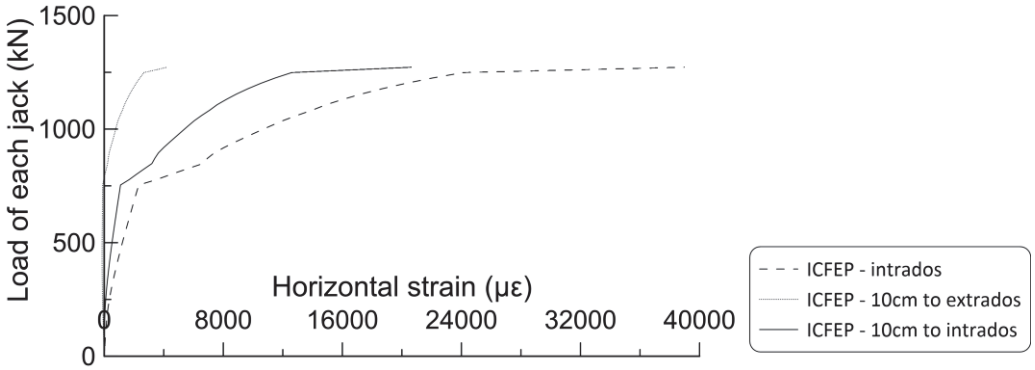


Figure 5.37: Evolution of concrete horizontal strain on the mid-arc intrados and two trisection points in PZW2 test

5.5.8 Failure mechanism of the single segment under jack loading for the tests

In summary of the mechanical response recorded in the laboratory and the numerical predictions, the failure mechanism of the single segment in both test is clear despite the difference in boundary conditions, and it can be divided into four stages:

- Stage 1: Elastic stage until visible crack occurs

The structure performs elastic behaviour under small load. The cracks have high probability to occur in the material once the yielding tensile stress is reached and consequently the concrete performed elasto-plastic behaviour. The appearance of visible crack on the surface indicates the formation of continuous crack inside the material.

- Stage 2: Expansion of crack width and depth

The expansion and extension of the cracks are followed after the formation of visible or continuous cracks with the increase of load. The major crack on the mid-arc position tend to grow from intrados towards the side of extrados.

- Stage 3: Cracks become continuous and open to failure.

The expansion of smear crack results in the acceleration of the failure. Consequently the whole structure performs 'yielding' and the resistance from external load decreases. The strain evolution of both reinforcement and the concrete speeds up after the yielding of the segment.

- Stage 4: Failure of the segment and the post peak behaviour

At the failure stage, the compressive stress acting on the extrados side leads to the shear failure of the concrete, and consequently some horizontal cracks can be found. After the overall failure of the segment, the deformation keeps growing and consequently the stress state of upper main reinforcement transformed from compression to tension. The entire bending moment acting on the middle cross section will be resisted by the compressive stress of the concrete and the tensile stress of the reinforcements on extrados side at this moment.

5.5.9 Investigation of the concrete grade (PZW1)

The concrete grade may affect the bending stiffness and the resistance of the segment. C30 grade concrete is widely used in the buildings and is considered of lower cost compared to C50. This parametric analysis refers to the same configuration of the C50 based simulation, and the only difference is the change of concrete material grade. The calibration of C30 concrete for the modified Chen concrete model is completed following the same procedure in section 5.3, and the input parameters are summarised in Table 5.12. A comparison on compressive and tensile design curves for

C30 and C50 concrete is shown in Figure 5.38.

Table 5.12: Parameters calibrated for C30 concrete in the modified Chen concrete model

Parameter	**C30**
Compressive yield stress, fcy (MPa)	15.18
Compress peak strength, fcp (Mpa)	37.95
Compressive failure strength, fcf (MPa)	28.16
Compressive ultimate strength, fcu (MPa)	4.0
Plastic compressive strain at peak strength, εcp (%)	0.179
Plastic compressive strain at failure strength, εcf (%)	0.299
Plastic compressive strain at ultimate strength, εcu (%)	0.5
Tensile yield stress, fty (MPa)	2.61
Tensile peak strength, ftp (MPa)	2.896
Tensile ultimate strength, ftu (MPa)	0.1
Plastic strain at peak strength in tension, εcp (%)	0.0072
Coefficient of exponential softening after ftp	0.02
Biaxial strength parameter, e	1.15

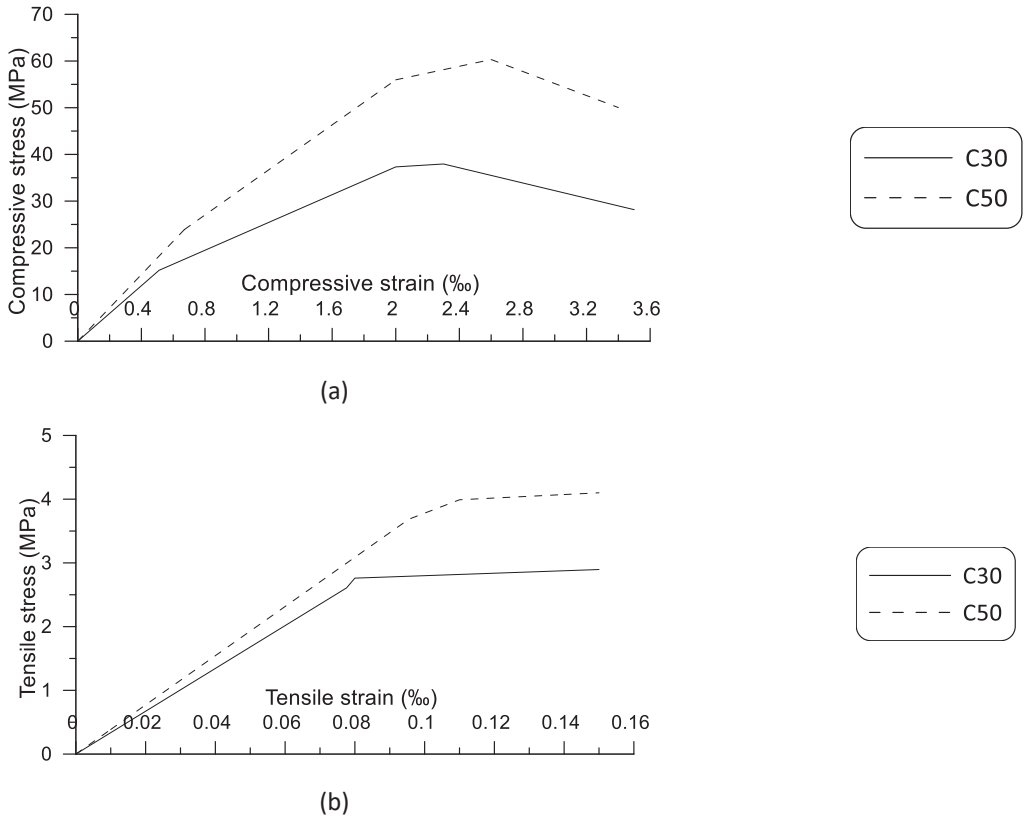


Figure 5.38: Comparison of mechanical behaviours between C30 and C50 a) compressive strain; b) tensile strain.

In this analysis, the identical loading pattern and boundary conditions are adopted as with the C50 concrete loading test. Therefore, the performance of deflection, main reinforcement strain and the evolution of side concrete strain are concerned, and the results are compared among the numerical results and the measured data of C50. It can be seen in Figure 5.39 that C30 concrete also performs reasonably well in terms of stiffness in the early stage of loading and has the same 'yielding' point. The obvious weakness of C30 concrete compared to C50 is lower peak strength (reduced by about 15%), and consequently an earlier failure occurs.

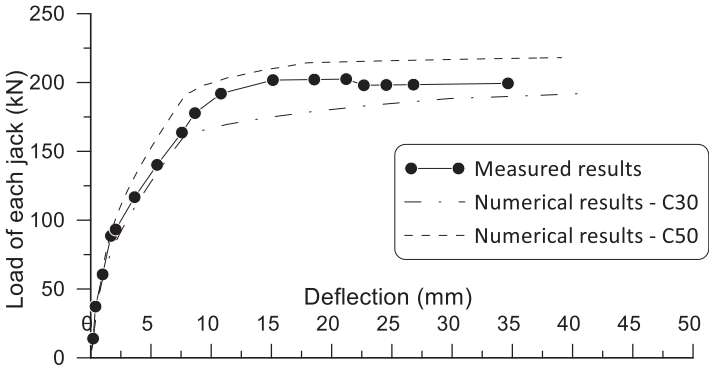


Figure 5.39: Deflection of C30 concrete segment under jack loading

Figure 5.40 shows that the main concrete reinforcement in a C30 segment deforms in a similar pattern as in a C50 segment and reaches similar values of the axial strain before the onset of failure, which happens at smaller jack load compared to the C50 segment.

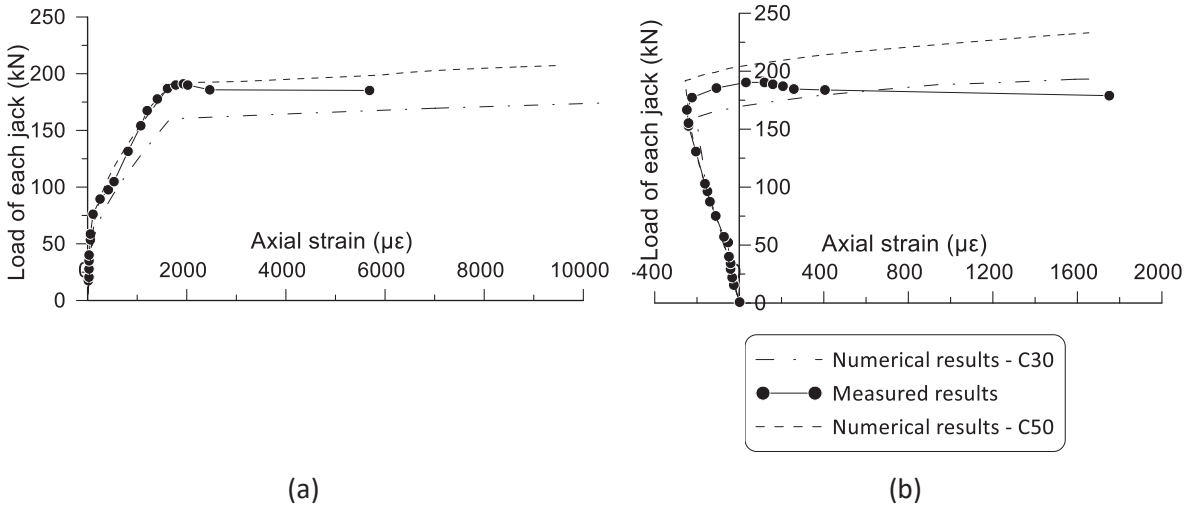


Figure 5.40: Axial strain of reinforcement at middle positions for C30 segment: a) Lower reinforcement; b) upper reinforcement.

5.6 3D analysis of the single segment PZW1 test

It can be argued that the 2D analysis cannot reflects the realistic mechanical response in the jack loading test because some obvious difference cannot be neglected between the plane-strain based 2D analysis and the laboratory test. Firstly, the alignment of the main reinforcements is designed as equally spaced steel bars along the extrados and intrados side instead of a 'layer' of the steel material with smeared properties. Secondly, the segment has the freedom of mobilising strain in the z-direction in the laboratory while it is assumed zero under plane strain condition. Thirdly, the measured concrete strain in the lab can only reflects the strain of the concrete on the side surface instead of the value inside the segment. Therefore, it is instructive to carry out a 3D numerical simulation to verify the accuracy of the 2D analysis as well as the strain of concrete measured on the side surface in the lab.

5.6.1 Mesh and boundary conditions of the 3D single segment test

The mesh for 3D analysis consists of 5400 (45*10*12) 20-noded solid elements modelling concrete, and 16 bars modelling main reinforcement, as shown in Figure 5.41 and Figure 5.42 respectively. Each bar consists of 45 3-noded bar elements and is located along the block side. The size and geometry information are the same with 2D mesh from the side view, but the width in the z-direction is set as 1.2m, divided into 12 elements, referring to the realistic segment in the laboratory test. The alignment of the main reinforcements in this mesh follows the design of the segment as illustrated in Figure 5.8. The modified Chen concrete model for solid elements and strain softening model for bar elements are employed, using the same material calibration as 2D analysis, to simulate the loading test.

The prescribed displacement boundary set up for the 3D analysis has been extended from 'two corners' at the footing of the segment to the 'two lines' for 3D footing. The left footing line is prescribed zero displacement in both x and y directions, whilst the other is fixed only in y direction. It is noted that the segment has the freedom to deform in z-direction but the displacement should be restricted. Therefore, the displacement of the left footing end (one corner) is fixed in z-direction. The jack load is applied on 'three stripes' on the extrados surface, simulating the three jacks and the load transmission using rubber plates. The loading pattern follows the configuration of 2D analysis, performs 20kPa incrementally over the first 40 increments and the 5kPa incrementally over the rest 60 increments on the three loading 'strips'.

The analysis was carried out in ICFEP and the modified Newton-Raphson approach was adopted for the non-linear solver. The parallel analysis, employing a number of threads for simultaneous calculation, is introduced for this simulation. This function is active using the PARELLEL card in the program and improves efficiency for calculation well. It has been found in the analyses that the default pattern without using parallel calculation takes 71 hours for this 3D single segment loading simulation,

whilst the time is 29 hours and 17 hours for using parallel card with 4 and 8 threads, respectively.

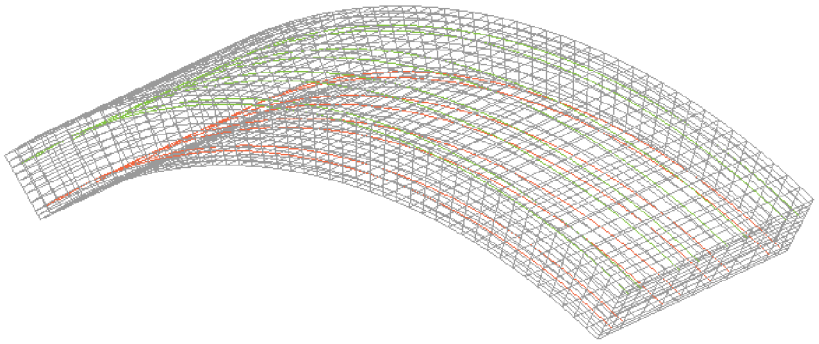


Figure 5.41: 3D mesh for single segment loading test

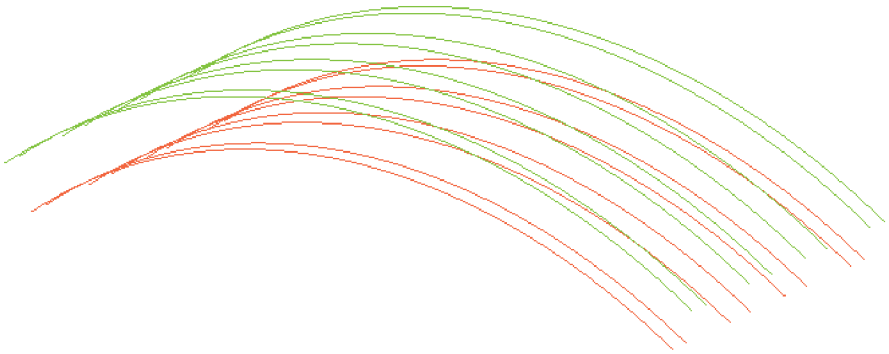


Figure 5.42: Distribution of main reinforcement in the 3D model

5.6.2 Comparison of the results between 3D and 2D analysis

The 3D analysis follows the same mechanical boundary conditions and constitutive modelling calibrated following the material properties of the base analysis in 2D, and therefore, the comparison is significant for verifying the model quality of 2D analysis and the correct configuration of the simulation. The discussion of the results on 3D analysis, which is considered having the most realistic modelling framework, is focused on the segment deflection, strain of reinforcement and the strain of concrete in comparison to the corresponding 2D data.

The evolution of deflection in 3D analysis is measured at the centre of the intrados surface, and it has been found the values are the same for the points with identical x and y coordinates along the z direction. The comparison shown in Figure 5.43 indicates that the numerical results of deflection based on 3D analysis realised the same value with 2D as two curves are almost overlapped. Therefore, the overall stiffness and the strength of the single concrete segment is modelled well in both 2D and 3D analysis.

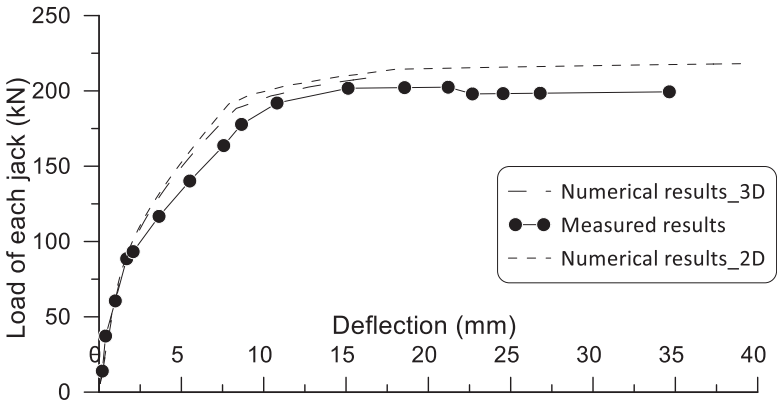


Figure 5.43: Comparison of segment deflection between 2D and 3D analysis

There are 8 main reinforcements aligned on the extrados and intrados side respectively, and the mid-arc strain evolution has been obtained. In this 3D analysis, it is found that there is little difference of the strain behaviour among the bars on the same side. Therefore, for both upper and lower reinforcement, the one located close to the side of segment is selected and the strain evolution is plotted and compared against 2D and measured results (see Figure 5.44). Apparently, the strain for both reinforcements in 3D analysis develops in the same manner with 2D model.

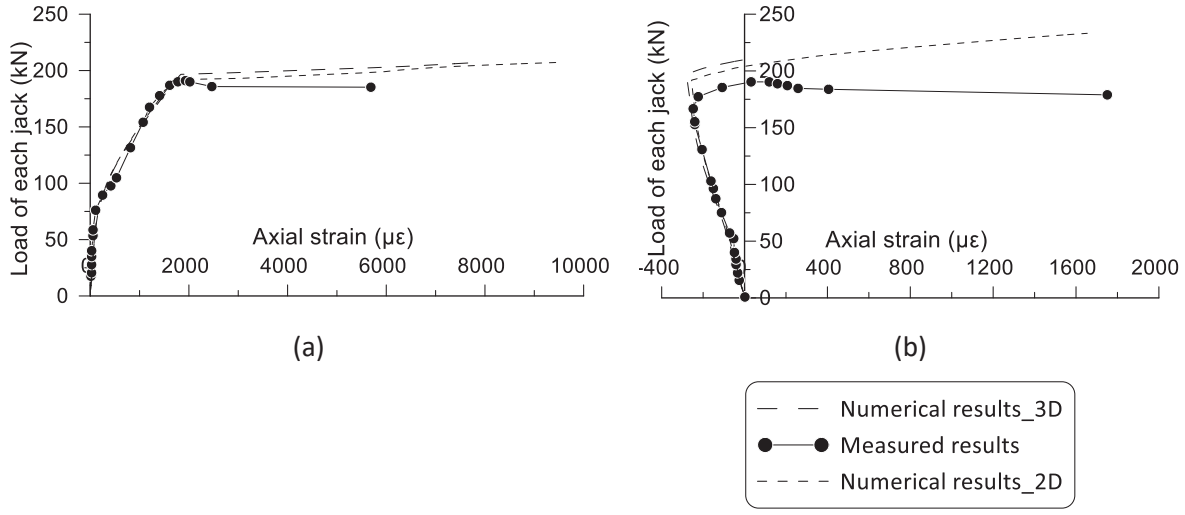
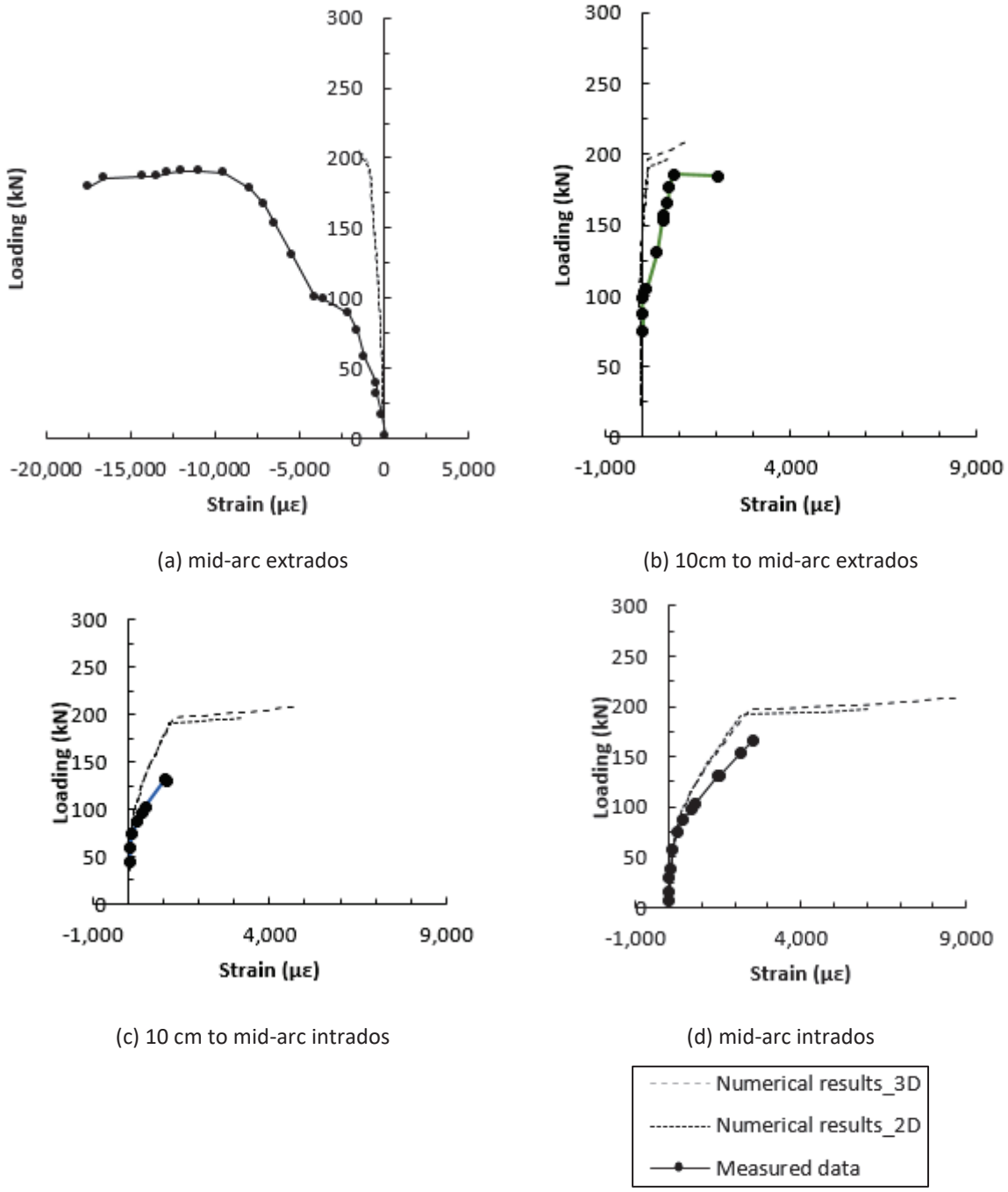


Figure 5.44: Axial strain of reinforcement at mid-arc position in 3D analysis: a) Lower reinforcement; b) upper reinforcement.

The evolution of horizontal strain of concrete at the mid-arc cross-section has also been output, and the strain data 'inside' the segment is available for 3D analysis. In fact, it has been found that the strain of the concrete with the same x and y coordinates but different depth in z direction still has the same value. For example, the strain on the side surface is the same with the one inside the segment at mid-width position at corresponding xy coordinates. The results are compared against the 2D and measured data as shown in Figure 5.45, and the overlapped curves of 3D and 2D analysis describing the strain evolution are presented.

Therefore, it is appropriate to measure the concrete strain with the strain gauge pasted on the side surface of the segment in the lab. It can also be concluded that 2D analysis has realised enough accuracy to reproduce the mechanical behaviour of the lining segment under loading.



(a) mid-arc extrados

(b) 10cm to mid-arc extrados

(c) 10 cm to mid-arc intrados

(d) mid-arc intrados

Figure 5.45: Horizontal strain of concrete at mid-arc position in 3D analysis: a) mid-arc extrados; b) 10cm to mid-arc extrados; c) 10 cm to mid-arc intrados; d) mid-arc intrados

5.7 Summary points

This chapter introduces the numerical study of an advanced concrete model by performing simulations of single segment tests. The research presented comprised:

- An introduction of the Modified Chen concrete constitutive model and of the strain softening constitutive model for steel reinforcement.
- Characterisation of the mechanical properties of C50 concrete and the HRB335 grade reinforcement from appropriate codes for both materials.
- Introduction of laboratory experiments performed on a single concrete segment that is used as part of DOT tunnel lining.
- Finite element analyses of two laboratory segment experiments for validation of the numerical model developed for the simulation of DOT lining segments.
- Detailed interpretation of numerical results and comparison with available measurements of lining deformation and mobilised stresses. Particular emphasis was placed on the development of cracks in the concrete and assessment of concrete and reinforcement stresses from intrados to extrados.
- Successful validation of the concrete numerical model for subsequent application in Chapter 6, for the advanced modelling of DOT concrete lining in the Shanghai Metro case study.

Chapter 6. Base case DOT tunnel analysis with advanced concrete model

6.1 Discretisation of the Shanghai case study with solid-element lining

This chapter introduces a new analysis of the base case study presented in Chapter 4, using an elasto-plastic modified Chen concrete model for characterising the tunnel lining. The case is based on DOT section of the Shanghai Metro Line 6, and the same boundary conditions and simulation configuration are followed. The concrete lining and reinforcement have been modelled with solid elements and bar elements respectively. The calibration of both materials has been completed and referred to in Chapter 5. In this simulation, only a 'half mesh' was built up for convenience (see Figure 6.1), following the symmetrical boundary conditions and the mesh geometry of the base case (see Figure 4.6 in Chapter 4). Therefore, the symmetry line, which is shown as the right side in the mesh, has the fixed horizontal displacement, zero force in the vertical direction (i.e. zero shear stress) and the impermeable boundary condition in this analysis. The bottom side has fixed displacement in both horizontal and vertical directions. Only horizontal displacement was fixed on the left side. The constant pore water pressure was prescribed on the bottom boundary and left vertical boundary. The phreatic surface was set up as 0.5m depth as shown in the figure.

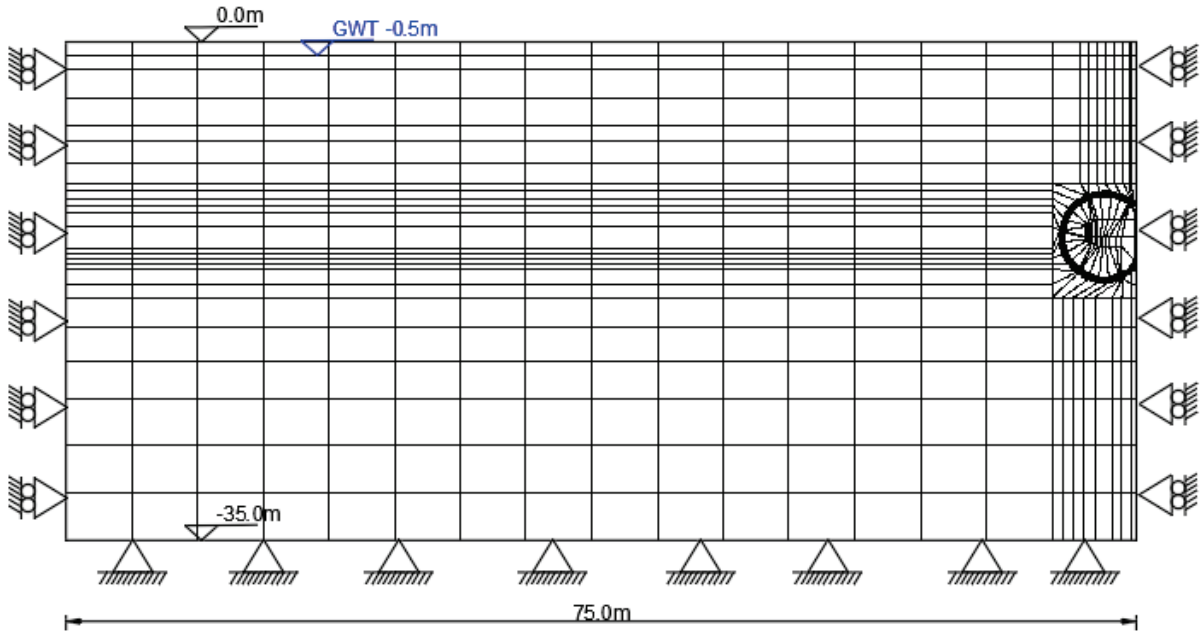
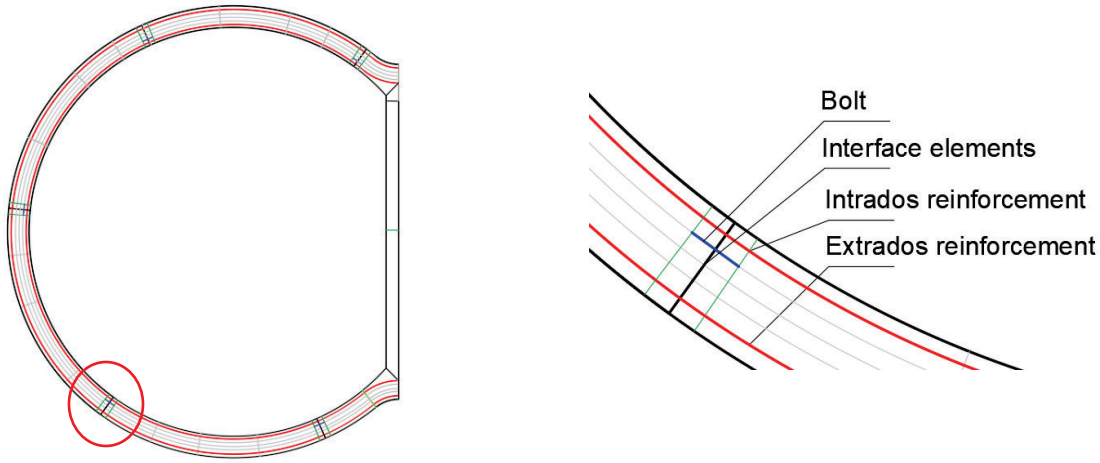


Figure 6.1: Two dimensional mesh for the base case analysis with solid element lining

The mesh section of half concrete ring consists of solid elements, which model the concrete, bar

elements, which model the reinforcement, interface elements, for the interface between the segments, and beam elements, to model the bolt connection between the segments, as shown in the detail of the lining ring in Figure 6.2. Figure 6.2b presents the detailed information of a segment interface circled in Figure 6.2a, indicating the relative positions and roles each element types played. Each concrete segment has 6 solid elements across the thickness in radial direction, and an interface element on each end. The reinforcements on extrados and intrados sides are modelled with bar elements coloured in red. The beam element, which is coloured blue, models the bolts for connecting the DOT segments in the circumferential direction. In this analysis, the deformation of the lining is expected to be small even after long term consolidation referring to the presented deformed shape (see Figure 4.15) in Chapter 4. Therefore, the lining ring was expected to stay at serviceability state, and consequently the plastic failure of the interface and bolt is unlikely to occur. Therefore, the beam elements modelling bolts are assumed elastic, and the linear properties are listed in Table 6.1.

Table *6.1*It is noted that the lining is set up impermeable (zero flow boundary), partially permeable and fully permeable from short term to long term. The zero pore water pressure condition along the intrados is prescribed after the construction of lining. The increase of permeability is realised by changing relative permeability value (RP) of the solid elements of lining following the incremental sequence introduced in Chapter 4 (Table 4.3, from 1%, 2%, 10%, 20% to 100%).



(a) (b)

Figure 6.2: Mesh details for the concrete lining. a) half DOT ring; b) detailed components at a joint.

Table 6.1: Linear properties of the bolt

Linear properties	Density (t/m^3)	Young's modulus (GPa)	Poisson's ratio	Cross-sectional area, A (m^2)	Moment of inertia, I (m^4)

Value	7.8	206	0.1	0.027	3.86E-5

It is noted that the realistic alignment of the bolts on the interface cross-section consists of two bolting sets as shown in Figure 6.3. The design of the triangular component enhances the stiffness of the bolting set against the bending moment at the interface. Therefore, the equivalent cross-sectional area and the moment of inertia was interpreted and given in the table. The position of the beam element is about 1/3 of the thickness from the intrados side as shown in Figure 6.2, where the centre of each bolting set shown. The length of the bolt is 20cm referring to the realistic data of M27 bolts applied in the base case, and the bolt is driven by 10cm into the segment on each side.

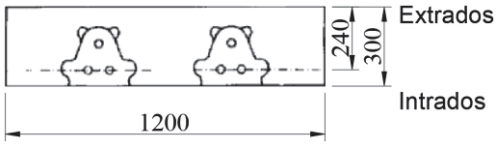


Figure 6.3: Alignment of the bolts on the joint

The alignment of reinforcements and the mechanical properties follow the data from the single segment test introduced in Chapter 5 (see Figure 5.9 & Table 5.1). The calibration of the main reinforcement is listed in Table 5.3, and the same softening plastic model has been used for characterising the nonlinear properties of the reinforcement bars. In fact, the reinforcements on either extrados side or intrados side is unlikely to develop yield stage under serviceability condition due to low deformation degree of the tunnel ring, but they are key factors that contribute to improving the overall stiffness of the lining ring in conjunction with the concrete.

The interface elements are introduced at the interface between two adjacent segments, and the higher stiffness *Ks* = 1E08 kN/m and *Kn* = 1E08 kN/m were determined to avoid the problem of unrealistic elements from adjacent segment 'overlapping' under the potentially high hoop forces. The bolt, which is modelled with beam element, crosses this element and hence has one shared node with the interface element on each side (see Figure 6.2b), while not having the physical bolt between those two nodes. Therefore, the respective displacement and rotation degrees of freedom at the two opposite nodes were tied together to enable the continuity of the bolt, as demonstrated in Figure 6.4.

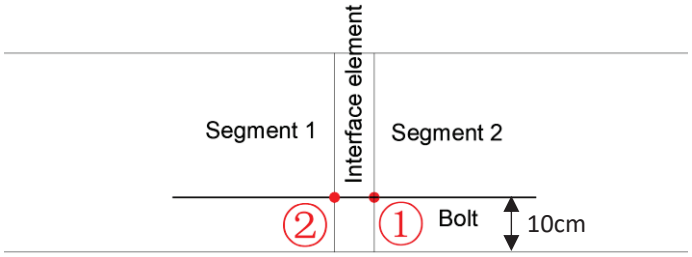


Figure 6.4: Tied degrees of freedom for the nodes 1 and 2.

The major material of the segment is the C50 grade concrete, as introduced in the previous chapter, and the modified Chen concrete model was used for its characterisation. The calibrated parameters for this model are listed in Table 5.3. The numerical simulation of single segment test performed demonstrated very good agreement against the measured data in the laboratory, especially for the early stage of the loading, when both the concrete and the reinforcement stays elastic. Therefore, the model and the calibration are considered reliable in this analysis for the lining under serviceability state.

6.2 Comparison of the results against beam-element lining

6.2.1 Ground response induced from tunnelling

The same sequence of tunnelling as shown in Table 4.3 Chapter 4 was followed. The excavation was carried out over 50 increments and the incremental supporting stress was applied along the tunnel boundary. The hydraulic boundary conditions are the same as in the base case analysis in Chapter 4. The objective for this simulation is to investigate the difference of the ground response and internal lining forces between the simple beam elements using elastic model and the solid elements using modified Chen concrete model.

The ground settlement of the model with concrete lining evolves almost into the same shapes as those in the base case analysis using beam elements, at 100 days and 1000 days after DOT tunnel excavation, as shown in Figure 6.5a. The maximum settlement of the solid lining is a little bit larger than that of the beam elements lining, most likely due to the difference in mesh size, since the 'half mesh' in this analysis is 75m wide whilst the half width for the base case analysis is 50m, as introduced in Chapter 4. The comparisons on subsurface settlements at 100 days after excavation at different depths are presented in Figure 6.5b, c & d. The long term settlement curves in Figure 6.6, when the lining is assumed fully permeable, also show similar maximum settlements and the width of inflection point between two types of elements. The difference of mesh size accounts for the larger maximum settlements in the analysis with solid element lining, beyond the distance of 25m from the tunnel central axis. This influence of the mesh size on the settlement trough for fully permeable lining is

expected and has also been discussed in Chapter 4.

Generally, the agreement of both curves indicates that the change of element form for modelling the lining from beam to solid elements, with calibrated reinforcements, does not affect the ground response.

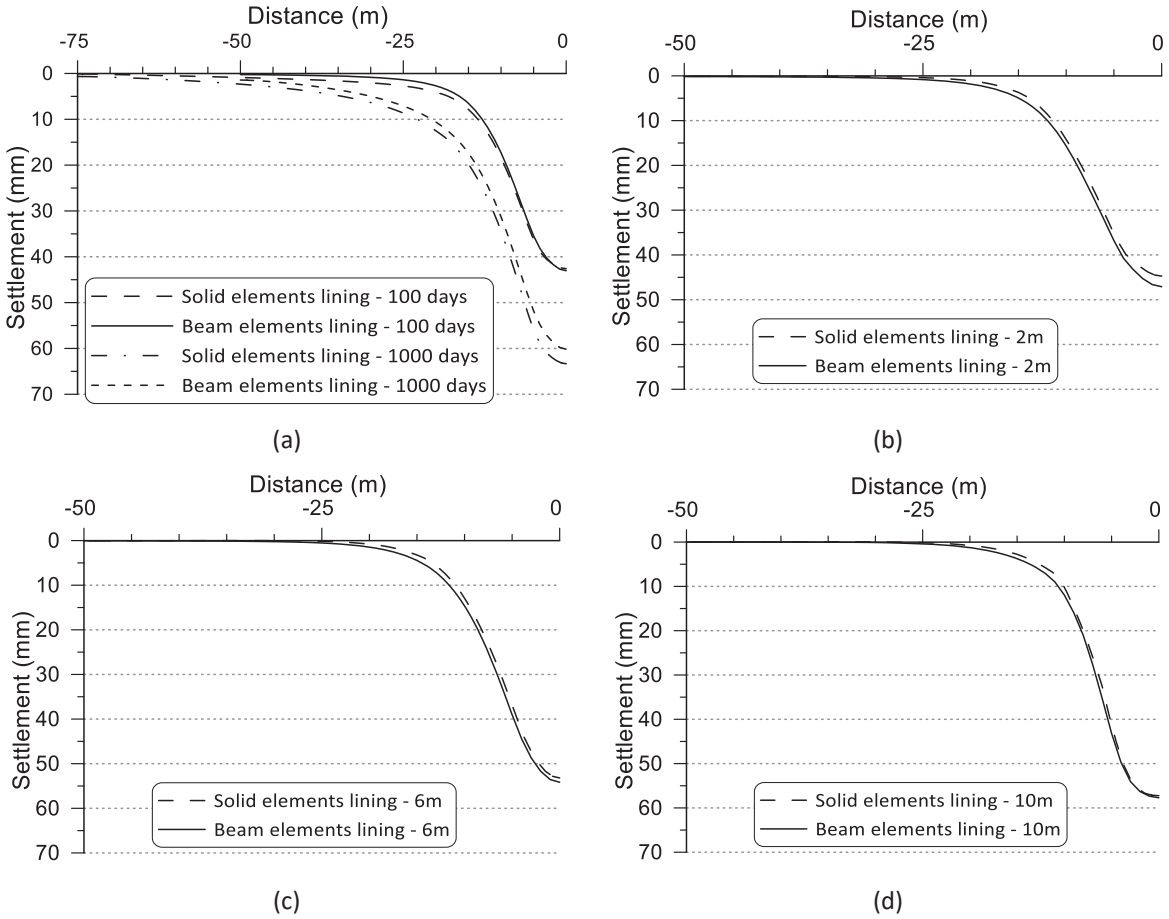


Figure 6.5: Comparison of ground settlement using two element types for modelling the DOT lining. a) surface settlement at 100 days and 100 days after excavation; b) 2m depth settlement at 100 days after excavation; c) 6m depth settlement at 100 days; d) 10m depth settlement at 100 days.

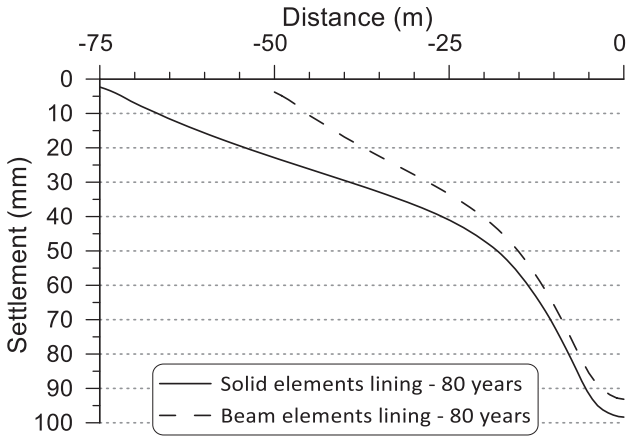


Figure 6.6: Comparison of long term settlement between two element types lining.

6.2.2 Internal forces of the lining

The distribution of bending moment along the lining, which is relevant to the distorted tunnel shape and the risk assessment, is interpreted in Figure 6.7. In this analysis, the bending moment on the cross-section of the lining segment is calculated from the integrated hoop stress distribution across the thickness of the segment. The results of bending moment distribution at representative short term (100 days, Figure 6.7a) and long term (80 years, Figure 6.7b) stages validate that the solid element lining shows similar values and distributions of the bending moment compared to the beam element lining. The maximum value in long term still occurs at the distance about 7m, where the interface (joint) number 3 is located. As for axial forces, the solid element lining performs smaller axial force in both short and long term (see Figure 6.8).

As mentioned in the parametric study of the joint stiffness in Chapter 4.3.2, the relatively softer joints compared to the concrete segment lead to the decreasing bending moment and axial force (see Figure 4.20). In this analysis, the results show sufficient stiffness of the joint modelled with bolts and interface element characterised with realistic design data since the bending moment is not significantly reduced (about 25% reduction in peak values). From the view of axial force, the solid elements lining also seems a little softer compared to elastic beam elements (also reduced by about 25% in peak value), implying softer joints and segment material has been modelled. This stiffness reduction may be explained by the elasto-plastic characteristics of the modified Chen concrete model, which shows stiffness degradation under loads. It indicates that the assumption of the elastic ring in the base case analysis is appropriate although some deviation of stiffness may develop. It is also noted that the positions with higher bending moment are at the distance about 0m, 3m, 7m, 11m and 15m, where exactly the joint number 1, 2, 3, 4 and 5 locate (see Figure 6.7 & Figure 6.8). Therefore, the construction of the lining following staggering rule, which avoids a continuous joint in the longitudinal direction, is

necessary to lower the risk of joint opening.

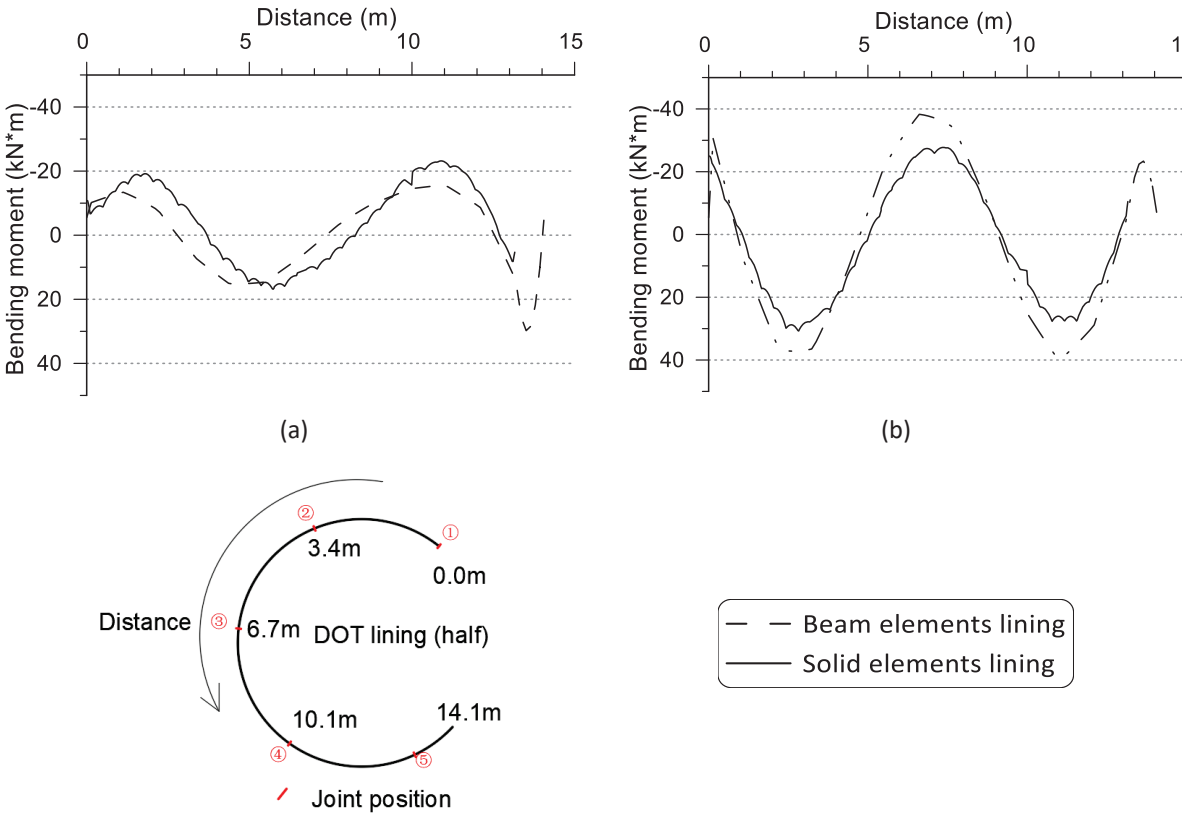


Figure 6.7: Bending moments along the distance curve. a) 100 days; b) 80 years.

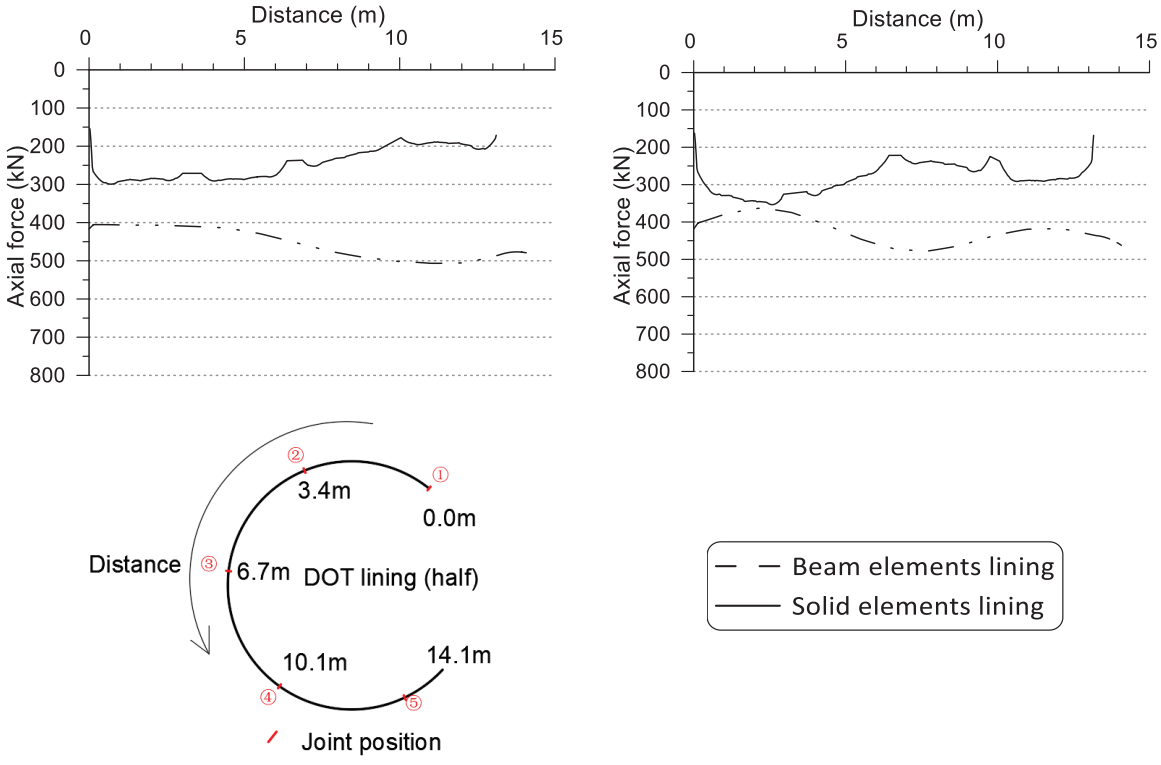
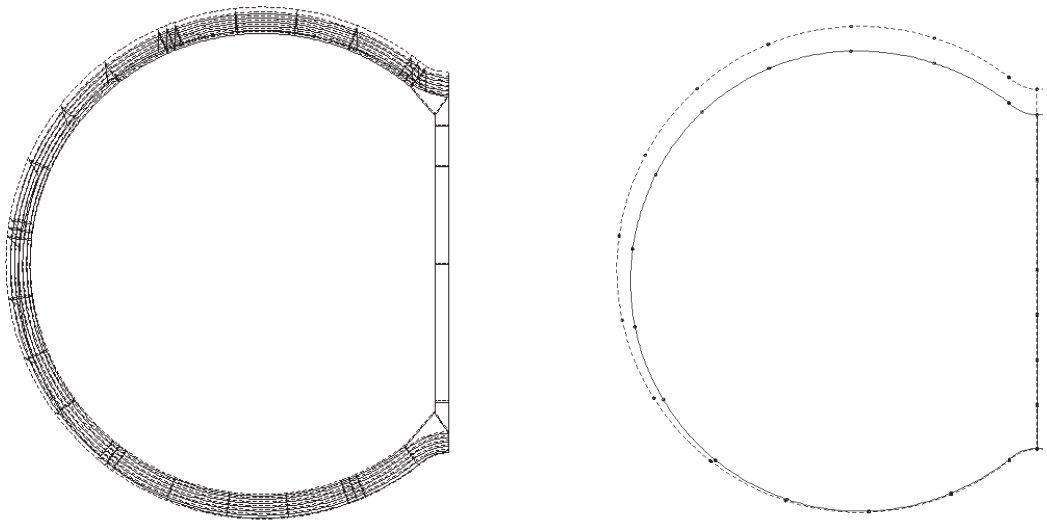


Figure 6.8: Axial forces (hoop force) along the distance curve. a) 100 days; b) 80 years.

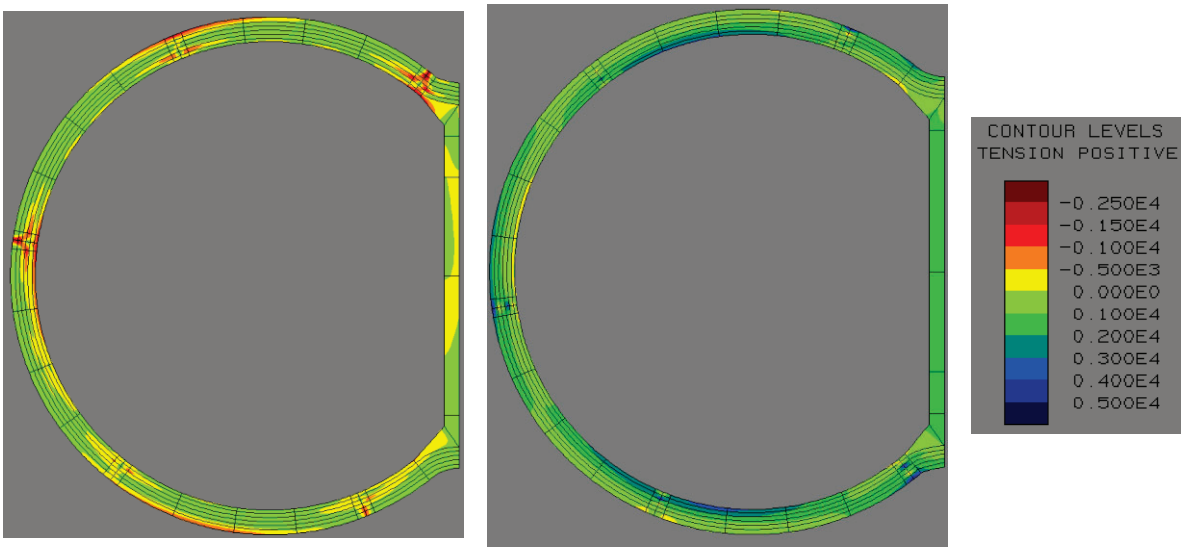
The corresponding comparison of the distorted shape of the lining after long term consolidation (80 years) is presented in Figure 6.9. It can be seen that both element types show a similar manners of 'squatting' deformation, supporting the occurrence of a larger bending moment at the spring-line position of the lining (joint number 3 in Figure 6.7a).



(a) (b)

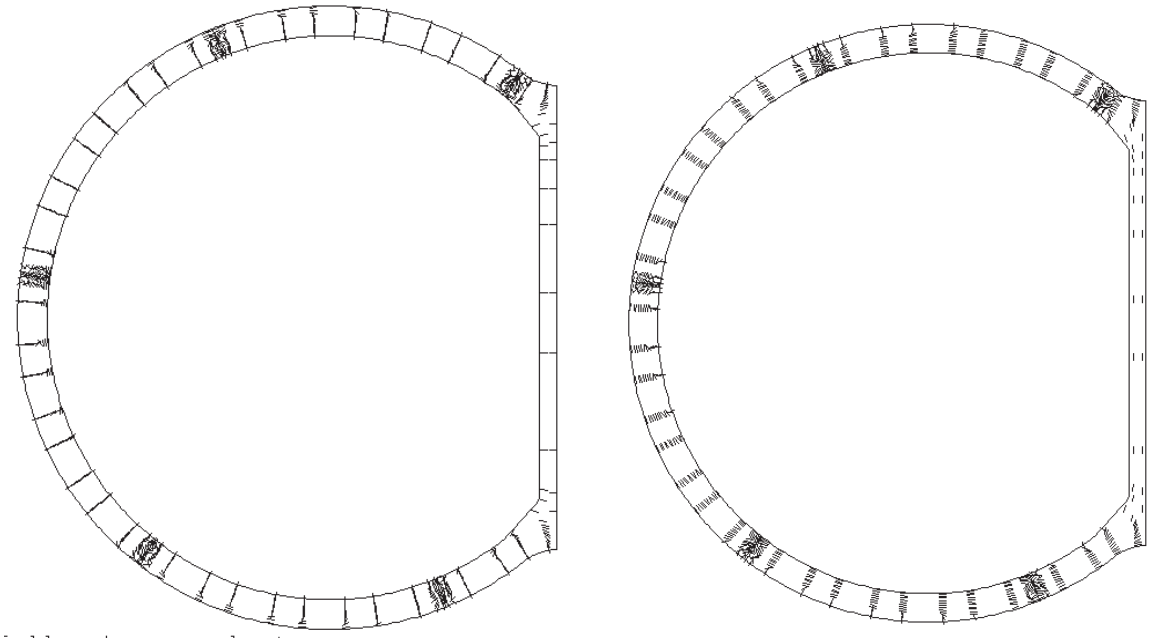
Figure 6.9: Lining deformation at 80 years after tunnelling. a) Solid-element lining; b) Beam element lining (dotted line – original lining geometry; solid line – deformed geometry)

The contours of major principal stresses reflecting the stress state after long term consolidation are shown in Figure 6.10, and the orientation of the stresses, represented by short bars are plotted in Figure 6.11. It can be seen that the tensile stress, which is notifies as σ_1 (due to tension +ve sign convention), shows larger value at positions of joint 1, 3 and 5 on their extrados side, while the compressive stress, which is notified as σ_3, is larger on the intrados side of the corresponding joints. Therefore, it can be concluded that the stress concentration still occurs at the joints despite the sufficient stiffness of the bolts. The risk of joint opening and concrete crashing failure should be of concern at the extrados and intrados sides of these positions. Meanwhile, the maximum major tensile stress reached almost 5MPa (see Figure 6.10a), and this reveals the higher risk of concrete cracking on the intrados side of tunnel crown and invert considering the peak tensile strength of C50 concrete is only 4.1MPa according to the calibration in Chapter 5. In general, the solid element lining model presents intuitive information of the stress distribution and provides convenience for risk assessment and design guidance of the lining.



(a) σ_3 (b) σ_1 Unit: kPa

Figure 6.10: Contours of principal stresses at 80 years. a) major (compressive) principle stress σ_3 ; b) minor (tensile) principle stress σ_1



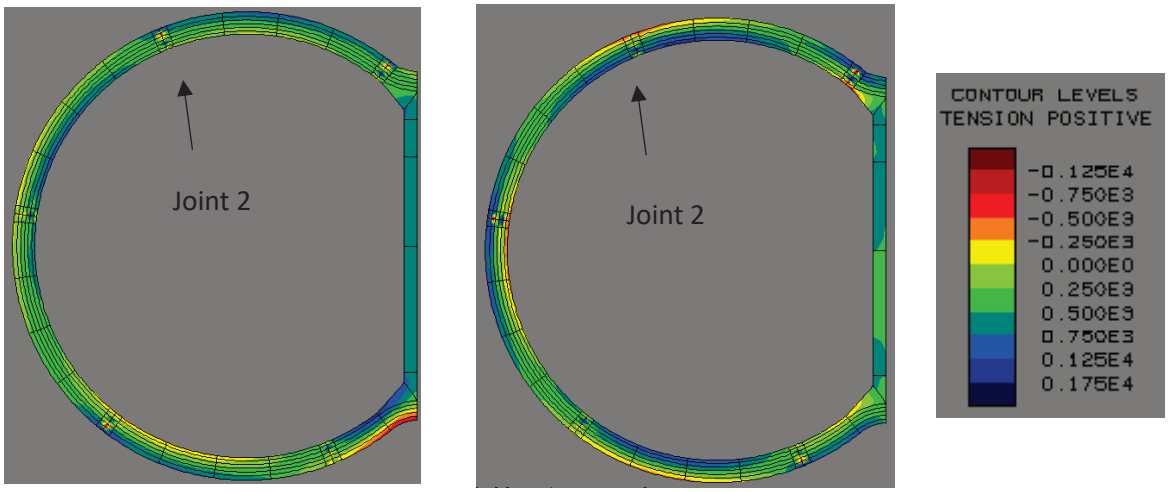
(a) σ_3 (b) σ_1

Figure 6.11: Orientations of principal stresses at 80 years. a) major (compressive) principle stress σ_3 ; b) minor (tensile) principle stress σ_1

A comparison of mean effective stress p' and deviatoric stress J between short term (represented by 100 days) and long term (represented by 80 years) are shown in Figure 6.12 & Figure 6.13. Corresponding to the change of distribution of bending moments in Figure 6.7, the distribution of both stresses in the lining also achieve significant change. For example, the bending moment on joint number 2 is almost zero at 100 days while a large negative value is reached at 80 years, the latter of which performs high tensile stress (positive value defined in this plot) as shown in Figure 6.12b. The

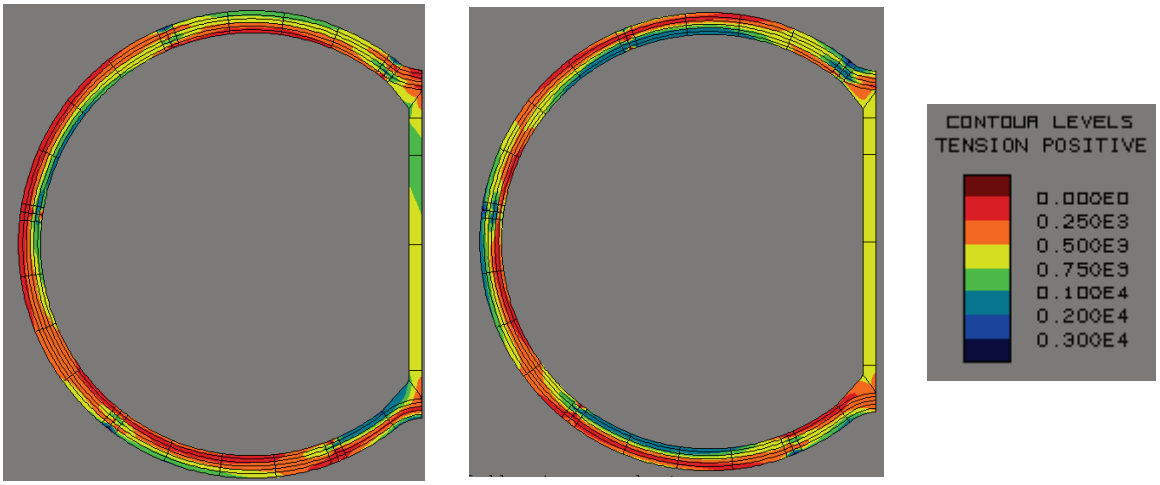
similar trend of deviatoric stress transformation on Joint 2 is also followed.

The change of stress level, which shows the degree of the stress state normalised by the ultimate stress level, also indicates that the material at joints are more likely to occur failure in long term (see Figure 6.14b), whereas only 20%-40% of the concrete strength is utilised for most parts of lining. In short term (100d), the intrados side of the lower seagull segment seems to undertake higher stress. In general, the long term results highlight the occurrence of higher stress on joints positions, and that should be an important concern in the design of lining.



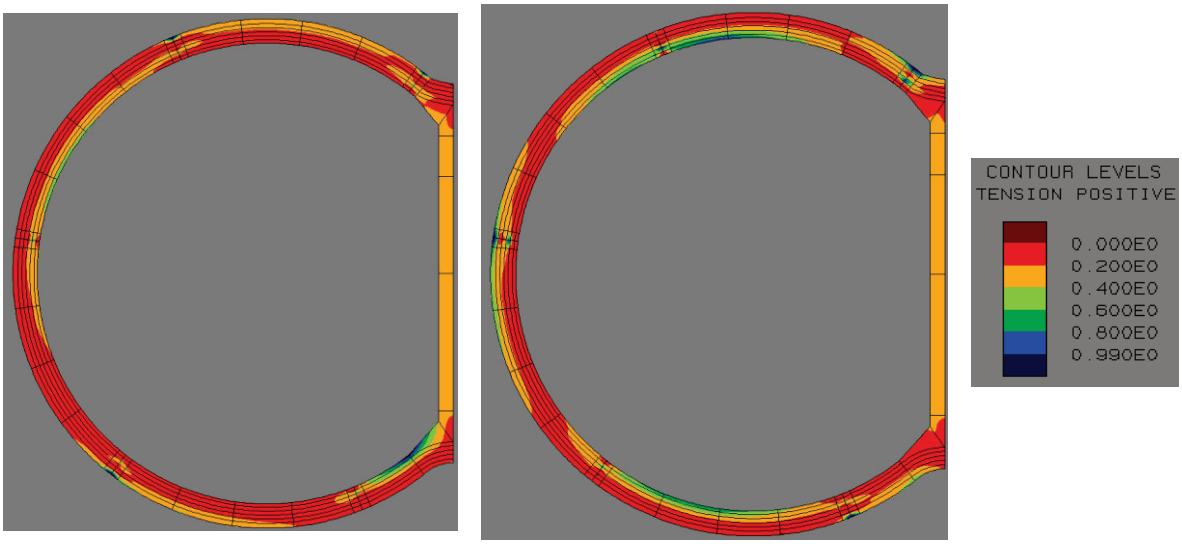
(a) 100 days (b) 80 years

Figure 6.12: Mean effective stress p' (positive in tension). a) 100 days ; b) 80 years



(a) 100 days (b) 80 years

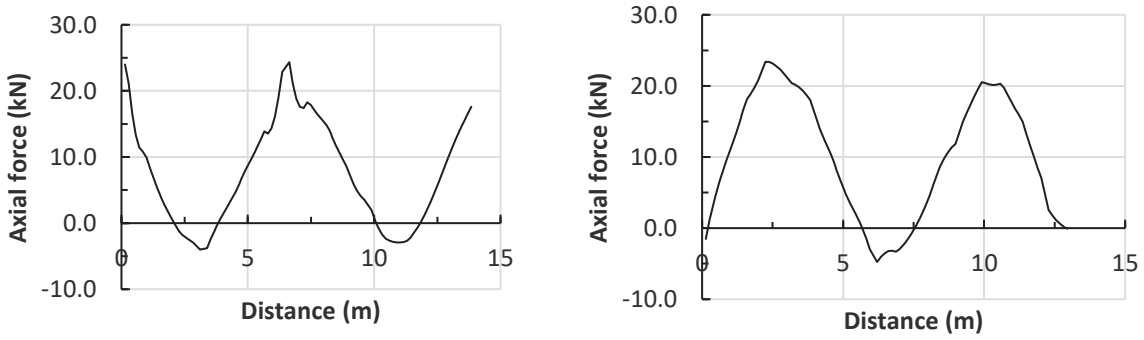
Figure 6.13: Deviatoric stress J. a) 100 days ; b) 80 years



(a) 100 days (c) 80 years

Figure 6.14: Change of stress level. a) 100 days; b) 80 years.

The characteristics of the bending moment distribution can also be inferred from the axial force in the reinforcements (Figure 6.15, +ve: tension). It can be seen form Figure 6.10(a) that the axial force distribution in the extrados reinforcement is tensile at joint number 3). The value is much lower than the peak axial force calibrated for the material (629kN, see Table 5.3 in Chapter 5). The mobilised axial force in the intrados reinforcement is of the opposite sign to that of extrados reinforcement, as expected. The reinforcement plays important role in the tensile resistance of the lining on the tension side of the bending moment while the concrete undertakes the compressive stress on the compression side.



(a) (b)

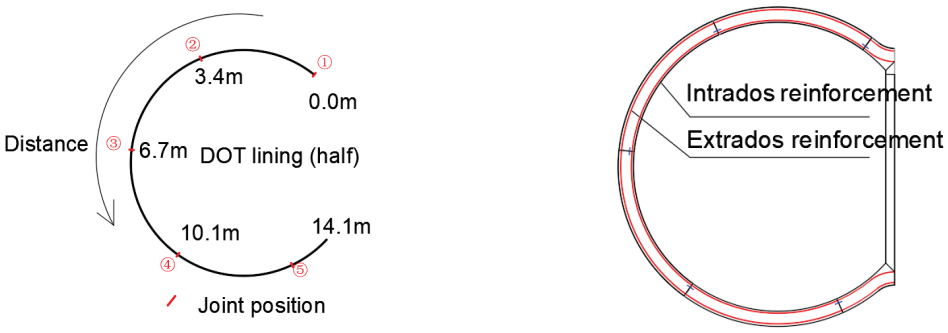


Figure 6.15: Axial force of reinforcement. a) Extrados reinforcement; b) Intrados reinforcement.

The internal forces in bolts have been output for validating the working state of bolts at 80 years after tunnelling. Each bolt is of 20cm length, and axial forces and bending moments are shown in Figure 6.16. The joint position is located at the distance of 0.1m (i.e. the mid-length of each bolt), where the maximum axial force and bending moments occur. It can be seen that the bolts number 1 & 3 undertake significantly higher bending moment (in absolute terms) and the peak values for bolt 1 and 3 are close, which matches the distribution graph in Figure 6.7. However, the bolts only take part of the bending moment resistance of the cross-section (Table 6.2), and the contribution from the concrete segment on the interface cannot be neglected. Table 6.2 compares the 'resultant bending moment' values at each joint calculated from the whole cross-section (Figure 6.7b) and the values taken by bolts. The 'percentage' indicates the percentage of the bending moment carried by each bolt.

Table 6.2: Proportion of bolts contributing to the bending resistance

Joint number	**1**	**2**	**3**	**4**	**5**
Resultant bending moment (kN*m)	-25.0	26.0	-26.2	16.5	-6.5
Bending moment undertaken by bolts (kN*m)	-12.5	5.4	-11.5	0.6	-2.22
Percentage (%)	50	21	44	3.6	34

As for axial force, all bolts are mobilising tensile force whereas the concrete resists compressive loads. It can be seen from Table 6.3 that the bolts at the positions of joints, where the joint opening is likely to occur on the extrados side (e.g., Joint 1, 3&5) and the bending moment are negative (see Figure 6.7b), undertake smaller axial force, whereas the joint opening on intrados side (e.g., Joint 2) shows much larger tension of bolts. On each interface of joint, the equilibrium among axial force, bolts tension and the concrete compression should be reached. The difference of tension values among bolts is expected according to the bending moment distribution.

Table 6.3: Contributions of bolts and concrete on joints to the axial force resistance

Joint number	1	2	3	4	5
Axial force (kN) (-ve: compression)	-162.3	-322.0	-221.7	-239.7	-168.1
Axial force undertaken by bolts (kN) (tensile)	221.1	326.5	153.4	237.1	155.2
Axial force undertaken by concrete (kN) (compressive, negative sign)	-383.4	-648.5	-375.1	-476.8	-323.3

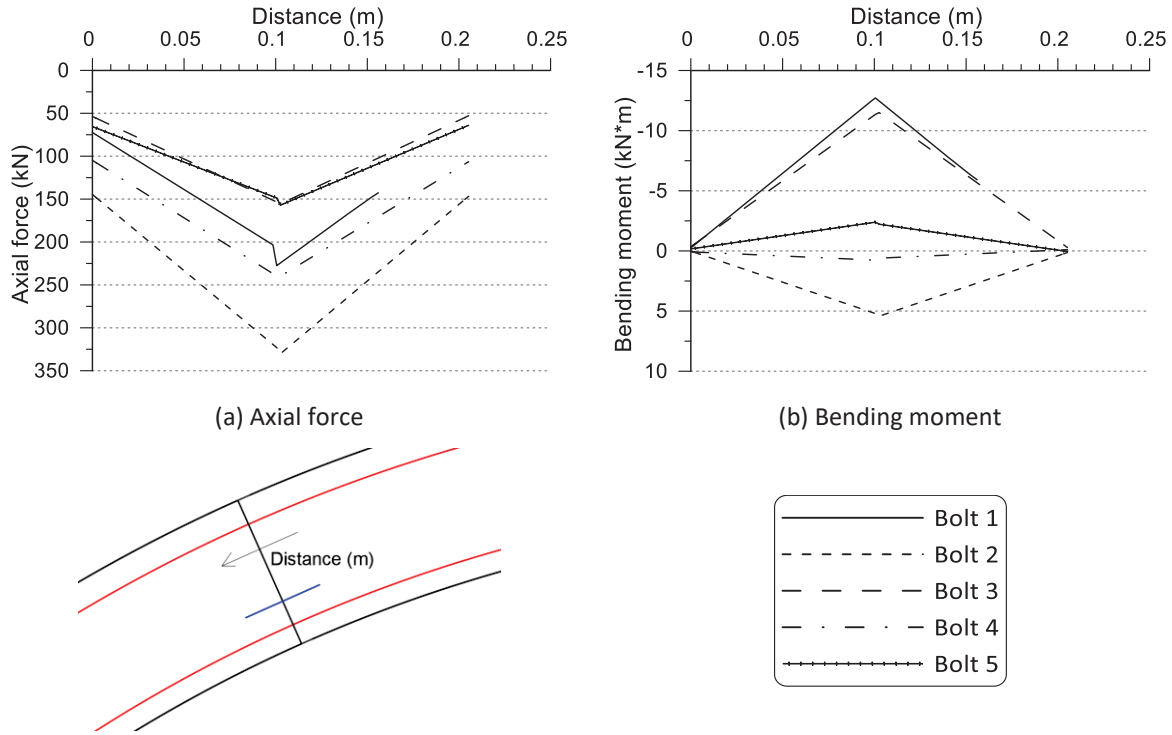


Figure 6.16: Internal force of the bolts. a) Axial force; b) Bending moment.

A trial test was carried out to investigate the lining force reaction from 'softer bolts' by adjusting their Young's modulus to 1/100 of the original value. Following the same boundary conditions and other calibrated values of parameters of bolts as listed in

Table 6.1, the resultant bending moment shows significant reduction along the lining at 80 years after tunnelling (see Figure 6.17) whereas the axial force stays almost the same. This trend is comparable with the results from sensitivity study in Chapter 4.3 (see Figure 4.20e), implying a similar mechanical behaviour of the lining with softer joints condition. However, further trial analysis found that the bending moment does not decrease further for even softer bolts (e.g. 1/1000 or 1/10000 of the original stiffness), showing the different sensitivity from the beam element lining, in which the moment decreases to zero for very soft joints. This could be explained by the characteristics of the solid element lining that a minimum value of bending resistance is still retained due to the existence

of the solid segment connected with interface element, of which the normal stiffness is characterised. The bolting system only contributes part of bending resistance of the lining. Therefore, the stiffness of the joint is dependent on both bolts and the concrete material, and the stiffness reduction cannot be simply understood or equalised as the lower Young's modulus of the bolts.

The comparison of stress levels, which show how close the material is to the failure state, between original stiffness of bolts and of softer bolts is given in Figure 6.18. It is apparent that the softer bolts result in larger stress levels mobilised at joints, and even in short term at 100 days, some parts of joints are approaching failure.

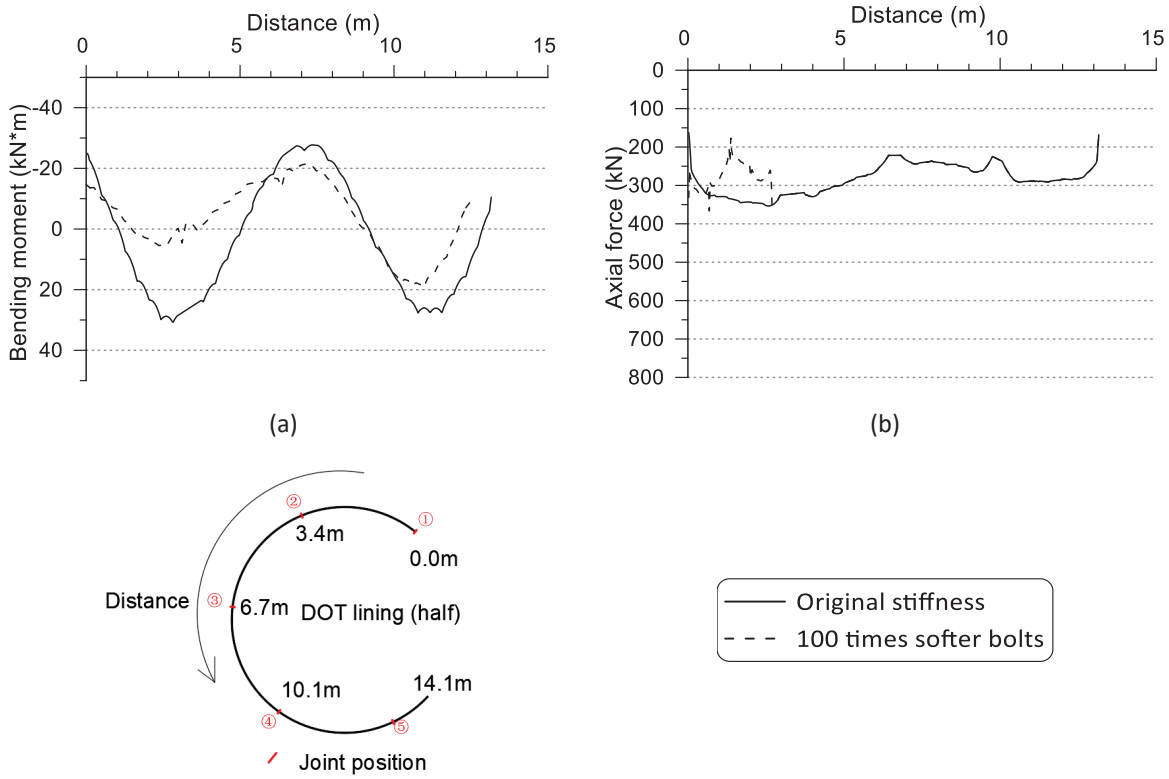
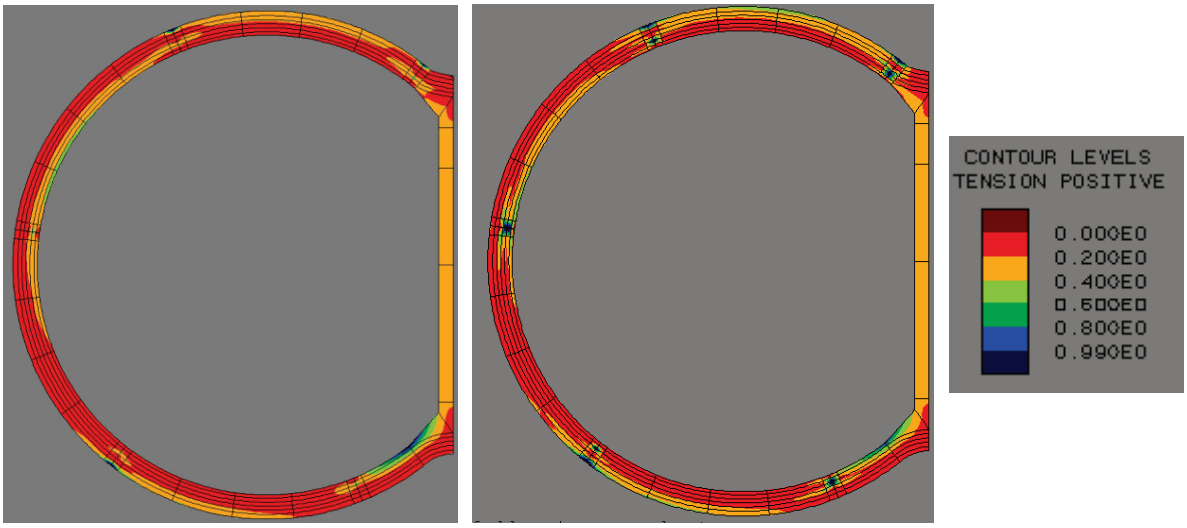


Figure 6.17: Comparison on bending moment between original and softer bolts (80 years). a) bending moment; b) axial force



(a-1) original stiffness (100d) (a-2) 100 times softer bolts (100d)

(b-1) original stiffness (80y) (b-2) 100 times softer bolts (80y)

Figure 6.18: Comparison on stress level between original and softer bolts. a) 100 days; b) 80 years.

In general, the application of modified Chen concrete model in the characterisation of DOT tunnel lining has reached good agreement with the base case analysis, where the beam elements were employed for the modelling of segments. The elastic ring assumption in some simulations of tunnelling, regardless of the existence of joints and the lining thickness, does not affect the ground response induced by tunnelling. It is noted that the lower joint stiffness has been found causing significant effect on the overall stiffness of the lining ring.

Hu & Zhang (2007) also pointed out that the elastic ring assumption may overestimate the overall stiffness of the lining, and consequently, the resultant bending moment is over-predicted. They introduced a reduction factor for the overall stiffness ($\eta = 0.7$) of the DOT lining considering the softer joints compared to the concrete segment. However, on the other hand, the staggered form for lining

construction, which avoids the continuous joints in longitudinal direction, enhances the unity of the multiple rings. Liu et al (2020) carried out laboratory tests on a single lining ring and multiple rings assembled in staggered form. They found that the joint opening and cracking occurs more often for single ring, while plastic hinge firstly appears on the segment body for multiple rings with strong staggered effect. That indicated the full utilisation of the segment strength in the ultimate condition for staggered multiple lining. Hu & Zhang (2007) proposed that the bending moment increases by about 30% due to the staggered effect of the DOT lining via analytical calculation. Yuan et al., (2005) revealed that the staggered effect may be not obvious for stiffer joints, and the overall stiffness is limited to a certain value instead of infinitely growing even stiffer joints are applied.

6.3 Summary points

This chapter presents analyses of DOT tunnelling where the lining was simulated with an advanced elasto-plastic concrete constitutive model and with its physical thickness in the mesh. The comparison of the results is made against the results from a similar analyses in which the lining was simulated with elastic beam elements. The broad agreement between the two types of analysis showed that:

- the numerical model of the lining presented in this chapter was capable of accurately taking account of the reinforcement in the concrete segment and of the bolt connection between the segments.
- the results of the two types of lining discretisation were broadly in agreement, but the analysis of the elasto-plastic concrete lining was able to demonstrate the mobilisation of the critical parts of lining with time.

Chapter 7. Study of Twin tunnels and DOT in stiff clay

7.1 Introduction

The DOT tunnelling in the Shanghai area, in the soft clay ground conditions, was simulated in Chapter 4 by using an extended modified Cam Clay (MCC) model for the soil and good comparison was demonstrated between the measured and predicted ground movements. The model was primarily extended by the incorporation of a nonlinear small strain stiffness formulation inside the MCC yield surface. In this chapter, the objective is to perform exploratory studies on the application of the DOT technology on tunnelling in stiff clays. For this purpose, two case studies of tunnels in London Clay were utilised, for which the measurements of ground movements were available.

This chapter first reviews the main characteristics of London clay and of ground conditions at the two sites in London. One site was located at St James' park and was associated with the tunnelling works on the extension of the Jubilee Line of the London Underground metro network. The second site was located at Hyde Park and was associated with the tunnelling works on the Crossrail underground rail line. The twin tunnel simulations for both sites were originally carried out by Avgerinos (2014), Avgerinos et al. (2016) and Avgerinos et al. (2018), using the same finite element software ICFEP (Potts & Zdravkovic, 1999). These studies utilised a modified 2-surface kinematic hardening constitutive model, M2-SKH (Gramatikopoulou et al. 2006), for the simulation of the London clay behaviour.

This chapter briefly presents the M2-SKH constitutive model and repeats the analyses performed on the tunnels constructed at the two sites with the conventional twin-tunnel technology. New analyses are then presented where twin tunnels were replaced by DOT technology. The predictions of DOT-induced ground movements are compared against the measurements and predictions of the two twin tunnelling cases, to quantify the effect of the DOT tunnelling method.

7.2 Ground conditions in London

London clay has experienced marine deposition in a subsiding chalk basin over 30 million years BP (Katherine et al., 2012; Hight et al., 2003). The Lambeth Group formed beneath contains clay, sand and silts. It is believed that the feature of high over consolidation is caused by a massive erosion of overlying sediments over late Tertiary and Pleistocene times. The eroded thickness is, depending on the position, about 150 m in Essex (Skempton, 1961) and 300 m in the Wraysbury (Bishop et al, 1965). This process has significantly influenced the mechanical behaviour of the London clay as the loading-unloading stress history has led to stiffness anisotropy and high coefficient of lateral earth pressure at rest, K_0. Atkinson et al. (1990) pointed out the influence of stress path on the stiffness by testing

reconstituted samples with particular emphasis at small strain range, while Clayton & Heymann (2001) showed the differences in stiffness degradation at larger strain. The latter took creep into account on the influence of stress history, as longer resting time between the stages of their tests led to re-initialisation of the higher stiffness before shearing. It is introduced later in the chapter that this behaviour could be represented by re-centring the stress state in a 'bubble' using M2-SKH model. Gasparre et al. (2007b) have additionally investigated the engagement of a yield surface Y2 (Jardine et al., 1991) on the stiffness response. They discovered that the stress state engaging Y2 surface resulted in stiffness dependency on the stress history when the creep could be neglected. Therefore, the corresponding stress path needs to be considered and modelled properly in numerical research. The necessity of stress history reproduction was also highlighted and discussed in the numerical modelling by Avgerinos (2014).

King (1981) identified 5 lithological units in the profile of London clay, from A to E, above the Woolwich and Reading Beds (presently known as Lambeth group), identified with different grain size distribution and micro-fauna. The divisions are following depositional sequencing at different stages under the corresponding geological environment, which implies difference of geotechnical properties of the soil in each layer. For simplicity, key mechanical properties such as angle of shearing resistance, unit weight and stiffness related characteristics are assumed constant within the London clay layer in this study.

Standing (2018) suggested that the identification of London clay divisions and sub-divisions could be realised with measurements of characteristics such as water content, Atterberg limits, clay content and activity, mineralogy, SPT and CPT testing. The data given in the study has revealed the transition of water content at the interface of adjacent divisions. A smaller change can also be observed for a sub-division interface. That supports the overall observation that the formation of London clay was completed over different depositional cycles.

The London clay is mainly lying above Lambeth Group, and only divisions of A and B are found in central London, for example, at St James' Park (Standing 2018). A ground profile of this tunnelling site was depicted in Avgerinos (2014), referring to borehole logs given by Nyren et al. (2001) and the data from the site at Heathrow T5 (Height et al., 2007). Similar division and sub-division are presented by Standing and Burland (2006) based on St. James' Park borehole data, with specific identification of water content.

For the numerical modelling in this chapter, the bottom of the mesh is at the depth of 52.5m below the ground surface, where A3 division is extending to, and the A3 unit is not sub-divided for the lack of data and the variance is deemed causing small influence on the results. Therefore, the ground

profile presented by Avgerinos (2014) is adopted in this study for both twin tunnels and DOT tunnel simulation (see Figure 7.1 and Figure 7.2 for twin tunnels simulation).

In the case of Crossrail tunnel constructed in Hyde Park, the twin tunnels are lying at the same depth of 34.2m. The site has similar ground divisions with St. James' Park, and the tunnels are lying in the layers of London clay B2 and A3 units.

The ground water profiles of both cases adopted for the modelling phases after geological history are shown in Figure 7.3. The profile of pore water pressure is assumed hydrostatic after the modelling of geological history, which is the first stage of the simulation, and is established after the sedimentation of top layers (Terrace gravel, made ground/Superficial deposit). In Jubilee Line Extension case at Saint James' Park, the water table lies at the top of Terrace gravel layer, and this prescribed ground water profile at both sides of mesh stays unchanged during the simulation. In the ground of Hyde Park site, however, there was a procedure of underdrainage taking place after the geological history due to ground water pumping in the Lambeth Group, and during this phase the distribution of pore water pressure changed from hydrostatic to the shape shown in Figure 7.3, featured with decreasing in the London clay unit A2 and upper Lambeth Group. This underdrainage is believed caused by the pumping of ground water in deeper aquifer over 70 years and the equilibrium condition has been reached due to very long time for consolidation (Avgverios, 2014), which will also be reproduced in the modelling.

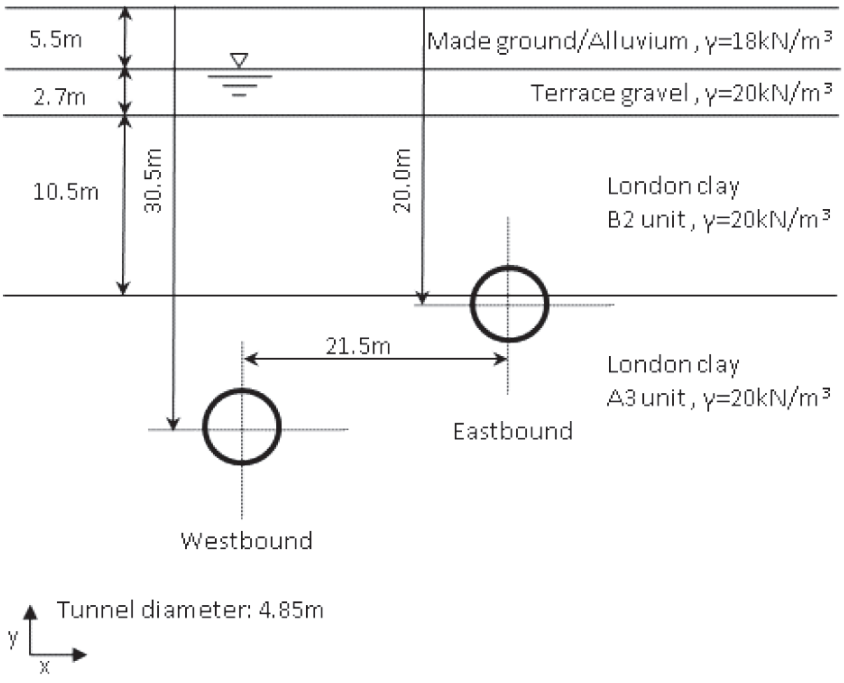


Figure 7.1: Ground profile and twin tunnel boring position at St. James' Park adopted for numerical modelling (Avgerinos, 2014)

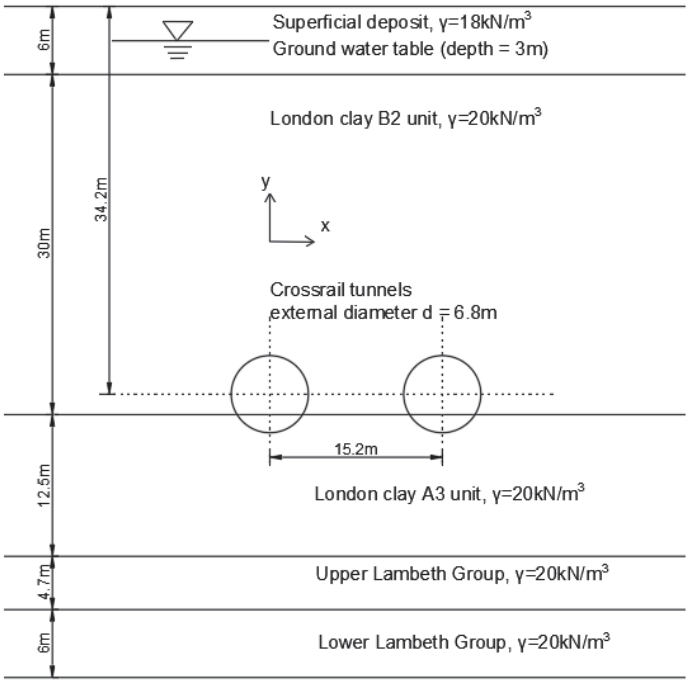


Figure 7.2: Ground profile and twin tunnel boring position at Hyde Park adopted for modelling

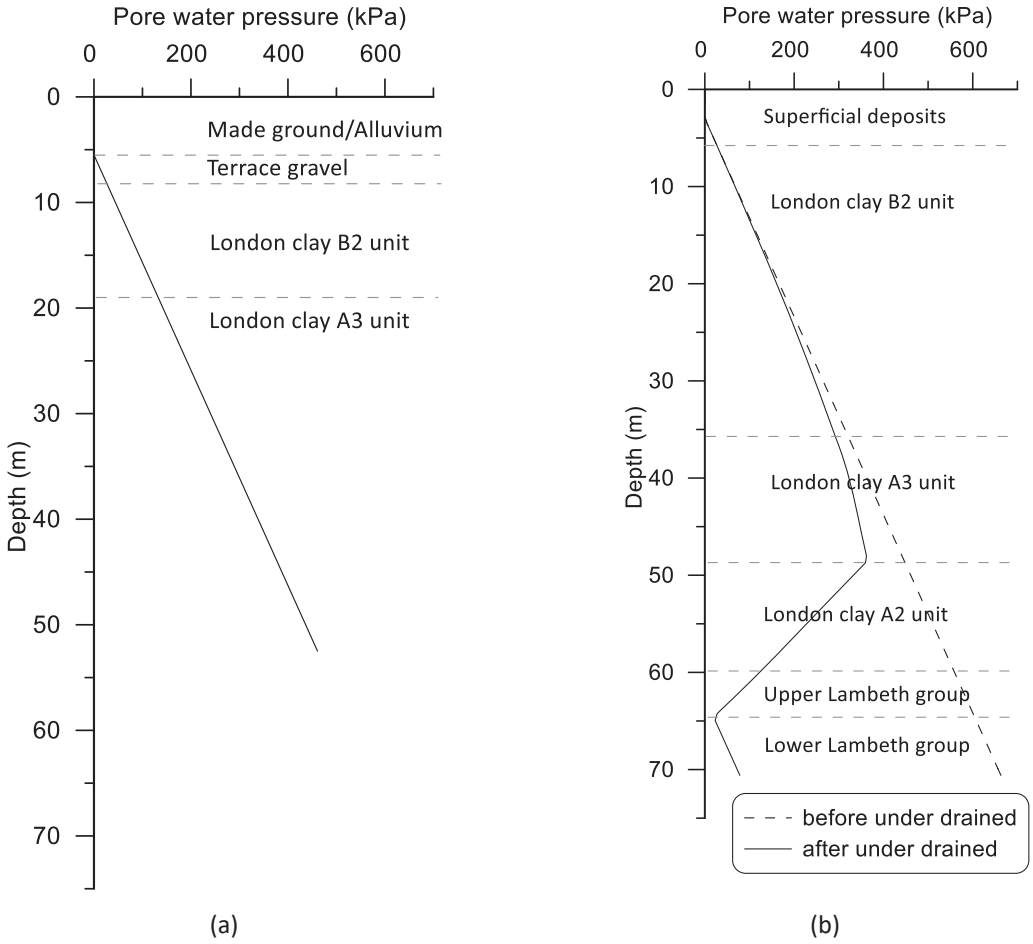
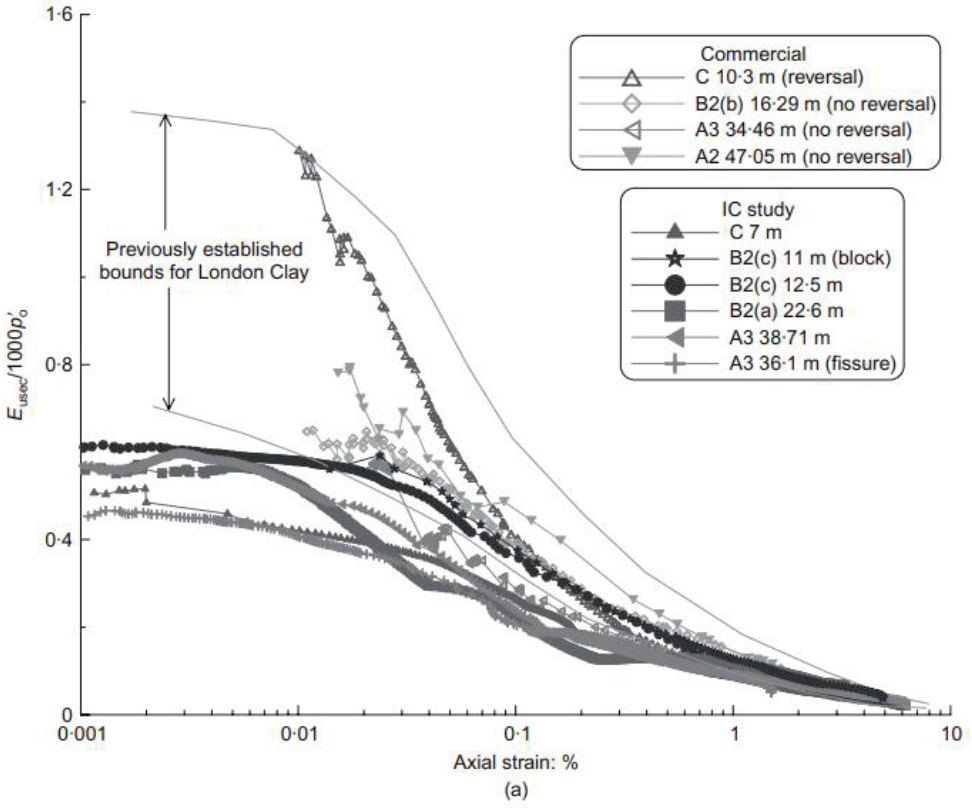


Figure 7.3： Ground profile and pore water distribution of (a) St. James' Park; (b) Hyde Park

7.3 Main characteristics of London clay

The stiffness degradation at small strains is dominant factor for the accurate assessment of ground movements due to tunnelling. The effects of recent stress history and changes in stress path direction were also highlighted in the testing of London clay as important in the small strain stiffness characterisation. A systematic laboratory testing of London clay specimens from Terminal 5 site at Heathrow Airport was carried out by Gasparre (2005) and interpretation of the small strain secant stiffness, summarised in Height et al (2007), is shown in Figure 7.4. It shows degradation of an undrained secant Young's modulus, $E_{u,sec}$, interpreted from London clay specimens subjected to undrained shearing in triaxial compression and extension. The significance of these graphs is the difference in the magnitude of stiffness established from the previous, mostly commercial, testing of London clay and testing performed by Gasparre (2005) and identified as 'IC study' in the legend.

Gasparre & Coop (2008) further presented data of oedometer tests on London clay from the site of Heathrow Terminal 5, shown in Figure 7.5. Both natural specimens (O17/O25/O28 etc.) and reconstituted specimens (rO17/rO25 etc.) were tested from samples taken at different depths. It is evident from the figure that the compression paths of natural specimens do not converge towards the compression paths of reconstituted specimens even for compressions of up to 20000 kPa of the vertical effective stress, indicating a stable structure of natural London clay.



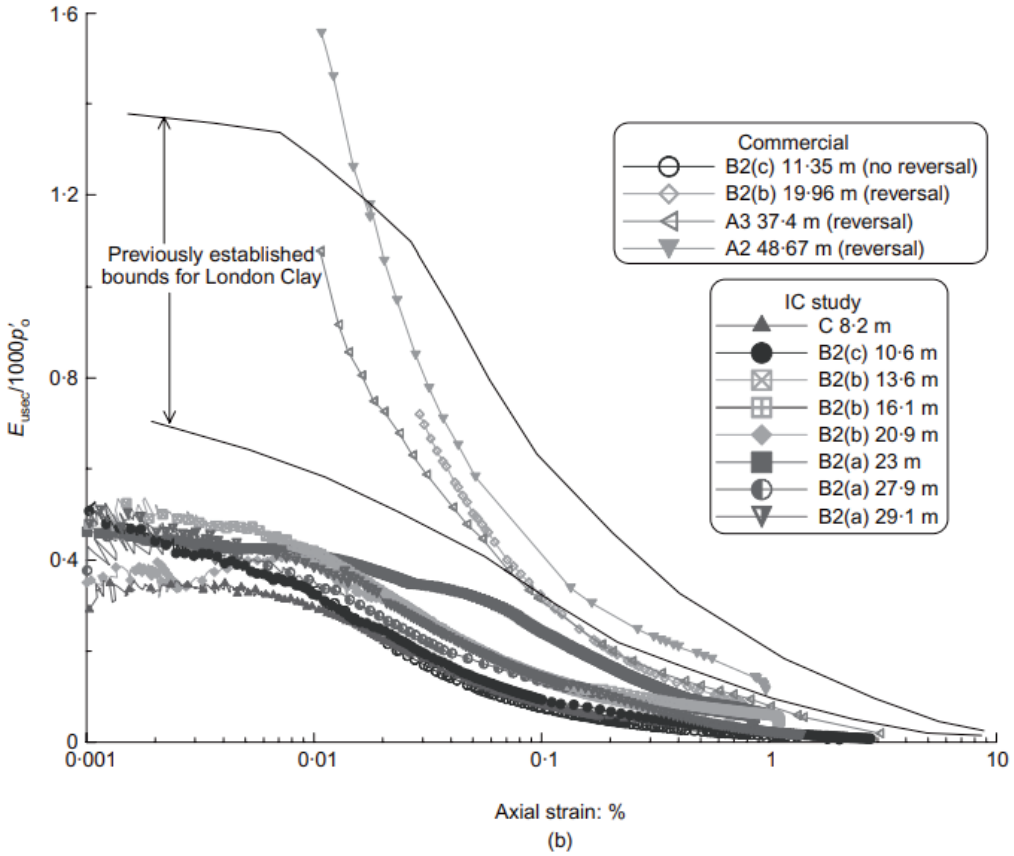


Figure 7.4: Normalised stiffness degradation curves for a) undrained triaxial compression; b) undrained triaxial extension (modified after Hight et al., 2007).

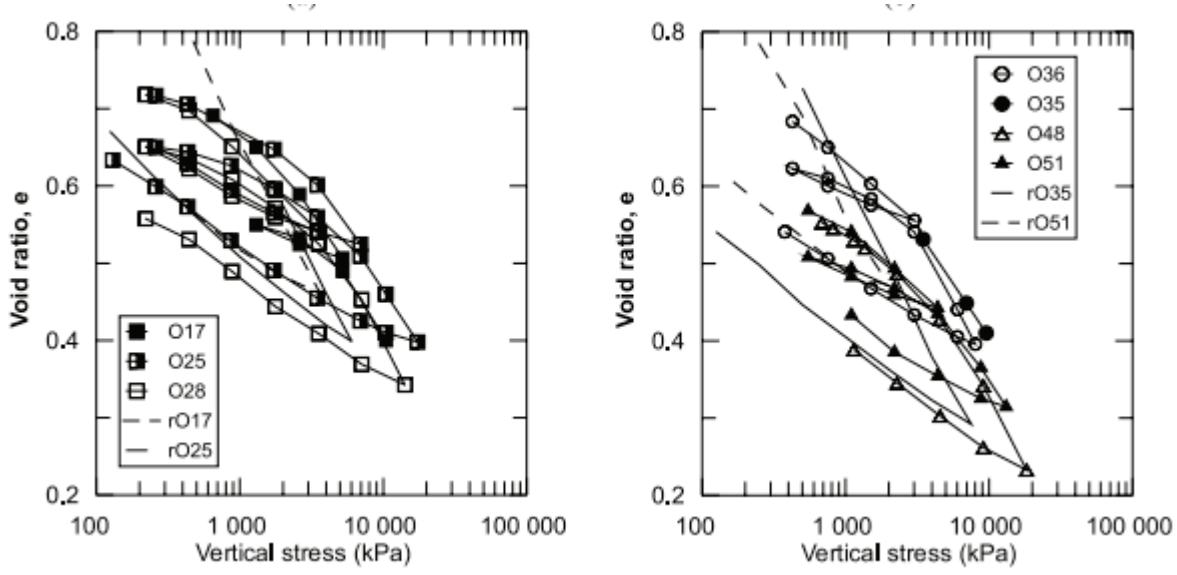


Figure 7.5: Compression and swelling curves from natural and reconstituted specimens of London clay unit A and B2 (Gasparre & Coop, 2008)

The effect of stress history, in terms of stress path, has been investigated by Gasparre et al. (2007b) via undrained shearing tests. The soil behaviour was interpreted in a kinematic hardening framework proposed by Jardine (1991) with two yield surface Y1 and Y2. The probing tests set up pairs of undrained compression and extension starting at the same isotropic initial stress point but achieved with different paths length and creep period. It has been concluded that after the creeping for a period, when the approaching path is not engaging Y2 surface, the stiffness response is little effected by the stress history, while a longer stress path passing through Y2 surface results in significant effect on stiffness from stress history.

Therefore, it is necessary to model the stress history appropriately as both creeping and the different stress paths are considered causing large effects on the soil stiffness response during the tunnelling, especially under the condition that the data from intact samples, which reflects the current properties of the soil, are not enough for calibration. The realistic stiffness modelling is the base of reproducing ground response from the tunnelling.

7.4 Selection and calibration of a constitutive models

7.4.1 The modified two surface kinematic hardening soil model (M2-SKH)

Because of the geological history of London clay, of the high K_0 profile and of the small strain nonlinearity with a small elastic range, a kinematic hardening model was considered suitable for the simulation of London clay. The modified two surface kinematic hardening soil model (M2-SKH) of Grammatikopoulou et al. (2006) was available in ICFEP and was selected for numerical analyses in this research. The model was based on the two-surface kinematic model of Al-Tabbaa and Wood (1989) and was used originally by Avgerinos (2014), Avgerinos et al. (2016) and Avgerinos et al. (2018) for the simulation of the two tunnelling case studies in London clay.

As shown in Figure 7.6a, the M2-SKH model adopts an elliptical outer bounding surface, similar to the MCC model, and also an elliptical smaller kinematic surface (bubble) inside the outer surface. This ‘bubble’ is scaled down from the outer surface by the ratio R and it represents a boundary of the elastic region within the model, i.e. the bubble is the yield surface in the model.

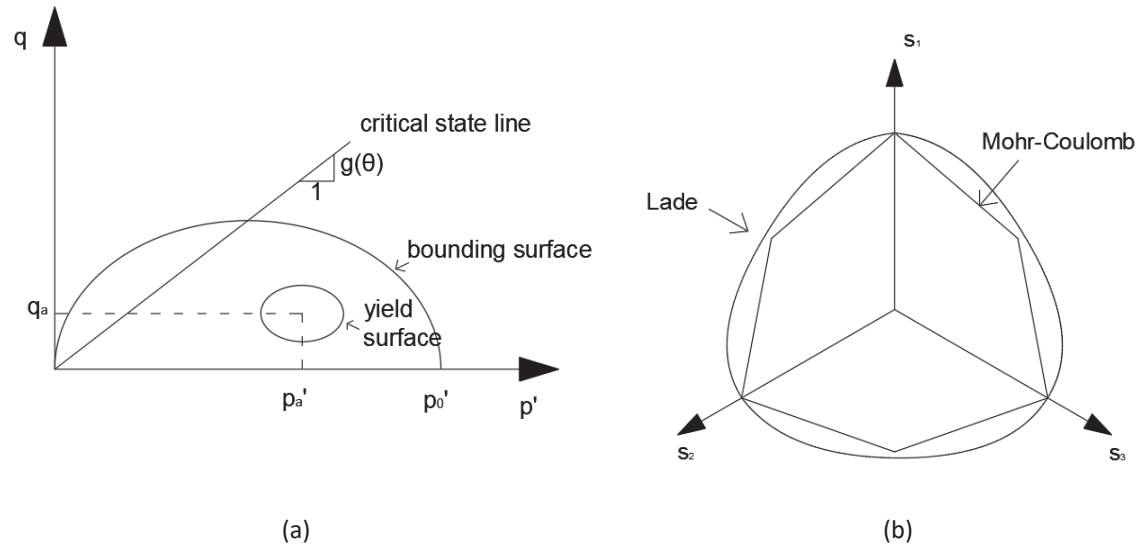


Figure 7.6: The M2-SKH model: a) outer bounding surface and the kinematic yield surface ('bubble'); b) different shapes for yield and potential surface in the deviatoric plane

The mechanical behaviour of the soil inside the 'bubble' is linear elastic, mobilising the highest value of stiffness. The stiffness degradation occurs once the stress state reaches this surface and the 'bubble' is dragged with the direction of the stress path development within the outer bounding surface. The soil behaviour is elastoplastic when the stress state is outside the 'bubble' and remains so until reaching the bounding surface, upon which the bounding surface becomes the main surface. A significant improvement of the M2-SKH model, compared to the Al-Tabbaa and Wood (1989) formulation, is the smooth transition from the linear elastic state (inside the 'bubble') to elastoplastic state, which is manifested in a realistic stiffness degradation curve achieved by a hardening modulus. Furthermore, the model can also adopt different shapes of yield and plastic potential surfaces in the deviatoric plane (see Figure 7.6b), such Mohr-Coulomb hexagon or Lade shape (Lade and Ducan 1975) for example. It can therefore simulate either a constant angle of shear resistance, ϕ', reproduced by the Mohr-Coulomb hexagon shape, or a variable ϕ' reproduce by the Lade surface, which is also experimentally verified.

The hardening modulus introduced in this model is the key element to achieve smooth transition from linear elastic to elastoplastic state. It implies infinite stiffness when the stress state reaches the yield surface, and hence the plastic strain initiates from zero. A general expression of this modulus for the yield surface is shown below.

$$A = A_0 + A_1 \tag{7-1}$$

$$A_0 = \frac{4}{\lambda - \kappa}\left[(p' - p'_a)\left[p'(p' - p'_a) + \frac{1}{2}\left(\frac{\delta F_y}{\delta s_{ij}} : S^a_{ij}\right) + \frac{(p'_0)^2 \cdot R^2}{4}\right]\right] \tag{7-2}$$

$$A_1 = \frac{4}{\lambda - \kappa}\alpha\left(\frac{b}{b_{max} - b}\right)^{\psi}\left(\frac{p_0'}{2}\right)^3 \quad (7\text{-}3)$$

where λ and $\kappa$are gradients of compression and swelling lines in the *v-lnp'* space respectively; *R* is the ratio between the axes of the yield surface and the bounding surface; *b* represents the measure of proximity from the current yield surface (YS) to the bonding surface (BS), and b_{max} is its maximum value. p_a' and s_{ij} are mean effective stress and deviatoric stress at the centre of YS respectively; p' is the mean effective stress and p_0' is the size of BS; F_y is the function of yield surface;α & ψ are the parameters in the hardening modulus.

A_1 is the function of distance *b*. That is to say, in the case when the surface of the 'bubble' contacts the bounding surface (*b = 0*), the modulus can simply reduce to the same expression as that of the MCC model:

$$A = \frac{4}{\lambda - \kappa}[(p' - \frac{p_0'}{2})p'\ \frac{p_0'}{2}] \quad (7\text{-}4)$$

At the beginning of elastoplastic stage ($b = b_{max}$), the hardening modulus is infinite as the denominator $b_{max} - b = 0$, which realises zero plastic strain at this point and therefore, a smooth transition from elastic to elastoplastic behaviour is achieved.

Isotropic elastic behaviour is assumed within the 'bubble' of this model and the following equation of elastic shear modulus proposed by Viggiani and Atkinson (1995) can be adopted:

$$\frac{G_e}{P_r} = A_G(\frac{p'}{p_r})^n R_0^m \quad (7\text{-}5)$$

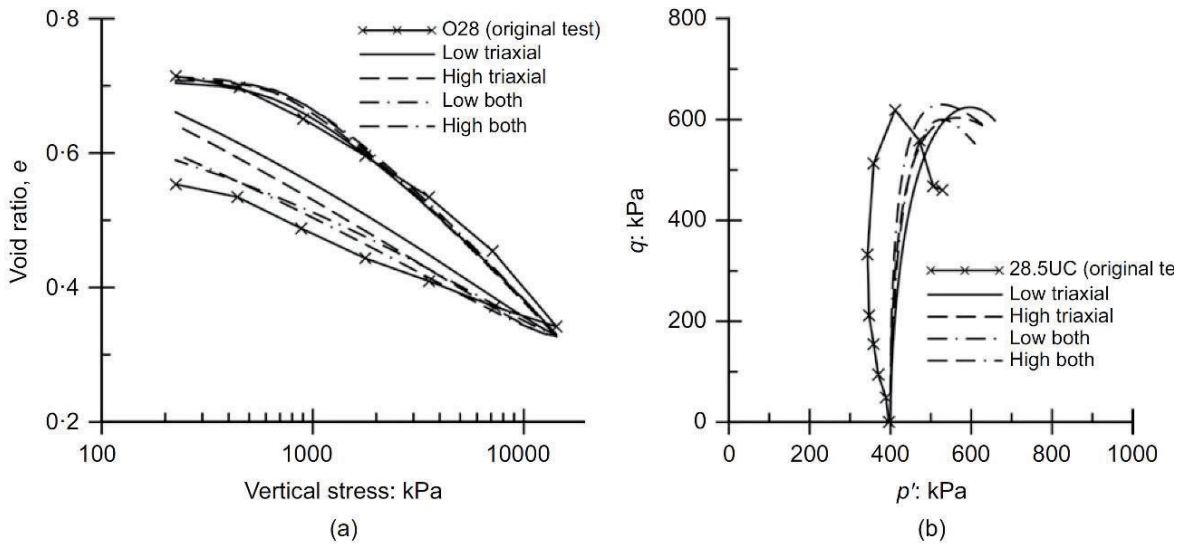
where A_G, n, and m are parameters determined by the material; $R_0 = {p_0'}/{p'}$, and $p_r = 1kPa$.

In calibrating the M2-SKH model for the simulation of tunnelling at St James' park, on the Jubilee Line Extension (JLE), Avgerinos (2014) and Avgerinos et al. (2016) concluded that it was not possible to achieve the same level of accuracy in predicting the short-and long-term ground response due to tunnelling by using a single set of model parameters. Consequently, Avgerinos (2014) and Avgerinos et al. (2016) derived four sets of model parameters from laboratory tests on intact samples of London clay performed by Gasparre (2005). Calibration was based on undrained triaxial tests and oedometer tests in particular. Based on Figure 7.1, JLE tunnels are located in the B2 and A3 divisions of London clay and the model was therefore calibrated for both divisions, with model parameters summarised in Table 7.1. The four sets of model parameters are named as 'low triaxial', 'high triaxial', 'low both'

and ‘high both’. The first two sets represent, respectively, parameters that reproduce well either the ‘low’ or the ‘high’ stiffness of London clay from undrained triaxial tests (as shown in Figure 7.7c), but ignore how these parameters reproduce the oedometer test results. From predictions in Figure 7.7a, these two sets of parameters overpredict the magnitude of the swelling coefficient, κ. On the other hand, the latter two sets of calibrations make compromise between the triaxial and oedometer data. While predicting slightly higher both ‘low’ and ‘high’ nonlinear stiffness from triaxial data (Figure 7.7c), the oedometer swelling line is much closer reproduced by these parameters (Figure 7.7a). The simulated effective stress paths from the four model calibration sets show very similar, and accurate, prediction of the peak undrained strength of London clay (Figure 7.7b).

The finite element analyses performed by Avgerinos (2014) and Avgerinos et al. (2016) showed that the ‘low triaxial’ calibration performed well in reproducing the short-term response of twin tunnel excavation, whilst the ‘high both’ and ‘low both’ calibrations reproduced more accurately the long term settlements of twin tunnels at St. James Park site. The same calibration sets were then applied by Avgerinos (2014) and Avgerinos (2018) in the simulation of twin tunnel excavations at Hyde Park site of the Crossrail project and have also been applied in the simulation of DOT tunnelling at both sites in the current research.

To finalise the mechanical modelling of the ground profiles for the two sites (Figure 7.1 and Figure 7.2), the Made Ground layer was modelled as linear elastic, adopting Young’s modulus E = 5000kPa and Poisson ratio $\mu = 0.3$. The Terrace Gravel layer is modelled as non-linear elastic-plastic, using a Mohr-Coulomb yield surface, which is defined by the angle of shearing resistance, $\phi' = 35^{o}$, and an angle of dilation, $\upsilon = 17.5°$ (Addenbrooke at al., 1997).



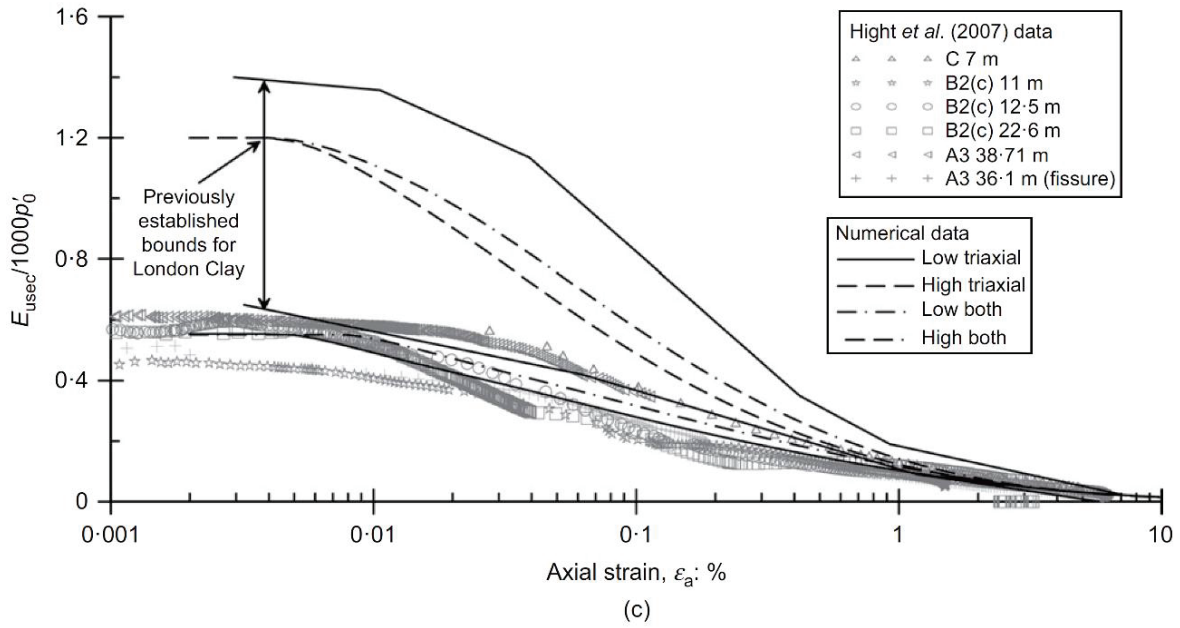


Figure 7.7: Calibration of B2 layer, comparing with tests (Avgerinos, 2014): a) oedometer compression curve; b) stress path from triaxial compression test; c) stiffness degradation from triaxial compression tests;

Table 7.1: Parameters of 'bubble' model calibrated for London clay

Model parameters	**Geotechnical significance**	**Calibrations (division B2/division A3)**			
		'Low triaixal'	**'High both'**	**'Low both'**	**'High triaxial'**
V_1	specific volume at unit pressure	2.5/2.75			
λ	slope of compression line	0.12/0.15			
κ	slope of swelling line	0.06/0.063			
n	exponent in shear modulus (see Equation 7-5)	0.87			
m	exponent in shear modulus (see Equation 7-5)	0.28			
A	shear modulus (see Equation 7-5)	250/180	550/455	260/190	550/455
ϕ'	angle of shearing resistance (Mohr-Coulomb hexagon is incorporated)	25°/20.3°			
R	ratio of the yield surface size to that of bounding surface	0.01/0.005	0.016/0.005	0.02/0.005	0.016/0.005
α	coefficient in the hardening term	0.8	2.0/2.5	1.5	1.2
ψ	exponent in the hardening term	0.7	1.0	0.7	1.0

Note: parameters V_1, λ and κ are based on v-lnp' space

7.4.2 Modelling of tunnel lining

The tunnel lining in both case studies was modelled with elastic beam elements, adopting properties of reinforced concrete as applicable to each case (Avgerinos, 2014). For the lining at Saint James' Park, the unit weight of concrete was taken as γ= 30kN/m^3, Young's modulus E = 2.8E7 kPa, Poisson ratio μ = 0.15 and lining thickness was 0.2m. As for the Hyde Park case, the unit weight of concrete was also γ = 30kN/m^3, Young's modulus E = 4.0E7 kPa, Poisson's ratio μ = 0.15, while the lining thickness was 0.3m. The simulations of DOT tunnelling at each site adopted the same modelling of the lining as in the Avgerinos (2014) study.

7.5 Numerical modelling of tunnels at St James Park and at Hyde Park

7.5.1 Numerical modelling of tunnelling at Saint James' Park

The London underground are typically excavated at the depth between 20m to 30m below the ground level. During the history of London underground construction, the London clay is considered and ideal material for tunnel excavation due to its satisfying strength and low permeability that guarantees the stability of the structure before the construction of lining (Burland et al., 2001). The Jubilee Line Extension project consists of twin tubes each with the length of 11.1km, and 11 tunnel machines are employed.

Finite element mesh for twin tunnels (JLE)

The finite element mesh used by Avgerinos (2014) is adopted for the twin tunnel analysis (see Figure 7.8). The zero X-coordinate (in horizontal direction) is set up in the vertical axis of the westbound tunnel. The elevation of the ground surface is at Y = 102.5m, while the spring-line axes of the two tunnels are at Y = 72.0m (WB) and Y = 82.5 (EB), with the horizontal distance between them of 21.5m, as per Figure 7.1. The WB tunnel was excavated first, under green-field conditions, followed by the EB tunnel 8 months later.

The analysis is two-dimensional (2D) plane strain and hydro-mechanically coupled. The superficial soil layers are treated as drained, while the London clay layers are considered as consolidating. The mesh consists of 910 8-noded quadrilateral solid elements modelling the soil and 64 3-noded beam elements modelling the tunnel lining. Each solid element has 2 displacement degrees of freedom per node, while the consolidating elements also have a pore pressure degree of freedom at corner nodes. Each beam element has 2 displacement and one rotational degrees of freedom per node. Rediced (2x2) Gaussian integration was adopted for each element. ICFEP employs a modified Newton-Rapson method with a sub-stepping stress-point algorithm as a non-linear solver.

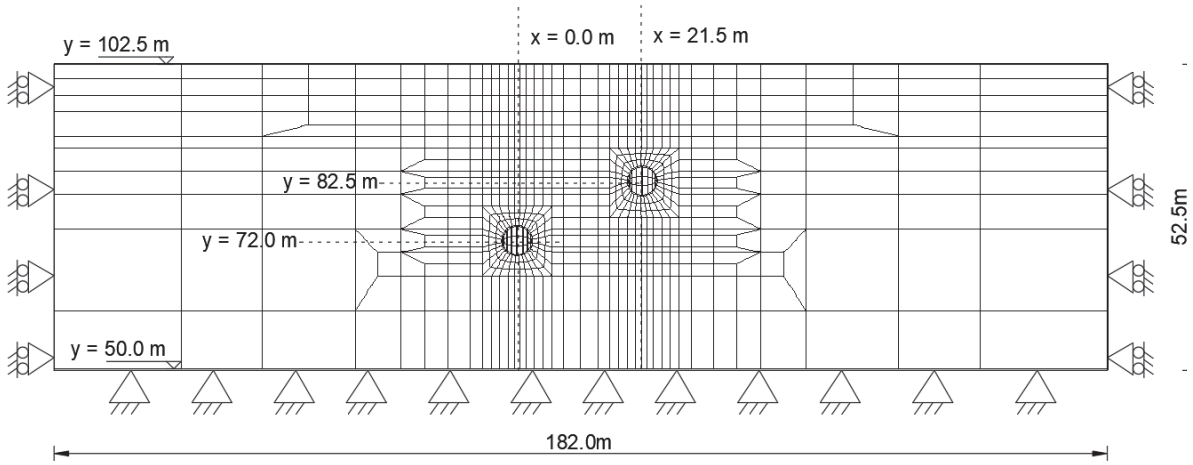


Figure 7.8: Finite element mesh for twin tunnels simulation at St. James' Park

Zero horizontal displacements are prescribed along the vertical boundaries of the mesh, whilst both horizontal and vertical displacement are fixed along the bottom boundary. The ground surface is a stress-free boundary. This condition is applied throughout the analysis. The hydraulic boundary conditions are applied from the start of tunnel excavation, when the analysis becomes couple. No change in pore water pressure is prescribed along the vertical and bottom boundaries, while the ground surface is impermeable. On the excavated tunnel boundary a precipitation boundary conditions is applied. This is a dual boundary condition which automatically applies either a zero flow or a zero pore pressure at nodes on the tunnel boundary. The former condition would be applicable for the whole tunnel boundary in the short term for tunnels excavated in low permeability soils, while the latter condition applies in the long term when the whole tunnel boundary may become fully permeable. During the transient stage, in between the short- and long-term, the hydraulic boundary condition is gradually changing around the tunnel boundary.

Stages of analysis for twin tunnels (JLE)

The stages of analysis, from the reproduction of stress history, to excavations of the two tunnels and into the long-term, are summarised in Table 7.2. During the stage of the geological history reproduction (increments 0 to 230 in Table 7.2), the analysis is performed as drained (i.e. uncoupled), as the time period of this stage is geologically very long. This stage is divided into three main steps:

1) Deactivation of the Made Ground (MG) and Terrace Gravels (TG) layers in the FE mesh (increment 0), maintaining ground water table at the top of London clay. Application of 180m of overburden on the top of London clay. According to Chandler (1999) this was equivalent to 1835 kPa of effective stress, as shown in the sketch in Figure 7.9a. The vertical effective stress in the mesh is initialised from the bulk unit weight of the two London clay units and the pore pressure. The horizontal effective stress is initialised by assuming $K_0 = 1 - \sin\phi'$ (Jaky,

1948), as applicable to a normally consolidated sediment. A constant value of $K_0 = 0.617$ was prescribed for the whole deposit, as an average value of the two London clay units. In terms of the constitutive model M2-SKH, the stress states within the mesh are on the bounding surface, corresponding to point A in Figure 7.11.

2) Incremental unloading (increment 1 to 200) of the overburden pressure from the top surface of London clay, simulating the erosion of the overburden soil (Figure 7.9b). This is equivalent to path AB in the M2-SKH model (Figure 7.11).
3) Construction of the MG and TG layers (increment 201-230), to bring the stress state in the ground to current levels. Both layers are initiated with $K_0 = 0.5$ and the ground water table is gradually raised to the top of TG layer, while remaining hydrostatic with depth. This is equivalent to path BC in Figure 7.11, with respect to the constitutive model, while the finial initial pore pressure at the end of geological history in shown in Figure 7.10.

Table 7.2: Analysis stages of twin tunnels simulation for the case at St. James' Park

Increment	**Time**		**Stage and boundary conditions**	
	Inc.	Total	Tunnelling simulation stage	Hydraulic boundary condition
0	drained	drained	Deactivation of Made Ground, Thames Gravel and tunnel linings; application of 180m overburden pressure on top of London clay	Hydrostatic pore water pressure (PWP = 0 at the top of London clay)
1-200	drained	drained	Surface erosion (180m)	
201-210	drained	drained	Construction of Terrace Gravel layer	Hydrostatic pore water pressure; water table rising up to the top of Terrace gravel
211-230	drained	drained	Construction of Made Ground	
201-230	drained	drained	Water table raised by 2.7m, to the top of Terrace Gravel layer	
231-430	0.03h/inc	6 hours	WB tunnel excavation and lining construction	
431-451	0.38m/inc	8 months	8 months consolidation period	Hydrostatic pore water pressure retains; Precipitation boundary condition specified on the tunnel boundary; zero change of pwp on vertical and bottom boundaries of the mesh
452-651	0.03h/inc	6 hours	EB tunnel excavation and lining construction	
652-675	0.5m/inc	1 year	Short term and long term response post-tunnel construction	
676-684	1 yr/inc	9 years	Short term and long term response post-tunnel construction	
684-689	0.83 yr/inc	5 years		
690-705	5.3 yr/inc	85 years		

Note: for the stages in drained condition, the consolidation card was not turned on, and therefore there is no time scale set up in these stages; The total time past after twin tunnelling is 1 year at inc. 675, 10 years at inc. 684, 15 years at inc. 689 and 100 years at inc. 705.

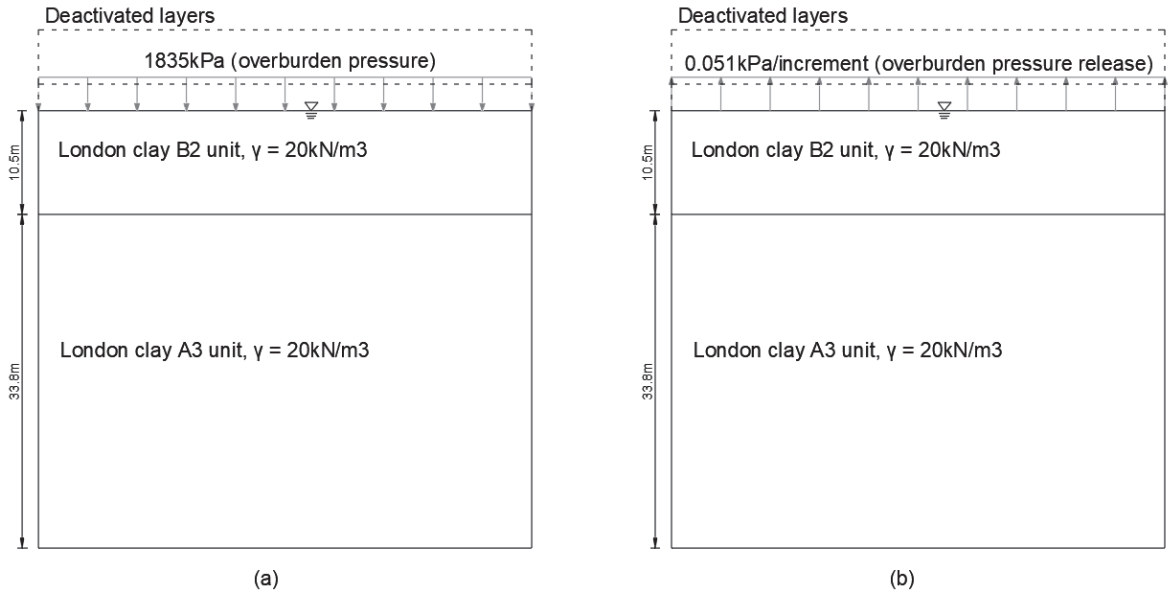


Figure 7.9: Schemes of stress history reproduction a) deactivating top two layers; b) incrementally unloading overburden pressure

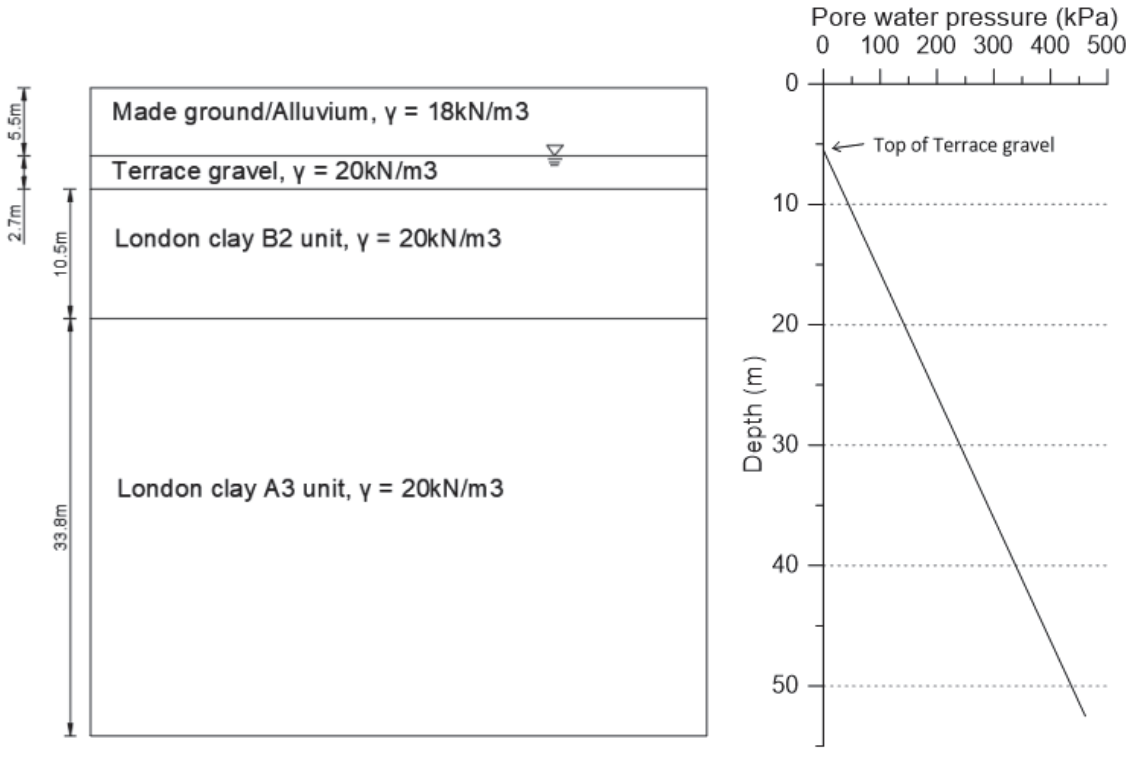


Figure 7.10: Ground profile and pore water distribution (hydrostatic) at the end of geological history

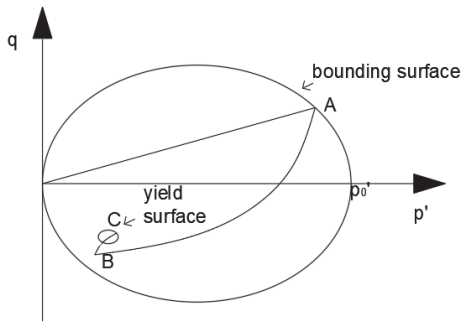


Figure 7.11: Sketch of the stress path in geoligical history reproduction for London clay

Avgerinos (2014) showed the results of the geological history simulation at St Jamses' park from all four sets of calibration data explained in Section 7.4. Here only two sets of calibrations are selected for analyses, the 'low triaxial' and 'high both', for which Avgerinos (2014) showed to reproduce more accurately the short and the long-term ground response, respectively.

The K_0 profiles predicted from these two calibrations are shown in Figure 7.12. The top layers, Terrace Gravel and Made Ground are manually assigned the $K_0 = 0.5$. This controls the evolution of the K_0 profile at the top of London clay (Figure 7.12b), which otherwise has a very large value at the end of the simulation of erosion at increment 200 (Figure 7.12a). Both calibrations develop a similar trend of the K_0 profile with depth, although the 'low triaxial' option results in a profile that is distinctly lower than 1 (Figure 7.12a).

The K_0 profile calculated from the Equation (4) of Mayne & Kulhawy (1982) is also shown in Figure 7.12b. It shows a similar trend with the two numerically predicted profiles and is particularly in close agreement with the prediction of the 'high both' calibration. The empirical approach for K_0 was formulated for the equation from a small database.

$$K_0 = (1 - \sin\varphi')[\left(\frac{OCR}{OCR_{max}^{1-\sin\varphi'}}\right) + \frac{3}{4}(1 - \frac{OCR}{OCR_{max}})] \quad (7\text{-}6)$$

This equation describes the $K_0 - OCR$ relation particularly for reloaded soil such as the London clay strata in St James' park. The OCR_{max} is defined as $\sigma'_{v,max}/\sigma'_{v,min}$, representing the maximum over-consolidation ratio in the history. Therefore, for normally consolidated soil, of which $OCR = OCR_{max}$, then the equation 7-6 is reduced to $K_0 = (1 - \sin\varphi')$.

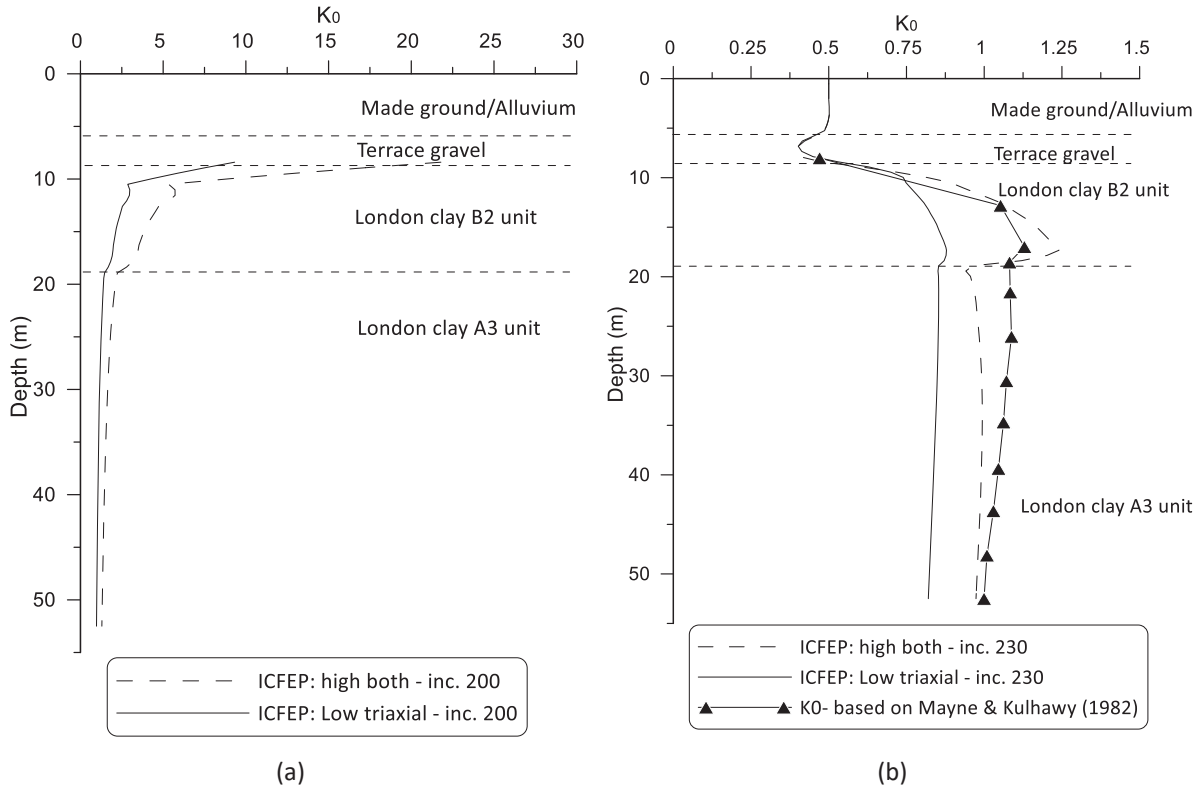


Figure 7.12: K_0 profile predicted for two calibrations a) at the end of erosion (inc 200);b) at the end of geological history (inc. 230).

The two sets of calibrations show very similar profiles of mean effective stress, p', with depth (Figure 7.13b), which is not surprising given that the applied stress changes are the same in both analyses of the geological history. The p'_0 profiles are different (Figure 7.13a), reflecting a bigger size of the bounding surface at the end of the geological history resulting from the 'high both' calibration. The p'_0/p' ratio in Figure 7.14 reflects broadly a yield stress ration (YSR) profile which reduces with depth. The YSR reflects the OCR state of the soil and therefore, is considered positively correlated to the K_0 value. Both curves show similar shape with the K_0 profile as shown in Figure 7.12b.

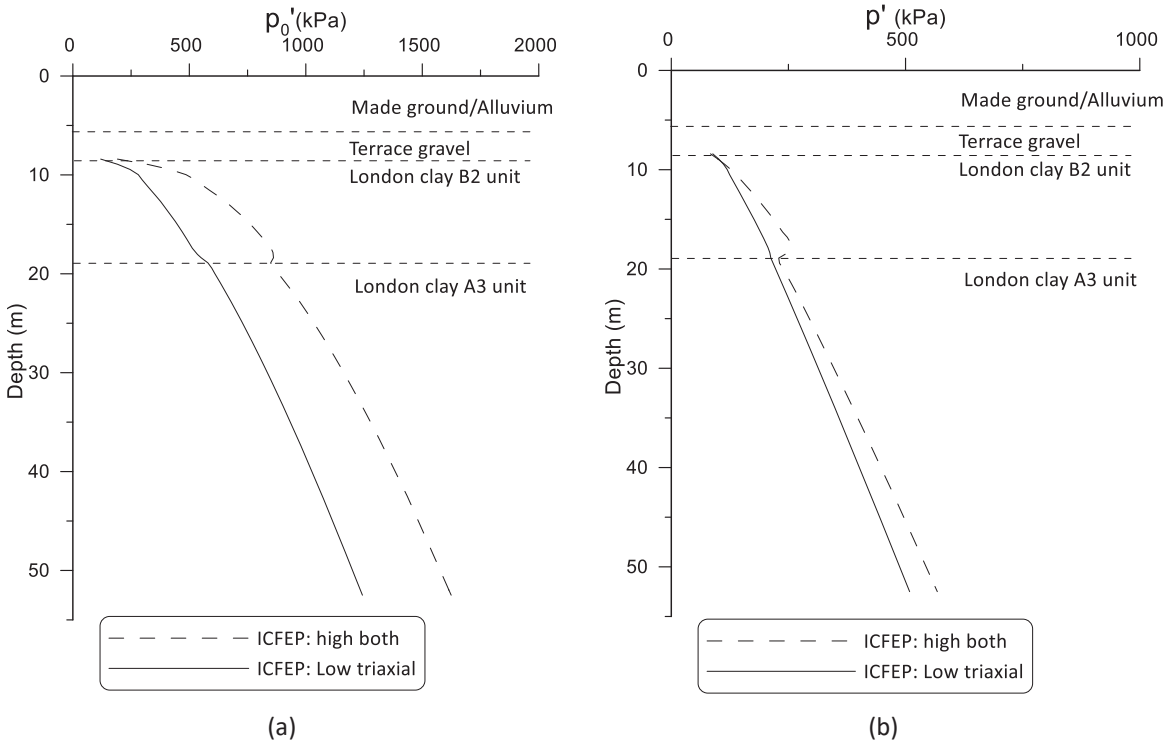


Figure 7.13: a) p_0' and b) p' profile along the depth at the end of geological history (inc. 230)

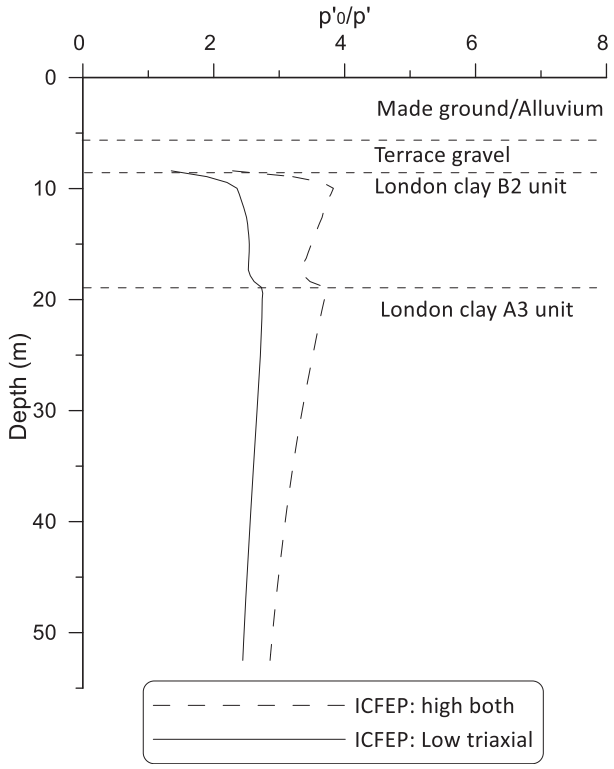


Figure 7.14: p_0'/p' profile along the depth at the end of geological history

Following the simulation of the geological history of London clay, which establishes the current conditions in the ground profile prior to tunnelling, the remaining stages of analysis, summarised in

Table 7.2, involve:

4) Excavation of the westbound tunnel (WB) from increment 231 to 430. The large number of increments in this stage is applied to enable a precise reproduction of the 3.3% volume loss evaluated during the excavation of this tunnel. Table 7.3 summarises the achieved volume loss and the percentage unloading for each of the two calibrations. The unloading percentage is the proportion of the increments of the bore without lining to the duration of excavation (e.g. the excavation is carried out over 200 increments, and the lining is constructed at the 25^{th} increment during the excavation, thus the unloading percentage is 25/200 = 12.5%). This parameter reflects the stiffness of the soil as the higher unloading percentage indicates the later lining is constructed, and hence the stiffer the soil is. Analyses were coupled from this stage. The total duration of tunnel construction is short (around 6 hours), simulating conditions of undrained excavation.
5) Consolidation period of 8 months post-WB tunnel construction, to simulate the real time period before the excavation of the eastbound tunnel (EB).
6) Excavation of the EB tunnel following the same process as in 4) above, justified with the target volume loss of 2.9%, as evaluated during the construction of this tunnel.
7) Consolidation into the short and long period post-tunnel construction.

Table 7.3: Volume loss and unloading percentage for DOT tunnel and westbound twin tunnel

Analysis	**Twin tunnels**		**DOT (shallower)**		**DOT (deeper)**	
	VL (%)	Unloading (%)	VL (%)	Unloading (%)	VL (%)	Unloading (%)
low triaxial	3.38	12.5	3.33	13.0	3.36	11.0
high both	3.21	37.0	3.21	40.5	3.66	35.0

Note: unloading percentage is the proportion of number of increments; According to the Shanghai analysis, the DOT tunnel has similar volume loss with single tunnel, and therefore, the similar target value is expected for DOT in London with twin tunnels.

Finite element model for DOT tunnel analysis (St James' Park)

Two FE meshes for DOT tunnel simulations in Figure 7.15 and Figure 7.16 represent two positions of the DOT tunnel: the 'deeper' is at the elevation of the WB twin tunnel and the 'shallower' is at the elevation of the EB twin tunnel. The two meshes are otherwise identical in their dimensions. The types of solid elements for modelling the soil, beam elements for modelling the lining and the prescribed mechanical boundary conditions are the same as those in the twin tunnel analysis introduced above.

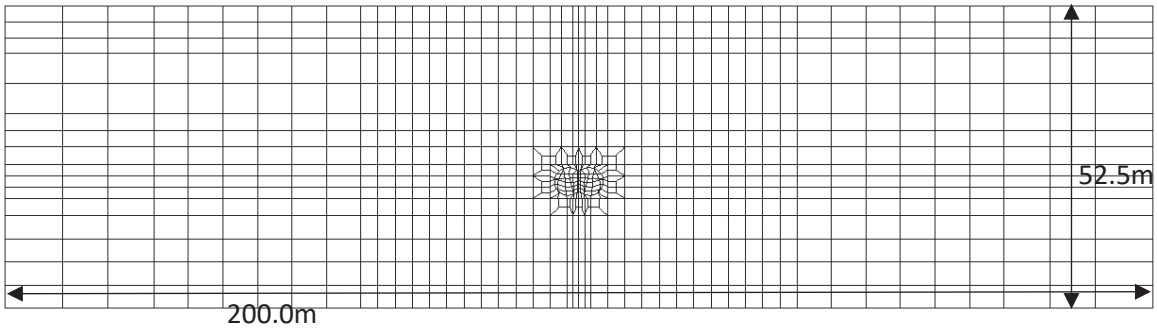


Figure 7.15: DOT mesh for 'deeper' case at St. James' Park

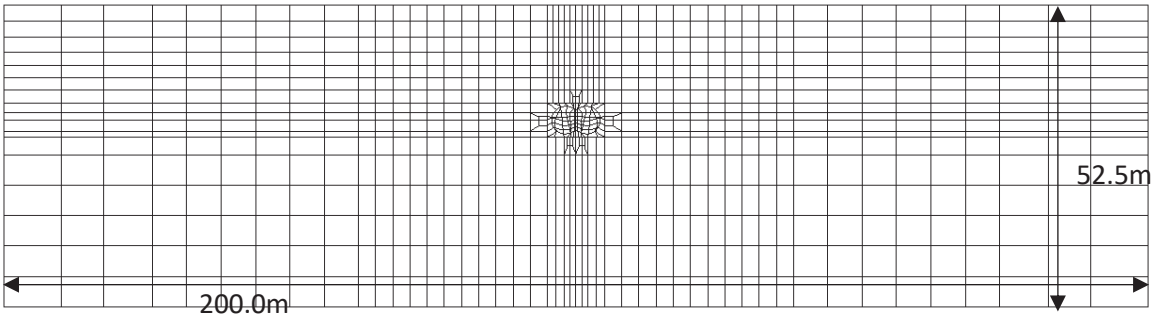


Figure 7.16: DOT mesh for 'shallower' case at St. James' Park

The diameter of a single bore in a DOT ring (4.85m) is identical to that of twin tunnels (*Figure 7.17*). Since there is no DOT case in reality with a diameter of 4.85m, the geometry is similar to that used in Shanghai Metro Line 6, but scaled down proportionally. The achieved volume losses for the two elevations of the DOT tunnel and for the two calibrations are summarise in Table 7.3.

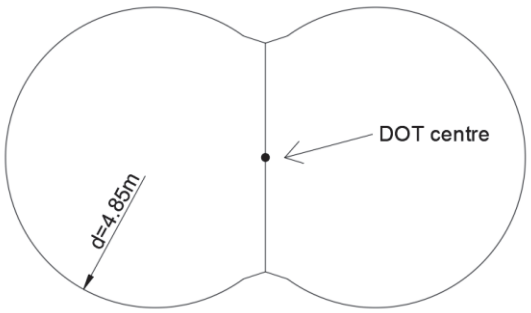


Figure 7.17: geometry of DOT ring applied in DOT simulations at St. James' Park

For DOT tunnel simulations, the geological history is the same as in twin tunnel simulations. The main difference is that in the tunnelling process, only one excavation stage is modelled since the two bores are excavated simultaneously. Identical time scales for short term and long term are used for comparison with twin tunnels. The analysis sequence is summarised in Table *7.4*.

Table 7.4: Analysis stages of DOT tunnels simulation for the case at St. James' Park

Increment	Time of consolidation after DOT excavation	Tunnelling simulation stage	Hydraulic boundary condition
0	drained	Excavation (deactivation) of Made Ground, Thames Gravel and linings	Hydrostatic pore water pressure (PWP = 0 at the top of B2 unit)
1-200	drained	Surface erosion (180m)	
201-230	drained	Water table risen by 2.7m across terrace gravel layer	Hydrostatic pore water pressure; water table rising up to the top of Terrace gravel
201-210	drained	Construction of terrace gravel layer	
211-230	drained	Construction of made ground	
231-430	6 hours	DOT tunnel excavation and lining construction	
431-452	1 year	Short term and long term consolidation	Hydrostatic pore water pressure stays; Precipitation boundary condition specified on the lining
452-458	10 years		
459	15 years		
460	20 years		
462	50 years		
462	100 years		

The volume loss in the tunnel excavation stage, which the excavation in the greenfield conditions, is targeted at 3.3%, corresponding to the volume loss of the WB tunnel excavation in the greenfield conditions of the real twin tunnel case.

Modelling of permeability

The consolidation in the soil, which starts from the stage of tunnel excavation, is governed by the permeability profile in London clay. Considering the high over consolidation of London clay, an anisotropic permeability model is employed in the analyses. This model prescribes different coefficient of permeability in the horizontal (k_h) and in the vertical (k_y) directions, the former being larger than the latter. The profiles of the two coefficients in Figure 7.18 are derived from the filed permeability data summarised in Hight et al. (2007), while the adopted values at the boundaries of the B2 and A3 units of London clay are summarised in Table 7.5.

Table 7.5: Permeability profile of the London clay (St James' Park)

Position	k_h (10^{-10}m/s)	k_v (10^{-10}m/s)
Top of B2 unit	4.7	2.35
Bottom of B2 / top of A3 units	3	1.5
Bottom of A3 unit	0.5	0.25

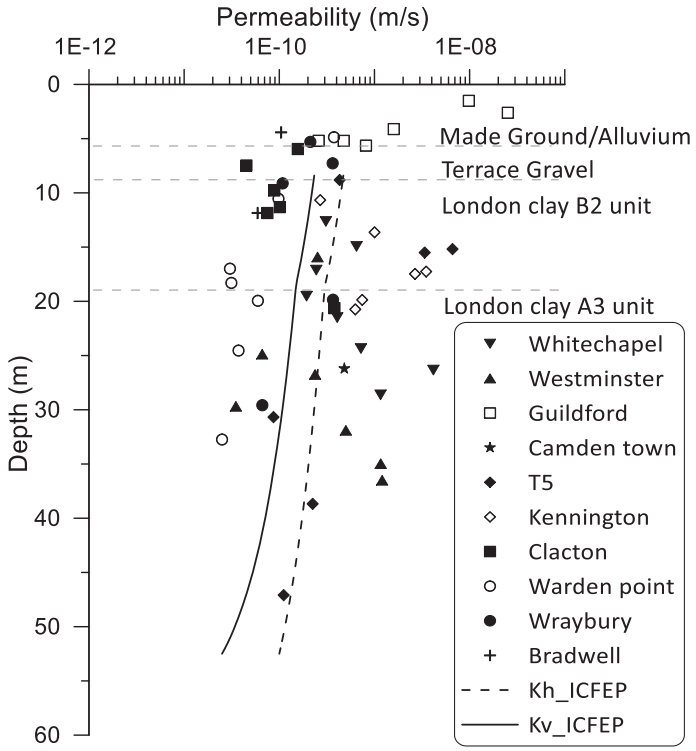


Figure 7.18: Profile of anisotropic permeability of London clay A3 and B2 units

7.5.2 Numerical modelling of tunnels at Hyde Park

The modelling of the tunnels at Hyde Park follows a similar sequence and boundary conditions to the study of St. James' Park tunnels. Therefore, only the features specific to this numerical model are highlighted in this section. The modelling of the soil is the same as in the St James' park study, employing the M2-SKH model (Grammatikopoulou et al., 2006) for the behaviour of London clay units. The modelling of the Lambeth Group units was simplified to a nonlinear Mohr-Coulomb model, as these layers are located significantly below the tunnels.

Finite element model for twin tunnels (Hyde Park)

The finite element mesh shown in **Error! Reference source not found.**19 is used for the simulation of C rossrail twin tunnels at Hyde Park site and is similar to the mesh used by Avgerions (2014) and Avgerinos et al. (2018). The mesh consists of 808 eight-noded quadrilateral solid elements and 48 beams elements, for modelling the ground and the tunnel lining, respectively. The mesh is 235m wide and 71m deep, the size of which is considered large enough to diminish the influence of the mesh boundaries. The analysis is 2D plane strain, hydro-mechanically coupled, adopting 2*2 integration. The FE software ICFEP (Potts & Zdravkovic, 1999) is also used for these analyses.

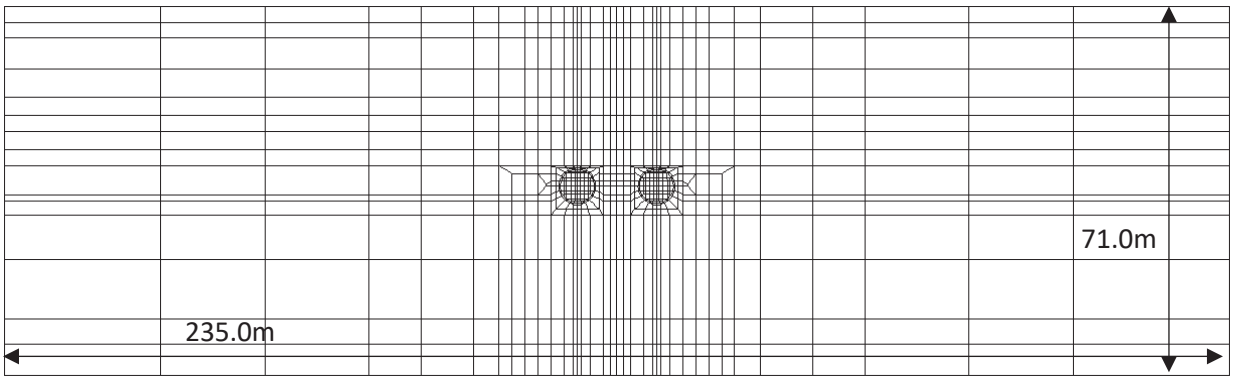


Figure 7.19: Mesh of twin tunnels analysis for Crossrail tunnel at Hyde Park site

Zero horizontal and vertical displacements are prescribed along the base of the mesh and the horizontal displacement is fixed on the vertical sides. The reproduction of the geological history for this case follows similar steps as the case of St. James' Park. The main difference is that the pore water pressure profile at this site is under-drained, compared to the hydrostatic profile at St James' park (see Figure 7.3b). Therefore, the initiation of such pore pressure profile requires additional steps, as indicated in Table 7.6. Once the geological loading and unloading is completed and the ground water level raised to its current position in Terrace Gravels (increment 20), the resulting K_0 profile is generated as shown in Figure 7.20a (the 'before under drained' line), from the analysis adopting the 'low triaxial' calibration of the M2-SKH model. Subsequent to this the consolidation is activated and the pore water pressure is set as zero at the ground water table in Terrace Gravels and at 19.62 kPa at the interface between the Upper and Lower Lambeth Group layers (see Figure 7.3b). A consolidation process is simulated over 140 years, which, in combination with the anisotropic permeability profile shown in Figure 7.22, gradually changes the initial hydrostatic pore pressure profile and results in a steady-state under drained pore pressure profile in Figure 7.3b and a K_0 profile in Figure 7.20a (the 'after under drained' line). This completes the simulation of the geological history before the start of tunnel excavations. As in the St James' park study, the superficial deposits are prescribed a $K_0 = 0.5$ and the overall K_0 profile in London clay is smaller than 1 for the 'low triaxial' calibration.

In terms of the construction process, the westbound tunnel is excavated first, with a volume loss of 0.78%, while the eastbound tunnel is excavated 73 days later, with a volume loss of 1.39%.

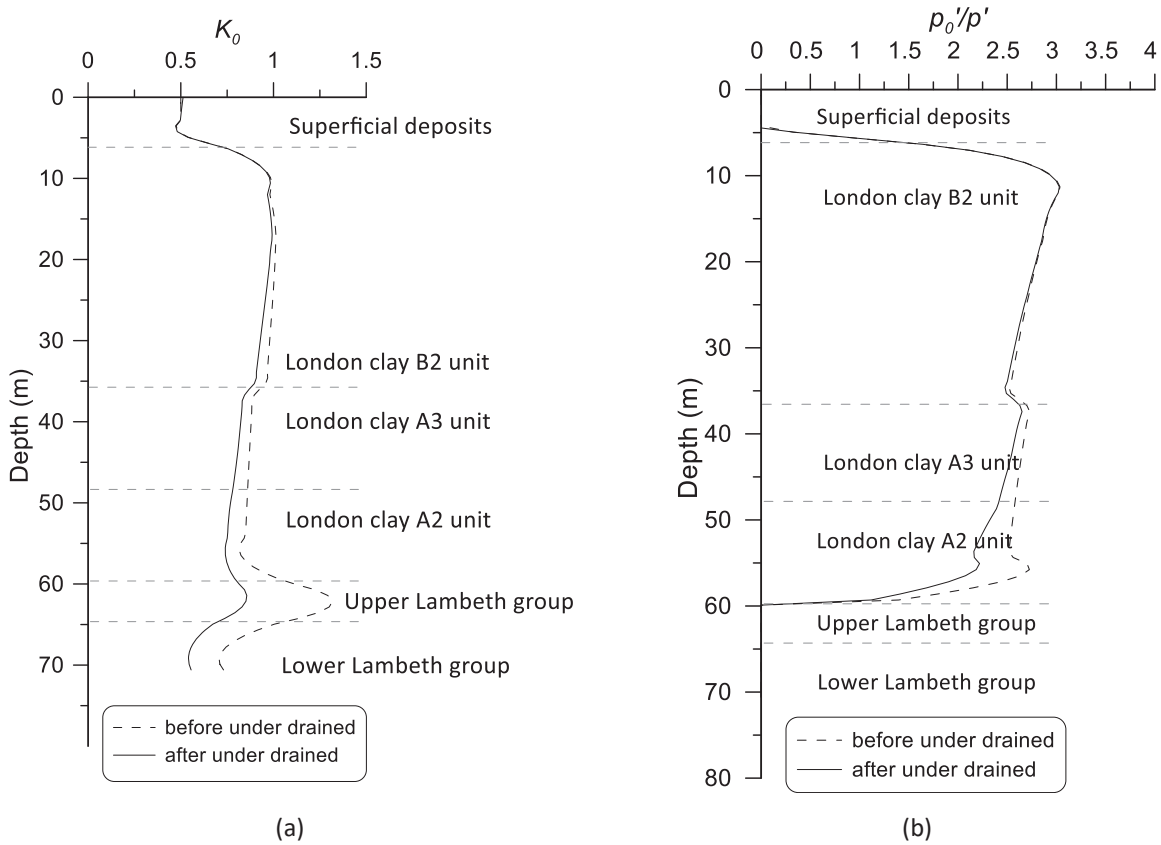


Figure 7.20: Profile of a) K_0 and b) Yield stress ratio (YSR) before and after the underdrainage

Table 7.6: Construction sequence of Crossrail tunnel modelling

Increments	Time		Analysis stages	Hydraulic boundary condition
	Inc.	Total		
0	drained	drained	Deactivation of Made Ground, Thames Gravel and tunnel linings; application of 180m overburden pressure on top of London clay	Hydrostatic pore water pressure (PWP = 0 at the top of London clay)
1 - 19	drained	drained	Erosion of the overburden soil (180m)	Hydrostatic pore water pressure (PWP = 0 at the top of London clay)
20	drained	drained	Construction of superficial deposits; water table risen to the 3m depth within the superficial deposits	Hydrostatic pore water pressure (PWP = 0 at the 3m depth)
21-25	14 yr/inc.	70 years	Underdrainage of the groundwater, generating new pore water profile shown in Figure 7.3b) ; 70 years' period for equilibrium of pore water pressure.	Underdrainage condition prescribed
26 - 30	14 yr/inc.	70 years		Stabilisation of the new hydraulic boundary condition

31 - 130	0.06 h/inc.	6h	Westbound bore excavation and lining construction	Precipitation boundary condition around the lining for permeable lining condition; Underdrainage hydraulic boundary condition as shown in Figure 7.3b
131 - 140	7.3 d/inc.	73 days	Intermediate period of 73 days for consolidation prior to the excavation of the eastbound bore	
141 - 240	0.06 h/inc.	6h	Eastbound bore excavation and lining construction	
241 - 275	0.067 yr/inc.	1y	Short term consolidation	
276 - 285	0.4 yr/inc.	4y	Long term consolidation	
286 - 290	1 yr/inc.	5y		
291 - 295	4 yr/inc.	20y		
296 - 300	14 yr/inc.	100y		

Finite element model for DOT analysis (Hyde Park)

The FE mesh for the DOT tunnel numerical model is shown in Figure 7.21, adopting similar discretisation as for the Crossrail twin tunnels in Figure 7.20. The external diameter in both left and right bore of DOT is 6.8m, and the tunnel is positioned at the same depth of 34.2m. The main difference in the construction process is that DOT tunnel has only one excavation and lining construction stage, which coincides with the westbound tunnel excavation in Table 7.6 (increment 31 to 130). All remaining increments simulate short and long-term consolidation post-DOT tunnelling (see Table 7.7: Construction sequence of DOT modelling at Hyde ParkTable 7.7).

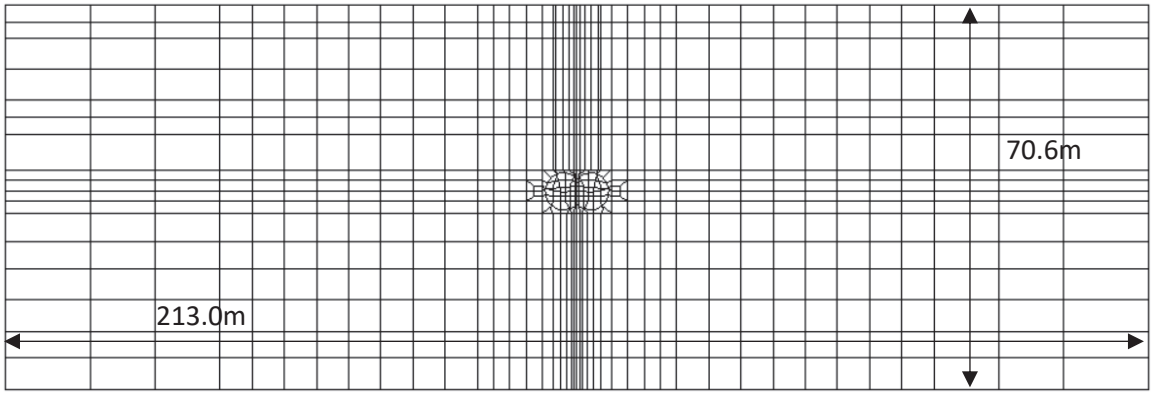


Figure 7.21: Mesh for DOT modelling at Hyde Park

Table 7.7: Construction sequence of DOT modelling at Hyde Park

Increments	**Time of consolidation after DOT**	**Analysis stages**	**Hydraulic boundary condition**

	excavation		
0 - 30	/	Simulation of geological history for Hyde Park site	The same as shown in Table *7.6*
31 - 130		DOT excavation and lining construction	
131 - 240		73 days for consolidation	
241 - 275	1y	Short term consolidation	
276 - 285	5y	Long term consolidation	
286 - 290	10y		
291 - 295	30y		
296 - 300	100y		

Modelling of permeability

The anisotropic permeability profile in *Figure 7.22*, with values reducing with depth, is consistent with the under-drained pore water pressure profile, ensuring that the latter is a steady state rather than a transient profile. The magnitudes of the k_v and k_h permeability coefficients at elevations where gradients change, as summarised in see Table *7.8*.

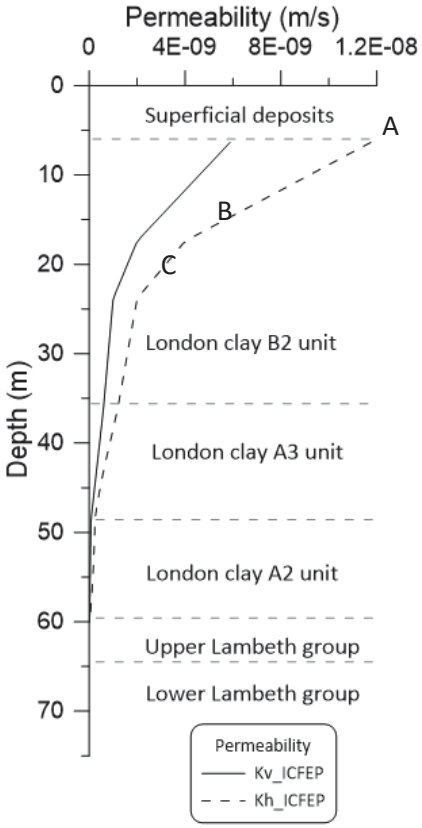


Figure 7.22: Profile of anisotropic permeability of London clay A3 and B2 units

Table 7.8: Anisotropic permeability adopted for the simulation of tunnelling in Hyde Park

Ground division/subdivision	K_h (m/s*E-10) (on the top)	K_v (m/s*E-10) (on the top)
London clay B2-A	117.51	58.76
London clay B2-B	39.22	19.62
London clay B2-C	19.92	9.96
London clay A3	11.99	5.99
London clay A2	2.38	0.78
Upper Lambeth Group	0.29	0.23
Lower Lambeth Group	0.41	0.41

7.6 Ground surface movements due to tunnelling

A filed monitoring system was set up for the twin tunnels of Jubilee Line Extension at St. James' Park, and the section of instrumentation, including rod extensometers, electrolevel inclinometers and other instruments, is shown in Figure 7.23. The ground movements were interpreted by Nyren (1998) and other researchers and were used in Avgerinos (2014) and in this chapter for comparison with numerical predictions of tunnelling-induced ground movements.

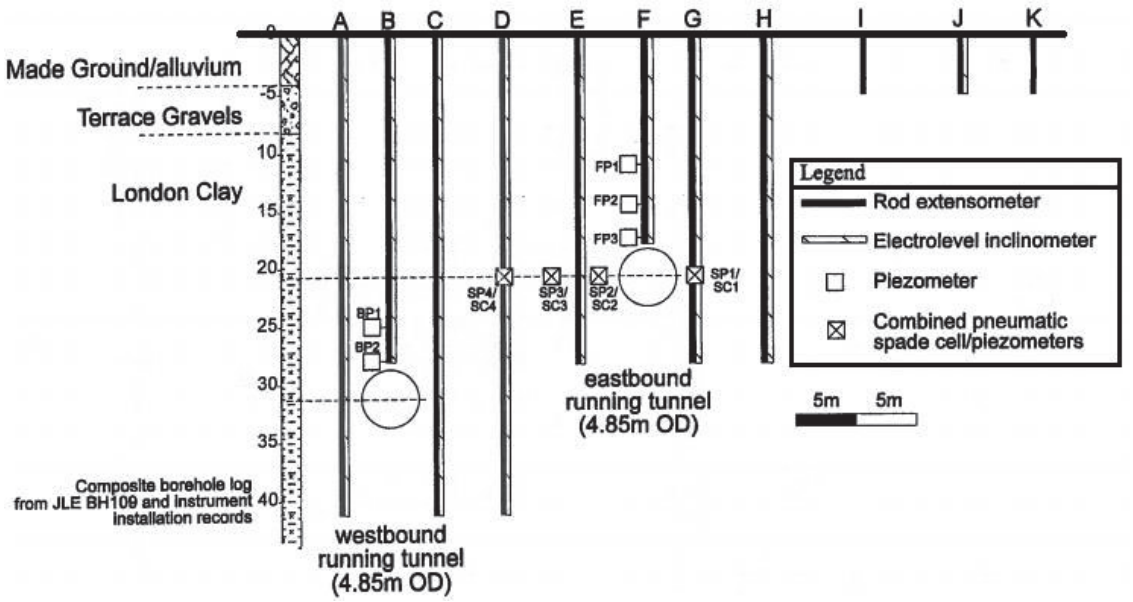


Figure 7.23: Cross-section map of rod extensometers and eletrolevel inclinometers installation positions (Nyren, 1998).

A similar field monitoring scheme was employed at Hyde park for the Crossrail tunnelling, with extents of various instruments shown in Figure 7.24. The interpretation of ground movements was performed

in Wan (2014) and used in Avgerinos (2014) and in this chapter for comparison with numerical predictions.

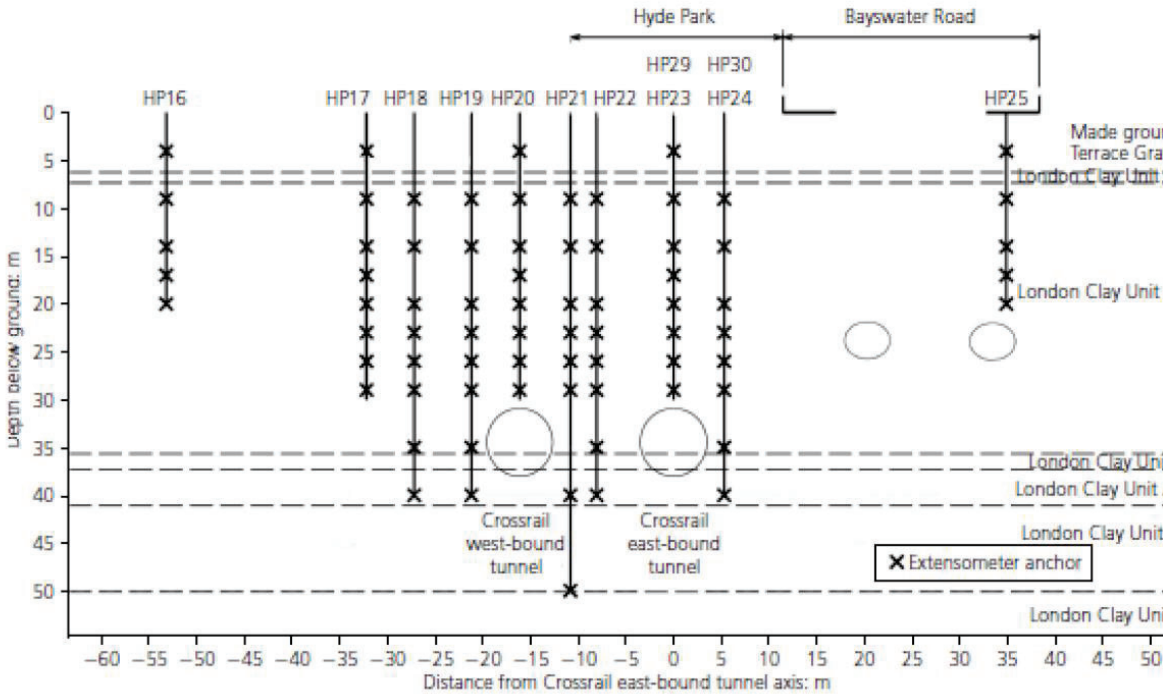


Figure 7.24: Cross-section map of rod extensometer boreholes in the main instrumentation alignment (after Wan, 2014b).

7.6.1 Ground surface movements due to tunnelling in short term

7.6.1.1 JLE twin tunnel and the DOT tunnel at St. James' Park

JEL twin tunnel

The ground surface settlement troughs immediately after the JLE westbound tunnel construction are plotted in Figure 7.25. The numerical results, based on 'low triaxial' and 'high both' calibrations, are compared with the field measurement. As also determined by Avgerinos (2014), the 'low triaxial' calibration simulates more accurately the short-term tunnel response., with the maximum settlement of 18.6mm compared to the measured 20.4mm. Although both calibrations resulted in similar volume losses (3.38% and 3.21%, respectively, see Table 7.3) compared to the measured 3.3% volume loss, the 'high both' calibration required 37% unloading of ground stresses to reach the target volume loss, compared to 12.5% unloading of the 'low triaxial' calibration. This is the result of the high soil stiffness in the former calibration case. The effect of the high soil stiffness is also manifested by the predicted wider settlement trough, as shown in the graphs of normalised settlement troughs in Figure 7.26.

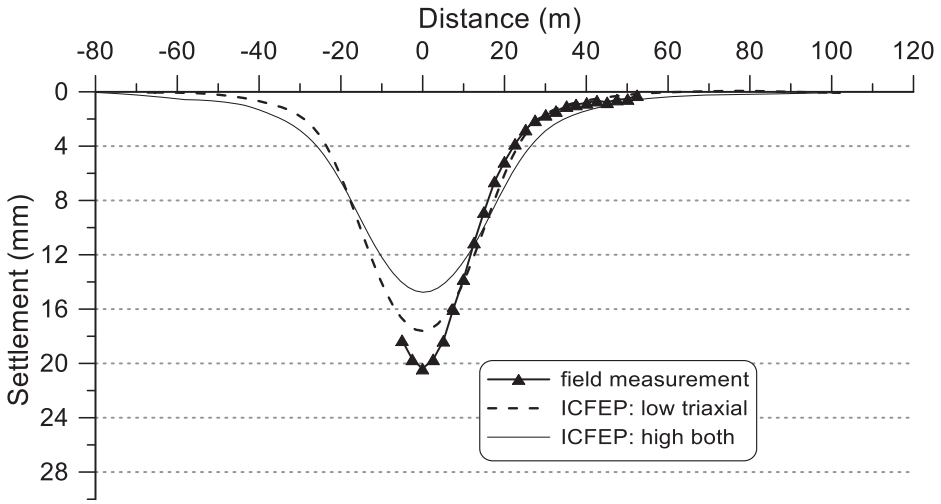


Figure 7.25: Ground surface settlement due to westbound tunnel construction

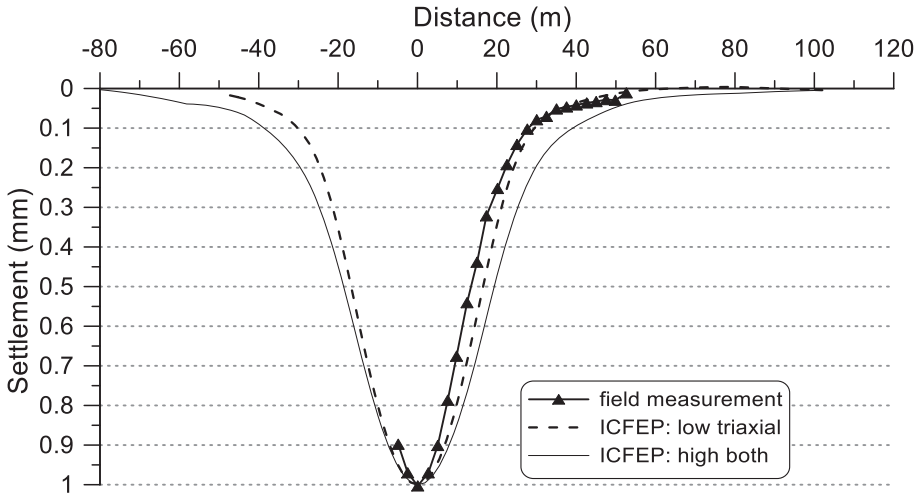


Figure 7.26: Normalised ground surface settlement troughs due to westbound tunnel

During the 8-month intermediate period before the eastbound tunnel excavation, the ground surface settlements are continuously increasing due to the transient soil consolidation. The evolution of settlements during this period is shown Figure 7.27, comparing the predictions from the analysis with 'low triaxial' calibration against field measurements, at stages immediately after westbound (wb) tunnel construction and immediately before and after eastbound (eb) tunnel construction. Despite some scatter in the field measurements the numerical results agree reasonably well with measurements. It can be also seen that the maximum settlement point is moving to the position between the two tunnels, reflecting the effect of soil disturbance caused by eastbound tunnelling. The deviation of peak point from the measured data shows an under estimate of soil softening effect, implying a larger disturbance occurs due to the second bore. The maximum calculated settlement has increased from 18.6mm to around 40mm, compared to the measured change from 20.4mm to around 36mm.

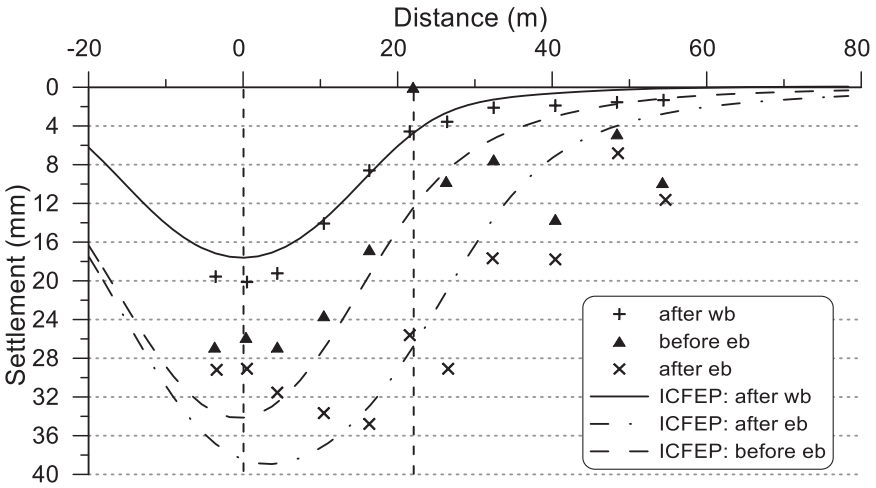


Figure 7.27: Settlement of twin tunnels compared to field data

Figure 7.28 plots in more detail ground surface settlement evolution during the intermediate period between wb and eb tunnel construction. It is clear that the settlement rate is reducing, from around 10mm over the first 4 months post-wb tunnel construction, to around 6 mm over the latter 4 months, but the consolidation and hence equilibration of pore pressures are not completed. Compared to the twin tunnels excavation in the Shanghai ground profile, the settlement after the first bore on the Shanghai Metro Line 4, which is a twin tunnel, only grew by 1mm in the 3-month intermediate period, due to higher permeability of the soft silty clary.

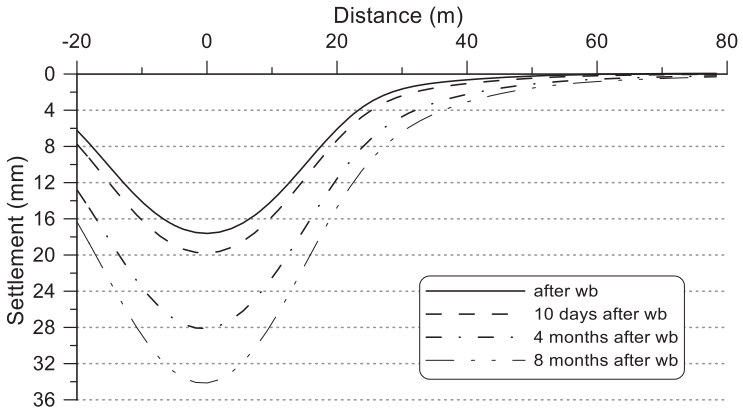


Figure 7.28: Development of westbound tunnel settlement during the intermediate period

DOT tunnel

The 'deeper' DOT tunnel is excavated at a depth of 30.5m, at the elevation of the JLE westbound tunnel, and the volume loss of 3.36% and 3.66% is achieved from the analyses with 'low triaixal' and 'high both' calibrations, respectively (see Table 7.3). It is also noted that the unloading percentages (11.0% and 35.0%) achieved for each calibration are very close to the values of the westbound tunnel excavation alone (12.5% and 37.0%) in the twin tunnel simulation. This agreement indicates a

consistent relationship between the volume loss and the unloading percentage with respect to soil shear strength and stiffness.

The 'shallower' DOT tunnel is excavated at a depth of 20m, at the elevation of the eastbound tunnel, achieving similar volume losses of 3.33% and 3.31% from the analyses with 'low triaxial' and 'high both' calibrations, respectively (see Table 7.3). Compared with the 'deeper' DOT and with the JLE wb tunnel, the unloading percentages are a slightly larger, at 13% and 40% for the two calibrations, respectively. This means that the lining construction is performed later in the tunnel excavation process because of the smaller ground stresses around the shallower tunnel, to allow sufficient deformation of the ground to mobilise for achieving the same volume loss. These observations are demonstrated through differences in predicted ground surface settlement troughs, as shown in Figure 7.29 and Figure 7.30 for the analyses with 'low triaxial' calibration. Based on the St James' park study, this calibration is employed for the analyses of the short-term ground response.

The predicted short-term ground surface settlements, within 1 year post-tunnel construction, are generally larger for the 'shallower' DOT tunnel. The largest difference is in settlements immediately after tunnel excavation. The maximum settlement induced by the 'deeper' DOT tunnel is 32mm (Figure 7.29) at this stage, while it is 40mm for the 'shallower' DOT tunnel (Figure 7.30). The difference between the two is 20% with respect to the 'shallower' tunnel settlement and explains the larger percentage unload needed for this DOT tunnel location. However, the predicted maximum settlements 1 year post-tunnel construction are closer, at 58mm and 62mm for the 'deeper' and 'shallower' DOT, respectively (around 6% difference with respect to 'shallower' tunnel). This implies smaller rate of ground surface settlement (22mm/year) induced by the 'shallower' DOT tunnel construction, compared to 26mm/year from the 'deeper' DOT tunnel.

The normalised ground surface settlement troughs of both deeper tunnels (DOT and JLE wb) are compared in Figure 7.31 for the stage immediately after excavation. They demonstrate practically the same shapes, unaffected by the volume of the excavated soil, and are also similar to the measured normalised settlement trough above the JLE wb tunnel. The comparison of the normalised surface settlement troughs of the DOT tunnels at different elevations in Figure 7.32 shows a distinctly narrower trough above the 'shallower' DOT tunnel.

Overall comparison of short-term ground surface settlements, induced by the actual JLE twin tunnel construction and a possible DOT tunnel construction at ST James' park, does not indicate dramatically different magnitudes due to the latter that would prevent its use in stiff clays.

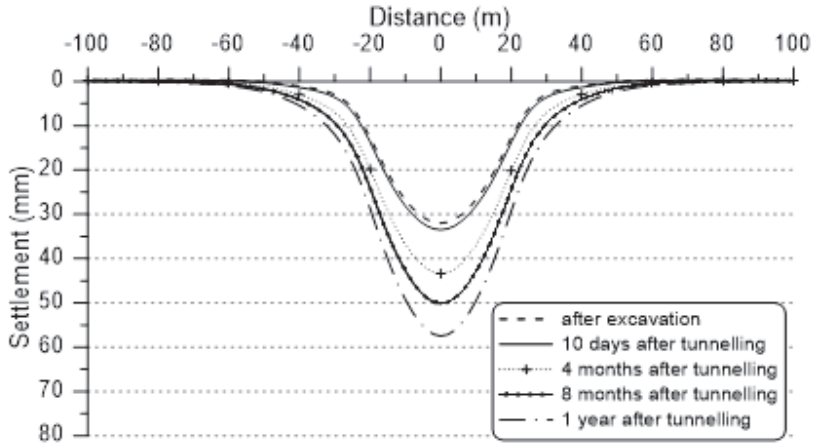


Figure 7.29: Predicted settlement for 'deeper' DOT in short term (low triaxial).

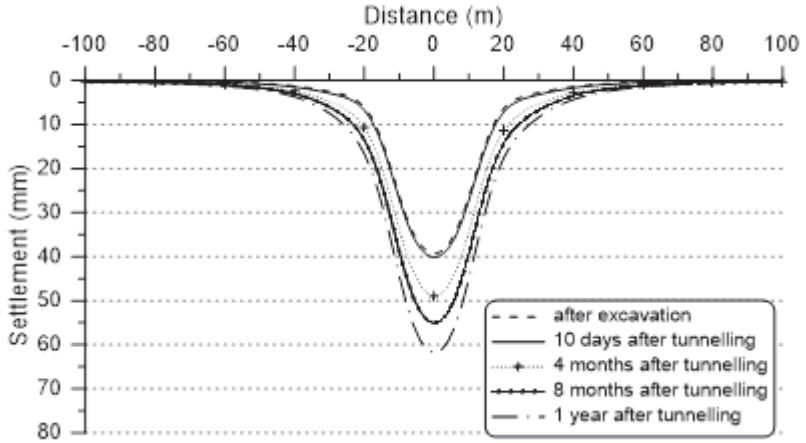


Figure 7.30: Predicted settlement for 'shallower' DOT in short term (low triaxial).

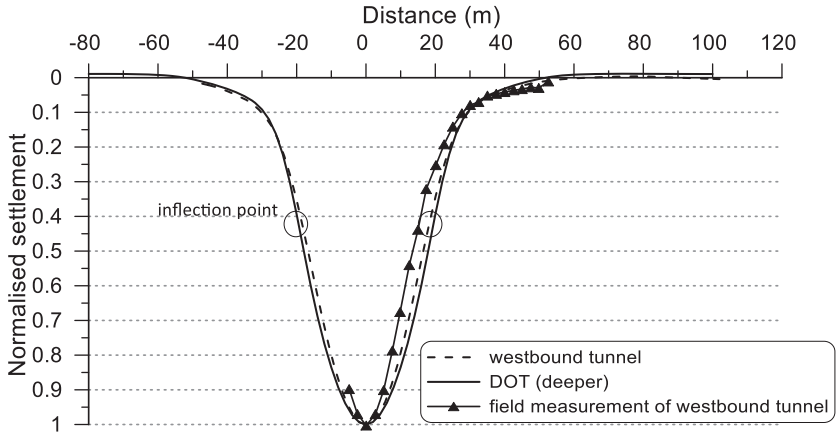


Figure 7.31: Normalised settlement of 'deeper' DOT and westbound tunnels immediately after excavation

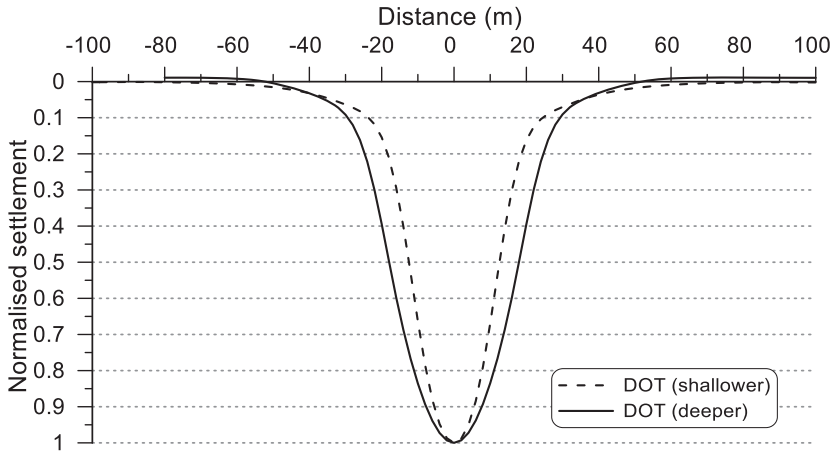


Figure 7.32: Normalised settlement of 'deeper' DOT and 'shallower' DOT.

Comparison of settlements between twin tunnels and DOT

The immediate settlement induced from westbound tunnel in the twin tunnelling case shows much smaller magnitude compared to the DOT excavation (see Figure 7.33). In this figure, the zero distance axis is defined on the centre of westbound and the centre of DOT for convenience of comparison. The deeper DOT causes about 32mm maximum immediate settlement, compared to that of the westbound tunnel (18.6mm). The immediate surface settlement of the shallower DOT tunnel reaches 39mm, which is almost twice the settlement of the wb tunnel alone. However, after the excavation of eastbound tunnel, the difference in the maximum settlement between twin tunnels and DOT tunnel is reduced (see Figure 7.34). The maximum settlement of twin tunnels reaches 39mm from the numerical result, which is comparable with the field data, while the values for deeper and shallower DOT after the same consolidation period of 8 months (but no further tunnelling) are 50mm and 55mm respectively. The deeper DOT, which is constructed at the same depth as the westbound tunnel, still has higher maximum settlement than the twin tunnels by around 25% after the same consolidation period (8 months). Therefore, it can be concluded that the DOT excavation causes obviously larger settlement compared to the twin tunnels in short term, but the difference reduces with consolidation.

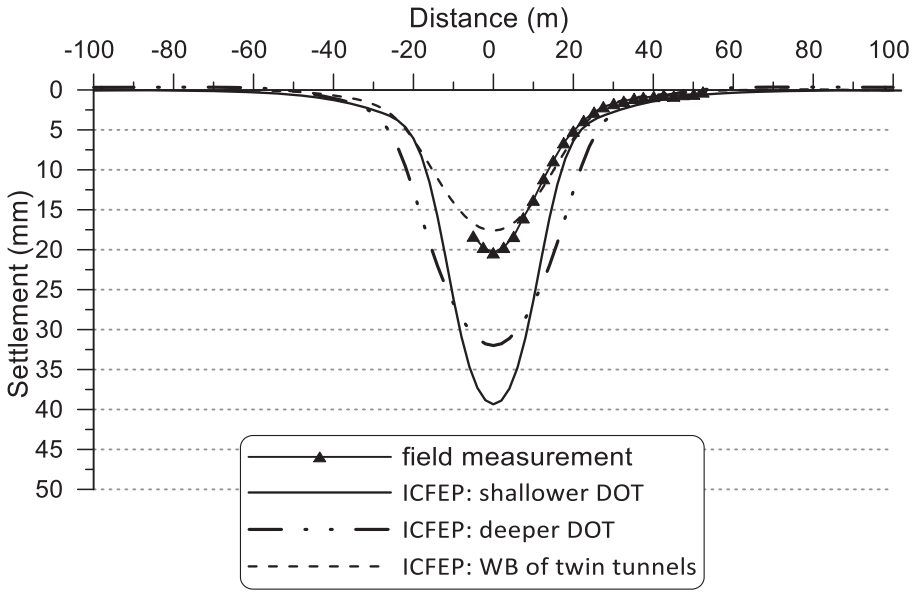


Figure 7.33: Comparison of settlement troughs after single tunnel (wb)/ DOT excavation.

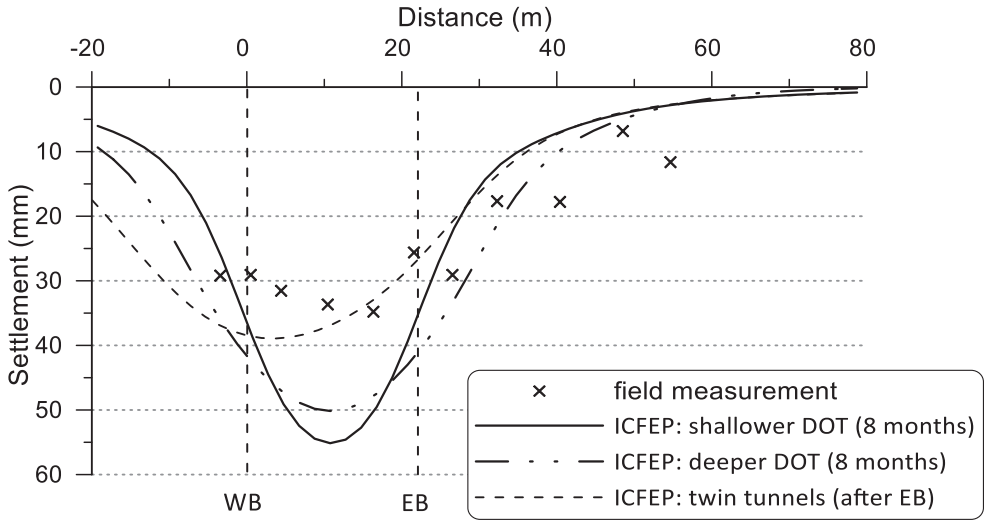


Figure 7.34: Comparison of settlement troughs after twin tunnels (wb&eb) / DOT excavation

7.6.1.2 Cross-rail tunnels and the DOT tunnel at Hyde Park

Twin tunnels

The ground profile at Hyde Park has an under drained pore water pressure profile, which reduces in magnitude from London clay unit A2 to Upper and Lower Lambeth groups. The influence of the hydraulic boundary conditions, in terms of the permeability of the tunnel lining, is investigated here with respect to the ground water profile and induced ground movements. The permeable lining is modelled by prescribing the precipitation boundary condition around the lining, which has been introduced in the modelling of JLE above, while the impermeable lining is modelled by specifying zero water flow around the boundary. The results of two analysis sets, assuming fully permeable or

impermeable lining, are shown and discussed.

According to the results in Avgerinos (2014), the 'low triaxial' and 'low both' reached good agreement on the surface settlement of the twin tunnelling in the Hyde Park for short term and long term simulation, respectively. Therefore, both calibrations are adopted in this study of twin tunnels and DOT construction simulation.

The target ground loss for the simulation, which is based on field measurements, is 0.8% and 1.4% for the westbound and eastbound tunnels, respectively. Table 7.9 summarises the achieved volume losses in FE simulations, for the two calibrations of the M2-SKH model and for two extreme permeability conditions (fully permeable and impermeable) of the tunnel lining, while Table 7.10 summarises the respective percentage unloading when the tunnel lining was constructed. With respect to DOT tunnel, the adopted target volume loss was a mean value (1.1%) of the two measured volume losses, to be on a conservative side as the volume loss on the WB tunnel was smaller than on the EB tunnel. This is slightly different from the St James' park study described in Section 7.6.1.1, where the DOT volume loss target was that of the firs-excavated WB tunnel, as this was larger than the EB tunnel volume loss

Table 7.9: Volume loss achieved in the analysis for each case

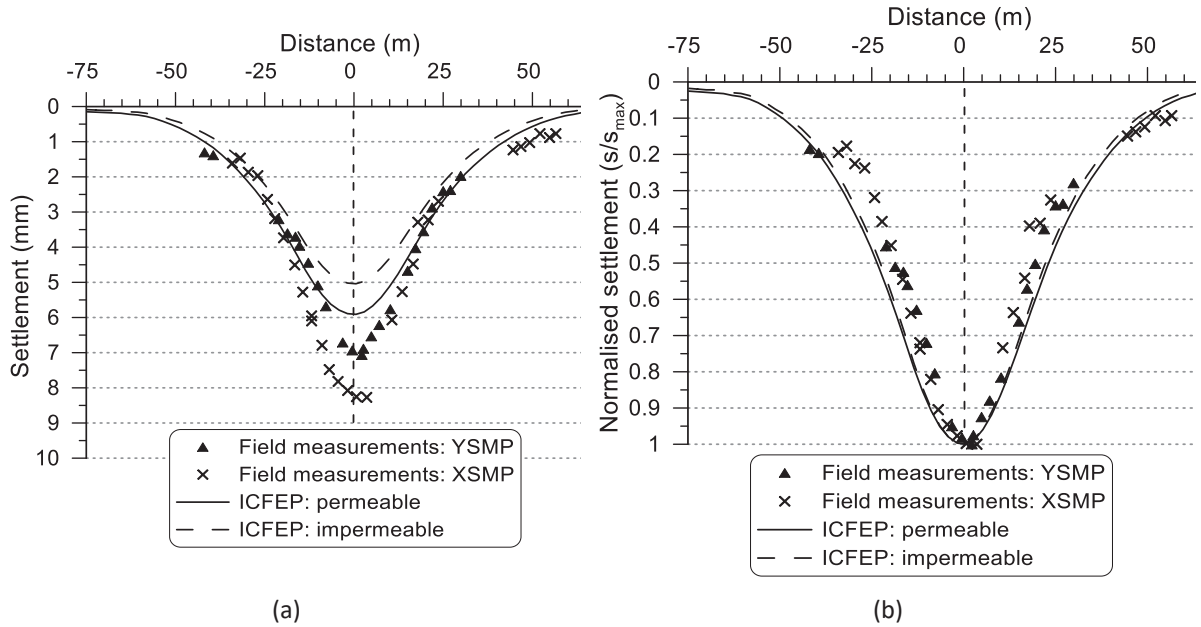
Volume loss (%)	**LOW TRIAXIAL**		**LOW BOTH**	
	permeable	impermeable	permeable	impermeable
WB	0.85	0.71	0.87	0.75
EB	1.26	1.20	1.29	1.25
DOT	1.03	0.72	1.06	0.81

Table 7.10: Unloading percentage of tunnelling analysis for Hyde Park site

Unloading percentage (%)	**LOW TRIAXIAL**		**LOW BOTH**	
	permeable	impermeable	permeable	impermeable
WB	7	7	17	17
EB	9	12	19	23
DOT	5	5	14	14

The 'low traixial' analysis results are presented for the short-term ground response, as this calibration was shown by Avgerinos (2014) to more applicable to short-term conditions. The ground surface settlements immediately after excavation of the WB tunnel at Hyde Park are plotted in Figure 7.35. As expected, the analysis with a permeable lining predicts larger settlements than the one with an impermeable lining (Figure 7.35a) and is in a closer agreement with measured settlements. The

measurements, recorded at two surface monitoring sections perpendicular to the tunnel axis, and about 100m apart (lines X and Y, Avgerinos (2018)), show slight mismatch of the two measured settlement troughs. The predicted and measured normalised settlement troughs show good agreement in Figure 7.35b.



(a) (b)

Figure 7.35: Settlement of ground surface after westbound excavation in Hyde Park site a) predicted settlement against field data; b) normalised settlement

The ground surface settlements at the end of the 74 days of transient period (consolidation) after WB tunnel construction and before EB tunnel construction are shown in Figure 7.36. It is evident that the assumption of an impermeable tunnel lining is underpredicting the magnitude of settlement, while the permeable lining predicts significantly larger settlement during this period. Therefore, neither of the assumptions seems appropriate and the lining should be simulated as partially permeable. However, it will be hard to precisely determine the water flow rate into the tunnel or the relative permeability of the lining to the permeability of the soil, as both parameters could be changing with time.

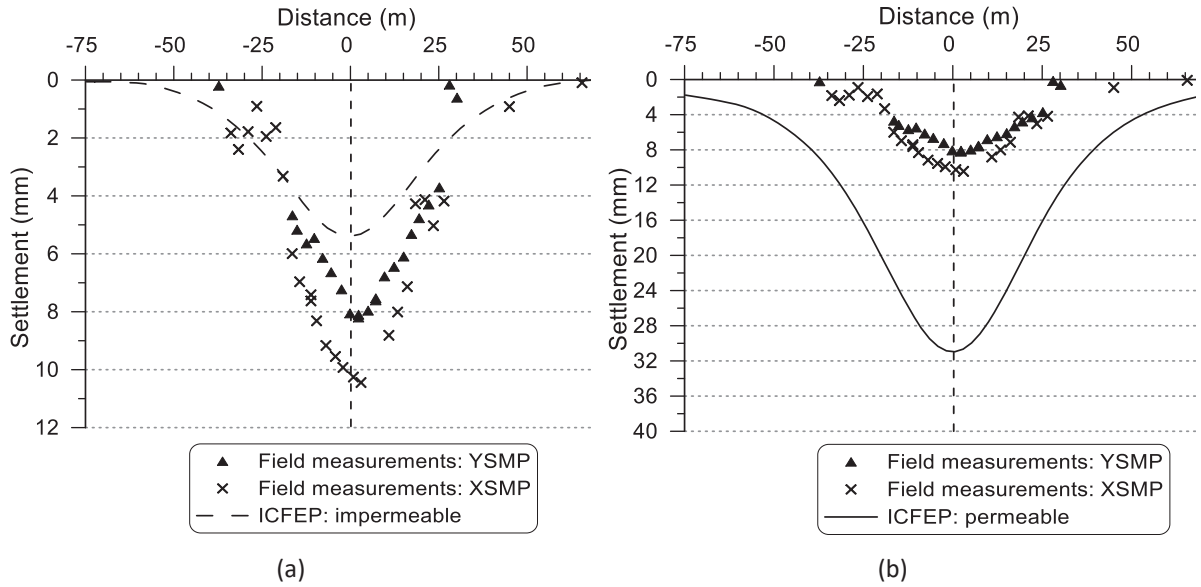


Figure 7.36: Settlement of ground surface prior to excavation of the eastbound tunnel: a) impermeable lining; b) permeable lining

As for the width and the shape of the settlement trough, the impermeable lining assumption leads to closer agreement with the field data (see normalised settlement troughs in Figure 7.37, indicating that the water inflow through the lining is perhaps small.

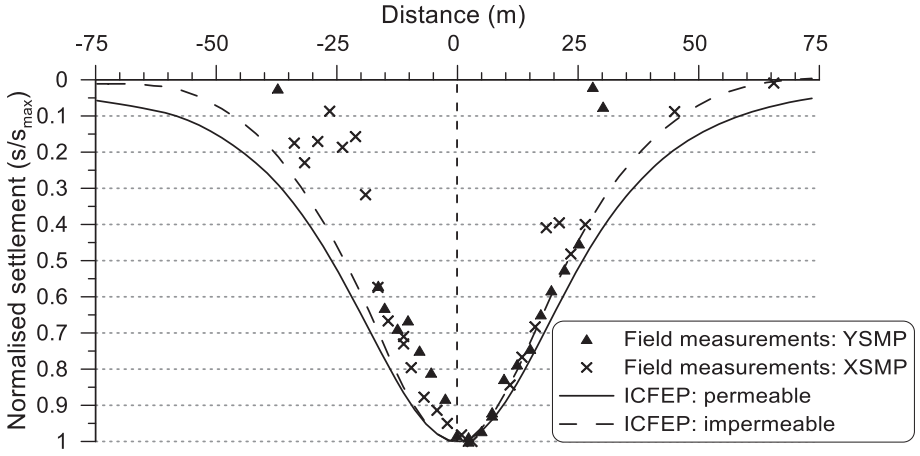
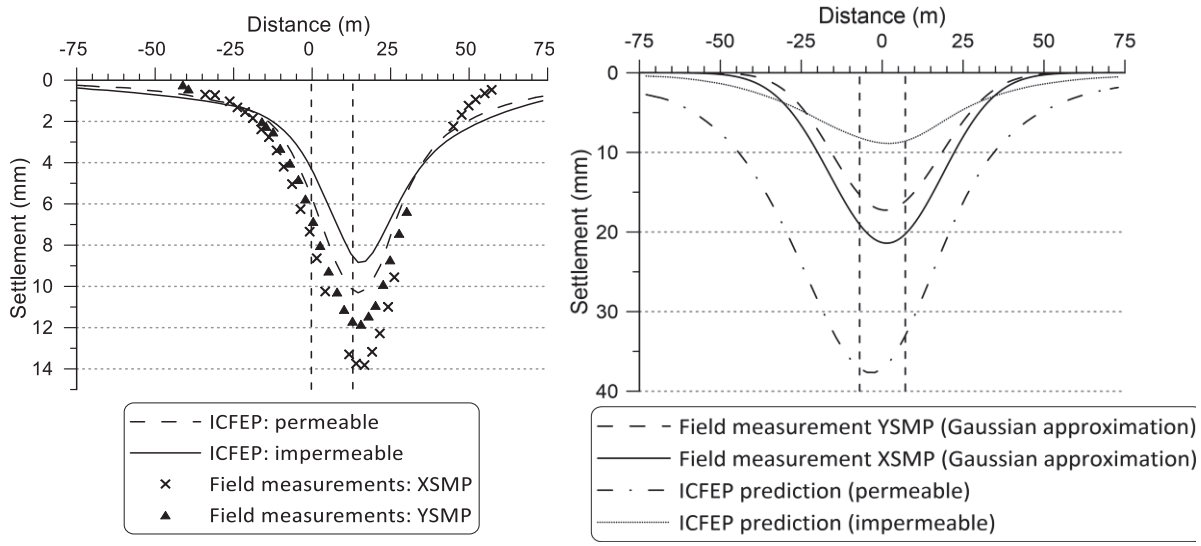


Figure 7.37: Normalised settlement of ground surface prior to eastbound excavation

The measured ground surface settlements due to the construction of the EB tunnel only (Wan et al., 2017) are compared against numerical prediction in Figure 7.38a, showing again that during a very short time of tunnel excavation (practically undrained conditions) the settlement trough predicted with permeable lining is closer to field measurements. However, the field data of the overall settlement of the twin tunnels, which reflects the overall ground response after the eastbound construction, is not given in the literature. Therefore, by using approximation of the Gaussian curve on the measured settlement data prior to the eastbound tunnel construction and the measured data

from the incremental settlement due to the eastbound tunnel construction, the likely overall 'measured' settlement is approximated with addition of both curves (see Figure 7.38b). In Figure 7.38a, the zero axis of the horizontal distance is still set on the westbound centre, and the maximum incremental settlement due to eastbound tunnelling, is hence taking place at the centre of eastbound. In Figure 7.38b, the zero axis lies at the centre of the mesh, and the curves of field measurement are deduced from composition of Gaussian approximation. The large deviation could be found from the permeable lining simulation and impermeable lining simulation, and the sets of field measurements, represented by Gaussian approximation are in between these two extreme conditions. In Figure 7.38b and Figure 7.39, the zero distance is redefined on the mid-position between two tunnel axes for convenience of comparison against DOT results below.



(a) (b)

Figure 7.38: Settlement of ground surface: a) due to eastbound tunnelling; b) overall settlement immediately after eb with field data deducted from Gaussian approximation

In short term up to one year post twin tunnelling, the numerical prediction results based on impermeable lining assumption (see Figure 7.39a) show the stabilisation of the settlement has reach after the eastbound excavation, implying the equilibrium of pore water pressure in the ground, and consequently, it can be expected that the ground movement cannot develop in longer term. However, the permeable lining leads to continuously developing settlement of the ground surface, with very large ground movement in short term post eastbound construction. It is noted that from 150 days to 1 year after eastbound tunnelling, the predicted maximum settlement grows from about 90mm to 132mm, and it seems the ground is still far from stabilisation one year after tunnelling. Therefore, long term behaviour of the ground is necessary to investigated for the case with permeable lining assumption.

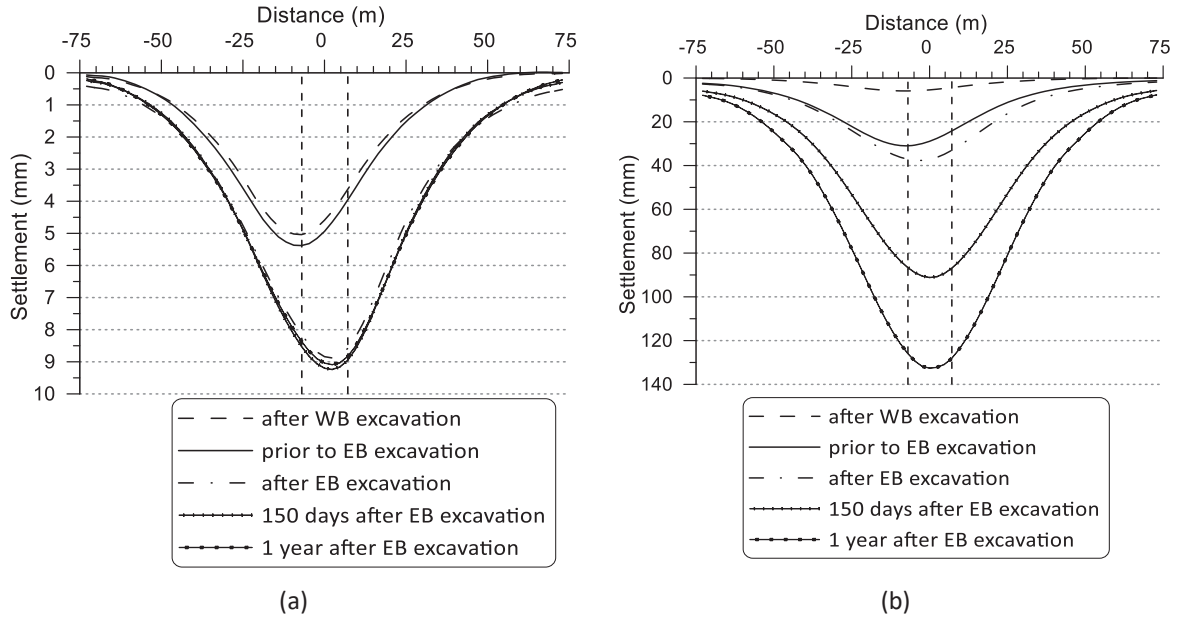
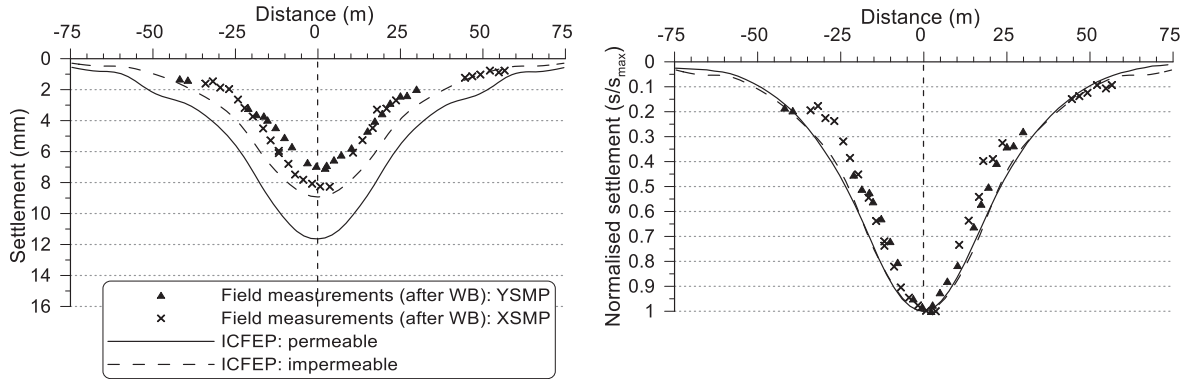


Figure 7.39: Predicted settlement of twin tunnelling for short term in Hyde Park site: a) impermeable lining; b) permeable lining

DOT tunnel

The DOT tunnel simulation is carried out under the same assumptions introduced in the twin tunnel analysis, and the ground response due to the DOT tunnel is compared with the WB tunnel excavation and with the twin tunnel excavation simulated above. The immediate settlement of the ground surface induced by DOT tunnel construction is shown in Figure 7.40, in comparison with field measurement due to twin tunnel construction (Figure 7.35a). The magnitude of settlements is larger in DOT simulations for both permeability of the tunnel lining, which reflects the larger excavated volume but also a slightly larger volume loss achieved in this simulation (1.03%), compared to the field volume loss (0.8%) and that achieved in the twin tunnel analysis for WB tunnel construction (0.85%). However, the normalised settlement trough of DOT tunnel has a similar shape compared to the normalised measured WB settlement through.



(a) (b)

Figure 7.40: Settlement of ground surface after DOT excavation in Hyde Park site. a) settlement troughs; b) normalised settlement

In short term, the evolution of surface settlement seems to finish in a very short period after DOT excavation (see Figure 7.41a). It is noted that the maximum settlement achieved with DOT excavation in short term after stabilisation under impermeable lining assumption is about 9mm, almost the same magnitude as the corresponding results from twin tunnels simulation (see Figure 7.39a). In fact, the enclosed area of the surface settlement trough for DOT simulation theoretically is the same with twin tunnels after excavation due to the same volume loss following. Since the distance between two tunnel axes is relatively small (only 15.2m) compared with the tunnel diameter (6.8m), the overall settlement curve envelops the independent troughs of each single bore. Both settlement troughs of the surface induced from DOT and twin tunnelling could be approximated with Gaussian distribution, and that results in the same settlement manner under identical ground loss in the same ground conditions. As for permeable lining condition, the settlement of the surface in DOT simulation is continuously developing in short term as well, and it is noteworthy that the magnitudes of maximum settlement, at 74 days, 150 days and 1 year post construction, are close to the corresponding values from twin tunnels (see Table 7.11, Figure 7.41b and Figure 7.39b, Figure 7.42). The DOT tunnel even leads to less settlement by about 10% in 1 year post construction.

Table 7.11: Maximum settlement of the ground surface post construction of WB and DOT

Maximum settlement of ground surface (mm)	**Impermeable**	**Permeable**		
	1 year	74 days (after EB)	224 days (74d+150d)	1 year
Twin	9.09	37.66	91.17	132.58
DOT	9.05	45.30	79.14	112.33

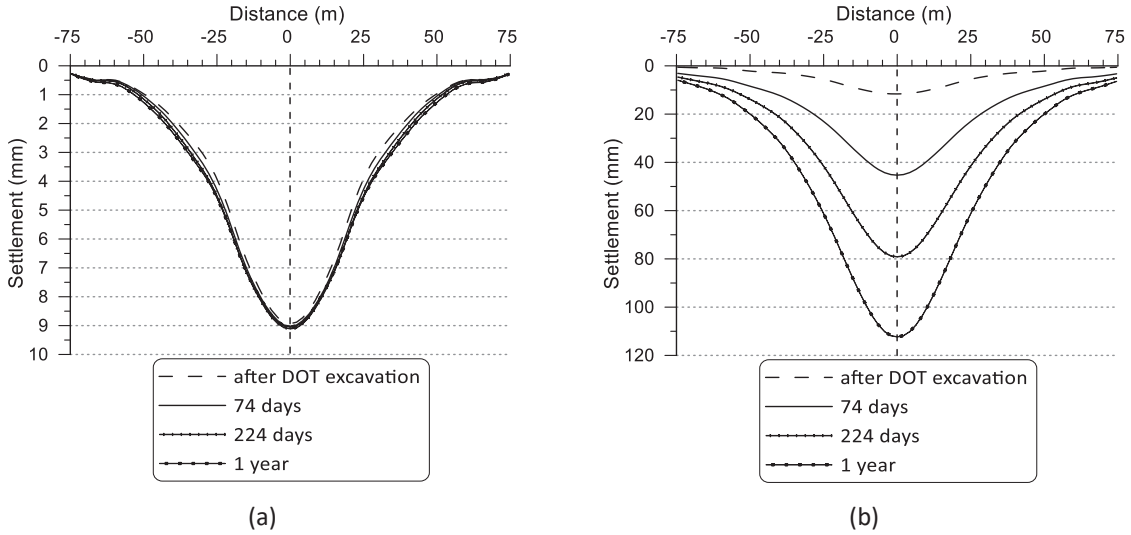


Figure 7.41: Evolution of surface settlement after DOT excavation for short term: a) impermeable lining; b) permeable lining

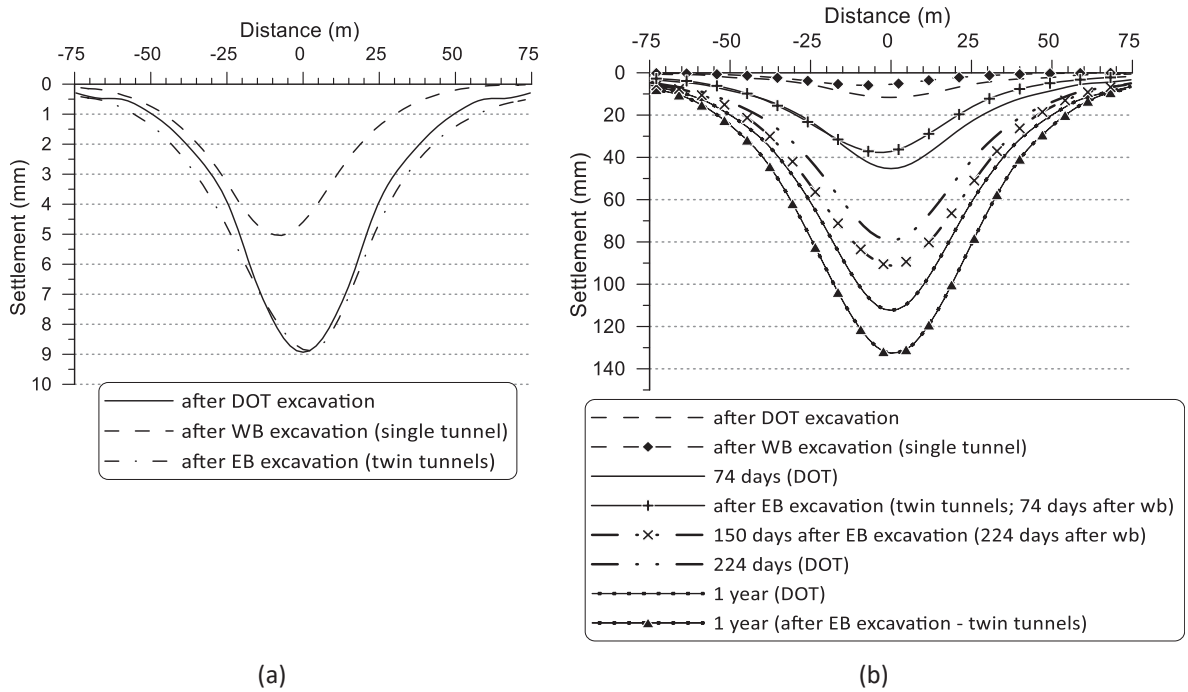


Figure 7.42: Comparison of settlement troughs between DOT and twin tunnels for short term. a) impermeable lining; b) permeable lining

7.6.2 Long term settlement of ground surface

7.6.2.1 Surface settlement of twin tunnels and the DOT in St. James' Park

Twin tunnel

The measured settlements of the ground surface in Figure 7.43 and Figure 7.44 are shown to increase at two distinct dates (10 and 15 years) after the excavation of the EB tunnel. The precipitation boundary condition on the lining allows transient change from the initial representation of the lining

as impermeable to the long-term permeable lining. The numerical predictions adopting the 'low triaxial' calibration significantly overpredict the measured settlements in later years, while the 'high both' calibration underpredicts the measurements. The latter predictions are, however, closer to measurements, demonstrating the conclusion of Avgerinos (2014) that the 'low triaxial calibration was more appropriate for the short-term ground response, while the 'high both' was more representative of ground movements in the long term. Moreover, the latter calibration reproduces very well the rate of settlement between 2006 and 2011 observed in measurements, while the former calibration overpredicts it. It also predicts a wider settlement trough, which is in closer agreement with measurements.

Figure 7.45 shows the predicted very long term ground surface settlements from the 'high both' calibration analysis, which indicates further slight increase of settlements until 100 years of the post-construction period. In this figure, the trough of 50 years and 100 years are almost overlapped, implying that the consolidation ends before 100 years post tunnelling.

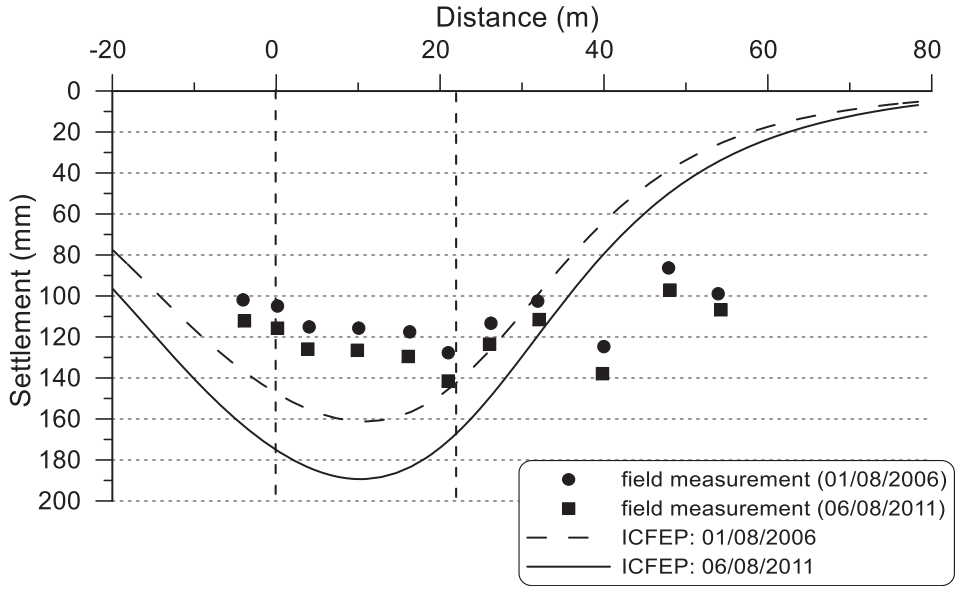


Figure 7.43: Predicted settlement for twin tunnels after eastbound tunnelling for long term (low triaxial).

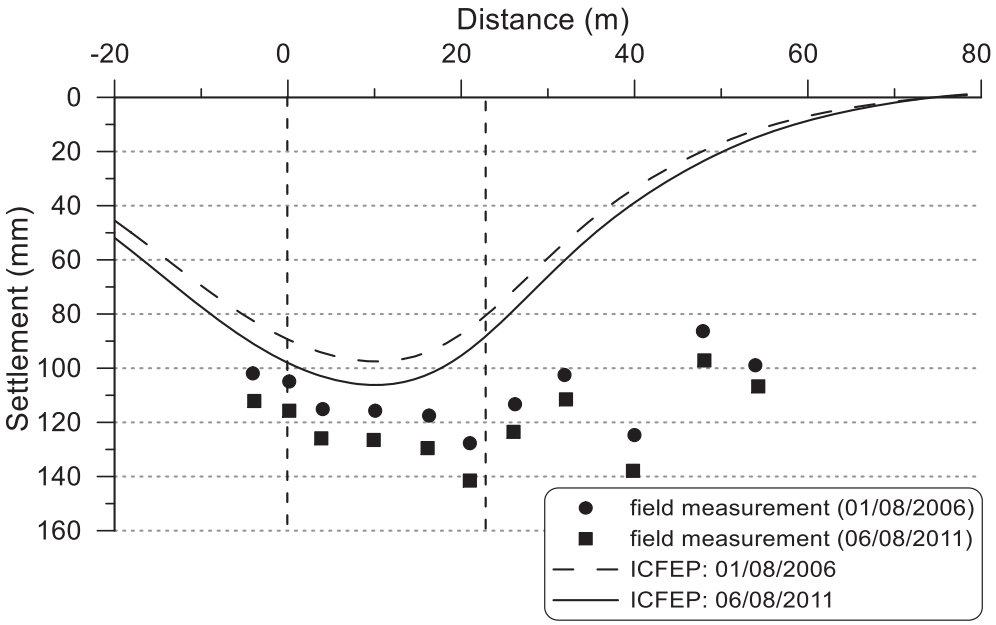


Figure 7.44: Predicted settlement for twin tunnels after eastbound tunnelling for long term (high both).

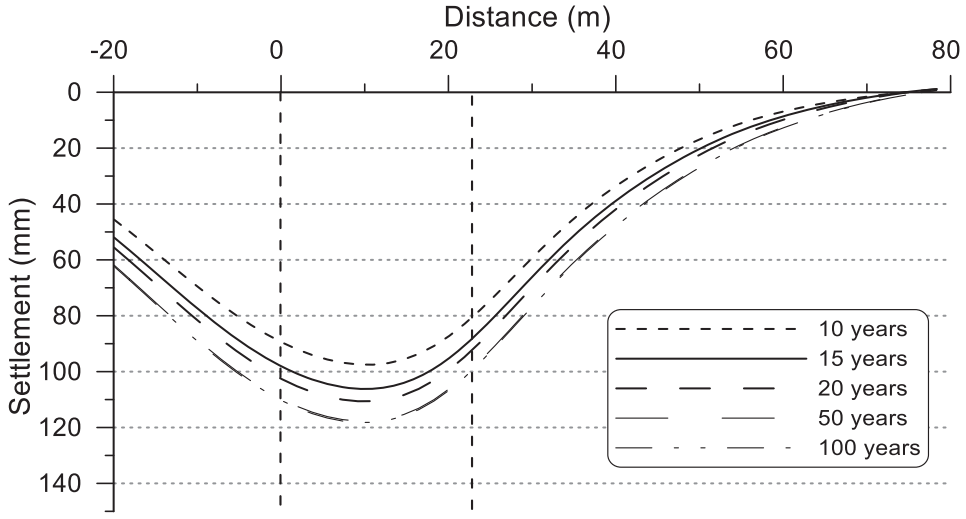


Figure 7.45: Predicted settlement for twin tunnels for tunnel life term (high both).

DOT tunnel

Long term consolidation of DOT tunnel simulation in London clay results in ground surface settlement troughs shown in Figure 7.46 and Figure 7.47, from the analysis with 'high both' calibration and for the two possible elevations of the DOT tunnel. The maximum time duration in the simulations is 100 years.

At both tunnel elevations the rate of settlement reduces with time. However, while the 'deeper' tunnel develops smaller settlements in short term (Figure 7.29) compared to the 'shallower' tunnel in Figure 7.30 (up to 1 year after completion of tunnel construction and with the 'low triaxial' calibration), the opposite is seen in the long term (up to 100 years) where the deeper tunnel (Figure 7.46) mobilises

larger settlements compared to the shallower tunnel (Figure 7.47). It may be explained with ground lowering in deeper tunnel which is conditioned with fully permeable lining. The magnitudes of settlement of the deeper tunnel are also comparable to ground surface settlements in the long term predicted for the twin tunnels (Figure 7.45) (around 125 mm). The predicted maximum settlement of the DOT tunnel at shallower elevation is around 80mm.

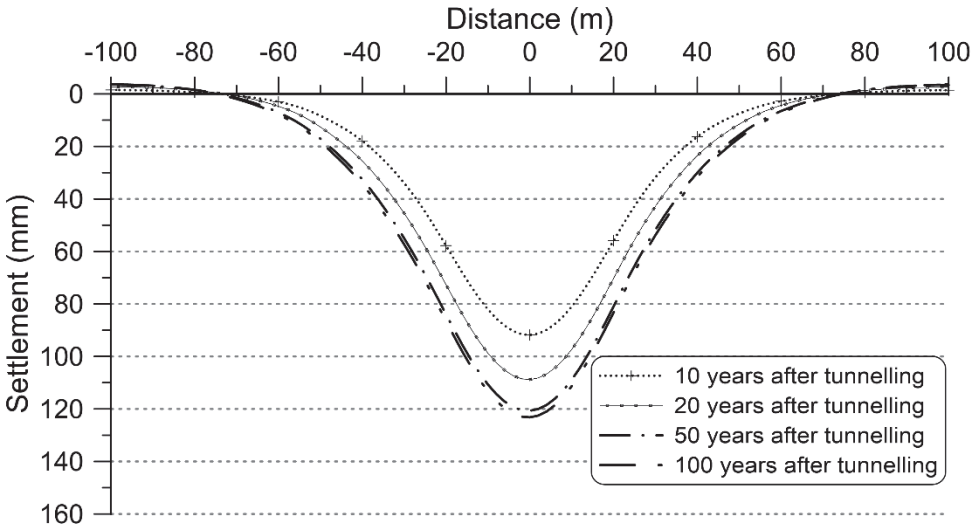


Figure 7.46: Long term settlement of 'deeper' DOT tunnel

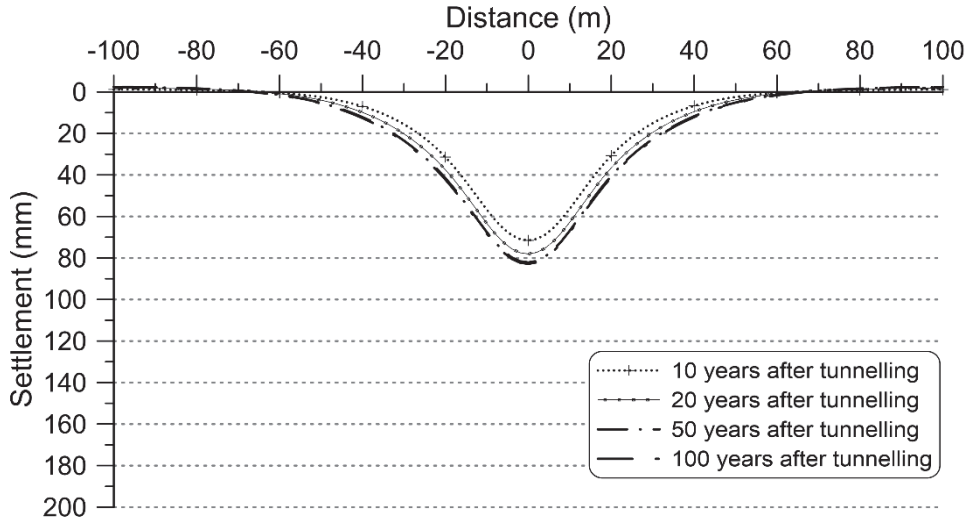


Figure 7.47: Long term settlement of 'shallower' DOT tunnel

The evolutions of the settlement in long term consolidation for both twin tunnels and DOT are shown in Figure 7.48. The DOT tunnel at deeper position shows very similar trend of settlement with the twin tunnels simulation results. The settlement is stabilised after 50 years for both DOT and twin tunnels simulations, implying the end of long term consolidation. The twin tunnel results of 'low triaxial' shows obviously over-predicted settlement, and maximum value at 100 years is 230% that of the 'high both'. The diagram indicates that the long term ground response of twin tunnels are close to the deeper DOT, and smaller settlement can be achieved for the DOT constructed at shallower depth.

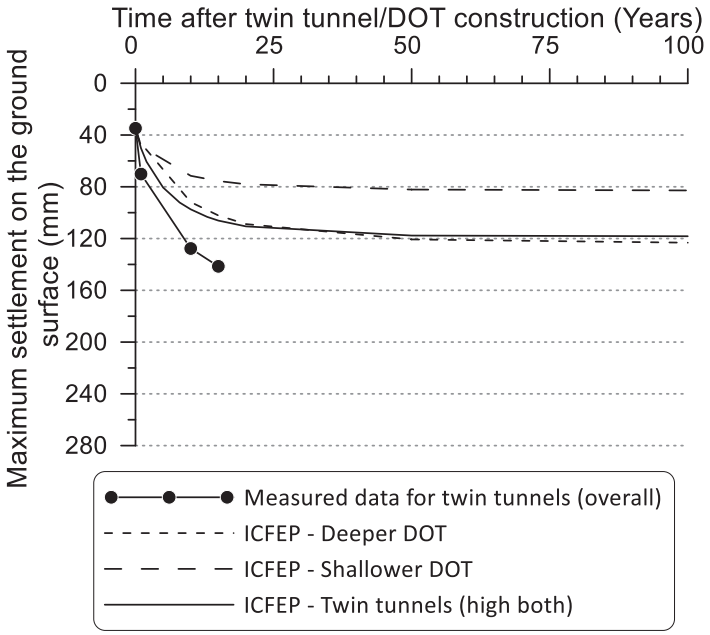


Figure 7.48: Evolution of the maximum ground surface settlement of tunnelling in St James' park

7.6.2.2 Surface settlement of twin tunnels and the DOT tunnel in Hyde Park

The predicted settlement troughs in the long term, in respect to twin tunnel and a DOT tunnel simulations for the Hyde Park ground conditions, are plotted in Figure 7.49 for the period of 10, 20 and 100 years after tunnelling. The settlement results of 50 years were found very close to 100 years (see Table 7.12), and hence the corresponding trough is not presented in the plots below. Both the twin tunnel and the DOT tunnel indicate a significant reduction in the settlement rate after 10 years post-construction and there is also practically no further settlement after 50 years. Although the predicted long-term movements from a DOT tunnel are smaller than from a twin tunnel construction, they are very comparable, indicating again no particularly adverse effects from DOT construction. Similar observations were made in the St James' park study.

Table 7.12: Maximum settlement of ground surface in long term

Maximum settlement (mm)	**After EB/74 days after DOT**	**10 years**	**20 years**	**50 years**	**100 years**
Twin tunnels	23.01	170.49	181.25	184.53	184.77
DOT	10.41	149.37	162.14	167.49	167.69

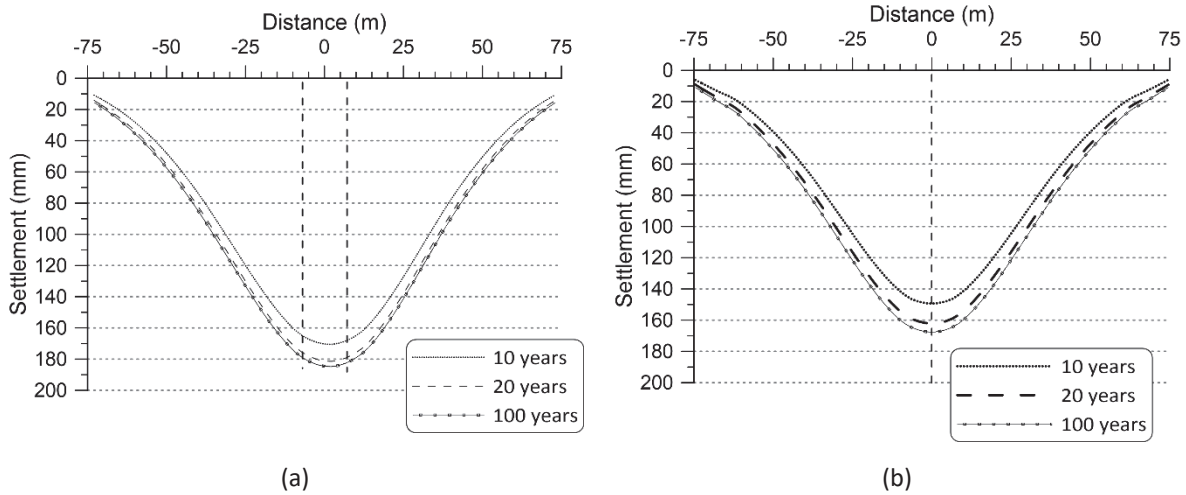


Figure 7.49: Predicted settlement of ground surface in Hyde Park site for long term: a) twin tunnels; b) DOT tunnel

7.7 Subsurface ground surface movements due to tunnelling

7.7.1 St James' Park

The subsurface settlement of both the twin tunnels and of the DOT tunnel have been studied. In the twin tunnel case, the vertical and horizontal displacements of subsurface layers were measured at measurement axes A, B and C shown *Figure 7.23*. The predicted vertical displacements immediately after WB tunnel construction are shown in Figure 7.50 for each of the axis and for the 'low triaxial' and 'high both' calibration, and are compared against monitoring data. The suitability of the 'low traxial' calibration for short-term ground response is further verified here as it achieves a very close agreement with field data.

The negative sign of vertical displacements indicates ground settlement above the WB tunnel crown, which, as expected, increases with depth and is the largest at the elevation of the tunnel crown in all three vertical instrumented axes. The maximum settlement of around 45mm is measured directly above the tunnel crown, in axis B. The measurements are not available for depths below the tunnel crown, but numerical predictions with both calibrations indicate slight swelling at the level of the tunnel invert. The ground movements in axes A and C are identical as these axes are symmetrical with the respect to the vertical tunnel axis (which coincides with the instrumentation axis B).

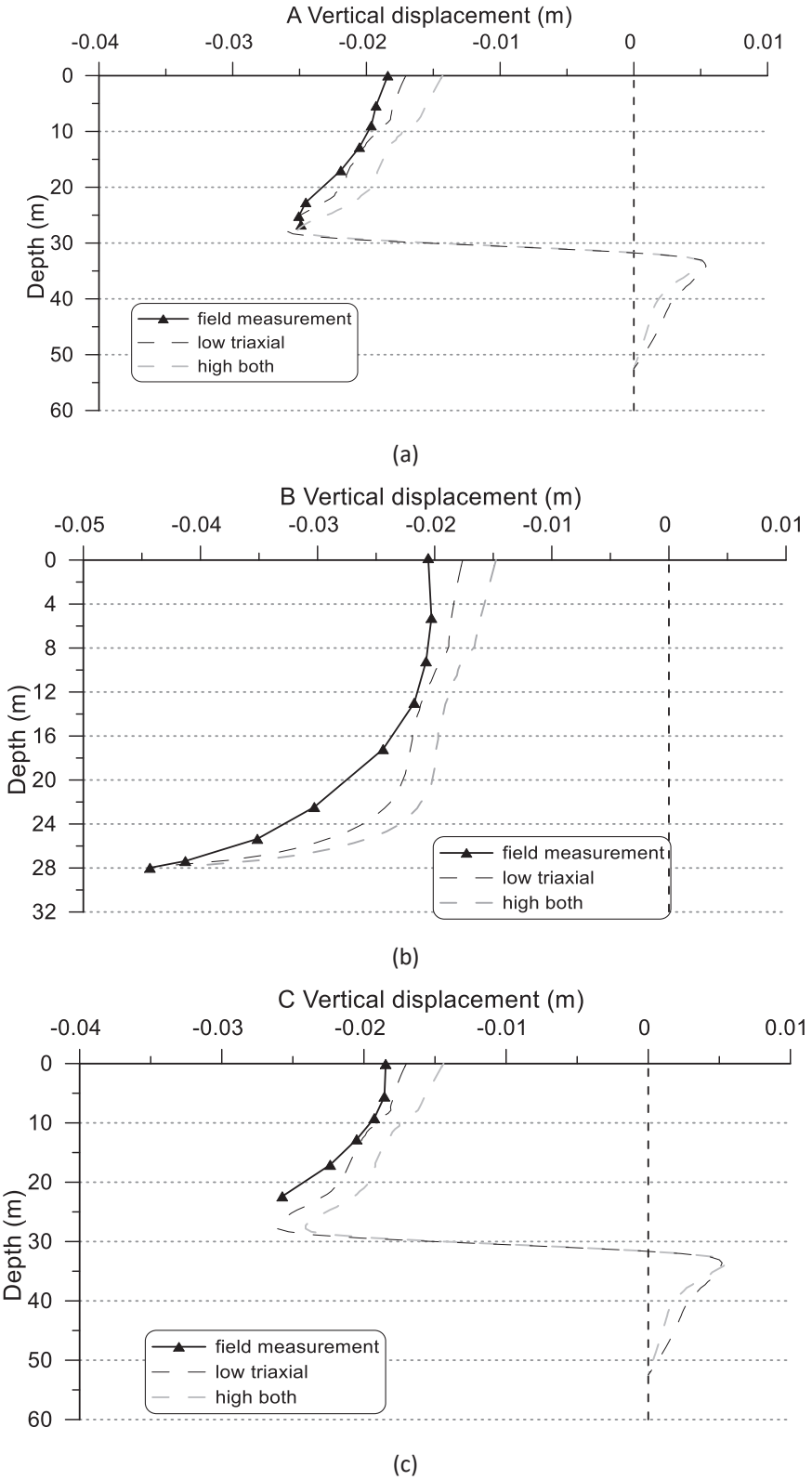


Figure 7.50: Subsurface settlement measured at A, B and C axes (-ve is settlement), after WB tunnel construction.

The horizontal displacements are shown in Figure 7.51 along the C axis, with measurements available from electrolevel inclinometers (Nyren, 1998). An unrealistic measured movement could be found in

the upper layers, as the soil seems to move away from the WB tunnel. Nyren (1998) explained that the error could be attributed to rapid gradient change between two adjacent instruments. However, the measurements further below correctly indicate horizontal displacements towards the tunnel (-ve sign), with the maximum reached at the elevation of the tunnel spring-line. The predicted displacements correctly indicate only negative horizontal movements (towards the tunnel) and are in good agreement with measurements in the vicinity of the tunnel.

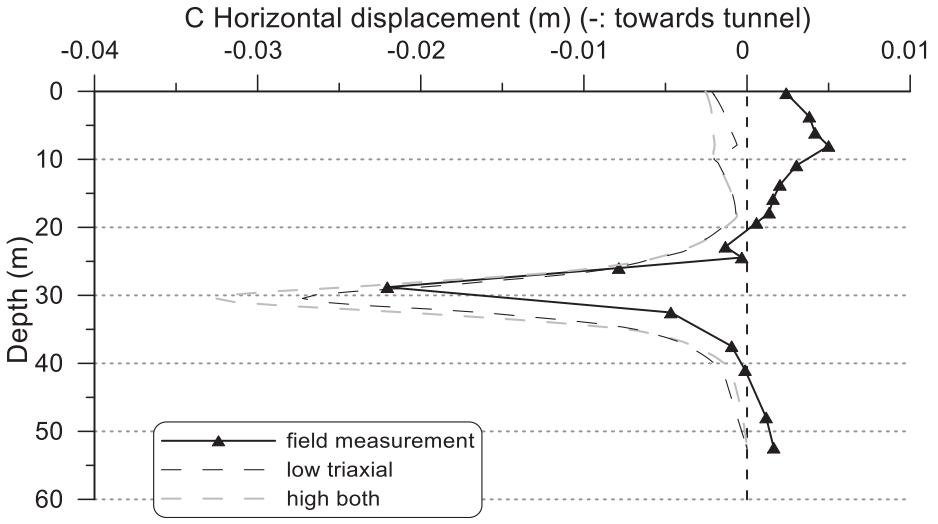


Figure 7.51: Horizontal displacement measured at C axis, after WB tunnel construction.

The corresponding comparison for the line A, B & C after the eastbound construction and the 1 year post that is given in *Figure 7.52*. It can be seen that the displacement values have been significantly increased due to the eastbound excavation and the short term consolidation. The 'high both' calibration retains the smaller subsurface settlement growth at both stages compared to the 'low triaxial' results. Both calibrations generated reasonably comparable troughs against the field data. The numerical results indicate an equally increase of the subsurface settlement above the tunnel crown along these axes, whereas the larger displacement occurs on shallower depth in reality according to the measurement data.

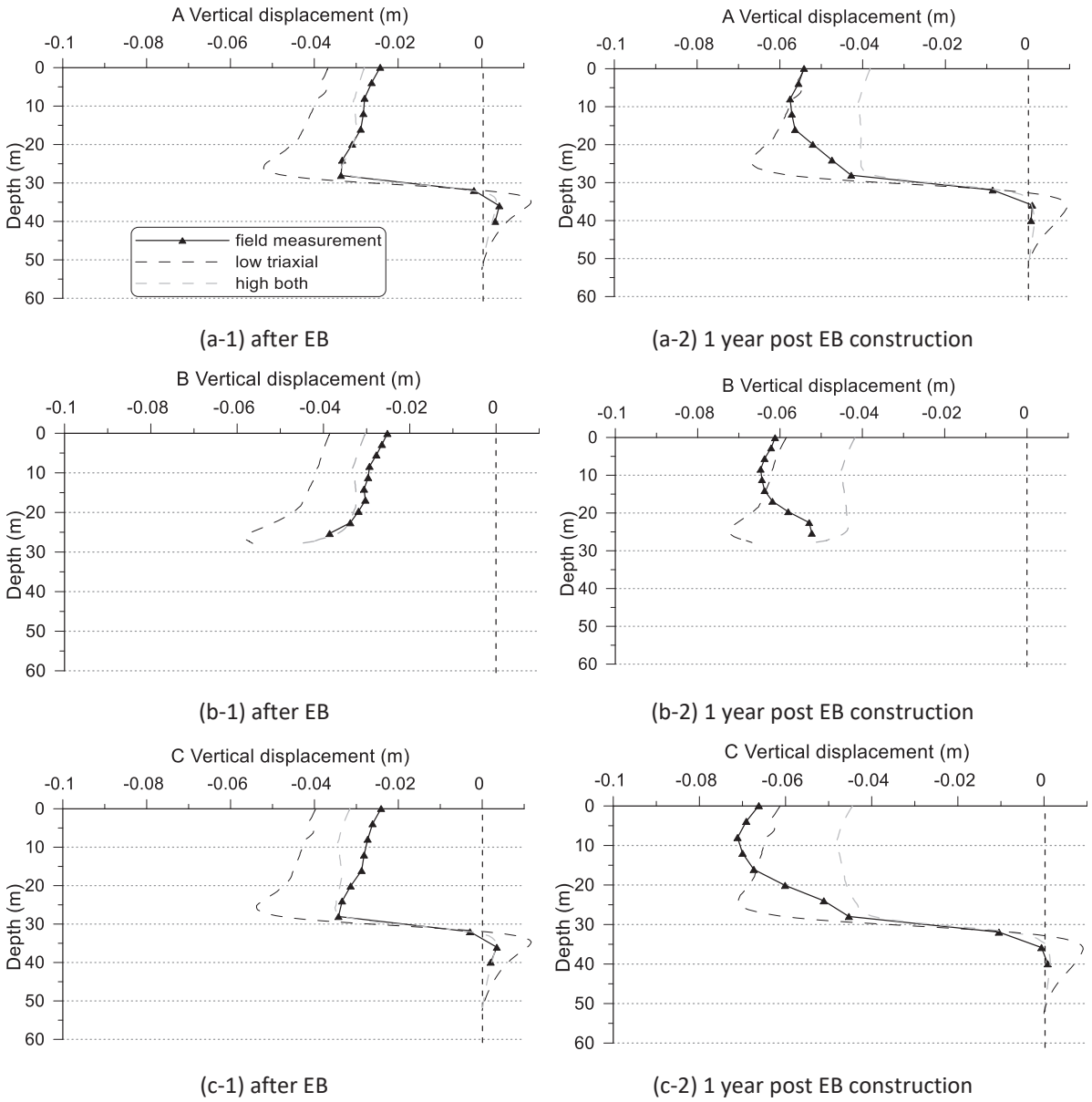


Figure 7.52: Comparison of subsurface vertical displacement on A, B &C lines after eastbound construction and 1 year post EB construction

For the assessment of ground movements caused by DOT tunnel excavation, a similar set of vertical monitoring axes is assumed, which are renamed as Ax, Bx & Cx for distinguishing from the twin tunnels case, as shown in Figure 7.53 for the two elevations of the DOT tunnel. The distance of the side axes Ax and Cx from the DOT spring line is the same as in the twin tunnel case and axis Bx extend to just above the DOT tunnel centre. The results along the Cx axis are not shown as they are identical to those in the Ax axis due to the symmetry of the mesh.

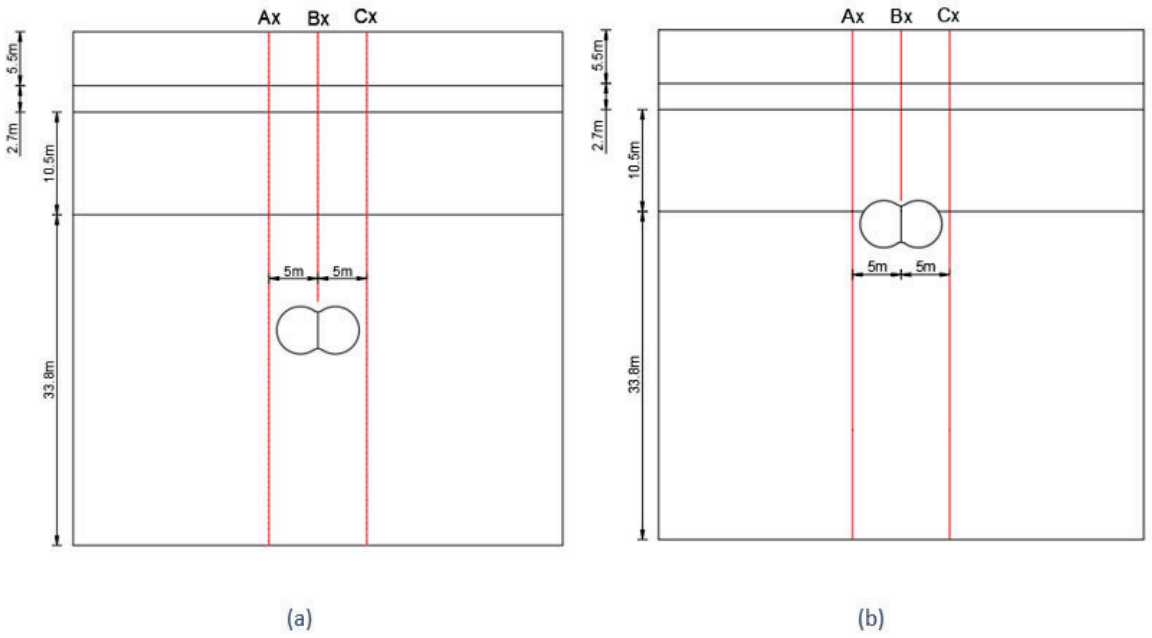


Figure 7.53: Alignment of monitoring axes in DOT simulation: (a) deeper DOT; (b) shallower DOT

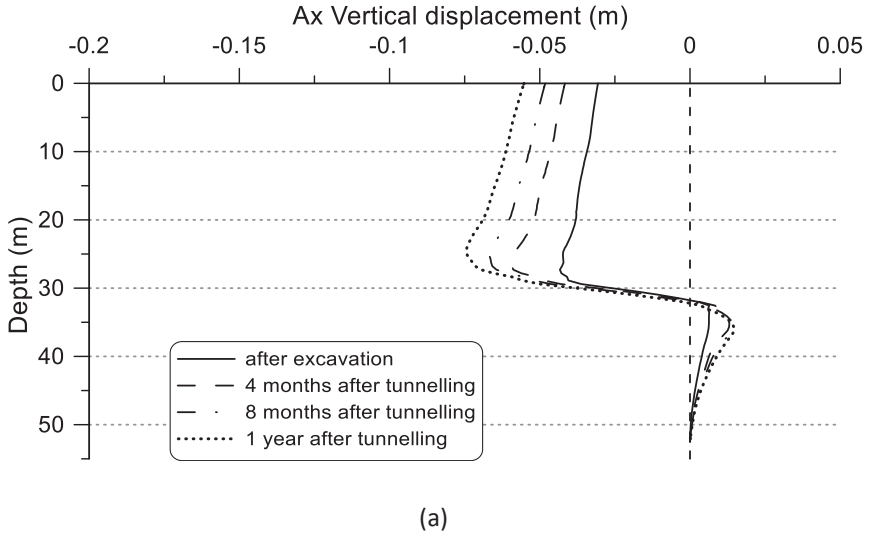
Predictions of the short term subsurface vertical and horizontal ground movements, shown in Figure 7.54 and Figure 7.55 for both DOT tunnel elevations, demonstrate the same trends as those discussed in Figure 7.50 and Figure 7.51 for the JLE WB tunnel. The subsurface soil experiences settlement above the tunnel crown, with uniformly increasing trend along the depth.

In short term, larger settlement takes place at the depth around 28m close to the tunnel crown (Figure 7.54). The maximum settlement along Ax line is 41.2mm at the depth of 27.8m, which takes place at the similar depth (28m) to westbound tunnel in twin tunnel simulation (see Figure 7.50a) whilst the magnitude of DOT is much larger (41mm>26mm). In the period of post tunnelling excavation within one year, the subsurface ground movement generally increases uniformly along the depth with time. The soil below tunnel invert, lying beneath 33m, has performed heaving after tunnelling, which indicates very similar settlement pattern with westbound tunnel in twin tunnels construction. This soil heaving is completed in the first 4 months after construction. Therefore, the behaviour of heaving at bottom soil could last for one year. This invert heaving could cause some potential problem such as increasing lining deformation and thus is of importance in design consideration. Both Ax and Bx have shown similar development trend of subsurface settlement of the soil above the tunnel crown.

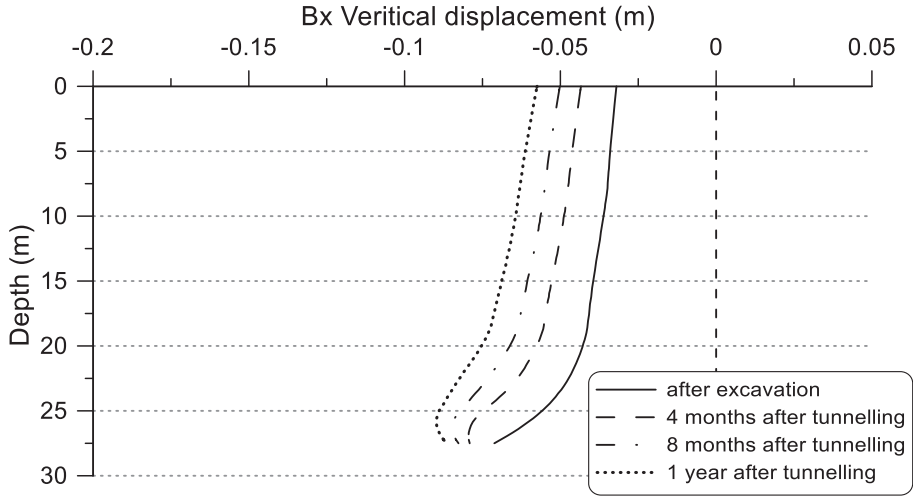
The horizontal displacement, performing in terms of moving towards the tunnel, has also experienced increasing with time on most parts except the soil at depth of tunnel axis. Therefore, it could be induced that the maximum horizontal displacement occurs at the depth of tunnel, where the soil has highest stress release horizontally and moves towards the tunnel, and this maximum horizontal

displacement is reached immediately after the excavation (see Figure 7.54c) in short term. It could be concluded that the ground response in subsurface layers of DOT excavation is very similar to that of conventional tunnels with a single bore, although the magnitudes of displacement is larger.

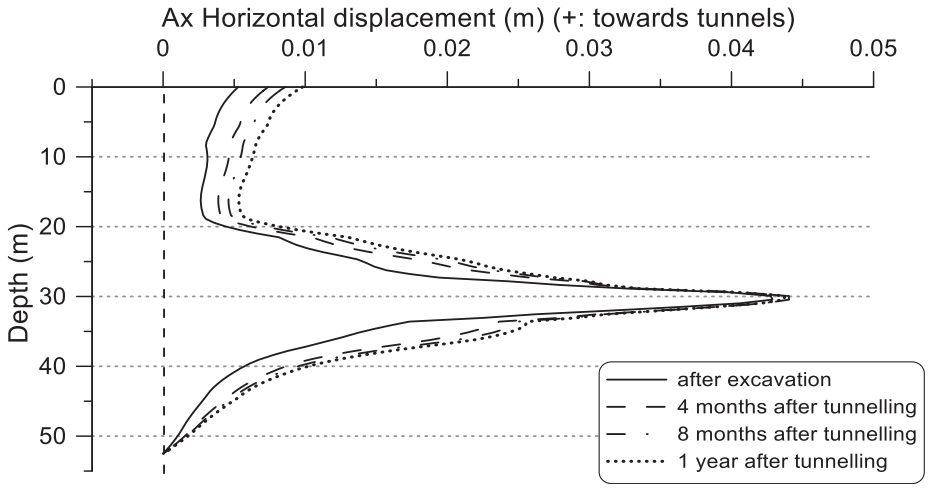
As for 'shallower DOT', troughs of displacement are shown in Figure 7.55 below. On the first 18m above the tunnel crown, the magnitude and the shapes of subsurface settlement troughs are close to the 'deeper DOT'. However, by comparing Figure 7.54c and Figure 7.55c, it is found that the horizontal displacement of Ax on the part close to the ground surface is significantly larger in 'shallower DOT' case. Regardless the small difference of volume loss from the 'deeper DOT' case, because the shallower tunnelling depth develops a relatively larger component of stress release horizontally for the surface soil, the displacement in horizontal direction is consequently larger.



(a)

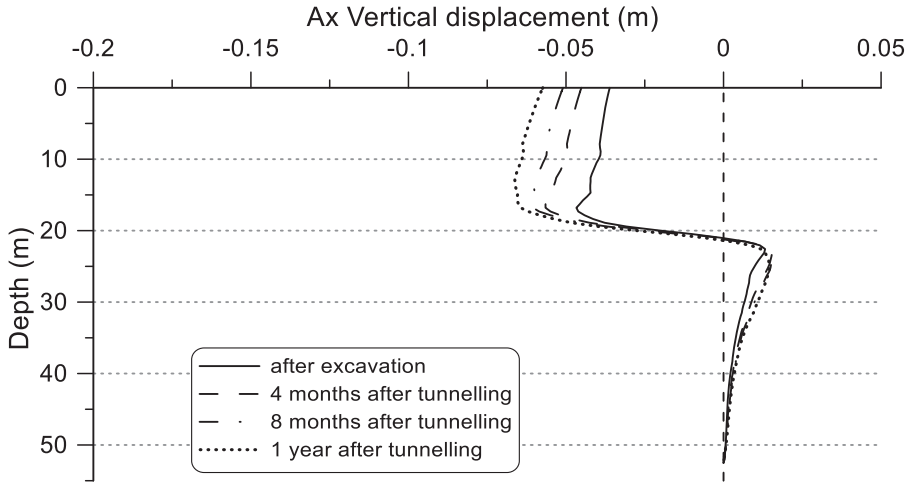


(b)

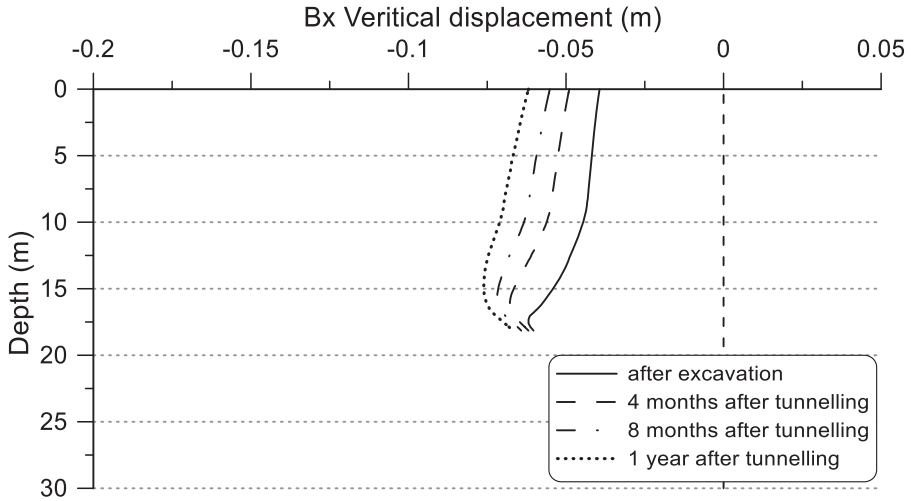


(c)

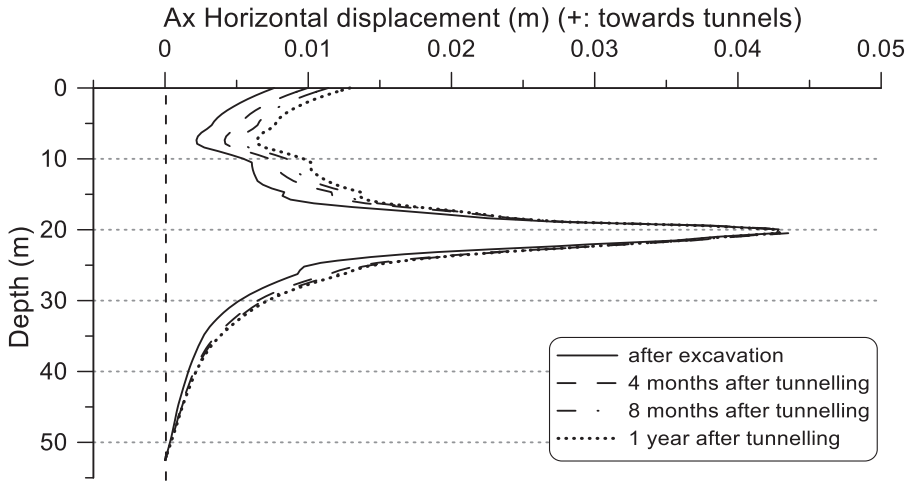
Figure 7.54: Subsurface vertical displacement along a) Ax and b) Bx axes; horizontal displacement along c) Ax axis; 'deeper DOT' simulation in short term; 'low triaxial' calibration



(a)



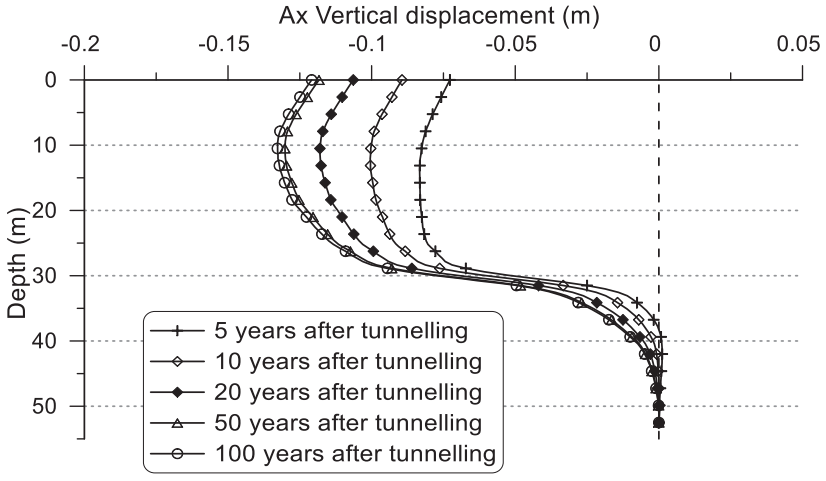
(b)



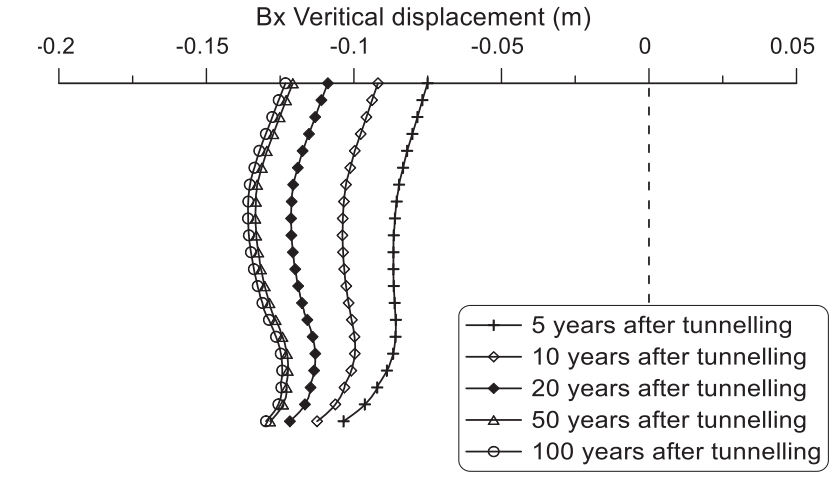
(c)

Figure 7.55: Subsurface vertical displacement along a) Ax and b) Bx axes; horizontal displacement along c) Ax axis; 'shallower DOT' simulation in short term; 'low triaxial' calibration

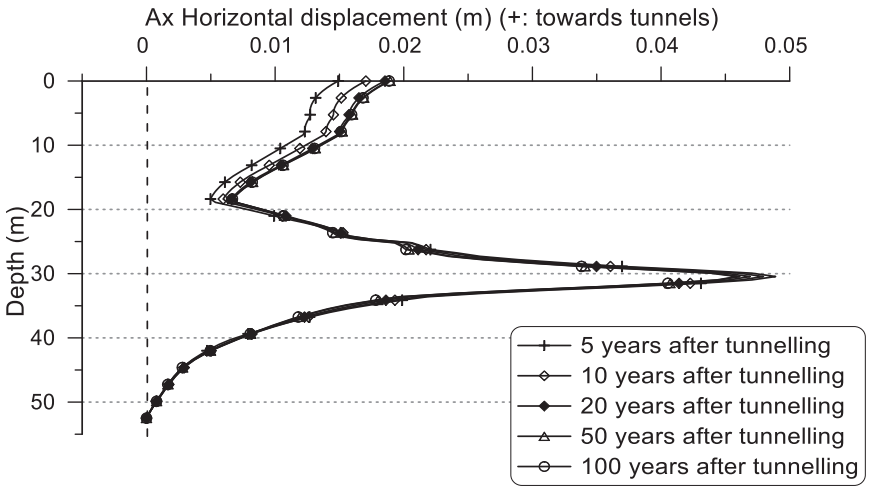
However, in long term, involved in soil consolidation and equilibrium of excessive pore water pressure, the bottom part of soil starts settling after 1 year, and hence the curve is bouncing leftward (see Figure 7.56a). Therefore, the vertical displacement of soil at line Ax could be ever larger with deeper soil bottom boundary. The equilibrium of pore water pressure, indicating the end of consolidation, seems to be reached before 100 years post construction since little further ground movement from 50 years to 100 years is observed in the diagram. The subsurface soil along both Ax and Bx have experienced continuous vertical settlement among the first 50 years. As for the horizontal displacement, it is creasing for the soil above the tunnel crown but does not change for the part beneath the invert.



(a)



(b)



(c)

Figure 7.56: Subsurface settlement along Ax and Bx of 'deeper DOT' simulation in long term

The comparison of stabilised subsurface settlements at 100 years post construction between DOT and twin tunnels is plotted in Figure 7.57. After the end of consolidation, the deeper DOT shows obviously larger settlement, indicating the greater ground movement around the tunnel. The shallower DOT, which is constructed at the depth of 20.5m, shows comparable prediction with the twin tunnels along the same axes.

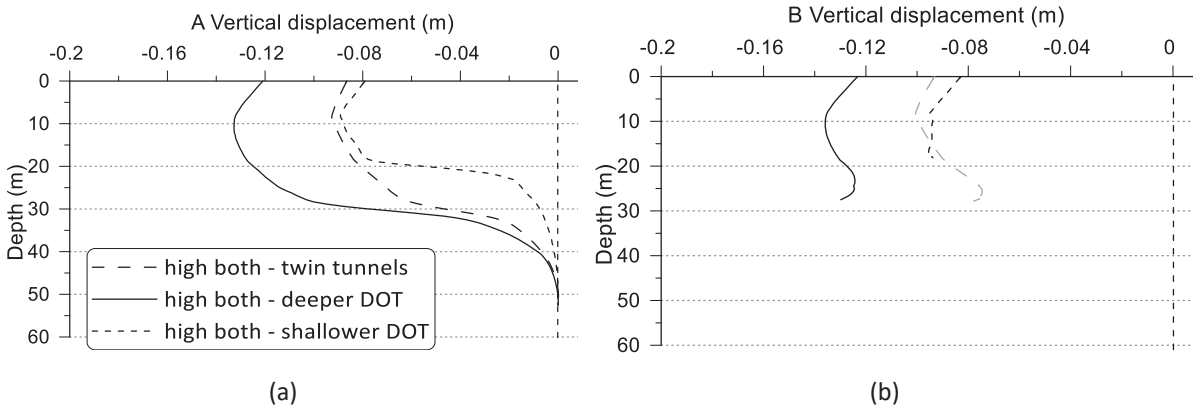


Figure 7.57: Long term (100 years) subsurface vertical displacement at a) A (Ax); b) B (Bx) axes

7.7.2 Hyde Park

The investigation of subsurface settlement for the behaviour of twin tunnels and DOT constructed in Hyde Park are mainly focusing on the overall settlement troughs at different depth, which presents the subsurface ground movement from a different dimension with the case study of St. James' Park. Since the twin tunnels in Hyde Park are constructed in a parallel manner, and high similarity of surface settlement troughs with corresponding DOT analysis has been observed, the comparison of overall settlement troughs against field data for both tunnelling approaches is considered meaningful.

Figure 7.58 shows a series of subsurface settlement curves for different depths after tunnelling (only WB for twin tunnels), including predicted results of DOT and westbound of twin tunnels, comparing against field data. The troughs for westbound tunnel, centred with westbound axis, has achieved good agreement with field measurements, and the maximum settlement of DOT in this case is about twice of the westbound due to larger cross-section area. The curves represented with permeable and impermeable lining conditions meets only small deviation between each because of short consolidation period (only a couple of hours for excavation) and relatively small cross-section area, whereas the subsurface settlement of DOT excavation develops differently. The predicted results for the end of excavation indicate a trend of narrower settlement trough and larger maximum settlement with the depth. The ground heaving below the depth of tunnel invert (see Figure 7.58f) follows similar manner in the sequence of magnitude with the settlement since the DOT tunnel results in larger excavated area.

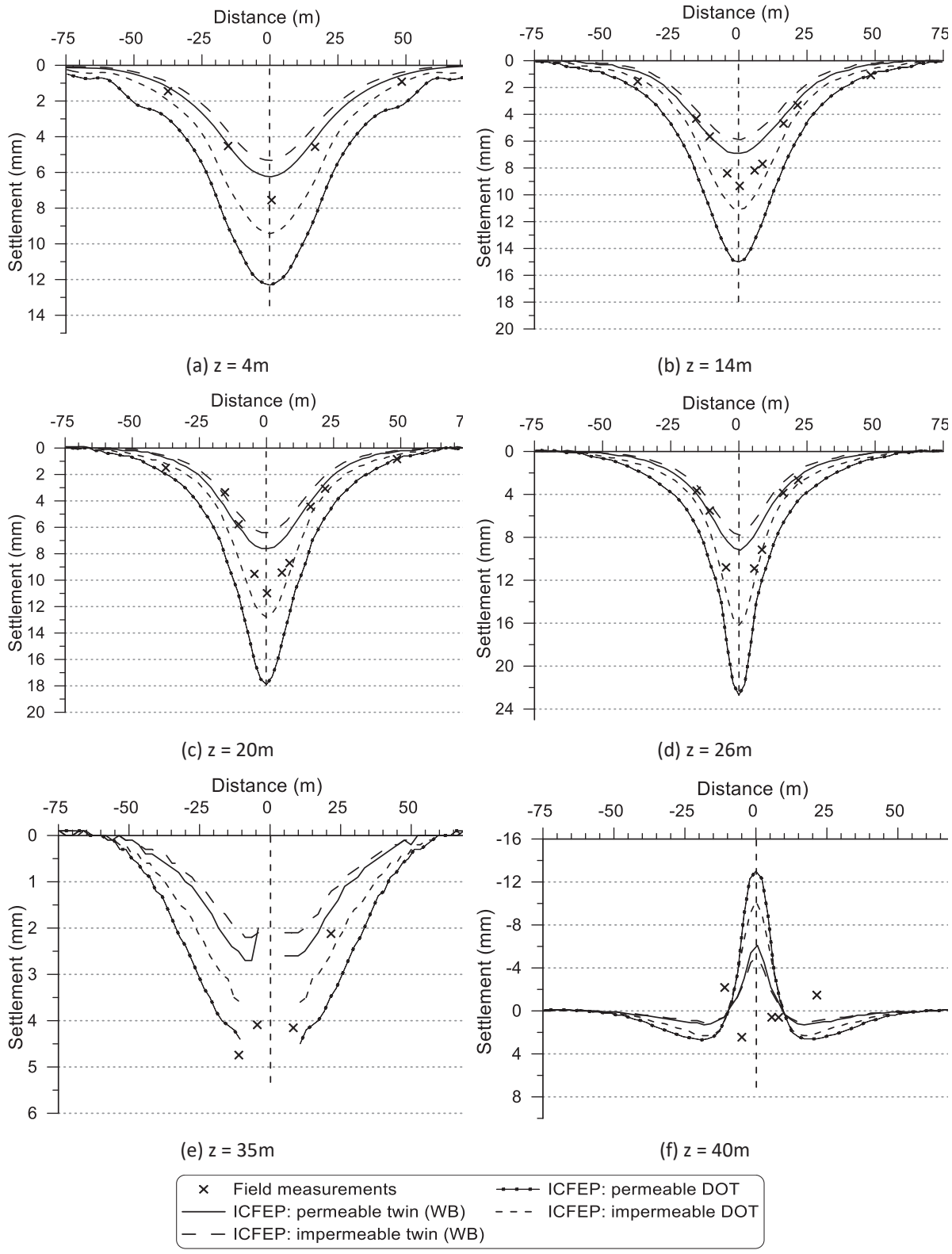
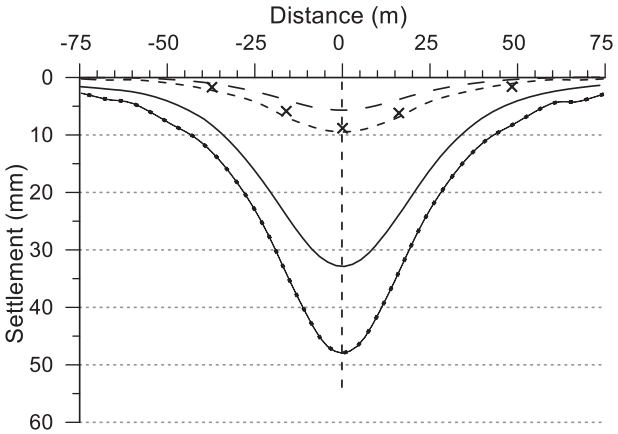


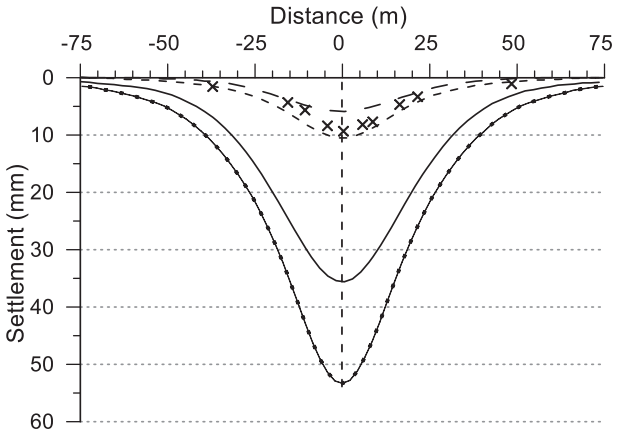
Figure 7.58: Subsurface settlement after WB/DOT excavation for twin/DOT tunnels at different depths

The subsurface ground response after the period of 74 days post construction is analysed (Figure 7.59), and the time point is exactly prior to eastbound tunnelling for twin tunnels case. It is noted that both subsurface settlement for twin tunnels and DOT have grown fast, enlarging the magnitudes by twice

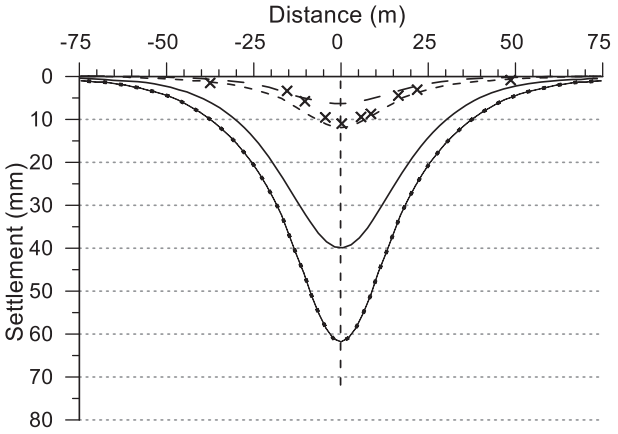
for different hydraulic boundary conditions. In particular, the overall subsidence at shallower depth (z = 4m) occurs in DOT simulation, and the curve shows larger ground movement in DOT than the single bore during this period. The predicted results based on permeable lining assumption of westbound tunnel achieve good agreement against field data as well. In general, it has to be specified that under the same boundary conditions in the identical field, the DOT tunnelling results in significantly larger ground response in short term after tunnelling.



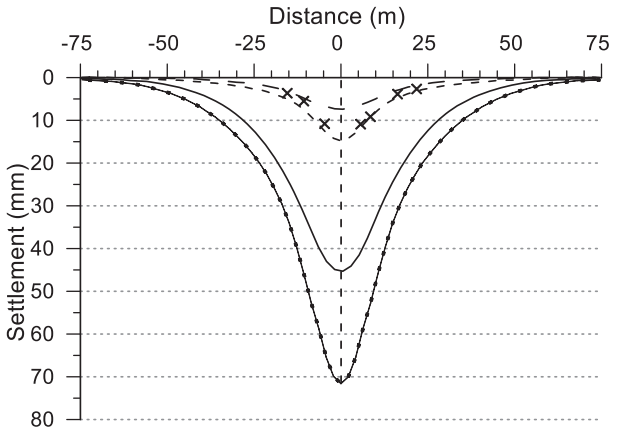
(a) z = 4m



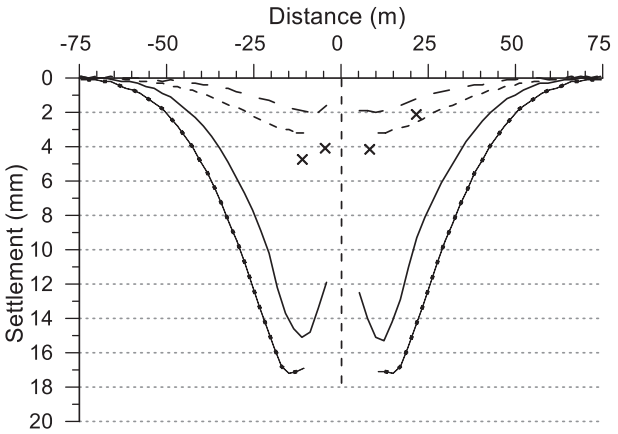
(b) z = 14m



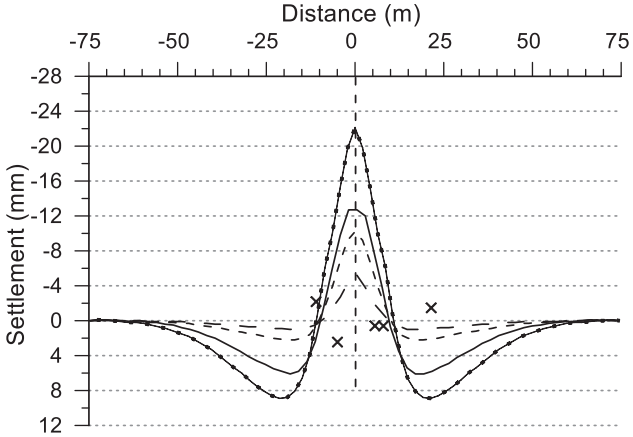
(c) z = 20m



(d) z = 26m



(e) z = 35m

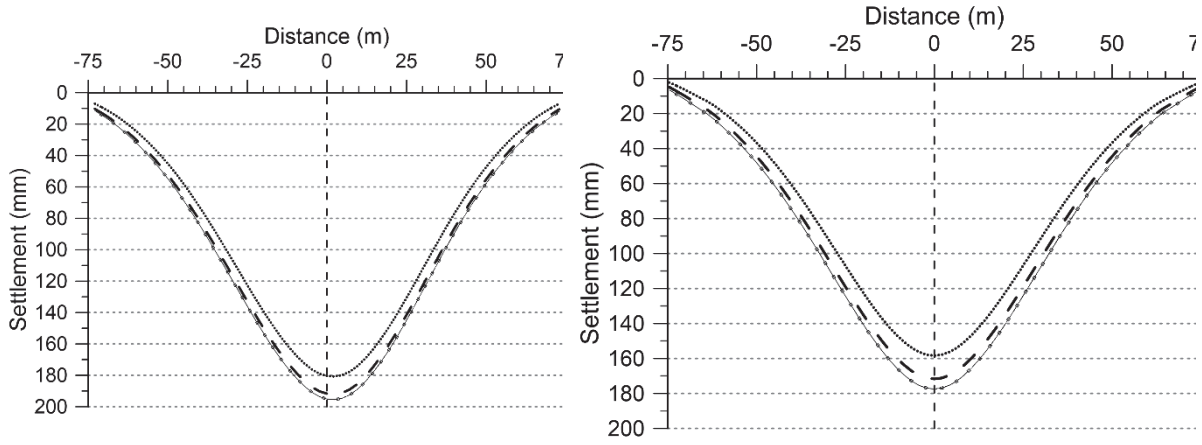


(f) z = 40m



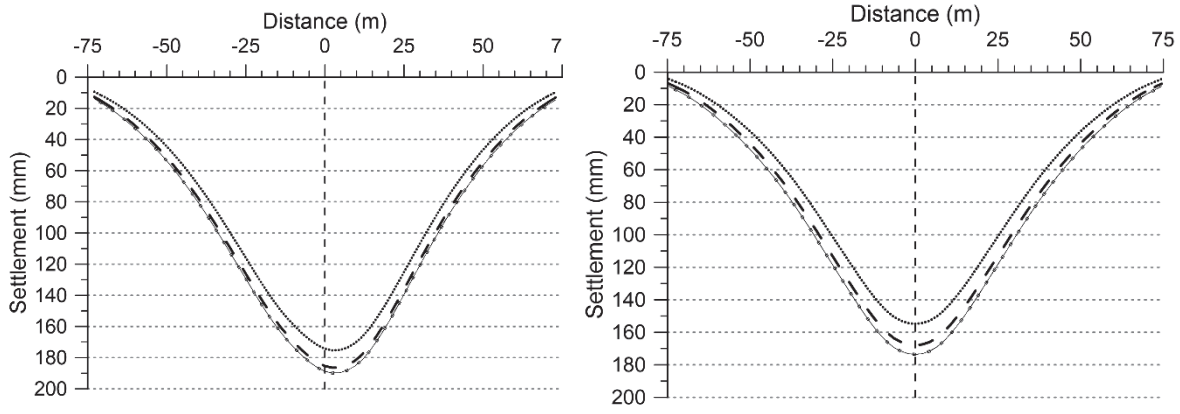
Figure 7.59: Subsurface settlement prior to EB excavation/74 days after DOT excavation for twin/DOT tunnels at different depths

The simulation of long term behaviour is based on the 'Low both' calibration, and the results of twin tunnels, the troughs of which is centred with the middle position of twin tubes, and DOT are presented in Figure 7.60 below. Only the results of permeable lining are given and discussed here due to its continuous evolution in long term consolidation period whilst the ground motion is accomplished soon conditioned with impermeable lining assumption. It is believed that after 100 years, the consolidation ends, and little further settlement is growing for either DOT or twin tunnels since only small value in growth of the troughs could be found from 20 years to 100 years. In long term, high similarity of the troughs on subsurface settlement could be found for DOT and twin tunnels, whilst the maximum magnitudes of DOT settlement are even smaller. Less differentiation settlement have been evolved from shallower (z = 4m) to deeper (z = 20m) depths (see Figure 7.60 a,b,c&d). Therefore, it could be concluded that in long term, the overall settlement (or subsidence), dominantly occurs over the soil layers instead.



(a) z = 4m - twin tunnels

(b) z = 4m - DOT



(c) z = 20m - twin tunnels

(d) z = 20m - DOT

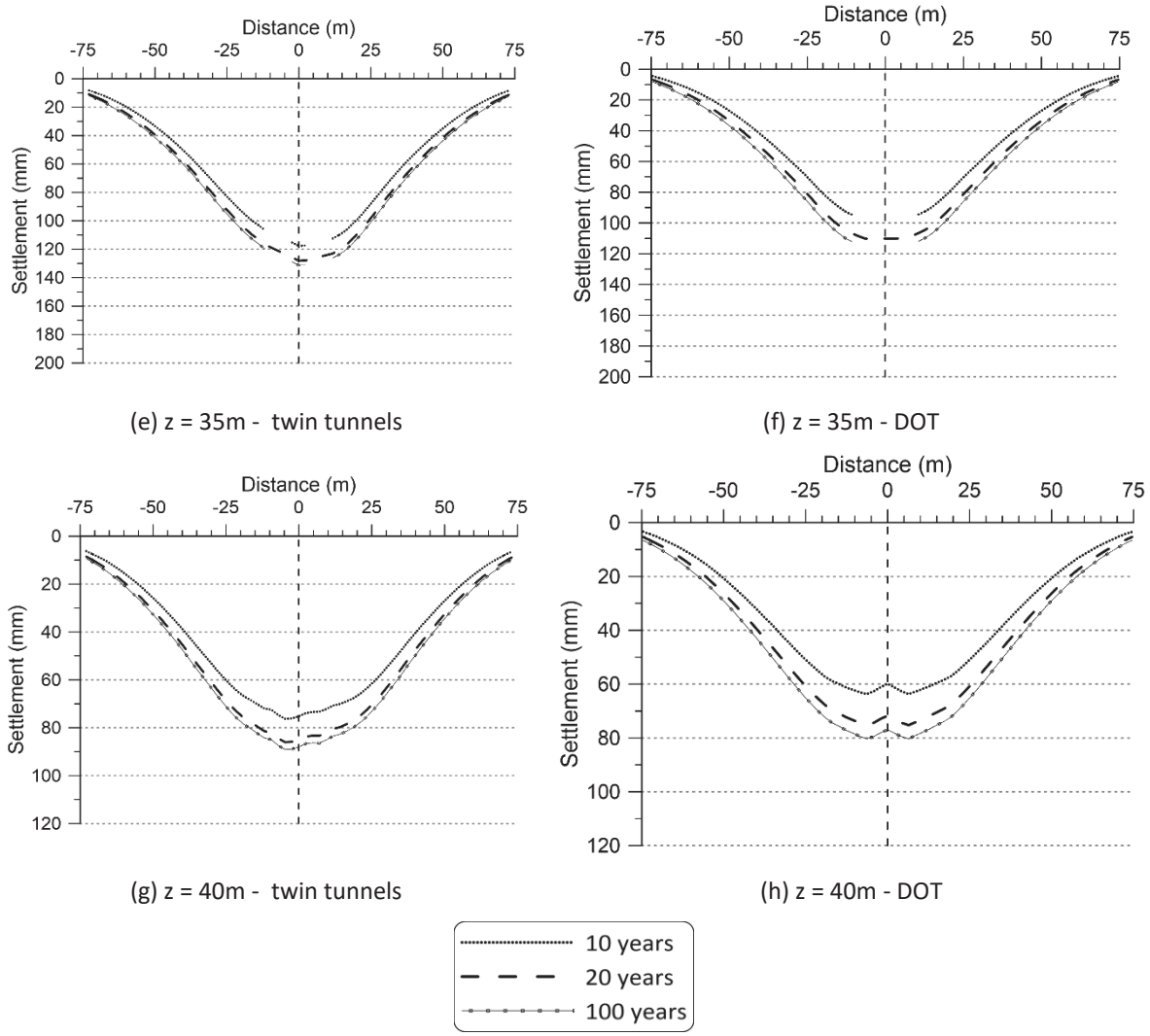


Figure 7.60: Predicted subsurface settlement troughs of twin/DOT tunnels at different depths for long term (permeable lining)

7.8 Summary points

This chapter examined a possibility of applying the DOT tunnel construction in the ground conditions of a stiff overconsolidated clay, as opposed to its predominant current application in soft clay tunnelling. For this purpose two case studies of twin tunnels in London ground conditions were utilised, the St James' Park on the Jubilee Line Extension tunnels and the Hyde Park on the Crossrail tunnels. In both cases the tunnels were excavated within the London clay formation and measurements of ground surface and subsurface settlements were available for comparison with numerical predictions. The research in this chapter comprised:

- application of a 2-surface kinematic hardening model, as a further extension of the modified Cam clay model (MCC) compared to that used in the analyses of soft ground tunnelling described in Chapter 3;

- finite element re-analysis of the twin tunnel cases at St James' Park and at Hyde Park, as per previous research of Avegerinos (2014);
- finite element analyses of the same tunnelling cases, but replacing the twin tunnels with a single DOT tunnel;
- in the St James' park study two depths of the DOT tunnel were analysed as the twin tunnels were constructed at different depths; in the Hyde Park study the twin tunnels were at the same depth;
- ground movements were interpreted and compared both at the ground surface and at selected sub-surface depths, and both in short and long-term conditions;
- the broad outcome of the research presented in this chapter is that DOT tunnelling seems to induce ground movements comparable to traditional twin tunnel construction, despite simultaneously excavating both bores, as opposed to the two real cases where a time of several months existed between the excavation of the two bores.

Chapter 8. Conclusions and recommendations for future research

8.1 Introduction

This research presented in this thesis has carried out a systematic investigation of Double-O-Tube (DOT) shield tunnelling, by utilising the approach of advanced numerical modelling and computational analysis. The main focuses of the work are on the soil response induced by DOT construction in the soft clay and stiff clay ground conditions, as well as on the internal forces of lining support system. The analyses used Imperial College Finite Element Program (ICFEP), and calibrations of different constitutive models selected for the soil and the concrete are validated by comparing the numerical results against laboratory or field measurements.

The motivation of the research, as introduced in the Chapter 1, is to systematically understand the mechanical behaviour of soil-structure interaction from the aspect of geotechnical engineering. The objectives, involving interpretation of the numerical modelling of DOT tunnelling under different hydraulic boundary conditions, the realistic reproduction of the ground response and the long term settlement predictions, are essentially realised via hydro-mechanical coupled analysis.

The literature survey conducted in Chapter 2 has given a brief overview of conventional tunnelling methods. The advantages and limitations of NATM, EPBM and other methods such as Cut-and-Cover have been systematically studied and validated in a large number of engineering projects around the world. The DOT technology has been reviewed in some literatures, and some specific problems such as DOT rolling and some key characteristics of DOT are discussed. However, the adaptability of DOT in different geological conditions and long term ground response is still unclear.

It is found that the lining behaviour of traditional single tunnel has been studied in detail by a lot of scholars, whereas the deformation and internal forces of DOT lining under serviceability states are still not fully quantitatively understood. Some simple analytical solutions have been suggested for evaluating the mechanical response of DOT lining under loading by some researchers, however, the models are usually separated from the in-situ ground conditions and consequently their reliability is limited.

The ground movements are the key effect of the tunnelling on the structures in vicinity of the DOT. Some simple conventional methods such as superposition of settlement troughs from individual tubes give basic illustration of the overall settlement trough, but the evolution of the settlement, and influence of the hydraulic conditions cannot be reflected from simple analytical methods. Therefore, the necessity of systematic numerical analysis is evident.

8.2 Shanghai geology and Development of the Shanghai ground model

The Shanghai geological conditions proposed in the macro introduction of geological history and divisions have been presented in Chapter 3. The ground layering of the Quaternary deposit, where the tunnelling work usually takes place, shows consistent major features among the geological records and literature. The quaternary stratigraphic chart is established and is referred to for ground modelling in numerical analysis of DOT tunnelling.

The fourth layer, defined as soft muddy clay layer in the ground division, is specifically concerned due to the main depth range for underground tunnelling in Shanghai. This layer is expected to attribute to the ground deformation mostly in excavation due to its high compressibility and low shear strength. Therefore, a complete investigation on the mechanical properties of the muddy clay layer via literature review was conducted for accurate reproduction of the ground conditions in the modelling. The presence of a thin sandy silt layer beneath the late phase of the Holocene strata in the ground model is found necessary, since the depth and thickness of this layer is consistently introduced in literatures.

The introduction of aquifer system in Shanghai ground helped to clarify the hydrostatic pore water pressure distribution, which was also adopted in the ground model, on shallow layers above 35m depth. The land subsidence of Shanghai has been found highly related to pumping in deeper layers in long term. The undrained strength of the Shanghai soil has been studied via different test methods such as field vane shear test, SPT and CPT, and part of results are employed for validating the quality of modelling. The high permeability identified for Shanghai clay, modelled as anisotropic, accounts for larger ground deformations compared to the tunnelling in London, which is introduced in Chapter 7. This high permeability feature could be explained with higher silts content.

The extended MCC model was shown to perform well in characterising the Shanghai soil, and the profile of undrained shear strength has achieved reasonably good agreement with measured data. Considering some variation of the parameters along the depth within the same division, different values of compressibility ratio and permeability are adopted for each layer.

The profile of an overconsolidation ratio, OCR, has been evaluated from conventional vane shear tests. It is generally reported that the Shanghai soil is normally consolidated and the OCR value is smaller than 2.0 for Holocene strata, and the variance is small along the depth. The OCR value on the ground surface is assumed with an appropriate high magnitude and it is believed that this assumption does not cause much influence on the overall strength of the ground due to its limited thickness and far distance from the excavated area.

As for the determination of small strain stiffness, the two essential functions, the maximum shear

stiffness for initial condition and the stiffness degradation have been characterised for the fourth layer based on laboratory testing results. Therefore, the small strain stiffness model (ICG3S) for the fourth layer, where the tunnel is excavated, has been calibrated in detail. Unfortunately due to data insufficiency, the stiffness degradation parameters were assumed consistent among the characterised layers, and a minimum value of tangent shear stiffness is assumed. According to the laboratory tests, the maximum shear stiffness, also known as initial stiffness, shows less dependency on the stress path under loading. While the degradation curve varies among the stress paths especially for small strain range. In this study, only a single degradation curve is adopted for modelling the soil for all layers due to lack of laboratory data.

8.3 Numerical model of the Shanghai DOT tunnelling case study

The extended MCC model, including the ICG3S small strain overlay, have been validated against available data for characterising the undrained shear strength and small strain stiffness of Shanghai clay. Using this combination of constitutive models good agreement of DOT surface settlement troughs has been demonstrated against the field measurements in short term. It is also concluded that in long term, the DOT in the soft clay develops similar settlement to traditional twin tunnels at the same depth, by comparing the numerical predictions against the measurement data of twin tunnels (Metro Line 2) in Shanghai.

The base case analysis adopts the assumption of elastic tunnel lining, and an increasing permeability of the tunnel lining. This hydraulic boundary condition is reasonable considering the tunnel reality in Shanghai.

The prediction of lining forces, including axial force (hoop force) and the bending moment seems to be underestimated in the base case analysis. The deviation may be caused by simplification of modelling tunnel lining as elastic and discretised with beam elements, therefore without considering the lining thickness. The forces are also correlated to the grouting pressure applied on the lining whilst tunnelling, which was not considered in the base case study.

The sensitivity study of lining material and joint stiffness between the segments (i.e. individual beam elements) shows that the lower stiffness of lining joint results in significant reduction of the lining axial force and bending moment. The influence of modelling ‘softer joints’ involves the lowering value and the change of force distribution shape along the lining. Therefore, the modelling of joints with an appropriate stiffness is essential.

The boundary stress support method for the simulation of tunnel excavation has the advantage of

accurately controlling the ground volume loss via defining the incremental unloading stress, and the ground deformation induced from excavation is completed over increments. It prevents the problem caused by volume loss control method that the tunnel is uplifting after the construction of lining, which is not realistic in the engineering reality without taking grouting into account.

It has been found that the grouting pressure and the reduction ratio of the pressure, which indicates a smaller loading on the segments, plays important role in controlling the ground settlement. The comparison among the series of testing results shows that the effect of grouting ends in short term but the induced influence on ground response is permanent. The methodology of grouting simulation introduced in this chapter could be referred to in the modelling of tunnels in the future.

8.4 Development of the modelling framework for DOT concrete segment

Two analysis of single segment tests PZW1 & PZW2 are performed to validate the calibration of the compression and tension aspects of the constitutive models selected for concrete and reinforcement bars. The characteristics of strain softening of the concrete in compression and tension are captured in the analyses by a non-local strain regularisation. The numerical results on the segment deflection, side concrete strain and the reinforcement strain have good agreement with the laboratory data. The modified Chen concrete model, incorporating elasto-plastic bar elements, is therefore considered suitable for the modelling of concrete lining segment.

The nonlocal softening method is introduced for the failure state of the concrete material. This method takes the contribution of the strain softening around the calculation points into account, and therefore, the concentration of the shear surface is more accurate and independent on mesh discretisation. The range of nonlocal strain area is determined based on the size and the mechanical observation such as the distance among cracks in the lab testing.

The corresponding mechanical behaviour including cracks from the intrados, compressive yielding on the extrados, tensile yielding for the lower reinforcement and the compressive yielding for the upper reinforcement are discussed. The differences between two tests are particularly revealed. It is concluded that the boundary restrictions on both ends of the segment (PZW2 test) significantly improve the bending resistance of the lining.

The main reinforcement bars aligned in the segment play important role in the bending resistance. The plasticity of the bars is found contributing to the flexibility of the structure in the stage of cracking extension. The alignment of reinforcement and the selected concrete grade for the segment (C50) is considered well designed since the strength of both materials are well utilised. A lower grade of

concrete (C30) clearly mobilises smaller bending resistance under jack load.

The cracks were observed under small load in both laboratory test and the analysis. It is expected as the concrete has low tensile strength. The cracks occur in the smeared form, and they may appear randomly in the region of tensile plastic strain of the segment. The numerical results show that under ultimate condition, the crack may become continuous and cross the whole thickness of the segment. It seems that the crack is inevitable for the concrete lining even under serviceability state. Therefore, the particular concern should be raised for the tunnel design with respect to cracks and some consequential problems such as water leakage.

The records of concrete strain measured on the side of the segment reflect the compressive and tensile stress distribution along the segment thickness. The measurement of laboratory data indicates the basic trend of the strain distribution although the accuracy for the late stage loading is not reliable as there are too many cracks disturbing the measurement of the strain gauge.

The 3D analysis on the PZW1 test was performed, which verifies the correctness and the efficiency of the plane strain analysis assumed for the two segments. The similar results show that it is completely acceptable for modelling the concrete tunnel lining using 2D plane strain analysis for the applied loading conditions. This may not be the case for a different experimental set up.

8.5 Base case DOT tunnel analysis with advanced concrete model

A full scale numerical simulation on the DOT tunnelling has been carried out in conjunction with the study on the internal lining force. The segments were modelled with solid elements using modified Chen concrete model. The simulations were compared against the results from base case analysis using elastic beam element lining introduced in Chapter 4. It has been found that the solid element lining results in the close ground response to the beam element lining, and the internal force performs in the similar manner after long term consolidation.

The distribution of the bending moment, which plays the important role in the lining deformation control under serviceability condition, shows similar sensitivity with respect to the stiffness of the joints. However, the joints are now dependent on both the stiffness of bolts and concrete material around the joints. A minimum bending resistance is guaranteed with the solid element segments connected with interface elements even if the bolting system is very soft..

The reinforcements and bolts are modelled using elasto-plastic bar elements and elastic beam elements, respectively. It is concluded that under serviceability state, the reinforcements do not undertake much bending resistance of the lining, while the bolting system is important for the joint

stiffness.

The plots of stress level contours about the lining ring indicates the transferred stress distribution from short term to long term. The concrete material at joint positions, where significant higher stress levels are shown, are considered may causing local failure in long term. The segments undertaking larger bending moment may also generates tensile failure in terms of cracks on the tension side of the concrete.

The results of '100 times softer bolts' in the lining force reflect the similar behaviour of lower bending moment as concluded in Chapter 4. However, the stress level on the lining, especially at joint positions, are found much higher in both short term and long term, implying the increase of risk for the local failure on joints.

The analyses of this chapter validates that the elastic ring assumption in the base case study introduced in Chapter 4 is appropriate. The simplification of the tunnel lining using elastic beam elements is reasonable and does not influence the results of ground response or lining internal force. However, the solid element lining helps to present the detailed mechanical information of the reinforcement and the bolts. The contours of major principle stress gives good indication on the risk assessment of lining concrete cracking and joint deterioration under serviceability condition. This could be significant in the structure design for the tunnel segment.

8.6 Study of Twin tunnels and DOT in stiff clay

This chapter investigates the tunnel constructions and induced ground movement in stiff clay, taking as an example the London ground profile where twin tunnels were excavated in London clay during the Jubilee Line Extension and Crossrail projects. The two surface kinematic hardening model (M2-SKH) is employed to characterise the behaviour of London clay in the numerical model, and its effectiveness for short term and long term simulation is verified by different sets of calibrations. The full tunnelling period simulation consists of geological history reproduction, tunnel excavation, lining construction and consolidation period of short term and long term. An introduction of the M2-SKH model and its significance for tunnel simulations are given at the beginning. Then the simulation for twin tunnels in London clay is carried out for validating this nonlinear model and the reality of the boundary conditions by comparing with field measurements obtained for both short term and long term, the calibrations are quoted and improved from available literature. Two case studies, Jubilee Line Extension at Saint James's Park site and the new cross-rail tunnels at Hyde Park are used. Based on that, the same geological conditions and modelling sequence are implemented for DOT simulation at the same site for producing significant predictions of ground movement in this area. Finally, the

comparison between both tunnelling forms and the features of tunnelling in stiff clay are discussed and some conclusions are summarised. All of analyses are performed with ICFEP (Imperial College Finite Element Program).

The function of M2-SKH model has been emphasized with the simulation of reproduction of geological history for tunnelling in London clay. The profiles of K0 and YSR built up after the geological history stages are compatible with field data of soil layers and divisions. The calibrations from four data sets based on triaxial and oedometer tests are introduced and the parameters of stiffness degradation are determined by approximation of the curve. The modelling of geological history is proved to be significant as it establishes realistic initial stiffness state of the soil among each layers of London clay. The constitutive model selected is considered suitable for characterising important features of stiffness degradation and the history of 'stress reversing'.

For short term response, the 'low triaxial' calibration is considered suitable for modelling both projects due to good agreement between the predicted surface settlements curves with field measurements in twin tunnels simulation. The predicted results of twin tunnels are obtained and match well with field measurements. In St. James' Park, smaller maximum surface settlement occurs for 'deeper DOT', which is excavated at the depth of westbound tunnel of Jubilee Line Extension, as well as wider shape of the trough. The settlement develops continuously and uniformly along the time with the 8-months intermediate period under the fully permeable condition along the lining, and that performs quite differently from the base analysis introduced about the DOT case in Shanghai, which ends the consolidation in a very short time after tunnelling and consequently the settlement is stabilised soon conditioned with the permeable lining assumption. Compared to the soft clay condition in Shanghai, the low permeability and higher stiffness of London clay is really beneficial for slow and uniform ground settling. The twin tunnels and DOT simulation in Hyde Park have generated very similar results of surface settlement due to similar geometrical features and alignment of the tunnels, and therefore, some conventional methods for predicting ground settlement such as Gaussian curve is still applicable for DOT study.

In long term, the change of pore water pressure distribution plays an important role in affecting the soil response around the tunnels. The evolutions of pore water pressure, in terms of gradient in vicinity of the tunnel and the amplitude of changing, is of high relevance of the tunnel depth. In the modelling of St. James' Park, the 'deeper DOT', which shows similar pore water pressure evolution shape with westbound in twin tunnels, develops lager maximum settlement in long term compared to 'shallower DOT'. This is caused by larger affected area presented by the change of pore water pressure and its steeper gradient around the tunnel. In the case of Jubilee Line Extension, the eastbound tunnel lies at shallower depth and leaves a relatively far distance from the westbound, and consequently it causes

larger disturbed area between two bores. Therefore, the ground response from 10 to 15 years after tunnelling shows an overall subsidence on the surface, and this behaviour is also supported in the simulation of DOT. According to the contours of pore water pressure for Hyde Park, the DOT tunnel and twin tunnels show similar shapes of pressure evolutions, and the influenced areas of both are expanded in long term. The priority of DOT is highlighted as the disturbed area represented by the change of pore water pressure is smaller.

The subsurface settlement in the modelling describes the trend of soil motion after tunnelling and the results of predictions are expected. It has been concluded that for the Hyde Park case study, neither fully permeable lining nor impermeable lining could represents realistic hydraulic boundary conditions around the tunnel as the magnitude of maximum settlement has been overestimated or underestimated. Therefore, a more realistic hydraulic boundary condition, such as partially permeable lining, is required for properly reproducing the behaviour of the subsurface soil movement.

Generally, the DOT tunnel shows larger maximum settlement in all stages compared to traditional single bore tunnel under the same volume loss condition, and the DOT need earlier lining construction while tunnelling, reflected by smaller unloading percentage in the simulation. However, the DOT evolves smaller disturbed area of the soil as well as the width of overall settlement compared with twin tunnels. The settlement increases continuously and slowly in long term consolidation due to the low permeability and high stiffness of London clay. Therefore, from the aspects of ground movement, the DOT tunnelling is considered a suitable technology for construction as underground structure in stiff clay area such as London.

8.7 Recommendations for future research

This research is mainly focusing on the DOT modelling in soft and stiff clay condition, and some factors influencing the ground response and mobilised lining forcea have been analysed.

The analysis of DOT tunnelling in Shanghai clay helps to understand the mechanical influence of DOT in soft clay area. Some further research may involve:

- Modelling twin tunnels and DOT in the Shanghai area at different depths following the developed modelling framework.
- Establishing more detailed profile of small strain stiffness properties for Shanghai clay for all layers, which requires further literature survey and more laboratory data source.
- Investigating the realistic and more adequate hydraulic boundary conditions along the lining from the field data, which provides approving information for reproducing the evolution of

the settlement.

- Taking grouting pressure into account for the tunnel simulation, and study in more detail the mechanical response of the ground.

The concrete lining has been successfully modelled with solid elements, characterised using advanced modified Chen concrete model. The potential extension of this study in the future may include the following aspects:

- Investigating the ultimate state of the tunnel lining in some extreme conditions such as over-large ground loading.
- The optimistic design of bolting system, which forms the tunnel joints, selection of concrete grade and the design of reinforcement cage, can be discussed via 3D numerical modelling.

The comparison between twin tunnels and DOT in London clay has validated the capability of application of DOT technology in stiff clay area. However, some other problems that are often concerned on single tunnel have not been analysed for DOT yet, such as the influence of DOT construction on existing tunnels and nearby structures. These topics are also worth discussing in the future.

Reference

- Al-Tabbaa, A. & Wood, D.M. 1989. An experimental based “bubble” model for clay. *Proceedings of International Conference on Numerical Models in Geomechanics*, A. Pietruszczak and G.N. Pande (eds.), Balkema, pp.91-99.
- Anagnostopoulos, C.A. & Chatziangelou, M., 2008. Compressive strength of cement stabilized soils: a new statistical model. *Electronic Journal of Geotechnical Engineering,* 13, pp.1-10.
- Anon, 1987. Steel-fiber-reinforced shotcrete for tunnel linings: the state of the art. 24 (2), pp.66–.
- Anon, 1996. Sprayed concrete linings (NATM) for tunnels in soft ground. London, Telford.
- Anon, 2000. The Collapse of NATM tunnels at Heathrow Airport: a report on the investigation by the Health and Safety Executive into the collapse of New Austrian Tunnelling Method (NATM) tunnels at the Central Terminal Area of Heathrow Airport on 20/21 October 1994. Sudbury, HSE Books.
- Anon, 2004. Press-in piling: a construction solution for cut ; cover tunnels. 19 (4), pp.484–484.
- Anon, 2005. Closed-face tunnelling machines and ground stability a guideline for best practice. London, Thomas Telford.
- Ao, R. & Zhang, Y., 2011. Analysis of consolidation settlements caused by shield tunneling. *Rock and Soil Mechanics.* 32(7), pp.2157-2161. (in Chinese)
- Atkinson, J.H., Richardson, D. and Stallebrass, S.E., 1990. Effect of recent stress history on the stiffness of overconsolidated soil. *Géotechnique*, *40*(4), pp.531-540.
- Avgerinos, V., 2014. *Numerical investigation of tunnelling beneath existing tunnels* (Doctoral dissertation, Imperial College London).
- Avgerinos, V., Potts, D.M. & Standing, J.R., 2016. The use of kinematic hardening models for predicting tunnelling-induced ground movements in London Clay. *Géotechnique*, *66*(2), pp.106-120.
- Avgerinos, V., Potts, D.M., Standing, J.R. & Wan, M.S.P., 2018. Predicting tunnelling-induced ground movements and interpreting field measurements using numerical analysis: Crossrail case study at Hyde Park. *Géotechnique*, *68*(1), pp.31-49.
- Bahar, R., Benazzoug, M. & Kenai, S., 2004. Performance of compacted cement-stabilised soil. *Cement and Concrete Composites*, 26(7), pp.811-820.
- Bai, y., Dai, Z., Zhang, S. & Peng, F., 2011. Study on grout pressure dissipation mode in simultaneous backfill grouting during shield tunneling. *China Railway Science*. 32(4), pp.38-45. (in Chinese)

- Barton, N., 2017. Minimizing the use of concrete in tunnels and caverns: comparing NATM and NMT. *Innovative Infrastructure Solutions*. 2 (1), pp.1–24.
- Beverly, P., 2013. *Model code for concrete structures 2010*. Berlin: Ernst & Sohn.
- Bishop, A.W., Webb, D.L. & Lewin, P.I., 1965. Undisturbed samples of London Clay from the Ashford Common shaft: strength–effective stress relationships. *Geotechnique*, *15*(1), pp.1-31.
- BRITISH STANDARDS INSTITUTION. (1990). BS5400-4:1990: Steel, concrete and composite bridges. Code of practice for design of concrete bridges, BSI.
- BRITISH STANDARDS INSTITUTION. (2005). Eurocode 3: design of steel structures. London, BSI.
- Broadhouse, B.J., 1995. AEA Technology The Winfrith Concrete Model in LS-DYNA3D.
- Burland, J.B., 1989. Ninth Laurits Bjerrum Memorial Lecture: 'Small is beautiful'the stiffness of soils at small strains. *Canadian geotechnical journal*. 26 (4), pp.499–516.
- Burland, J.B., Standing, J.R., & Jardine, F.M. 2001. Assessing the risk of building damage due to tunnelling - lessons from the Jubilee Line Extension, London. *Geotechnical Engineering. Meeting society's need, Vol.1*., Swets and Zeitlinger, Lisse, pp.17–44.
- Chai, J., Shen, S., Zhu, H. & Zhang, X., 2004. Land subsidence due to groundwater drawdown in Shanghai. *Géotechnique*, 54(2), pp.143-147.
- Chapman, D.N., Metje, N. & Stark, A., 2010. *Introduction to tunnel construction*. Abingdon, Spon.
- Chen, A.C. & Chen, W.F., 1975. Constitutive relations for concrete. *Journal of the Engineering Mechanics Division*, *101*(4), pp.465-481.
- Cho, Kim, J., Won, J., & Kim, M. K., 2016. Effects of jack force and construction steps on the change of lining stresses in a TBM tunnel. *KSCE Journal of Civil Engineering*, 21(4), pp.1135–1146.
- Chow, B., 2006. Double-O-tube shield tunneling technology in the Shanghai Rail Transit Project. Tunnelling and Underground Space Technology, 21(6), pp.594-601.
- Clayton, C.R.I. and Heymann, G., 2001. Stiffness of geomaterials at very small strains. *Géotechnique*, *51*(3), pp.245-255.
- Crawford, J.E., Magallanes, J.M., Lan, S., & Wu, Y., 2011. User's manual and documentation for release III of the K&C concrete material model in LS-DYNA. *Technical Report*, Karagozian & Case, Burbank, CA. TR-11-36-1.
- Ding, Y., Wang, J., Xu, Z. & Chen, J., 2007. Monitoring analysis of a deep excavation in Shanghai soft soil deposit. *J.Xi'an Univ of Arch & Tech (Natural Science Edition).* 38(3), pp.333-338. (in Chinese)
- Do, Dias, D., Oreste, P., & Djeran-Maigre, I., 2013. 2D numerical investigation of segmental tunnel lining behavior. *Tunnelling and Underground Space Technology*, 37, pp.115–127.

- Fang, Q., Zhang, D. & Wong, L.N.Y., 2012. Shallow tunnelling method (STM) for subway station construction in soft ground. *Tunnelling and underground space technology.* 29, pp.10–30.
- Fang, Y., Kao, C. & Shiu, Y., 2012. Double-O-Tube shield tunneling for Taoyuan International Airport Access MRT. *Tunnelling and Underground Space Technology*, 30, pp.233-245.
- Fang, Y., Lin, J. & Su, C., 1994. An estimation of ground settlement due to shield tunnelling by the Peck–Fujita method. *Canadian Geotechnical Journal*, 31(3), pp.431-443.
- Fatahi, B., Fatahi, B., Le, T. & Khabbaz, H., 2013. Small-strain properties of soft clay treated with fibre and cement. *Geosynthetics International*, 20(4), pp.286-300.
- Galavi, V. & Schweiger, H.F., 2010. Nonlocal multilaminate model for strain softening analysis. *International Journal of Geomechanics*, *10*(1), pp.30-44.
- Gao, Y. & Chen, Z., 2017. Analysis of the OCR of soft clay in coastal areas based on field vane strength. *Chinese Journal of Rock Mechanics and Engineering*, 36(10), pp.1-8. (in Chinese)
- Gasparre, A. & Coop, M.R. 2008. The quantification of the effects of structure on the compression of a stiff clay. *Canadian Geotechnical Journal,* Vol.45, pp.1324-1334.
- Gasparre, A. 2005. *Advanced laboratory characterisation of London Clay*. PhD thesis, Univ. of London, London.
- Gasparre, A., Nishimura, S., Coop, M.R. & Jardine, R.J., 2007a. The influence of structure on the behaviour of London Clay. *Géotechnique*. 57 (1), pp.19–31.
- Gasparre, A., Nishimura, S., Minh, N.A., Coop, M.R., & Jardine, R.J. 2007b. The stiffness of natural London Clay. Géotechnique, Vol.57, No.1, pp.33–47.
- GB50010-2010, Code for Design of Concrete Structures. Ministry of Housing and Urban-Rural Development of the People's Republic of China, Beijing, China, 2010.
- GB 50164-2011; Standard for Quality Control of Concrete. China Architecture & Building Press: Beijing, China, 2012. (In Chinese)
- Golser, J., Keuschnig, M. & Weichenberger, F.P., 2020. NATM – Review and Outlook. *Geomechanik und Tunnelbau*. 13 (5), 466–474.
- Gong, S., Wu, J. & Yan, X., 2005. Analysis on land subsidence due to construction engineering in soft soil region of Shanghai. In: Zhang AG, Gong SL, Carbognin L, Johnson AI (eds) Proceedings of the seventh international symposium on land subsidence, vol 1, pp 82–87
- Grammatikopoulou, A., Zdravkovic, L. & Potts, D.M., 2007. The effect of the yield and plastic potential deviatoric surfaces on the failure height of an embankment. *Géotechnique*, *57*(10), pp.795-806.
- Gu, X., Li, Y., Liang, F. & Huang, M., 2019. Stress path dependent small strain stiffness of Shanghai clay. *E3S Web of Conferences*, 92, p.04003.

- Hardin, B. and Drnevich, V., 1972. Shear Modulus and Damping in Soils: Design Equations and Curves. *Journal of the Soil Mechanics and Foundations Division*, 98(7), pp.667-692.
- Haruyama, K., Teramoto, S. & Taira, K., 2005. Construction of large cross-section double-tier Metropolitan Inter-city Highway (Ken-O-Do) Ome Tunnel by NATM. *Tunnelling and underground space technology*. 20 (2), pp.111–119.
- Health and Safety Executive, 1996. Safety of New Austrian Tunnelling Method (NATM) tunnels: A review of sprayed concrete lined tunnels with particular reference to London Clay.
- Hight D.W., McMillan F., Powell J.J.M., Jardine R.J. & Allenou C.P., 2003. *Some characteristics of London Clay.* Proc. Conf. Characterisation and Engineering, National University Singapore. Tan T.S., Phoon, K.K., Hight D.W., Lerouil S. (eds). Balkema, Vol. 2, pp851-907.
- Hight, D.W., Gasparre, A., Nishimura, S., Minh, N.A., Jardine, R.J. & Coop, M.R., 2007. Characteristics of the London Clay from the terminal 5 site at Heathrow airport. *Géotechnique*, Vol.57, No.1, pp.3–18.
- Hong, G., Zheng, Y.. & Chen, H., 2006. Characteristics of soil surface settlement for double-o-tube shield tunnel [J]. Journal of Architecture and Civil Engineering, **23**(2), 62-67. (in Chinese)
- Huang, D. and Zeng, B., 2017. Influence of Double-O-Tube Shield Rolling on Soil Deformation during Tunneling. *International Journal of Geomechanics*, 17(11), p.04017105.
- Irshad, M. & H. Heflin, L., 1988. Soft-ground NATM tunnel designs for the Washington, D.C. Metro. Tunnelling and underground space technology. 3 (4), pp.385–392.
- Jamiolkowski, M., 1985. New developments in field and laboratory testing of soils, State of the Art Report." In Proc. 11th Int. Conf. on SMFE, vol. 1, pp. 57-153.
- Jardine R.J., Potts D.M., St. John H.D. and Hight D.W. 1991. Some practical applications of a non-linear ground model. *Proceedings of the 10th European Conference on Soil Mechanics and Foundation Engineering,* Florence, Vol.1, pp.223-228
- Jeong, Han, Y.-C., Kim, Y.-M., & Kim, D.-H., 2014. Evaluation of the NATM tunnel load on concrete lining using the ground lining interaction model. *KSCE Journal of Civil Engineering*, 18(2), pp.672–682.
- Jiu, Y. & Huang, M., 2017. Coefficient of earth pressure at rest and undrained shear strength of over-consolidated soft clays. *Rock and Soil Mechanics*, 38(4), pp.951-957. (in Chinese)
- Jodl, H.G. & Resch, D., 2011. NATM and TBM - comparison with regard to construction operation / NÖT und TBM - eine baubetriebliche Gegenüberstellung. *Geomechanik und Tunnelbau.* 4 (4), pp.337–345.
- King, C., 1981. The stratigraphy of the London Clay and associated deposits. *Tertiary Research Special Paper*, 6, pp.3-58

- Koyama, Y., 2003. Present status and technology of shield tunneling method in Japan. *Tunneling and Underground Space Technology*, 18, pp.145–159.
- Koyama, Y., Okano, N., Shimizu, M., Fujiki, I., & Yoneshima, K., 1995. "In-situ measurement and consideration on shield tunnel in diluvium deposit." *Proceedings of tunnel Engineering, JSCE*, Vol. 7, pp.385-390.
- Lade, P.V. and Ducan, J.M., 1975. Elasto-Plastic Triaxial Tests on Cohesionless Soil. *J. Geotech. Eng. Div*.
- Laefer, & Kim, W. S., 2004. Predicting Tunneling-Induced Ground Movement. *Transportation Research Record*, 1892(1), pp.208–217.
- Lalagüe, A., Lebens, M.A., Hoff, I. & Grøv, E., 2016. Detection of Rockfall on a Tunnel Concrete Lining with Ground-Penetrating Radar (GPR). *Rock mechanics and rock engineering*. 49 (7), pp.2811–2823.
- Lee, K., Ji, H., Shen, C., Liu, J. & Bai, T., 1999. Ground Response to the Construction of Shanghai Metro Tunnel-Line 2. *Soils and Foundations*, 39(3), pp.113-134.
- Li, Soga, K., Wang, F., Wright, P., & Tsuno, K., 2014. Behaviour of cast-iron tunnel segmental joint from the 3D FE analyses and development of a new bolt-spring model. *Tunnelling and Underground Space Technology*, 41, pp.176–192.
- Ling, Z., Wang, W., Wu, J., Huang, M. & Yuan, J., 2019. Shaft resistance of pre-bored precast piles in Shanghai clay. *Proceedings of the Institution of Civil Engineers - Geotechnical Engineering*, 172(3), pp.228-242.
- Liu, G., Jiang, R., Ng, C. and Hong, Y., 2011. Deformation characteristics of a 38 m deep excavation in soft clay. *Canadian Geotechnical Journal*, 48(12), pp.1817-1828.
- Liu, G., Luo, X., Chen, Q., Huang, D. & Ding, X., 2008. Detecting Land Subsidence in Shanghai by PS-Networking SAR Interferometry. *Sensors*, 8(8), pp.4725-4741.
- Liu, J.Q. & Liu, Q., 2000. Quaternary stratigraphy in China. *Quaternary Sciences* 20 (2), pp.129–141 (in Chinese)
- Liu, Y., Xiang, B. & Fu, M., 2019. Observed Performance of a Large-Scale Deep Triangular Excavation in Shanghai Soft Clays. Geotechnical and geological engineering. 37 (4), pp.2791–2809.
- Lv, H. & Zhang, Q., 2006. A model of ground settlement induced by underground Double-O-Tube shield tunnelling [J]. *Mine Construction Technology*. 27 (1), pp.32-34. (in Chinese)
- MAIR, R.J., TAYLOR, R.N. & BRACEGIRDLE, A., 1993. Subsurface settlement profiles above tunnels in clays. *Géotechnique*. 43 (2), pp.315–320.
- Malvar, L.J., Wesevich, J.W., & Crawford, J.E., 1997. Procedures for including fragment loading and damage in the response predictions of reinforced concrete slabs. *Eighth International Symposium on Interaction of the Effects of Munitions with Structures*, McLean, VA

- Mashimo, & Ishimura, T., 2003. Evaluation of the load on shield tunnel lining in gravel. *Tunnelling and Underground Space Technology*, 18(2), pp.233–241.
- Masing, G., 1926. Eigenspannungen und Verfestingung beim Messing. *Proceedings Second International Congress of Applied Mechanics*, pp. 332-335.
- Matallah, M. & La Borderie, C., 2009. Inelasticity–damage-based model for numerical modeling of concrete cracking. *Engineering Fracture Mechanics*, *76*(8), pp.1087-1108.
- Mayne, P. W. & Kulhawy, F. H., 1982. K0 –OCR relationship in clay. *J. Geotech. Div., ASCE 108*, No. GT6, pp.851–870.
- Mayne, P.W. and Kulhawy, F.H. 1982. Ko-OCR relationships in soil. *Journal of the Geotechnical Engineering Division*, ASCE, Vol.108 (GT6), pp.851-872.
- Morgan D., 1993. Advances in shotcrete technology for support of underground openings in Canada. *Shotcrete for underground support V. In: Proceedings of the Engineering Foundation Conference. New York: American Society of Civil Engineers*, pp.358–382.
- Murray, Y.D., 2007. *Users manual for LS-DYNA concrete material model 159* (No. FHWA-HRT-05-062). United States. Federal Highway Administration. Office of Research, Development, and Technology.
- Niedbalski, Z., Małkowski, P. & Majcherczyk, T., 2018. Application of the NATM method in the road tunneling works in difficult geological conditions – The Carpathian flysch. Tunnelling and underground space technology. 74, pp.41–59.
- Nyren, R.J. 1998. *Field measurements above twin tunnels in London clay*. Ph.D. thesis, Imperial College, University of London, UK
- Nyren, R.J., Standing, J.R. and Burland, J.B. 2001. Surface displacements at St James's Park greenfield reference site above twin tunnels through the London Clay. *Building response to tunnelling; Vol.2: case studies*, J.B. Burland, J.R. Standing and F.M. Jardine (eds.), Thomas Telford, London, UK, pp.387-400.
- O'Reilly, M.P. & New, B.M., 1983. 831153 Settlement above tunnels in the United Kingdom — their magnitude and prediction. *International journal of rock mechanics and mining sciences & geomechanics abstracts.* 20 (1), A18–.
- Ocak, I. & Selcuk, E., 2017. Comparison of NATM and umbrella arch method in terms of cost, completion time, and deformation. Arabian journal of geosciences. 10 (7), pp.1–11.
- Oh, J.Y. & Ziegler, M., 2014. Investigation on influence of tail void grouting on the surface settlements during shield tunneling using a stress-pore pressure coupled analysis. *KSCE Journal of Civil Engineering*, *18*(3), pp.803-811.
- Oraee, B., Tavassoli, M. & Oraee, K., 2011. Designing shotcrete as primary support in tunnels. International Conference on Ground Control in Mining.

- Potts, D.M. & Zdravkovicì, L., 1999. *Finite element analysis in geotechnical engineering : theory*. London, Thomas Telford.
- Potts, D.M. & Zdravkovic, L., 2001. *Finite element analysis in geotechnical engineering. Application*. London, Thomas Telford.
- Powderham, A.J., 1994. An overview of the observational method: development in cut and cover and bored tunnelling projects. *Géotechnique.* 44 (4), pp.619–636.
- Qiao, Y., Zhao, T. & Ding, W., 2018. Simulating Synchronous Grouting in Shield Tunnels with the Consideration of Evolution of Grouting Pressure. In: Zhang D., Huang X. (eds) Proceedings of GeoShanghai 2018 International Conference: Tunnelling and Underground Construction. GSIC 2018. Springer, Singapore.
- Reichenspurner, P. & Riedel, T., 2020. Rohtang Tunnel – NATM in the Indian Himalayas. *Geomechanik und Tunnelbau*. 13 (5), pp.489–497.
- Rinaldi, V.A. & Santamarina, J.C., 2008. Cemented soils: small strain stiffness. *Deformational Characteristics of Geomaterials*, *1*, pp.267-273.
- Roscoe, K. & Burland, J.B., 1968. On the generalized stress-strain behaviour of wet clay.
- Roscoe, K., Schofield, A. & Thurairajah, A., 1963. Yielding of Clays in States Wetter than Critical. *Géotechnique*, 13(3), pp.211-240.
- Roscoe, K., Schofield, A. & Wroth, C., 1958. On The Yielding of Soils. *Géotechnique*, 8(1), pp.22-53.
- Royse, K.R., de Freitas, M., Burgess, W.G., Cosgrove, J., Ghail, R.C., Gibbard, P., King, C., Lawrence, U., Mortimore, R.N., Owen, H. & Skipper, J., 2012. Geology of London, UK. *Proceedings of the Geologists' Association*, *123*(1), pp.22-45.
- Schutz, R., 2010. *Numerical modelling of shotcrete for tunnelling* (Doctoral dissertation, Imperial College London).
- Schütz, R., Potts, D.M. & Zdravkovic, L., 2011. Advanced constitutive modelling of shotcrete: Model formulation and calibration. *Computers and Geotechnics*, *38*(6), pp.834-845.
- Schwer, L.E. & Murray, Y.D., 1994. A three-invariant smooth cap model with mixed hardening. *International journal for numerical and analytical methods in geomechanics*, *18*(10), pp.657-688.
- Shah, R., A. Lavasan, A., Peila, D., Todaro, C., Luciani, A. and Schanz, T., 2018. Numerical Study on Backfilling the Tail Void Using a Two-Component Grout. *Journal of Materials in Civil Engineering*, 30(3), p.04018003.
- Shanghai Geological Environmental Atlas Editorial Board (SGEAEB), 2002. *Shanghai Geological Environmental Atlas (SGEA).* Geology Press, Beijing
- Shanghai Municipal Bureau of Planning and Land Resources (SMBPLR) (2001–2009*). Shanghai geological environmental bulletin (2001–2009)* (in Chinese)

- Shen, S.-L., Cai, F.-X., Bai, T.-H., and Zhu, J.-M., 2006. Direction deviation control during double-O-tube (DOT) tunnel construction. *Underground Construction and Ground Movement, ASCE*, Reston, VA, pp.185–192.
- Shen, S.-L., Du, Y.-J. & Luo, C.-Y., 2010. Evaluation of the effect of rolling correction of double-o-tunnel shields via one-side loading. Canadian geotechnical journal. 47 (10), pp.1060–1070.
- Shen, S.-L., Horpibulsuk, S., Liao, S.-M. & Peng, F.-L., 2009. Analysis of the behavior of DOT tunnel lining caused by rolling correction operation. *Tunnelling and underground space technology*. 24 (1), pp.84–90.
- Shin, J.H., Potts, D.M. & Zdravkovic, L., 2005. The effect of pore-water pressure on NATM tunnel linings in decomposed granite soil. Canadian geotechnical journal. 42 (6), pp.1585–1599.
- Skempton, A.W., 1961. Horizontal stresses in an overconsolidated Eocene clay. In *Proc. of 5th Int. Conf. on SMFE* (Vol. 1, pp. 351-357).
- Song, Y., Wu, C. & Ye, G., 2018. Permeability and anisotropy of upper Shanghai clay. *Rock and Soil Mechanics.* 39(6), pp.2139-2144. (in Chinese)
- STANDING, J. & SELEMETAS, D., 2013. Greenfield ground response to EPBM tunnelling in London Clay. *Géotechnique*, 63(12), pp.989-1007.
- Standing, J.R. & Burland, J.B. 2006. Unexpected tunnelling volume losses in the Westminster area, London. *Géotechnique* Vol.56, No.1, pp.:11–26.

  Standing, J.R., 2020. Identification and implications of the London Clay Formation divisions from an engineering perspective. Proceedings of the Geologists' Association, 131(5), pp.486-499.
- Summersgill, F.C., Kontoe, S. and Potts, D.M., 2017. Critical assessment of nonlocal strain-softening methods in biaxial compression. *International Journal of Geomechanics*, *17*(7), p.04017006.
- Sun, D. Chen, B. & Zhou. K., 2010. Experimental study of compression and shear deformation characteristics of remolded Shanghai soft clay. *Rock and Soil Mechanics*, 31(5), pp.1389-1394. (in Chinese)
- Sun, T., 2007. *Research on the ground movement induced by the disturbance of multi-circular shield construction and its control technology.* PhD Thesis. Tongji University, Shang hai. (in Chinese)
- Suwansawat, S. & Einstein, H., 2007. Describing Settlement Troughs over Twin Tunnels Using a Superposition Technique. *Journal of Geotechnical and Geoenvironmental Engineering*, 133(4), pp.445-468.
- Taborda, D. & Zdravkovic, L., 2012. Application of a Hill-Climbing technique to the formulation of a new cyclic nonlinear elastic constitutive model. *Computers and Geotechnics*, 43, pp.80-91.

- Taborda, D., Potts, D. & Zdravković, L., 2016. On the assessment of energy dissipated through hysteresis in finite element analysis. *Computers and Geotechnics*, 71, pp.180-194.
- Tan, Y. & Wang, D., 2013. Characteristics of a Large-Scale Deep Foundation Pit Excavated by the Central-Island Technique in Shanghai Soft Clay. I: Bottom-Up Construction of the Central Cylindrical Shaft. *Journal of geotechnical and geoenvironmental engineering*. 139 (11), pp.1875–1893.
- Tan, Y., Wei, B., Diao, Y. & Zhou, X., 2014. Spatial Corner Effects of Long and Narrow Multipropped Deep Excavations in Shanghai Soft Clay. *Journal of performance of constructed facilities*. 28 (4), 4014015–.
- Teachavorasinskun, & Chub-uppakarn, T., 2010. Influence of segmental joints on tunnel lining. *Tunnelling and Underground Space Technology*, 25(4), pp.490–494.
- Thomée, B., 2005. *Physikalisch nichtlineare Berechnung von Stahlfaserbeton Konstruktionen* (Doctoral dissertation, Technische Universität München).
- TRHLíKOVá, J., MAšíN, D. & BOHáč, J., 2012. Small-strain behaviour of cemented soils. *Géotechnique,* 62(10), pp.943-947.
- Tsiampousi, A., Yu, J., Standing, J., Vollum, R. & Potts, D., 2017. Behaviour of bolted cast iron joints. *Tunnelling and Underground Space Technology*, 68, pp.113-129.
- Viggiani, G. and Atkinson, J.H., 1995. Interpretation of bender element tests. *Geotechnique*, *45*(1), pp.149-154.
- Wan, M., Standing, J., Potts, D. & Burland, J., 2017. Measured short-term ground surface response to EPBM tunnelling in London Clay. *Géotechnique*, 67(5), pp.420-445.
- Wan, M., Standing, J., Potts, D. & Burland, J., 2019. Pore water pressure and total horizontal stress response to EPBM tunnelling in London Clay. *Géotechnique*, 69(5), pp.434-457.
- Wan, M.S.P. 2014. *Field monitoring of ground response to EPBM tunnelling close to existing tunnels in London Clay*. PhD Thesis, Imperial College London.
- Wang, L., Shen, S., Bai, Y. & Peng, S., 2010. Characteristics of strength increase of cement treated Shanghai clayey soils. *Rock and Soil Mechanics*, 31(3), pp.743-747. (in Chinese)
- Wang, W., Xu, Z. & Li, Q., 2018. Design and construction of deep excavations in Shanghai, China. *Geotechnical research*. 5 (3), pp.143–161.
- Wei, D. & Hu, Z., 1980. Experimental study of preconsolidation pressure and compressibility of Shanghai subsoil. *Chinese Journal of Geotechnical Engineering*. 2(4), pp.13–22. (in Chinese)
- Wei, G., Chen, J. & Wei, X., 2011. Prediction of surface settlement induced by double-o-tube shield tunnel excavation. *Rock and Soil Mechanics.* 32(4), pp.991–996. (in Chinese)

- Wei, X., Honh, J. & Wei, G., 2012. Research on DOT Shield Tunnel Back-filled Synchronous Grouting Diffusion and Segments Circumferential Pressure Distribution. *Journal of Wuhan University of Technology. 34(10), pp.106-110.* (in Chinese)
- Wei, Z., 2003. *Quaternary Environmental Evolution in Eastern Yangtze Delta: Coupling of Neotectonic Movement, Paleoclimate and Sea-Level Fluctuation*. PhD Dissertation, East China Normal University, Shanghai. (in Chinese)
- Wu, C., Ye, G., Zhang, L., Bishop, D. & Wang, J., 2014. Depositional environment and geotechnical properties of Shanghai clay: a comparison with Ariake and Bangkok clays. *Bulletin of Engineering Geology and the Environment*, 74(3), pp.717-732.
- Wu, H., Shen, S. and Yang, J., 2017. Identification of Tunnel Settlement Caused by Land Subsidence in Soft Deposit of Shanghai. *Journal of Performance of Constructed Facilities*, 31(6), p.04017092.
- Wu, Y., Crawford, J.E. and Magallanes, J.M., 2012, June. Performance of LS-DYNA concrete constitutive models. In *12th International LS-DYNA users conference* (Vol. 1, pp. 1-14).
- Xie, D., Guan, F., Ding, W., 2016. Determination and Sensitivity Analysis of the Parameters of Hardening Soil Model with Small Strain Stiffness. China Earthquake Engineering Journal, 39(5), pp.898-906. (in Chinese)
- Xu, Y., Ma, L., Du, Y. & Shen, S., 2012. Analysis of urbanisation-induced land subsidence in Shanghai. *Natural Hazards*, 63(2), pp.1255-1267.
- Xu, Y., Ma, L., Shen, S. and Sun, W., 2012. Evaluation of land subsidence by considering underground structures that penetrate the aquifers of Shanghai, China. *Hydrogeology Journal*, 20(8), pp.1623-1634.
- Xu, Y., Shen, S. & Du, Y., 2009. Geological and hydrogeological environment in Shanghai with geohazards to construction and maintenance of infrastructures. *Engineering Geology*, 109(3-4), pp.241-254.
- Xu, Y., Shen, S., Ren, D. & Wu, H., 2016. Analysis of Factors in Land Subsidence in Shanghai: A View Based on a Strategic Environmental Assessment. *Sustainability*, 8(6), p.573.
- Yang, Zhou, Q., Li, H., Huang, X., & Tu, X., 2013. Analysis of Face Stability during Excavation of Double-O-Tube Shield Tunnel. *The Scientific World*, 2013, 781968–11.
- Yasuda, N., Misaki, N., Shimada, Y. & Kotyaev, O., 2021. Applicability of non-contact inspection using laser ablation-induced vibration in a reinforced concrete tunnel lining. *Tunnelling and underground space technology*. 113, 103977–.
- Ye, F., Yang, T., Mao, J., Qin, X. & Zhao, R., 2019. Half-spherical surface diffusion model of shield tunnel back-fill grouting based on infiltration effect. *Tunnelling and Underground Space Technology*, 83, pp.274-281.

- Ye, G. & Ye, B., 2016. Investigation of the overconsolidation and structural behavior of Shanghai clays by element testing and constitutive modeling. *Underground Space*, 1(1), pp.62-77.
- Ye, G., Hashimoto, T., Shen, S., Zhu, H. & Bai, T., 2015. Lessons learnt from unusual ground settlement during Double-O-Tube tunnelling in soft ground. *Tunnelling and Underground Space Technology*, 49, pp.79-91.
- Ye, S., Luo, Y., Wu, J., Teatini, P., Wang, H. & Jiao, X., 2015. Three dimensional numerical modeling of land subsidence in Shanghai. *Proceedings of the International Association of Hydrological Sciences*, 372, pp.443-448.
- Yonei, Y., 2000. Construction of common underground municipal facility using large diameter DOT shield. *Construction Technology Shield Tunnel.* Civil Engineering Press, Tokyo, pp.190–197 (in Japanese).
- Yu, J., Standing, J., Vollum, R., Potts, D. & Burland, J., 2017. Experimental investigations of bolted segmental grey cast iron lining behaviour. *Tunnelling and Underground Space Technology*, 61, pp.161-178.
- Yu, Z., Zhang, Y.,Wang, R. & Liang, X., 2004. The division and age of the Neogene strata in the Yangtze Delta Area. *Journal of Stratigraphy* 28 (3), pp.257–264 [in Chinese].
- Zeng, B. & Huang, D., 2016. Soil deformation induced by Double-O-Tube shield tunneling with rolling based on stochastic medium theory. *Tunnelling and underground space technology*. 60, pp.165–177.
- Zhang, & Koizumi, A., 2010. Behavior of composite segment for shield tunnel. *Tunnelling and Underground Space Technology*, 25(4), pp.325–332.
- Zhang, C., Wang, B. & Wan Z., 1981. The consolidated condition and shear strength behavior of soft clay at the bank of Huang-pu river, Shanghai. *Hydro-Science and Engineering*. (1), pp.12–22. (in Chinese)
- Zhang, J., Wang, W., Xu, Z., Li, Q., 2017. Laboratory test of small-strain characteristics of typical Shanghai cohesive soils. *Rock and Soil Mechanics,* 38(12), pp.1001-1008. (in Chinese)
- Zhang, Z., Shi, X., Wang, B. & Li, H., 2018. Stability of NATM tunnel faces in soft surrounding rocks. *Computers and geotechnics*. 96, pp.90–102.
- Zheng, G., Lu, P. & Diao, Y., 2015. Advance speed-based parametric study of greenfield deformation induced by EPBM tunneling in soft ground. *Computers and Geotechnics*, 65, pp.220-232.
- Zhou, H., Chen, T. & Li, L., 2012. Test and numerical analysis on performance of reinforced concrete segment in subway tunnel. *Transactions of Tianjin University*, *18*(1), pp.57-61.